THE ASSOCIATED PRODUCTION OF A Z GAUGE BOSON AND B-JETS AT LHC WITH THE ATLAS EXPERIMENT: FIRST DIFFERENTIAL CROSS SECTION MEASUREMENTS

PhD Candidate

Nicola Orlando

Supervisors

Dr. Stefania Spagnolo Dr. Gabriele Chiodini

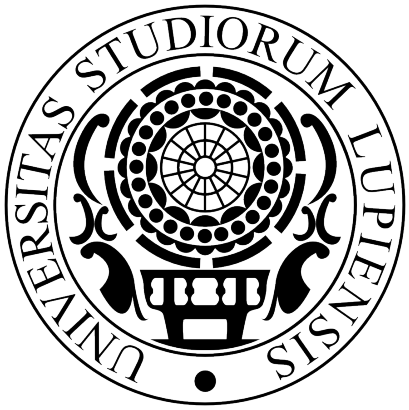

Dipartimento di Matematica e Fisica “Ennio De Giorgi”
Facoltà di Scienze MM.FF.NN.
Università del Salento

Lecce, Dottorato di ricerca in Fisica XXVI ciclo

CONTENTS

LIST OF TABLES

INTRODUCTION

The Large Hadron Collider (LHC) operating at Conseil Européen pour la Recherche Nucléaire (CERN) offers an unprecedented opportunity to study the elementary interactions occurring in nature, by colliding protons at design center of mass energy of 14 TeV.

The wide program of discovery physics at LHC requires a broad spectrum of measurements of known SM processes which are the physical background to the "New Physics" signatures.

The analysis presented as main subject of this PhD thesis is the measurement of the cross section for a SM process: the Z boson production in association with at least one or at least two b–jets (Z+b and Z+bb) at LHC at $\sqrt{s} = 7$ TeV; it has been carried out in the context of the Run 1 physics program of the ATLAS experiment.

The measurement of vector boson production in association with b–jets offers the opportunity to improve the understanding of the main irreducible backgrounds to Higgs boson production in association with a vector boson with the Higgs decaying into a $b\bar{b}$ pair; this is the Higgs boson discovery mode at Tevatron while at LHC, along with the "$\tau\tau$ channel", it is the most sensitive experimental final state for studying the Higgs coupling to fermions.

The production of b–jet in association with a Z boson has been measured only recently at Tevatron and at LHC. The differential and inclusive Z+b cross sections have been measured for the first time at Tevatron with limited data statistics; the results are apparently controversial showing that the available theoretical predictions are rarely in a satisfying agreement with the data; the measurements highlight a poor modeling of the angular correlations between the Z boson and the b–jets, whereas simple observables, like the b–jet transverse momentum, are well predicted; it has been also observed a typical offset of the total cross section among the data and the theory predictions. At LHC the first Z+b cross section measurements confirm the tension between the total measured and predicted cross section. The CMS experiment has also recently published a measurement of the angular correlations between two b–hadrons produced in association with the Z boson; this analysis points to an interesting data excess in the kinematic region where the two b–hadrons are collinear suggesting the need for a refinement of the theory predictions for the rate of gluon splitting in a b–quark pair.

In spite of the variety of results published by the experiments at LHC, it is currently still missing a study of the Z boson production in association with a single b–jet as a function of the kinematic properties of the Z+b system. This gap is covered by the ATLAS measurement which is the main topic of this work.

The interest for this study has several reasons. The predictions for this process are subject to rather large uncertainties compared to the experimental precision that can be achieved. The measurement of the cross section as a function of the Z transverse momentum and rapidity is a key ingredient to validate event generators and, in principle, it can offer a remarkable experimental handle to constrain with

data the b–quark parton distribution function of the proton. The kinematics of the b–jets and the angular correlations between b–jets and Z boson are of great interest mainly for testing the modeling of event generators since these observables are used as signal to background discriminators in New Physics searches or Higgs measurements.

A variety of theory approaches have been developed in the context of perturbative Quantum Chromo Dynamics for the description of heavy flavor production in hadron–hadron collisions. They exploit different kinds of approximations in the matrix element, in the PDF, for the definition of the initial state, and in the treatment of the parton showering, and typically they lead to predictions not fully in agreement with each other.

The comparison of Z+b cross section measurements with the corresponding measurements for Z+bb may help to identify the most suitable theoretical tools and approaches for the description of processes with heavy quarks in the initial and final state at LHC.

The first part of this work is mainly an introduction to basic concepts, phenomenological and experimental, which will be extensively used to describe the data analysis and the results presented in the second part. The introductory part is split in two chapters; in Chap. 1 a brief summary of the Standard Model phenomenology at LHC is given; in Chap. 2 the ATLAS experiment is introduced and the definitions and reconstruction procedures of the physics objects (e.g., leptons and jets) used in the data analysis are discussed. The performance measurements used to estimate the experimental uncertainty on reconstructed physics objects are introduced. The measurement of the low–p_T muon reconstruction efficiency is discussed in some detail as an example since I developed the procedure and performed the measurement with the 2010 dataset.

The second part of the thesis is devoted to a detailed discussion of the work leading to the first differential measurement of the cross section for the Z production in association with at least one b–jet.

In Chap. 3 the measurement of the Z+b production at Tevatron and, with early data, at LHC is presented. Among these results, the first ATLAS measurement with the low statistic dataset of 2010 is described. This analysis, that I contributed to produce during 2011, is based on techniques which have been refined and optimized for the measurement described in this thesis. In Chap. 4 the $Z + b$ selection, based on two same flavor leptons (electrons or muons) and at least one b–tagged jet, is described along with the background processes. The estimation of the background from Z+light and Z+charm jets is a key step of the analysis implemented through a fit of the distribution of a b–sensitive variable. In Chap. 5 the measurement of the integrated and differential cross section is performed based on the selection results. The most relevant uncertainties are discussed. Finally in Chap. 6 the results of the analysis are discussed along with the measurements of four differential cross sections for Z boson production in association with at least two b–jets. The similarities and also the differences between the two final states strengthen the physical interpretation of the data–theory comparison. Several state of the art theory predictions, produced specifically for the signal definition of this analysis, with a wide spectrum of tools implementing different types of calculations are compared to data allowing for a solid interpretation of the results.

All the steps of the analysis, from the optimization and the implementation of the selection up to the derivation of the theory predictions, are directly the result of my own work, which has been clearly discussed and cross checked within a small team of ATLAS colleagues. In particular I've been taking responsibilities within the analysis group for the selection, background estimation, including the derivation of the multijet contamination from data, flavor fit and its optimization, detector effects unfolding and most of the systematic checks for the Z+b final state; in addition I've been directly working to the derivation of the theory predictions for both the Z+b and Z+bb final state.

The results presented in this thesis are the most complete study to date of heavy flavor production in association with a vector boson; they will be presented in an incoming publication [1].

Part I

EXPERIMENTAL AND PHENOMENOLOGICAL FRAMEWORK

1

PHENOMENOLOGY OF STRONG INTERACTIONS AT LHC

The current accepted description of the elementary particle interactions is based on the Standard Model [2, 3, 4] (SM) of particle physics; it provides simultaneously a common ground for describing the electromagnetic, the weak and the strong interactions and it has been tested over a few decades with several measurements by different experiments [5]. Nevertheless, at the beginning of the 21th century a few compelling problems in the field of the elementary particle physics are still open:

- the experimental establishment of the mass generation mechanism for the observed particles is just started;
- the observed fermions mass hierarchy and the mixing of the quark flavors in the SM have a very characteristic structure which is believed to originate from unknown physics at high energy scales not yet explored;
- the neutrino flavor oscillation is a well established experimental observation which can not be explained within the SM;
- the nature of the Dark Matter and Dark Energy, which account respectively for $\sim 27\%$ and $\sim 68\%$ of the observed content of the Universe is still unknown;
- the fine tuning of the SM parameters in the electroweak sector, necessary to preserve a finite mass of the Higgs boson, suggests that more fundamental symmetries exist in nature; in spite of the missing evidence for Beyond Standard Model (BSM) physics so far, most of the theory models based on Supersymmetry [6], or based on extended space time dimensions [7, 8, 9] predict new phenomena at the TeV scale.

In the last decades of the 20th century a general experimental strategy aiming at addressing these problems was defined with the construction of the Large Hadron Collider, a proton–proton collider of unprecedented energy and luminosity. The experiments *A Toroidal LHC ApparatuS*, ATLAS, and the *Compact Muon Solenoid*, CMS, were designed as "general purpose" detectors in order to be able to explore the largest possible variety of experimental signatures. Their performance was optimized to guarantee the success in the observation of the SM Higgs boson in the entire mass range theoretically motivated (below $\sim$ 1–2 TeV) and experimentally not tested in previous experiments (above $\sim$ 100 GeV).

The first data taking period at LHC, *Run* 1, from April 2010 to December 2012, culminated with the discovery of a new massive neutral particle, of mass of about 126 GeV, announced on the 4th July 2012 at CERN by a joint ATLAS/CMS seminar [10, 11, 12]; this result has been also confirmed by a weaker experimental signal in the Tevatron data [13] by the CDF and D$\emptyset$ experiments. Soon later it has been understood that this newly discovered particle is a spin–0 boson with the

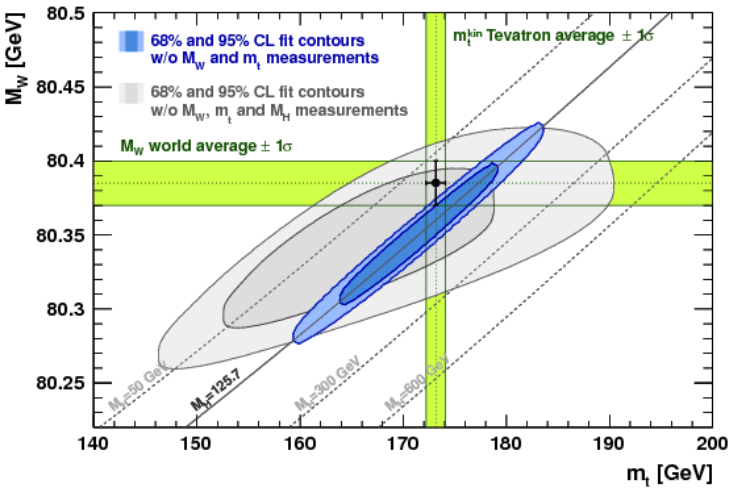

Figure 1: Contour plots in the m_t–M_W from the global electroweak fits [18] with (blu area) and without (grey area) the inclusion of the Higgs mass measurements at the LHC [19, 20].

same quantum numbers associated to the Higgs boson which is introduced in the Standard Model by the Higgs mechanism for the mass generation.

This discovery was immediately realized as a breakthrough in the field of elementary particle physics and it led on the 8th October 2013 to the assignment of the Nobel Prize in Physics to F. Englert and P. Higgs for the theoretical proposal of the Higgs boson [14, 15, 16, 17] observed by the ATLAS and the CMS experiments.

In this chapter a basic phenomenological description of the elementary particle interactions in the Standard Model is given, with emphasis on the strong interactions phenomenology relevant at the Large Hadron Collider.

The Standard Model is introduced in Sec. 1.1. The main aspects concerning the phenomenological description of proton–proton collisions at the LHC are summarized in Sec. 1.2; namely, the structure of the perturbative expansion and the parton–shower method implemented in modern Monte Carlo event generators are described; the modeling of non–perturbative strong dynamic relevant for high-p_T phenomenology at LHC is briefly summarized. A short collection of some recent and significant tests and studies of strong interactions at the LHC are presented in Sec. 1.3.

1.1 THE STANDARD MODEL OF PARTICLE PHYSICS

The Standard Model of particle physics is a gauge theory which successfully describes in a common framework the strong, weak and electromagnetic interactions occurring in nature. It is based on the gauge group $SU(3)_C \otimes SU(2)_L \otimes U(1)_Y$. This symmetry is however "hidden" by the electroweak breaking (EWSB) mechanism, which preserves the explicit symmetry under $SU(3)_C \otimes U(1)_{QED}$.

The SM interactions are mediated by spin–1 particles, the gauge bosons. Eight massless gluons are responsible for the strong interactions, one massless photon mediates the electromagnetic interaction and three massive bosons, $W^{\pm}$ and Z, are

the weak force carriers. The gluons are simultaneously mass and gauge eigenstates corresponding to the generators of the unbroken $SU(3)_C$ symmetry. In the electroweak sector, because of the EWSB, the gauge (massless) eigenstates corresponding to the generators of $SU(2)_L \otimes U(1)_Y$ do not correspond to the mass eigenstates ($W^{\pm}$, Z and the photon, γ) of the theory; the physical gauge bosons are obtained by a rotation with angle θ_W, the Weinberg (or mixing) angle, which is determined at tree level only by the $SU(2)_L$ and $U(1)_Y$ gauge couplings.

The matter content of the Standard Model consists of spin–1/2 fermions: three flavor families of quarks and leptons. The left handed fields, which are $SU(2)_L$ doublets are

$$\text{Left handed quarks:} \quad \begin{pmatrix} q_u \\ q_d \end{pmatrix}_L = \left[\begin{pmatrix} u \\ d \end{pmatrix}_L , \begin{pmatrix} c \\ s \end{pmatrix}_L , \begin{pmatrix} t \\ b \end{pmatrix}_L \right] ,$$

$$\text{Left handed leptons:} \quad \begin{pmatrix} \ell \\ \nu_\ell \end{pmatrix}_L = \left[\begin{pmatrix} \nu_e \\ e \end{pmatrix}_L , \begin{pmatrix} \nu_\mu \\ \mu \end{pmatrix}_L , \begin{pmatrix} \nu_\tau \\ \tau \end{pmatrix}_L \right] .$$

The corresponding right handed states of quarks and charged leptons

$$\text{Right handed quarks:} \quad q_R = (u, d, c, s, t, b)_R ,$$
$$\text{Right handed leptons:} \quad \ell_R = (e, \mu, \tau)_R ,$$

are $SU(2)_L$ singlets.

The physical mass eigenstate fermions are superposition of left and right handed fields. In the minimal formulation of the Standard Model the neutrinos ν_e, ν_μ and ν_τ are assumed to be pure left handed states under $SU(2)_L$. This is clearly an assumption which conflicts with the well established evidence for neutrino oscillations, implying non null masses.

The Standard Model spectrum is completed by the Higgs boson, the only spin–0 particle of the SM, which corresponds to the fluctuation of the Higgs field around the vacuum triggering the electroweak symmetry breaking with the so called Higgs mechanism. The non–zero value of the Higgs field vacuum is responsible for generating the masses in the Standard Model, both for the massive gauge bosons, via kinetic coupling to the Higgs field, and for the fermions, by means of Yukawa–like interactions between the Higgs field, the right handed and the left handed fermionic fields.

The particle content of the Standard Model is summarized in Tab. 1 along with quantum charge assignments.

In the Standard Model the gauge interactions are almost completely determined by the underlying symmetry group, provided that the strong, α_s, the weak, α_{EW}[1], and the electromagnetic, α_{em}, couplings are measured. However the model does

1 Usually the α_{EW} is not used, instead the coupling of the weak interactions is given in terms of the Fermi coupling constant

$$G_F = \frac{\sqrt{2} g_{EW}^2}{8 M_W} = \frac{\sqrt{2}\pi}{2} \frac{\alpha_{EW}}{M_W} ,$$

being M_W the W boson mass and g_{EW} the gauge coupling associated to the $SU_L(2)$ gauge sector.

Particle name	Symbol	Color state	Electric charge
Bosons			
Higgs	H	singlet	0
W^-	W^-	singlet	-1
Z^0	Z	singlet	0
Photon	γ	singlet	0
Gluon	g	octet	0
Quarks			
Top	t	triplet	$2/3$
Bottom	b	triplet	$-1/3$
Charm	c	triplet	$2/3$
Strange	s	triplet	$-1/3$
Up	u	triplet	$2/3$
Down	d	triplet	$-1/3$
Leptons			
τ^-	τ^-	singlet	-1
τ neutrino	ν_τ	singlet	0
Muon	μ^-	singlet	-1
Muonic neutrino	ν_μ	singlet	0
Electron	e^-	singlet	-1
Electronic neutrino	ν_e	singlet	0

Table 1: Particle content of the Standard Model and quantum charge assignment for the gauge sectors $SU(3)_C$ and $U(1)_{QED}$.

not predict the masses of particles which need to be directly measured or indirectly constrained fitting the model parameters to the data measurements. One additional complication arises in the quark sector, where the mass eigenstates of the quark fields are a mixture of gauge eigenstates determined by a 3–dimensional complex unitary matrix, the Cabibbo–Kobayashi–Maskawa (CKM) matrix, which introduces four more free parameters: three angles and one phase. In the leptonic sector, assuming massless neutrinos, the fermions are simultaneously gauge and mass eigenstates, thus the corresponding mixing matrix is proportional to the identity matrix.

The world average Particle–Data–Group (PDG) [5] values for the free parameters of the Standard Model are summarized in Tab. 2.

With the observation of the Higgs boson by ATLAS and CMS experiments at LHC and its mass measurements, all the Standard Model input parameters have been measured. This allows to test the Standard Model with global fit to the experimental data; recently the global fit to the electroweak sector, "electroweak fit", have received significant updates [21] and the effect of including the Higgs mass measurement has been studied as well [18].

Couplings		
$\alpha_s = 0.1184(7)$		
$\alpha_{em} = 7.2973525698(24) \times 10^{-3}$		
$G_F = 1.1663787(6) \times 10^{-5} GeV^{-2}$		
Higgs mass [GeV]		
$M_H = 125.9 \pm 0.4$		
Z mass [GeV]		
$M_Z = 91.1876 \pm 0.0021$		
Up–type quarks masses [GeV]		
$m_t = 173.07 \pm 0.52 \pm 0.72$	$m_c = 1.275 \pm 0.025$	$m_u = (2.3^{+0.7}_{-0.5}) \times 10^{-3}$
Down–type quarks masses [GeV]		
$m_b = 4.66 \pm 0.03$	$m_s = (95 \pm 5) \times 10^{-3}$	$m_d = (4.8^{+0.5}_{-0.3}) \times 10^{-3}$
Leptons masses [MeV]		
$m_\tau = 1776.82(16)$	$m_\mu = 105.6583715(35)$	$m_e = 0.510998928(11)$
CKM matrix parameters		
$\lambda = 0.22535 \pm 0.00065$	$A = 0.811^{+0.022}_{-0.012}$	$\overline{\rho} = 0.131^{+0.026}_{-0.013}$
	$\overline{\eta} = 0.345^{+0.013}_{-0.014}$	

Table 2: Free parameters of the Standard Model; the neutrinos are taken to be massless so no neutrinos masses and leptonic flavor mixing matrix elements are given.

The status of the electroweak fit and the impact of the direct Higgs mass (M_H) measurement is summarized in Fig. 1, where the 2–D contour in the m_t–M_W plane is shown with and without the inclusion of M_H measurement in the fitted observables. As a test of compatibility between the Standard Model and the global electroweak fits the fit p–value has been calculated to be [18]:

$$p(\chi^2_{min} = 21.8, N_{dof} = 14; data|SM) = 0.07 \qquad \text{(including } M_H \text{ data)}\,, \qquad (1)$$

where χ^2_{min} is the global χ^2 and N_{dof} is the number of degrees of freedom. The same fit performed without the inclusion of the Higgs mass has a slightly higher p–value:

$$p(\chi^2_{min} = 17.96, N_{dof} = 14; data|SM) = 0.22 \qquad \text{(excluding } M_H \text{ data)}\,, \qquad (2)$$

due to the preference of the electroweak precision data for values of the Higgs mass lower that the direct measurements. Another stringent test of the Standard Model comes from the study of the flavor structure in the Yukawa quark sector. The CKM matrix elements have been measured without assumptions of symmetry on the matrix, in several experimental final states. The global PDG fit to the flavor data is summarized in Fig. 2 in the $\overline{\eta}$–$\overline{\rho}$ plane[2], with the global fit result shown in red shaded area at 95% confidence level.

2 The standard notation for the $\overline{\eta}$ and $\overline{\rho}$ Wolfenstein parameters has been used, see for example Ref. [22]

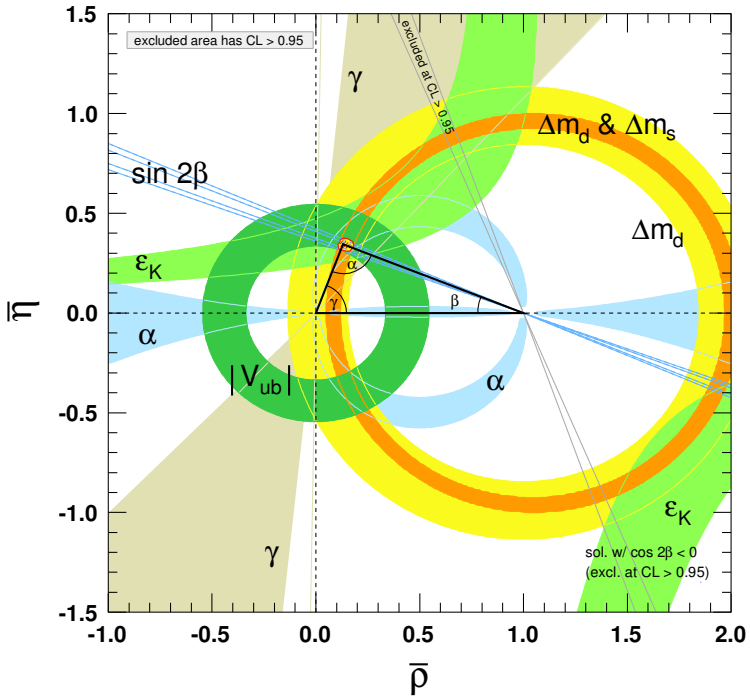

Figure 2: Global fit to flavor data [5] shown in the $\overline{\eta}$–$\overline{\rho}$ plane.

1.2 PROTON–PROTON INTERACTIONS AT LHC

The theoretical description of a proton–proton collision at LHC relies on a complex interplay between perturbative theoretical computations based on the SM lagrangian, phenomenological models and use of experimental data. A typical hard event at LHC involves the production of tens of charged and neutral particles; some of them are unstable, thus decay immediately after the production. Moreover, during the collision, being the protons complex objects, rescattering phenomena involving proton remnants occur in addition to the hard primary interaction leading to the so called underlying event (UE). Finally, in order to provide a reliable theory prediction, all the particles produced in pp collisions have to be described fully differentially in order to take into account the finite acceptance of the detectors.

The average number of events, $N(X)$, for a given precess $pp \to X$ at LHC is given by

$$\langle N(X) \rangle = \epsilon \cdot \sigma(X) \cdot \int_{\Delta t} \mathcal{L} dt \; ; \tag{3}$$

where $\sigma(X)$ is the production cross section, ϵ is the efficiency, and $\mathcal{L}$ is the instantaneous luminosity.

A full theory prediction for $\sigma(X)$ should be defined in terms of final states stable particles[3]. Symbolically, a generic cross section, σ, can be defined by a convolution of perturbative and non perturbative "kernels":

$$\sigma = \overbrace{\mathrm{PDFs}(\{x_i\},\{\theta_1\})}^{\text{Parton Distribution Functions}} \otimes \overbrace{\mathrm{M.E.}(\{x_i\},\{p_i\}^{(1)},\{\theta_2\})}^{\text{Matrix Element}} \otimes \overbrace{\mathrm{P.S.}(\{p_i\}^{(2)},\{\theta_3\})}^{\text{Parton Shower}} \otimes \\ \otimes \underbrace{\mathrm{Had.+Frag.}(\{p_i\}^{(3)},\{\theta_4\})}_{\text{Hadronization + Fragmentation}} \otimes \underbrace{\mathrm{U.E.}(\{p_i\}^{(3)},\{\theta_4\})}_{\text{Underlying event}} \otimes \underbrace{\mathrm{Decays}(\{p_i\}^{(4)},\{\theta_5\})}_{\text{Unstable particle decays}} , \quad (4)$$

where the building blocks depend on theory parameters $\{\theta_i\}$, parton and/or particle four–momenta $\{p_i\}^{(j)}$, and on the fraction of longitudinal momentum carried by the incoming partons $\{x_i\}$. The $\{\theta_i\}$ parameters are either fundamental theory constants or model parameters extracted from data, or energy scales related to the residual error on the perturbative expansion.

Several theory predictions are based on the calculation of the matrix element convoluted only with PDFs and are referred to as *parton level* predictions. They can be obtained by perturbative expansions at a fixed α_s order (Fixed–Order, FO) and sometimes are supplemented by resummation at all orders of a subset of perturbative corrections which can be particularly relevant in specific phase space regions. In this approach the description of the non perturbative physics, like the underlying event, which leads to changes to the perturbative observables, is not taken into account. These limitations are overcome by Monte Carlo (MC) event generators which provide fully differential theory predictions by implementing a model or a calculation for each of the contributions listed in Eq. 4.

In the following a short description of the building blocks of Eq. 4 is given.

1.2.1 *Parton distribution functions for the LHC*

The parton distribution functions, introduced in the context of the *collinear factorization theorems* [23, 24, 25], describe the probability density of the longitudinal momentum fraction carried by partons inside hadrons. They are intrinsically non–perturbative objects derived from a global fit to experimental data and perturbatively evolved to different energy scales by solving the DGLAP evolution equations.

The parton distribution function sets typically used by LHC experiments are accessible through a common software interface, LHAPDF [26].

Broadly speaking, the PDF families differ by the choice of input experimental data, statistical treatment of the data, theoretical methods and assumptions. From the point of view of PDF users, the statistical treatment of the data is the most relevant feature of each PDF family as it determines how the PDF sets are delivered to the user and how they are used to calculate hadronic cross sections and PDF related uncertainties. In this context the PDF sets can be split into two classes: the PDFs which use the "Hessian" method and the sets based on Monte–Carlo approach; the only PDF family based on the Monte Carlo method are the NNPDF [27],

3 The word stable in this context is used to refer to particles with a lifetime long enough to allow the particle to hit the detectors and to be possibly identified. This definition is subject to conventions and will be further discussed afterwards.

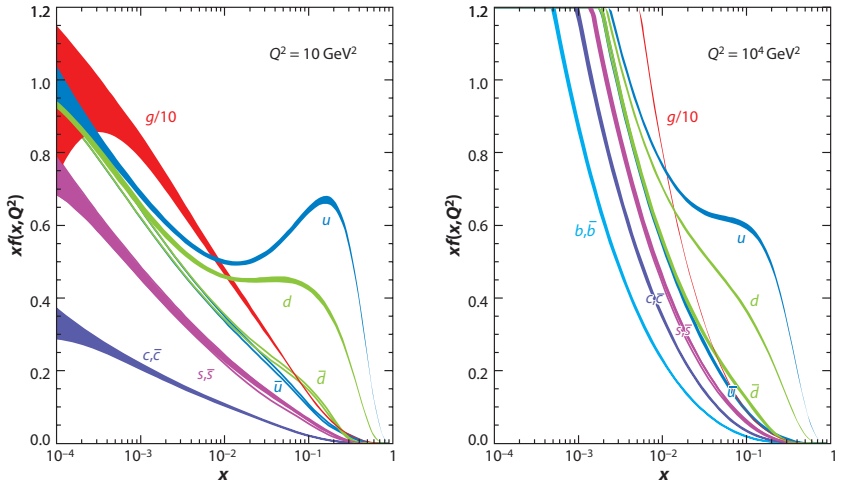

Figure 3: Momentum fraction density $xf(x, Q^2)$ as a function of x at two energy scales $Q^2 = 10$ GeV^2 and $Q^2 = 10^4$ GeV^2 for the NNLO MSTW2008 from Ref. [32].

while all the other commonly used PDF families, CT10 [28], MSTW2008 [29] and ABKM09 [30], employ the Hessian method.

In the next section the main features of the PDFs are described; extensive reviews are [31, 32].

1.2.1.1 *Experimental data input*

The experimental data used as input to the PDF fits are deep–inelastic–scattering (DIS) data coming from fixed–target and HERA experiments, and hadron collider data from Tevatron and, more recently, from LHC. Different experimental data are sensitive to different parton density functions and probe complementary ranges of the Bjorken variable x and of the partonic center–of–mass energy squared Q^2. In Tab. 3 the data used in the PDFs fit for four examples of PDF sets, namely CT10, MSTW2008, NNPDF2.3 and ABKM09, are summarized.

	Fixed–target DIS	HERA DIS	Tevatron	LHC
x range	$10^{-3} - 1$	$10^{-6} - 0.1$	$10^{-3} - 1$	$10^{-4} - 1$
Q^2 range [GeV]	$0.2 - 3 \cdot 10^2$	$2 \cdot 10^{-2} - 4 \cdot 10^3$	$2 \cdot 10^3 - 2.5 \cdot 10^5$	$10^2 - 10^8$
CT10	yes	yes	yes	no
MSTW2008	yes	yes	yes	no
NNPDF2.3	yes	yes	yes	yes
ABKM09	yes	yes	no	no

Table 3: Brief summary of experimental data used in global fit for the determination of the PDF sets CT10, MSTW2008, NNPDF2.3 and ABKM09. The range of x and Q^2 reported to the experimental data is only a qualitative order of magnitude estimation based on the talk [33].

The ABKM09 set has the special feature of been based only on DIS data; the only commonly used PDFs family which includes the LHC data is NNPDF2.3. However,

several progresses toward the inclusion of the LHC data have been reported by all the PDF Collaborations in specialized meetings [34] and future releases of PDF sets with more use of LHC data are foreseen.

A global view of different parton density functions is given in Fig. 3 using the NNLO MSTW2008 set from Ref. [32]; the momentum fraction density $xf(x, Q^2)$ is shown as a function of x at the scale $Q^2 = 10\ GeV^2$ and $Q^2 = 10^4\ GeV^2$ for the active flavors at each scale.

1.2.1.2 *PDFs related uncertainties*

As already anticipated in Sec. 1.2.1 the statistical treatment of the experimental data has the most direct impact on the PDFs usage as it induces different prescription for the calculation of hadronic cross section and uncertainties related to PDFs.

The PDF Collaborations determine the PDFs with a χ^2 fit of the PDFs–dependent theory predictions to the experimental data; the fitted free parameters determine the PDF shapes.

The PDFs are parametrized at some initial scale Q_o typically by using a polynomial representation where the density function for the i–th parton $f_i(x, Q_o)$ can be expressed, for example, as in Ref. [31]:

$$f_i(x, Q_o) = Ax^{\alpha_i}(1-x)^{\beta_i}(1 + a_i\sqrt{x} + b_i x + c_i x^2) \tag{5}$$

indicating with A the normalization factor and α_i, β_i, a_i, b_i and c_i a set of parameters which define the shape of $f_i(x, Q_o)$ at the initial scale Q_o. The parametrization of the PDFs are chosen to provide sufficient flexibility, however they introduce some subjectivity in the choice and a potential, though small, bias in the PDF determination.

In the Monte Carlo approach used by the NNPDF Collaboration the experimental data are not directly used to perform a global fit. Instead a set of N_{rep} dataset replicas are built and for each dataset a χ^2 fit is performed; correspondingly, N_{rep} PDF sets are derived. In this framework a fit to the data replica is used to obtain the PDF replica $f_i(x, Q_o)$ expressed in the form

$$f_i(x, Q_o) = g_i(x)NN_i(x) \tag{6}$$

where $NN_i(x)$ is the response of a neural network and $g_i(x)$ is the so called "preprocessing" function which is set a priori to a functional form like $Ax^{\alpha_i}(1-x)^{\beta_i}$; thus the PDF parametrization Eq. 6 turns out to be consistent with the choice of Eq. 5 but with a more general weighting function than a polynomial. The global PDF fit determines the shape of the neural network $NN_i(x)$ where the function $g_i(x)$ is fixed a priori. The central prediction for the cross section, $\langle\sigma\rangle^{(PDFs)}$, can be obtained by averaging over the N_{rep} PDF replicas.

In addition to the difference in the determination of the central value for the cross sections there are substantial differences in the determination of the PDFs related uncertainties.

The NNPDF Collaboration uses the PDF replicas to define the cross section uncertainty due to the PDFs determination, driven by the uncertainty on the input

experimental data. The 68% confidence level for the central value of the cross sections prediction $\langle\sigma\rangle^{(PDFs)}$ is then defined as the ensamble standard deviation over the PDFs replicas

$$\Delta\sigma_{PDFs} = \sqrt{\frac{1}{N_{rep}-1}\sum_{k=1}^{N_{rep}}\left(\sigma(\{f^{(k)}\}) - \langle\sigma\rangle^{(PDFs)}\right)^2}\,. \tag{7}$$

In the Hessian approach the covariance matrix is diagonalized and the resulting 2·N new PDF sets, $\{f^{+,(k)}\}$ and $\{f^{-,(k)}\}$ (with $k = 1,..,N$), N being the total of parameters used to define the shape of the PDFs, can be defined by a 68% confidence level shifts along the eigenvector directions. The PDFs upward and downward uncertainties, $\Delta\sigma^{+}_{PDFs}$ and $\Delta\sigma^{-}_{PDFs}$, on the cross section central values σ_0 are given by

$$\Delta\sigma^{+}_{PDFs} = \sqrt{\sum_{j=1}^{N}\left[max(\sigma^{+}_{j}-\sigma^{0}, \sigma^{-}_{j}-\sigma_0, 0)\right]^2}\,, \tag{8}$$

$$\Delta\sigma^{-}_{PDFs} = \sqrt{\sum_{j=1}^{N}\left[max(\sigma_0-\sigma^{+}_{j}, \sigma_0-\sigma^{-}_{j}, 0)\right]^2}\,, \tag{9}$$

where σ^{+}_{j} (σ^{-}_{j}) is a short notation for $\sigma(\{f^{+,(k)}\})$ ($\sigma(\{f^{-,(k)}\})$) and the central value of the cross section is calculated evaluating the cross section with the central PDFs set, namely $\sigma_0 = \sigma(\{f^{(0)}\})$.

Beyond the PDF uncertainties from the experimental data input, the cross section predictions are affected also by the uncertainties on the value of α_s which is correlated with the PDFs.

	Nominal $\alpha_s(M_Z)$ value	$\alpha_s(M_Z)$ variations
CT10	0.1180 (input)	$\{0.112, 0.113, ..., 0.126\}$
MSTW2008	0.1202 (NLO fit)	$0.1202^{+0.0012}_{-0.0015}$
NNPDF2.3	0.119 (input)	$\{0.114, 0.115, ..., 0.124\}$
ABKM09	0.1129 (NNLO fit)	0.1129 ± 0.0014

Table 4: Summary of central values and variations of $\alpha_s(M_Z)$ used by CT10, NNPDF, MSTW2008, ABKM09.

All the PDF sets are given at a specific α_s value; some PDF Collaborations (e.g. CT10, NNPDF) use α_s as an input parameter in the global fit, while other Collaborations (e.g. MSTW2008, ABKM09) derive α_s from the fit. The α_s values used or determined by the different PDF families are listed in Tab.4 together with the available variations of α_s. Different methods are used for the treatment of the α_s uncertainty, some of them are listed below as examples.

- ABKM09: the uncertainties on α_s are already included in the eigenvectors variations of the Hessian matrix.

- CT10: the central value of α_s is fixed to be 0.118; four additional PDF sets are generated with $\alpha_s = 0.116,\ 0.117,\ 0.119,\ 0.120$. The variations with respect to the nominal cross section are then evaluates as

$$\Delta\sigma^{+}_{\alpha_s} = \sigma((\alpha_s + \Delta\alpha_s), \{f^{(\alpha_s+\Delta\alpha_s)}\}) - \sigma_0 \,, \quad (10)$$

$$\Delta\sigma^{-}_{\alpha_s} = \sigma((\alpha_s - \Delta\alpha_s), \{f^{(\alpha_s-\Delta\alpha_s)}\}) - \sigma_0 \,, \quad (11)$$

  with $\Delta\alpha_s = 0.001$ ($\Delta\alpha_s = 0.002$) at 68% (90%) of confidence level; the combined PDFs $+ \alpha_s$ uncertainty is given by the sum in quadrature of the two components

$$\Delta\sigma^{+}_{\mathrm{PDFs}+\alpha_s} = \sqrt{(\Delta\sigma^{+}_{\mathrm{PDF}})^2 + (\Delta\sigma^{+}_{\alpha_s})^2} \quad (12)$$

$$\Delta\sigma^{-}_{\mathrm{PDFs}+\alpha_s} = \sqrt{(\Delta\sigma^{-}_{\mathrm{PDF}})^2 + (\Delta\sigma^{-}_{\alpha_s})^2} \quad (13)$$

- MSTW2008: additional global fits are performed with fixed values of α_s (treated as an input parameter) corresponding to shifts of the fitted value by $\pm 0.5\Delta\alpha_s$ and $\pm\Delta\alpha_s$, being $\Delta\alpha_s$ the uncertainty on the fitted value associated to the central PDFs set. The combined PDFs $+ \alpha_s$ uncertainty is then evaluated as

$$\Delta\sigma^{+}_{\mathrm{PDFs}+\alpha_s} = \max_{\alpha_s}\{\sigma^{(\alpha_s)}(\{f^{(0)}\}) + \Delta\sigma^{+\,(\alpha_s)}_{\mathrm{PDF}}\} - \sigma_0 \,, \quad (14)$$

$$\Delta\sigma^{-}_{\mathrm{PDFs}+\alpha_s} = \sigma_0 - \min_{\alpha_s}\{\sigma^{(\alpha_s)}(\{f^{(0)}\}) - \Delta\sigma^{-\,(\alpha_s)}_{\mathrm{PDF}}\} \,, \quad (15)$$

  where $\Delta\sigma^{+\,(\alpha_s)}_{\mathrm{PDF}}$ ($\Delta\sigma^{-\,(\alpha_s)}_{\mathrm{PDF}}$) is the PDFs uncertainty evaluated as in Eq. 8 (Eq. 9) calculating the QCD matrix element at the given α_s value.

- NNPDF: the combined PDFs $+ \alpha_s$ uncertainty is derived as a generalization of Eq. 7, where the ensemble standard deviation is calculated over a set PDFs, which includes replicas associated to α_s variations each of them weighted according to the gaussian probability for the specific α_s value.

1.2.2 *Fixed order predictions in perturbative QCD*

As already mentioned in Sec. 1.2 several publicly available tools make use of a simplified approach for the cross section predictions by providing only the PDFs convoluted partonic cross sections. Although this approach introduces inherent approximations it is worth noting that there are no available procedures to have a full implementation of Eq. 4 with the same accuracy currently reached in most advanced parton level calculations. These limitations are driven by the lack of a general procedure to combine high order perturbative parton level calculations with parton shower algorithms as it will be discussed in Sec. 1.2.3.1.

There have been impressive advances in parton level calculations in the past ten years and more advances are foreseen in the next years. The current state of the art is partially illustrated in Tab. 5. Here the desired and planned improvements in 2007 are reported as defined by the "wishlist" of the Les Houches workshop [35]; these calculations are today all completed. The next challenge is illustrated by the 2013 wishlist [36] where high multiplicity predictions at NNLO accuracy in QCD

From 2007 [35] LH wishlist (completed)	From 2013 LH wishlist
NLO QCD $pp \to H + 2jets$	NNLO QCD + NLO EW $pp \to H + 2jets$
NLO QCD $pp \to t\bar{t}b\bar{b}$	NNLO QCD $pp \to HH$
NLO QCD $pp \to b\bar{b}b\bar{b}$	NNLO QCD + NLO EW $pp \to 2jets$
NNLO QCD $pp \to t\bar{t}$	NNLO QCD + NLO EW $pp \to 3jets$
NLO QCD $pp \to V + 3jets$	NNLO QCD + NLO EW $pp \to \gamma + jets$
NNLO QCD + NLO EW $pp \to W/Z$	NNLO QCD $pp \to V + b\bar{b}$

Table 5: Representative processes relevant for the LHC physics, calculated and planned perturbative order of the predictions according to the 2007 [35] and 2013 [36] Les Houches wishlists.

are listed; most of them includes electroweak (EW) corrections at NLO as a future benchmark.

Although unphysical, these kinds of calculations are typically well suited for describing observables which are fully inclusive with respect to QCD radiation; the most common example being the Drell–Yan production, see e.g. [37].

The partonic cross section for a generic process $pp \to X$ is given by

$$\sigma = \sum_{ab} \int_0^1 dx_a \int_0^1 dx_b f_a(x_a, \mu_F) f_b(x_b, \mu_F) \hat{\sigma}_{ab\to X}(x_a, x_b, \mu_F, \mu_R) \,, \tag{16}$$

and the unconvoluted partonic cross section $\hat{\sigma}_{ab\to X}(\mu_F, \mu_R)$ is expressed in terms of the transition matrix element $\mathcal{M}_{ab\to X}(\Phi_X, \mu_F, \mu_R)$ integrated over the phase space Φ_X

$$\hat{\sigma}_{ab\to X} = \hat{\sigma}_{ab\to X}(\mu_F, \mu_R) = \int \frac{d\Phi_X}{2\hat{s}} |\mathcal{M}_{ab\to X}(\Phi_X, x_a, x_b, \mu_F, \mu_R)|^2 \,. \tag{17}$$

The PDF f_a (f_b) describes the probability density that a fraction x_1 (x_2) of the longitudinal momentum of the incoming proton is carried by the parton a (b) and $\hat{s}$ is the partonic center–of–mass energy. More formally, the factorization scale μ_F and the renormalization scale μ_R are also introduced [25]. The renormalization scale is defined as the energy scale where the ultraviolet divergences are regularized; similarly, the factorization scale is introduced to regularize the QCD divergences due to collinear parton emissions from the initial state. Both the energy scales are therefore related to the finite theoretical accuracy, thus cancel out in exact predictions (e.g., in a full all–order calculation). The choice for their values is mainly driven by the expected energy scale of the hard process under investigation; however, in multiscale problems the scale choice is maybe non trivial and a validation using the data is mandatory.

Several scale choices have been studied, including fixed scales and dynamic scales setting built with invariant mass, energy and transverse momentum of final state partons and particles.

In general the cross section $\hat{\sigma}_{ab\to X}$ is known up to a certain perturbative order, for example in α_s; it can be written as a perturbative expansion as

$$\hat{\sigma}_{ab\to n} = \hat{\sigma}^{LO}_{ab\to n} + \alpha_s \hat{\sigma}^{NLO}_{ab\to n} + \alpha_s^2 \hat{\sigma}^{NNLO}_{ab\to n} + \alpha_s^3 \hat{\sigma}^{N^3LO}_{ab\to n} + \mathcal{O}(\alpha_s^4) \,; \tag{18}$$

the leading–order (LO), next–to–leading–order (NLO) and the next–to–next–leading–order (NNLO) terms can be identified.

In a final state with more than one parton the amplitude with collinear of soft configurations will be divergent due to soft and collinear singularities in QCD. The application of Eq. 18 may be restricted to some specific phase space regions in order to avoid the singularities for example considering kinematic configurations with hard and well separated jets; however this introduces logarithmic corrections in the cross section of the form [38]:

$$\alpha_s^n \ln^m \left(\frac{Q^2}{Q_k^2} \right) \qquad m \leqslant 2n \,, \tag{19}$$

where Q^2/Q_k^2 is the ratio between the hard process energy scale (Q^2) and the energy scale associated to the emission of additional partons (Q_k^2).

These logarithmic corrections can be relatively large and needs to be resummed at all orders in α_s. The structure of the logarithmic corrections depends on the perturbative order of the expansion; typically, at a given order, are identified in Eq. 19 the leading–logs (LL), $\sim \alpha_s^n \ln^{2n}$, next–to–leading logs (NLL), $\sim \alpha_s^n \ln^{2n-1}$, etc.. Well known cases of calculations with a LL (or NLL) resummation are Monte Carlo generators where the resummation is achieved by the parton–shower algorithm.

Other important complications arise in final states with of several well separated high p_T partons, where the emission of additional partons induces a distortions of some kinematic distributions. These kinematic features are typically not described in "naive" perturbative expansions unless high perturbative orders are calculated. A new approach to the problem has been developed in the last two decades, see Ref. [39] for a review, referred as multileg matrix element calculations; the basic feature of the multileg calculations is a reordering of the perturbative expansion which includes high parton multiplicities calculated at born level; thus, Eq.18 read as

$$\hat{\sigma}_{ab\to n} = \hat{\sigma}^{LO}_{ab\to 1} + \alpha_s \hat{\sigma}^{LO}_{ab\to 2} + \alpha_s^2 \hat{\sigma}^{LO}_{ab\to 3} + \alpha_s^3 \hat{\sigma}^{LO}_{ab\to 4} + ... + \alpha_s^{n-1} \hat{\sigma}^{LO}_{ab\to n} \,. \tag{20}$$

Electroweak corrections to hadronic cross sections for the LHC are not discussed here but there are significant recent developments in this direction; the combination of QCD and electroweak corrections has been provided for some processes in full Monte Carlo generators [40] exploiting the absence of interference terms at leading order in perturbation theory.

1.2.3 *Monte Carlo event generators*

In the Monte Carlo approach it is possible to provide a cross section prediction including parton–showering, parton hadronization and fragmentation, hadron decays and underlying event; these ingredients are highlighted in the following subsections; a review is given in [38, 41]. The high particle multiplicities handled by MC programs requires numerical Monte Carlo integration methods based on Markov Chain techniques [5].

1.2.3.1 *Parton shower*

The parton shower approach provides a process independent approximation of cross sections in kinematic regimes corresponding to soft or collinear configurations of strongly interacting partons. This approximation is based on a resummation at all order in α_s of a subset of (leading) logarithmic corrections associated to soft and collinear emissions.

Due to underlying approximations the parton–shower method is not expected to provide reliable predictions for hard and angularly well resolved parton configurations where instead the matrix element description is more appropriate.

Moreover, the parton shower method can't be extended below scales of order $\Lambda_{QCD} \sim 1$ GeV typically associated to hadron formation; indeed an artificial scale $Q_{IR} \sim \Lambda_{QCD}$ defines the limit of the parton shower evolution; below this scale, QCD inspired hadronization models are used as described in Sec. 1.2.3.2.

The main idea beyond the parton shower method is the factorization proprieties of the soft and collinear dynamic with respect to the hard part of the cross section. In this framework, additional parton emissions are described by universal, process independent, soft and collinear emission probabilities; massive partons, such as b–quarks, can be taken into account by using a set of modified probability functions [41].

The parton shower method can be combined with matrix element calculations by means of matching and merging algorithms. The matching algorithms are used to correct the first (hardest) emission to the best accuracy and are implemented both in tree level born matrix element and NLO matrix element. On the other side the merging algorithms are fully developed for multi–jet production but require the inclusion of one additional fictitious scale, the merging scale, which slice the phase space into two regions, the matrix element and the parton shower regions.

There are no general and automated formulation of the matching algorithms beyond the NLO; in particular is not currently possible to perform a matching for multileg calculations. Instead in the context of multijet cross section calculations the CKKW [42] and MLM [43] merging algorithms are of wide use; they are based on the generation of exclusive parton configurations for the lowest parton multiplicities available with the matrix element calculations. In the CKKW approach the overlap between the parton shower and the matrix element is removed by generating the nth emission with the parton shower if the parton has an energy below the matching scale and with the matrix element otherwise. The MLM algorithm is instead based on an angular matching between the hard partons and the post–showering "clustered jets", see Sec. 1.2.4 for the exact definition of "a jet"; an event is said to be matched if all the hard partons match a parton jet and there are no unmatched jets left in the event. The matching is based on a ΔR (for the ΔR definition see App. A) criteria with a characteristic angular scale, the MLM merging scale.

1.2.3.2 *From partons to stable particles*

After the parton showering a set of partons at the energy scale Q_{IR}, defined by the infrared cut–off of the shower algorithm, are typically produced. The goal of an hadronization model is to map the low energy partons into a set of hadrons; this mapping is not described by first principles, instead phenomenological QCD

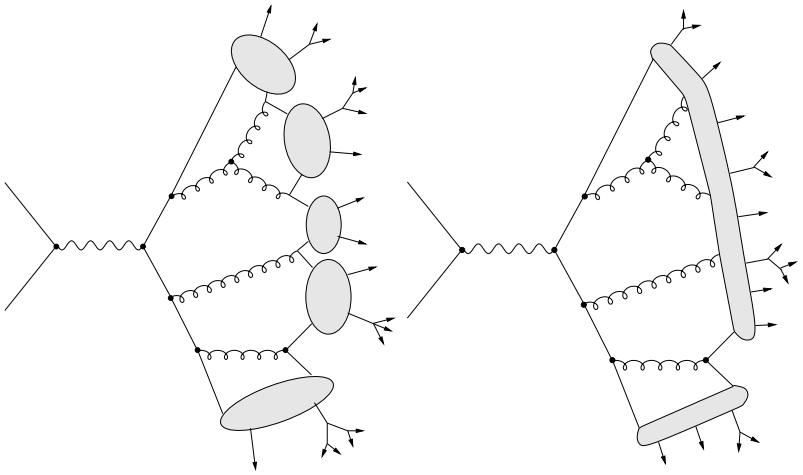

Figure 4: Graphical illustration of cluster formation and decays (left) and the string evolution (right) from Ref. [45].

inspired models have to be used. The goodness of a model is reflected by its predictive power and its capability of describing the available data.

Two classes of hadronization models are currently used in Monte Carlo generators: the String model implemented in PYTHIA [46] and the Cluster model used in HERWIG6.6 [47], HERWIG++ [48] and SHERPA [49].

The String model implementation more developed in literature is the PYTHIA Lund String model. The String exploits the idea of a linear confinement potential between colored objects (initially developed for quark–antiquark pairs); post–showering partons are grouped in "objects" called "strings", quark–antiquarks pairs, or in "kinks", gluons and a cascade of additional partons is generated by their breaking following a probability density of the form

$$P(m_q^2, p_T^2) \propto e^{-\frac{\pi m_q^2}{\kappa}} e^{-\frac{\pi p_T^2}{\kappa}} \qquad \text{with } \kappa/\pi \sim (250\ MeV)^2\ , \tag{21}$$

which encodes both the p_T[4] and the mass suppression of produced quarks; for example, the production of a b–quark in the hadronization phase will be suppressed by a factor $\sim 10^{-7}$ with respect to light flavors. The partons produced from strings and kinks breaking are grouped into hadrons which acquire a longitudinal momentum fraction determined by the fragmentation function depending only on the quark mass, transverse momentum and adjustable free parameters of the model. An illustration of a string breaking is given in Fig. 4 (right).

The implementation details of the Cluster model are pretty much generator dependent. The main idea behind it is to form non perturbative objects, the "clusters", from the quarks produced after the parton shower; gluons are not used to the cluster building but they are "decayed" in quark–antiquark pairs just after the shower. The clusters undergo to a chain of decays into hadrons and other lighter clusters until no clusters are left. The suppression for the generation of heavy flavors

4 Here the transverse momentum is defined in the string rest frame; the quarks and the antiquarks are constrained to be produced with the same absolute value of p_T but opposite direction in the string rest frame.

in the hadronization phase is achieved by the exponential decay of the clusters invariant mass distribution. During the cluster formation and decays, probability weights are applied depending on the populated phase space region, hadrons flavor, hadrons spin, etc. The formation of a cluster pair from a quark–antiquark–gluon system is shown in Fig. 4 (left).

The hadrons produced subsequently to the hadronization phase are not yet the physical particles needed to define the hadron–level cross section because most of them will decay on time scales much smaller than a few ps[5]; moreover, Standard Model particles with mass close to the electroweak scale, like W/Z bosons, the top quark and the Higgs boson, are all unstable and the description of their decays is then of crucial importance at the LHC.

The treatment of particles decay is not uniform among the available generators and it is often subject to simplifications and assumptions. In the most simple approaches, the particle decays are factorized from the event generation by treating the particles as mass–shell states and using a simple Dirac delta function or Breit–Wigner functions (relativistic or non–relativistic) to describe the mass distributions of their decay products; an isotropic spatial distribution for the decay products is assumed in the rest frame of the decaying particle. However, these simplifications are not wanted if the Monte Carlo programs have to be used to describe decays of off mass–shell particles, like, for example, off peak Drell–Yan process or high mass BSM Higgs decays where the Higgs width becomes comparable to the mass scale [38]. Moreover a precise description of the angular distributions of the decay products is interesting in various contexts like Higgs physics and top quark properties determination where the angular information of the decay products is used as signal–background discriminator or is used to infer a fundamental particle property like their spin or polarization. On the other hand, there are specific cases, such as heavy flavor measurements, when the decays of stable particles is also of primary importance. Indeed, as is discussed in Sec. 2.7, the description of the heavy flavor decay chains (including angular distributions) is a substantial information used by the b–tagging algorithms in ATLAS and need to be properly modeled. A complete treatment of decays simulation involve the treatment of spin–correlation of the decay products with calculation based on the full matrix element to describe the decays or the decay chains. Some specialized generators for heavy flavor decays, like EvtGen [50] or Sherpa, use this approach augmented with data driven constraints.

1.2.3.3 *Soft QCD interactions and underlying event*

During the LHC data taking in Run 1, LHC has provided proton–proton collisions with an average number of interactions per bunch crossing as high as 20.7. The dominant contribution to the event topology due to additional pile–up interactions is given by additional particles produced by soft proton–proton interactions typically referred to as *minimum bias* events.

5 As earlier mentioned we define "stable" all particles with lifetime greater than 15 ps.

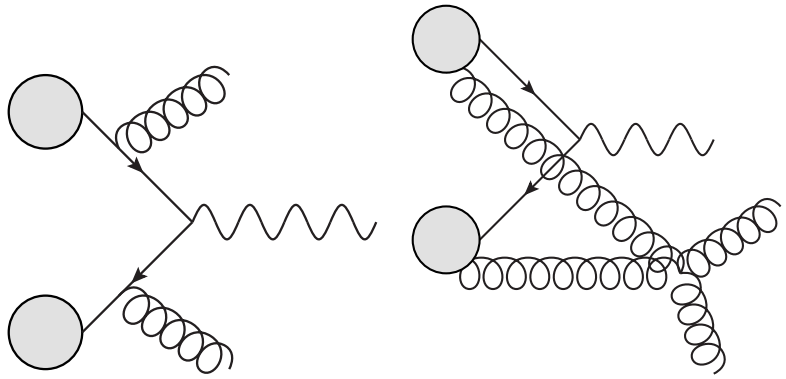

Figure 5: Diagrams showing the production of a Z boson in association with two partons from a single parton interaction (a) and from a double parton interaction (b).

The total inelastic cross section $\sigma_{In}(s)$ is typically described in terms of contributions corresponding to different final states topologies:

$$\sigma_{In}(s) = \overbrace{\sigma_{SD}(s)}^{\text{Single Diffractive}} + \underbrace{\sigma_{DD}(s)}_{\text{Double Diffractive}} + \overbrace{\sigma_{CD}(s)}^{\text{Central Diffractive}} + \underbrace{\sigma_{ND}(s)}_{\text{Non Diffractive}} . \quad (22)$$

The single(double) diffractive cross section describes process where one(both) of the colliding protons are excited to a resonant unstable state (like a Δ^+) which then decays into a number of particles. In the single diffractive category the second proton is left intact in the final state. In central diffractive events both protons survive intact to the inelastic interaction where a system of particles is produced in the central region of the detector. Non diffractive events exhibit a diffuse hadron activity in the final state with an emerging jet–like structure; these events are the boundary between soft QCD interactions and high p_T jet production. Typically, by the miminum bias events one refers to non–diffractive and double diffractive events.

The simulation of soft pp interactions is available in Monte Carlo generators and it is used to emulate the pile–up by superimposing a number, N, of minimum bias simulated events to each simulated hard process, where N is poissonian distributed around the average expected multiplicity of interactions per bunch crossing.

In a single proton–proton collision the final states coming from the hard parton scattering is embedded into additional particle productions resulting from multiple parton interactions (MPI).

These are low momentum transfer processes among the proton remnants leading to soft hadron production or additional hard parton–parton scattering, double–parton–interactions (DPI). Likewise pile–up interactions, the underlying event contribute to distort the event topology by adding soft hadrons, or, less frequently, hard jets which are indistinguishable from the primary interaction final state on an event–by–event basis.

Currently, MC generators model the MPI by overlaying additional $2 \to 2$ parton scatterings to the hard primary interaction. In the HERWIG and HERWIG++ models the average number of parton–parton collisions $\langle n(b) \rangle$ is proportional to the "overlap function" $A(b)$, being b the impact parameter of the proton–proton interaction. Because of the assumption of independence for different partonic scatterings, the number of scatters n is given by a Poisson distribution

$$\mathcal{P}(b) = \frac{\langle n(b) \rangle^n}{n!} \exp[-\langle n(b) \rangle] \, . \tag{23}$$

A different probability density is postulated in the SHERPA and PYTHIA models which is expressed in terms of the non diffractive cross section σ_{ND}, the hard di–jet cross section σ_{Hard} and the proton shape function $f(b)$

$$\mathcal{P}(b, p_T) \sim f(b) \frac{1}{\sigma_{ND}} \frac{d\sigma_{Hard}}{dp_T} \, . \tag{24}$$

The underlying event, in particular the hard double parton interactions, are currently included in the observables measured at LHC. In general, when performing a measurement of a given process no attempt is made of separating events where the process under study is produced in a single hard primary interaction from events where the same final state is produced as a result of the double parton interaction. Proper tunings of Monte Carlo models are thus mandatory.

1.2.4 *Jet algorithms*

A typical proton–proton interaction at LHC involves scattering of hard partons producing "sprays" of collimated hadrons generated by parton evolution around the hard partons and by the subsequent hadronization. Jet algorithms are used to redefine a hadronic final state in terms of *jets*, which allow to define physically meaningful observables and cross sections. A jet algorithm is a set of rules and parameters which define a "metric" among the constituents, partons or hadrons or detector objects[6], and a recursive recombination rule (recombination schema).

The use of jet algorithms is mandatory since hard partons are not physically well defined objects and hadrons do not retain individually the information associated to the hard scattering and are often unpractical for data–theory comparison.

A jet algorithm has to satisfy some specific requirements. The most common demand is the infrared and collinear safety (IRC safety), namely the robustness of a jet algorithm against the addition of soft or collinear constituents (or pseudo–jets) to a predefined set of constituents; in other words, the IRC safety implies that for a given event the number of clustered jets is invariant under perturbations of the soft and collinear radiation spectrum.

The definition of a metric involves the use of both angular separation among the constituents and their energy scales. As an example a short list of the most widely used IRC safe jet algorithms is given in Tab. 6 along with their metric definition, $d_{i,j}$.

6 The concrete use at detector level of the jet algorithms is summarized in Sec. 2.6.

Algorithm	IRC safety	Metric
k_t [51]	yes	$min(p_{T,i}^2, p_{T,j}^2)\Delta R_{ij}^2/R^2$
anti–k_t [106]	yes	$min(p_{T,i}^{-2}, p_{T,j}^{-2})\Delta R_{ij}^2/R^2$
Cambridge–Aachen [53, 54]	yes	$\Delta R_{ij}^2/R^2$

Table 6: Most widely used jet algorithms at LHC and their metric definition. For all the jet algorithms there is only one free parameter, typically referred to as the radius parameter R, which defines the angular scale of the clustering.

The benchmark jet algorithm at LHC is the anti–k_t algorithm with the use of $R = 0.4, 0.6$ by ATLAS and $R = 0.5, 0.7$ by CMS while the k_t and Cambridge–Aachen algorithms are used as tools for jet–substructure studies, see e.g. [55].

All the jet clustering algorithms mentioned in Tab. 6 are based on a sequential recombination scheme. Specifically, for the anti–k_t algorithm the sequential recombination works through the following steps:

1. The distances $d_{ij} = min(p_{T,i}^{-2}, p_{T,j}^{-2})\Delta R_{ij}^2/R^2$ among all pairs of objects in the event are computed; i, j can be either particles or *pseudo–jets* built in previous steps of the recombination procedure.

2. The distances $d_{iB} = p_{T,i}^{-2}$ among the object i and the "beam" B are computed.

3. If, for some i, j, d_{ij} is the smallest distance in the event, then the objects i, j are recombined into a so called pseudo–jet by adding their four momentum; objects i and j are removed from the event and all distances d_{ij} are recomputed based on the remaining objects and the new redefined pseudo–jet.

4. If, for some i, d_{iB} is the smallest distance, the object i is defined as a jet and removed from the set of event objects processed by the procedure.

This procedure is iterated until no objects are left.

1.3 COMPARING MEASUREMENTS AT LHC WITH QCD PREDICTIONS

The wide program of Standard Model measurements at LHC is currently moving towards the completion of its initial phase with the aim of using the full Run I data sample in order to test in detail theory predictions used by the experimental collaborations in many BSM searches and Higgs measurements. This experimental effort will provide more data for Monte Carlo tuning and PDF fits, and will challenge the current calculations in extreme phase space regions or exclusive final states. Here a few examples of measurements.

The understanding of the minimum bias events has been tested by CMS and TOTEM [56] experiments in an extended phase space region compared to previous measurements; the charged track multiplicity as a function of the leading track pseudo–rapidity is shown in Fig. 6 (a) where it can be observed the inability of the available tunes and models to properly describe simultaneously the central ($|\eta| < 2.4$) and the forward ($5.3 < |\eta| < 6.5$) regions.

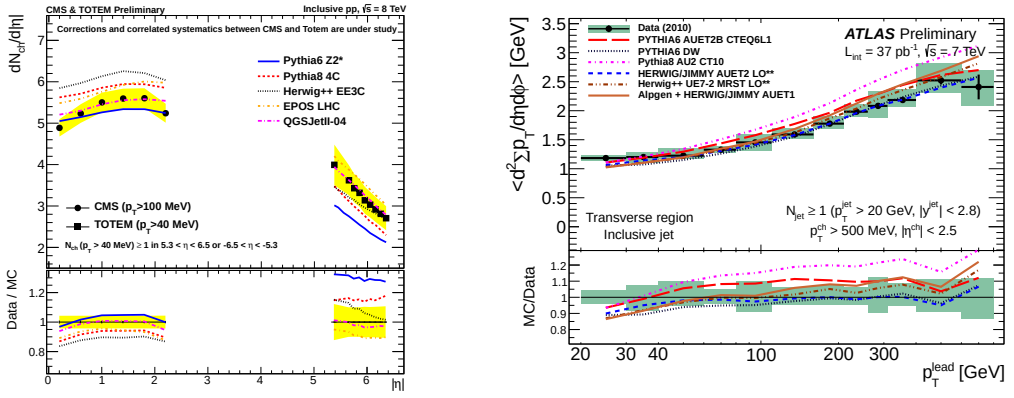

(a) (b)

Figure 6: Charged track multiplicity N_{ch} in inclusive pp collisions as a function of the leading charged track pseudo–rapidity $|\eta|$ [56] (a) and profiles of charged particle $\sum p_T$ as a function of p_T^{lead} [57] for the inclusive jet event selection (b).

The LHC data has shown once more the ability of Monte Carlo generators to describe and predict globally well the underlying event features both in inclusive and exclusive final states involving high–p_T jet production [57]. This can be appreciated in Fig. 6 (b) where the charged track multiplicity as a function of the leading jet p_T is reported.

Among the most interesting features of the LHC data there is the significant sensitivity to the gluon parton density function; for example, can be recalled that the gluon PDF precision is the limiting factor in the theoretical uncertainty on the Higgs cross section in its dominant production mode, gluon–gluon fusion, which has been calculated up to N^3LO accuracy [58, 59, 60] in perturbation theory. The ATLAS measurement of the ratio of jet cross section measured at $\sqrt{s} = 2.76$ TeV and $\sqrt{s} = 7$ TeV [61] has been used to refit the gluon density function extracted from the HERA data.

Fig. 7 shows that the introduction of the ATLAS data induces a shift at high–x of the gluon density and an improvement on the uncertainty. In CMS, a global PDF analysis [62] has been performed by using the jet data; the analysis favors a harder gluon spectrum, confirming the ATLAS results, and a softer spectrum for the valence up–quark density, see Fig. 7 (b).

Multijet production in association with massive gauge bosons W/Z is an important background for several searches and electroweak studies; event generators are typically used in combination with data driven methods to constrain these backgrounds. The common requirements on event generators is to provide reliable prediction of the W/Z cross sections and a very good description of the shapes of the distributions commonly used to define signal regions for BSM searches. It has been observed that the use of multileg matrix element calculations (e.g. ALPGEN and SHERPA) corrected with global k–factors fulfill these requirements and describe well the data also in extreme phase space regions and high jet multiplicity as can be seen from Fig. 8 (a) and (b). Moreover, NLO calculation of Z production in association with up to four jets [63] provides a simultaneous good prediction for both

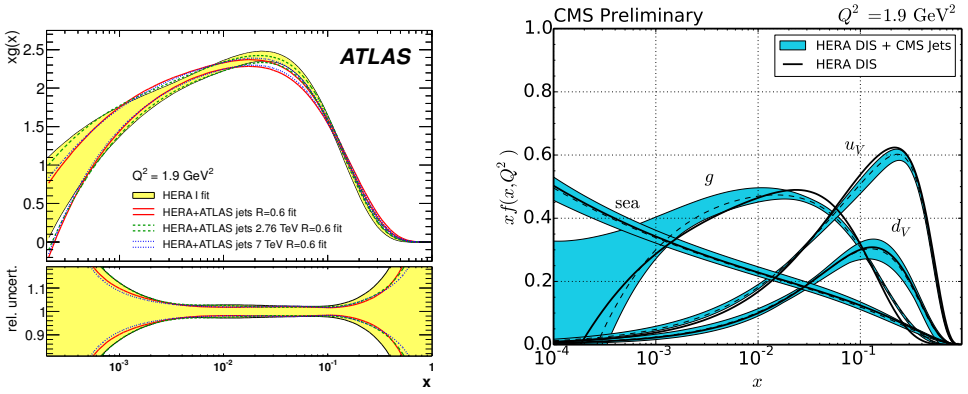

(a) (b)

Figure 7: Gluon density (a) extracted from jet ratio data in ATLAS, gluon, valence quarks and sea densities (b) fitted using the CMS jets data as functions of x at the scale $Q^2 = 1.9\ \text{GeV}^2$.

the total cross section and differential distributions without the use of additional k–factors.

The di–photon final state shows in a dramatic way the advantage of multileg event generators over fixed order QCD calculations. Fig. 9 (a) from ATLAS [65] shows that the NLO QCD calculation fails to describe the transverse momentum spectrum of the di–photon system while the NNLO QCD calculation is much closer to the data but not accurate enough especially for this distribution, particularly sensitive to the recoil of the $\gamma\gamma$ system against hard QCD radiation. On the other hand the LO Monte Carlo calculation based on multileg–matrix element (SHERPA) does a good job on the full kinematic range, as it can be observed from Fig. 9 (b), although it does not predict correctly the total cross section.

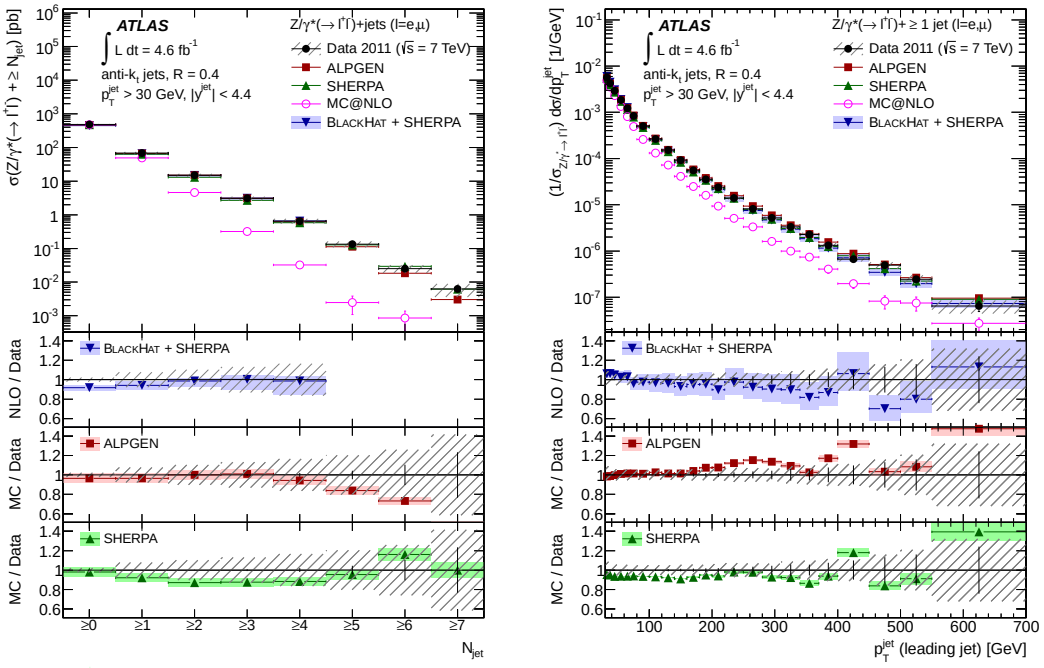

(a) (b)

Figure 8: Measured cross section for Z($\to \ell\ell$)+jets as a function of the inclusive jet multiplicity (a), and as a function of the leading jet p_T (b) [64].

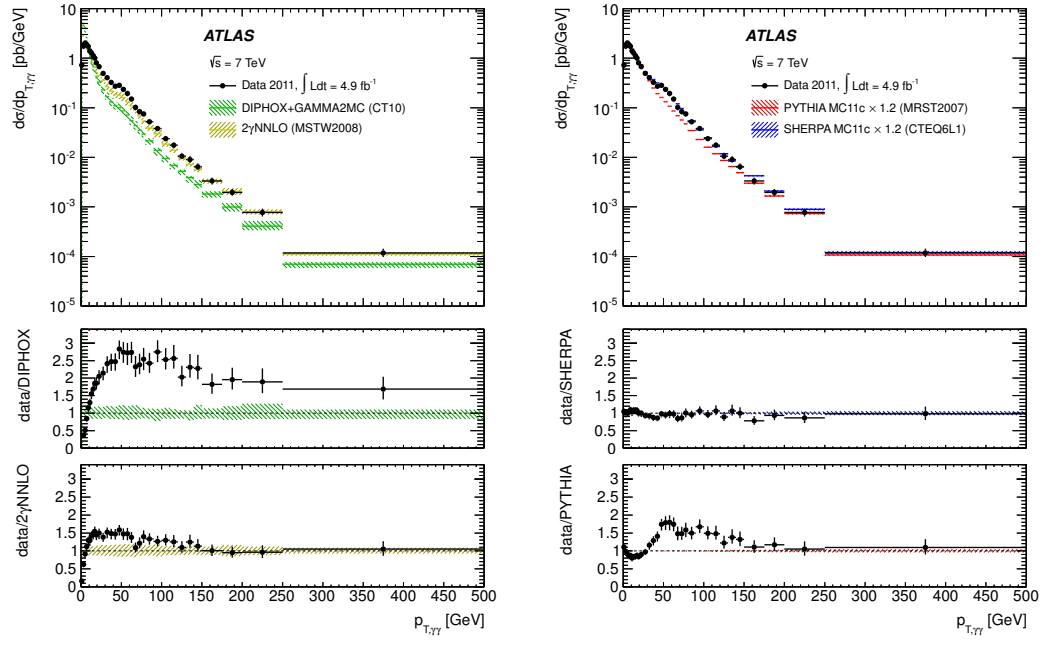

(a) (b)

Figure 9: Transverse momentum $p_{T,\gamma\gamma}$ of the di–photon system measured in ATLAS [65] the data are compared to fixed order NLO and NNLO calculations in (a) and to multileg matrix element predictions (b).

2

RECONSTRUCTION OF PHYSICS OBJECTS IN THE ATLAS EXPERIMENT

The ATLAS experiment at the Large Hadron Collider is designed to operate at the TeV energy scale and in extreme data taking conditions well beyond the challenge that previous experiments have faced.

The strategy for particle identification is typically based on a combination of several detector subsystems and robust reconstruction techniques for pile–up mitigation.

The performance obtained in physics object reconstruction is evaluated by means of data–driven (or *in situ*) methods and compared to performance studies based on detailed Monte Carlo simulations of the detector response.

The residual mis–modeling of the detector response in simulation is corrected by applying data to MC scale factors to the simulated samples. The data taking conditions are also emulated in simulation, including the pile–up environment, which is simulated as a Poisson distributed number of minimum bias interactions overlaid to the nominal hard scattering.

A short summary of the ATLAS detector is given in Sec. 2.1; more details can be found in Ref. [66]. The data taking conditions in Run 1 are recap in Sec. 2.2. A description of the muon identification is given in Sec. 2.3; the basic definitions for electron and photon identification methods are briefly illustrated in Sec. 2.4. A concise summary of performance measurements of hadronic jet and hadronic τ leptons is given in Sec. 2.5; the missing transverse energy reconstruction is summarized in Sec. 2.6. Finally, the b–tagging methods are discussed in Sec. 2.7; the b–tagging is a key ingredient for the measurement presented in Chap. 4– 5–6 and will be further discussed in Chap. 4.

2.1 THE ATLAS DETECTOR

The ATLAS detector [66] design has been driven by the main goal of observing the SM Higgs boson in a wide mass range. Benchkmark scenarios are the Higgs decays in the discovery channels for a "low mass" Higgs boson, the $\gamma\gamma$ mode ($H \to \gamma\gamma$) and the "four leptons" channels ($H \to ZZ \to 4\ell$), which require very high resolutions for photons with transverse energy above $\sim$ 50 GeV and good lepton efficiency and resolution for leptons with p_T from a few GeV ($\sim$ 8 GeV) up to $\sim$ 100 GeV, respectively. In Beyond Standard Model scenarios leptonic and di–jets decays in resonances with TeV mass scale are common and require a good understanding of the identification and reconstruction performances for leptons and jets with energies up to few TeV. The most common signature of new physics in many BSM models is a large missing transverse energy, up to few TeV, which need to be well understood in the challenging pile–up conditions at LHC. Another common features of many BSM scenarios is the typical strong coupling of the top quark to a new spectrum of particles, leading to enhanced top quark production

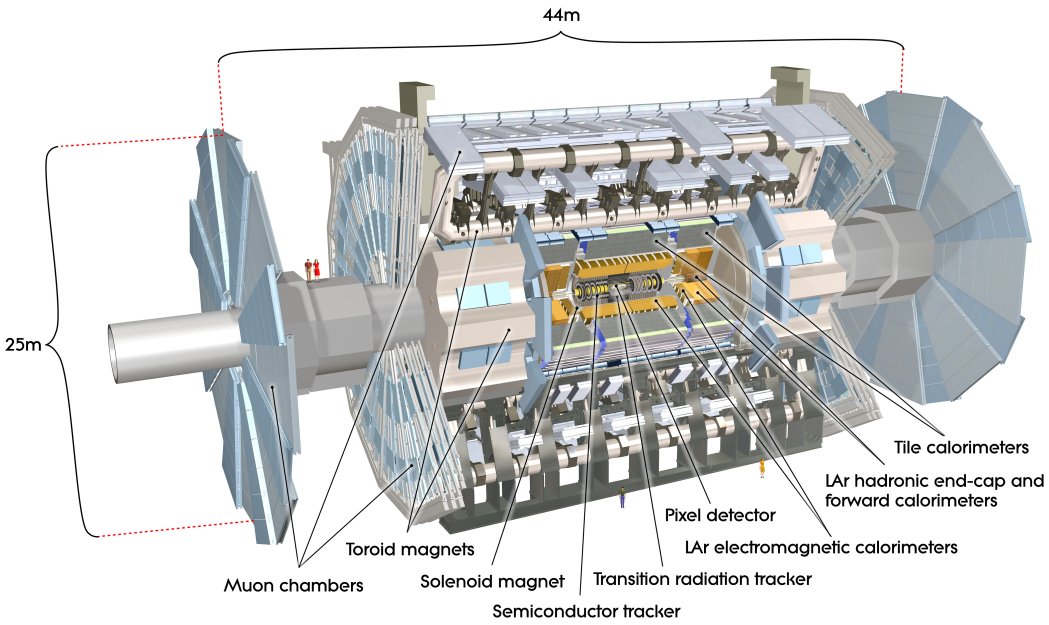

Figure 10: Overview of the ATLAS detector [66] with all the main subsystems highlighted.

rates and resonances; the top quark decays with a branching ratio close to 100% in a W boson and a b quark; the latter can be identified with complex *b–tagging* algorithms, which rely on a very good tracking efficiency for charged tracks with p_T down to a few hundreds of MeV and very good impact parameter resolution.

The ATLAS detector, shown in Fig. 10, uses a combination of three detector subsystems: the Inner Detector (ID) for track and vertex reconstruction, an electromagnetic and a hadronic calorimeter (ECAL and HCAL) and a Muon Spectrometer (MS).

ATLAS uses a right–handed coordinate system with its origin at the nominal interaction point (IP) in the centre of the detector and the z–axis along the beam pipe. The x–axis points from the IP to the centre of the LHC ring, and the y–axis points upward. Cylindrical coordinates (r,φ) are used in the transverse plane, φ being the azimuthal angle around the beam pipe. The pseudorapidity is defined in terms of the polar angle θ as $\eta = -\ln[\tan(\theta/2)]$. Transverse momentum and energy are defined as $p_T = p\sin\theta$ and $E_T = E\sin\theta$, respectively.

The ID is close to the proton–proton interaction point and it performs the tracking of charged particles, for pseudorapidity up to $|\eta| < 2.5$, which are bent by an axial magnetic field with intensity of 2T providing an almost homogeneous bending power in the R–ϕ plane. The ID is based on three detector subsystems: a pixel detector, a silicon strip SemiConductor Tracker (SCT) and a straw tube Transition Radiation Tracker (TRT). In the barrel region, ($|\eta| < 2$), the ID consists of three pixel layers, four SCT layers with strips oriented at ± 40 mrad with respect to the beam axis for the two views, and 73 layers of TRT straw tubes. In the end–cap ($1.5 < |\eta| < 2.5$), to have a uniform number of hits per track as a function of η, the

number of SCT and TRT layers are increased to 9 and 160 for each side, respectively. The best resolution for a single hit is achieved with the pixel detector, 10 μm in the R–ϕ plane and 115 μm in the z–axis direction; the TRT system, besides enhancing the electron–pion separation by means of the transition radiation effects, provides a resolution of 130 μm in the R–ϕ plane; the SCT instead has a resolution comparable with the pixel system in the R–ϕ plane, 17 μm, but poor along z, 580 μm.

The calorimetric system is designed to be highly hermetic, with a 4π coverage in azimuth and up to $|\eta| < 4.9$ in pseudorapidity, to perform jets, electrons, and photons identification in a wide phase space and with a good shower (electromagnetic and hadronic) containment. The electromagnetic calorimeter uses a sampling technology based on lead and Liquid Argon (LAr); it covers the pseudorapidity region $|\eta| < 1.475$ in the barrel and $1.375 < |\eta| < 3.2$ in the end–caps with about 24 radiation lengths in the barrel and about 26 in the end–caps. The hadronic calorimeter in the barrel ($|\eta| < 1.7$) is a "tile" calorimeter, made of layers of scintillator tiles and steel foils covering about 11 interactions lengths. In the end–caps, $1.5 < |\eta| < 3.2$, hadron calorimetry is accomplished with a sampling calorimeter consisting of copper and LAr. The forward region, $3.1 < |\eta| < 4.9$, is instrumented on both sides with another LAr sampling calorimeter which has three longitudinal sections: the innermost, using copper as absorber, is devoted to electromagnetic calorimetry, while the second and third sections use tungsten as passive material for the containment of hadronic showers. In the ECAL transition regions between the barrel and the end–caps ($1.37 < |\eta| < 2.47$), and between the end–caps and forward calorimeters ($|\eta| \sim 3.2$), the large amount of passive material, up to 12 radiation lengths, due to service installation, leads to a decrease of performances for electron and photon showers reconstruction.

The Muon Spectrometer (MS) is the outermost detector system; it is based on a combination of four gas detector technologies providing standalone tracking (for $|\eta| < 2.7$) and triggering (for $|\eta| < 2.4$) capability in a toroidal magnetic field of intensity up to 1 T. The Monitored Drift Tube (MDT) subsystem, based on drift tubes filled at three bar with Argon (93%) and carbon dioxide gas mixture (7%), provides precise tracking information in the full MS acceptance with three stations of chambers; typically a prompt muon with $p_T > 6$ GeV and $|\eta| < 2.7$ can cross three well separated layers of muon detectors. In the end–caps the MDT tracking information is supplemented with Cathode Strip Chambers (CSC), which provides tracking ($2.0 < |\eta| < 2.7$) in the innermost station with high granularity in ϕ and η.

The muon trigger system is based on three stations of Resistive Plate Chambers (RPC) in the barrel ($|\eta| < 1.05$) and Thin Gap Chambers (TGC) in the end–caps($1.05 < |\eta| < 2.4$). Several p_T thresholds can be implemented in the hardware configuration of the muon LVL1 trigger, by requiring the coincidence between hits in two or three stations. The trigger detectors provide also a coarse measurement of the ϕ coordinate.

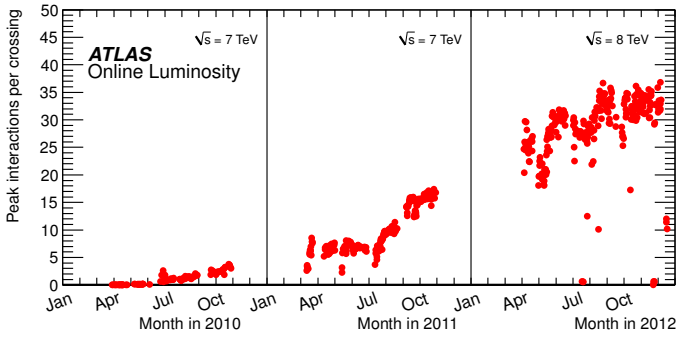

(a)

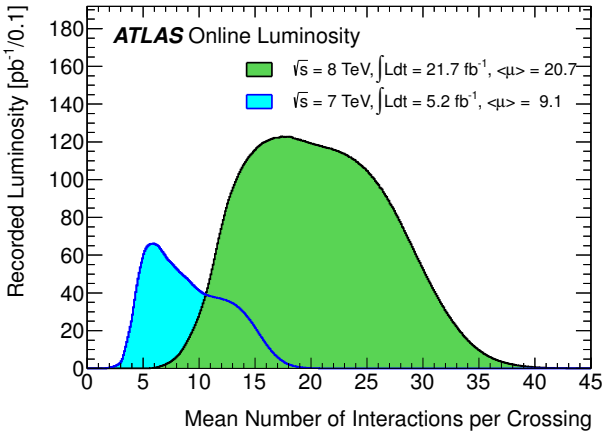

(b)

Figure 11: Peak number of interactions per bunch crossing during the Run 1 data taking periods [67] (a) and integrated luminosity collected in 2011 and 2012 as function of the mean number of interactions per bunch crossing [67] (b).

2.2 DATA TAKING CONDITIONS

During Run 1 data taking, from November 2009 to December 2012, the ATLAS detector has operated in a wide spectrum of pile–up conditions summarized by the maximum number of interactions per bunch crossing in Fig. 11 (a) and by the recorded integrated luminosity as a function of the mean number of interactions per bunch crossing (μ), in Fig. 11 (b), for the 2011 and 2012 data taking periods. The majors data taking periods are the 2011, with a recorded luminosity of 5.2 fb^{-1} and a mean average number of interactions per bunch crossing $\langle\mu\rangle = 9.1$, and the 2012, with a recorded luminosity of 21.7 fb^{-1} and $\langle\mu\rangle = 20.7$. The pile–up affects the data in two ways:

- multiple proton–proton interactions in the same bunch crossing induce additional hadronic activity overlapping with the triggered events, in time pile–up;
- additional signal in the calorimeter system due to proton–proton collisions occurred in bunch crossing nearby the bunch collision where the hard triggered interaction takes place, out of time pile–up.

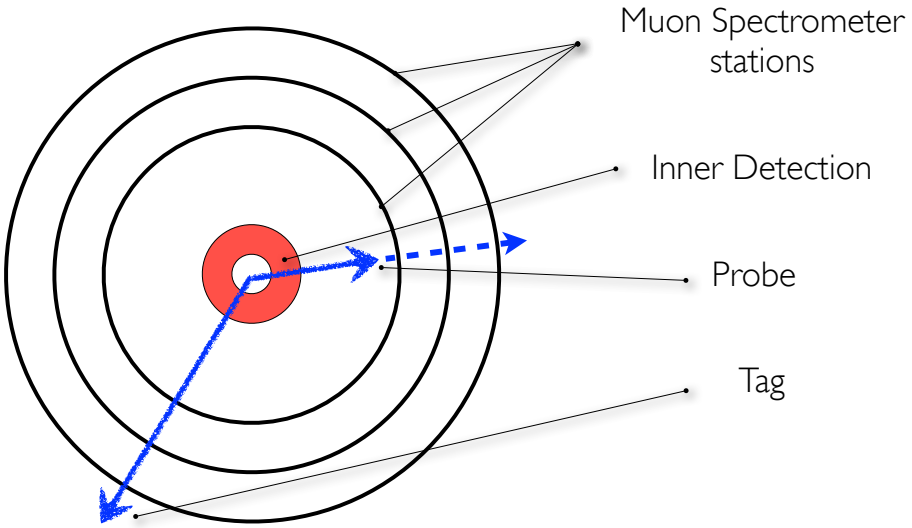

Figure 12: Tag and probe pair in a transverse section of the Muon Spectrometer. The tag is represented by the long arrow which travels from the interaction point, crosses the ID and reaches the MS stations and is reconstructed in both the systems; the probe is reconstructed in the ID and it is used to test the muon identification efficiency.

The ATLAS trigger is based on a three level system: a hardware level, *level one* (L1), and two software levels, *level two* (L2) and event filter (EF) globally referred to as *high level trigger* (HLT). The L1 is designed to reduce the event rate in input to the HLT from the 40 MHz nominal LHC bunch crossing rate to a maximum of 100 kHz and to provide topological information associated to potentially interesting objects which are used to identify *region of interest* (RoI), to be read–out by the second level trigger. The L2 and the EF are based on fast software algorithms able to perform a first particle identification, including muons, photons, electrons, jets, b–jets, τ's and to provide a first calculation of the missing transverse energy of the event. The L1, the L2 and the EF information are sequentially combined to build trigger chains; all the trigger chains are collected in the *trigger menu* where four main classes of trigger items exist: single and multiple objects chains, combined triggers (more than one class of objects are used) and topological triggers (which access simultaneously to more than one RoI). The events passing a trigger chain are recorded for offline reconstruction at the rate of about 200 Hz.

2.3 MUON IDENTIFICATION AND DETERMINATION OF THE PERFORMANCE WITH DATA

Muons produced at the nominal interaction point and with at least an energy of three GeV are expected to traverse all the detector subsystems, the Inner Detector, the ECAL, the HCAL and reach the Muon Spectrometer. Since all the particles (excluding neutrinos), but the muons, typically deposit all their energy in the calorimeters, the most powerful muon identification method is based on a combination of the information of ID and MS systems; the MS provides identification

capability and momentum resolution above ~ 100 GeV; the ID provides momentum resolution at low and intermediate transverse momentum. A few other muon identification strategies are currently used in ATLAS in order to recover the residual inefficiencies introduced in specific detector regions by acceptance limitations of the Muon Spectrometer, such as in the central barrel region and in the transition region as discussed in Sec. 2.1.

There are four classes of reconstructed muons in ATLAS.

- Combined (CB). Combined muons are the default choice of many physics analyses; the CB reconstruction is based on the combination of the ID and MS tracking systems. There are two slightly different methods of combining ID and MS information corresponding to the "chain 1" and "chain 2" algorithms: in chain 1 the measurement of the muon kinematics is obtained by a statistical combination of the parameters measured in the ID and MS, while in chain 2 a global fit on the ID and MS track is performed recovering also muon candidates with associated MS track not fully reconstructed.

- Stand–Alone (SA). The muon track is reconstructed in the Muon Spectrometer only; usually these muons are close to the edge of the ID acceptance ($|\eta| \sim 2.5$) and are recovered by the extended MS η coverage. The SA muon kinematics extrapolated to the point of closest approach to the beam axis is corrected for energy loss in the MS and in the calorimeters.

- Calorimeter–Tagged (CT). Tracks reconstructed in the ID are associated to energy deposits in the calorimeters consistent with a minimum ionizing particle. In order to suppress the background further, cuts on calorimeter and track isolation are applied and optimized as a function of $|\eta|$ and p_T. This muon class is particularly suited to recover the efficiency loss for the muon reconstruction in the region $|\eta| \sim 0$ and are widely used in multi–leptons analyses where a low hadronic activity is expected.

- Segment–Tagged (ST). Muons with a low number of precision hits in the MS usually fall in this category; the muon track is not fully reconstructed in the MS, only segments are identified in the muon chambers but they are associated to an ID track.

2.3.1 *Muon reconstruction efficiency measurements*

The muon identification efficiency in data is studied with the tag and probe (T&P) method and data to MC scale factors are derived in order to correct the MC simulation and to reproduce the efficiency observed in data. The T&P sample is provided by di–muon decays of the J/ψ and Z resonances covering respectively the transverse momentum regions of $p_T < 20$ GeV[1] and $p_T > 20$ GeV.

The T&P method allows to select an unbiased sample of muons by searching for an Inner Detector track, the *probe*, that along with a well reconstructed muon, the

1 The p_T range of the J/ψ measurement was initially limited to the region $p_T < 10$ GeV in [68, 69, 70]; a more recent analysis of the full 2011 dataset and a change in the trigger strategy has been shown to provide an extended kinematic reach up to $p_T < 20$ GeV.

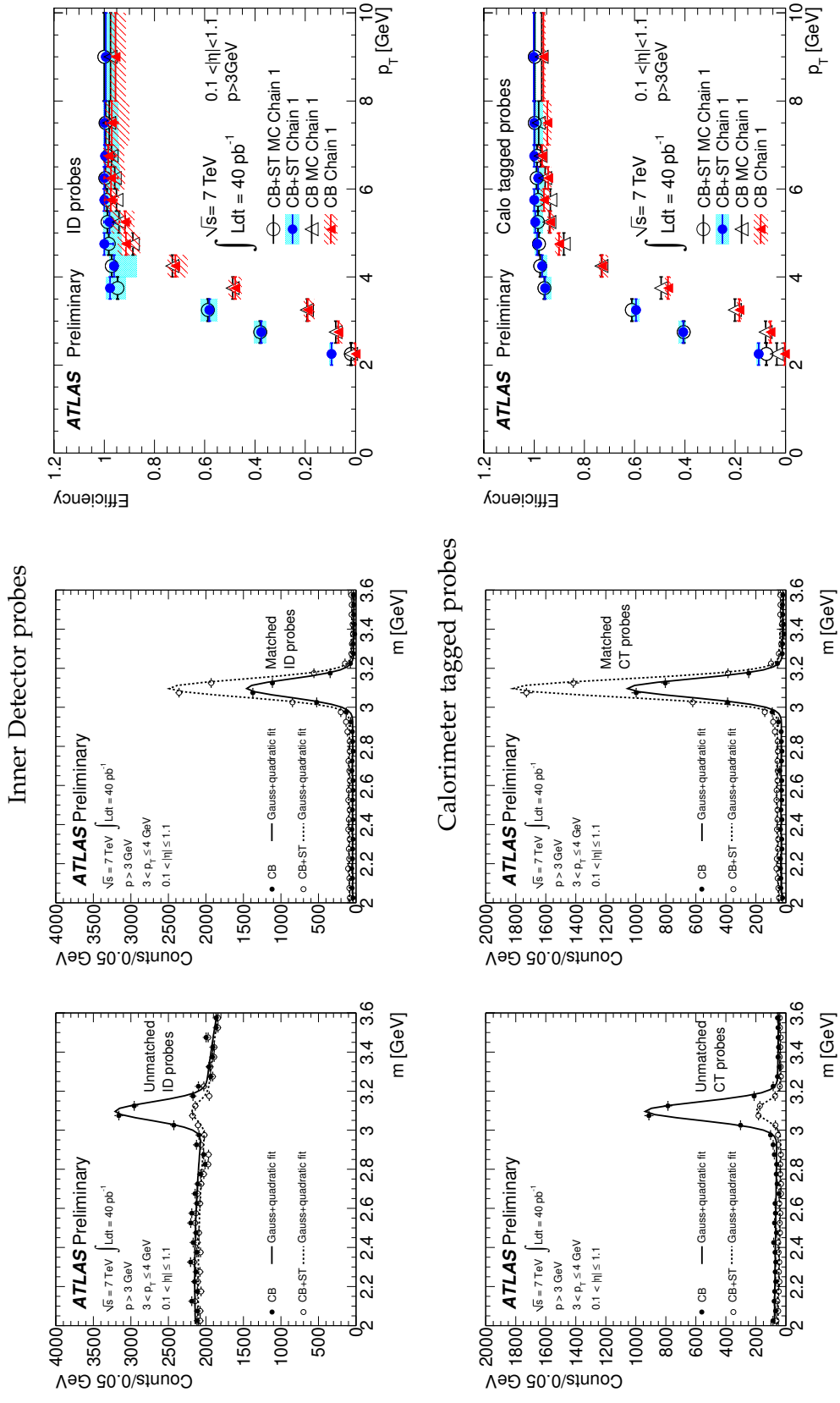

Figure 13: Invariant mass of the unmatched and matched tag and probe pairs for CB (filled circles) and CB+ST (empty circles) muons of chain 1 for ID probes (top) and CT probes (bottom) in the barrel region ($0.1 < |\eta| < 1.1$) and for 3 GeV$< p_T < 4$ GeV [68, 69, 70]. The efficiency turn–on curves are also shown for the same $|\eta|$ region as function of the probe p_T.

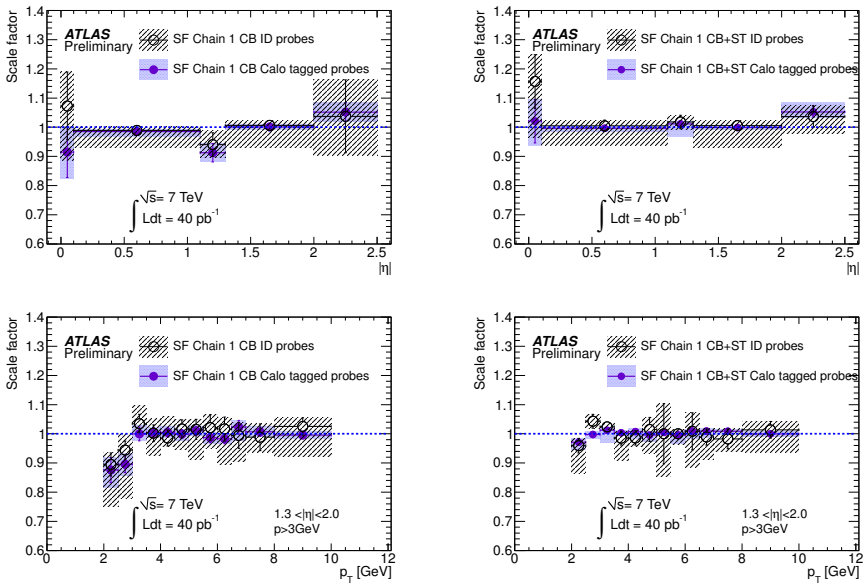

Figure 14: Muon reconstruction efficiency scale factors as a function of $|\eta|$ for $p_T > 8$ GeV (top) and as a function of the muon p_T for $1.3 < |\eta| < 2.0$ (bottom) from $J/\psi \to \mu\mu$ T&P analysis. Scale factors derived with CT probes are compared with the one obtained with ID probes for CB muons (left) and CB+ST muons (right). The inner error bars are the statistical uncertainty; the band around each data point is the systematic uncertainty added in quadrature to the statistical error.

tag, forms a system with invariant mass consistent with a di–muon resonance. By this procedure a sample of low p_T probes (from the $J/\psi \to \mu\mu$ decay) and high p_T probes (coming from $Z \to \mu\mu$ decay) are selected without relying on the Muon Spectrometer and can be used to measure the efficiency for reconstructing a muon with MS measurements.

A scheme of the tag and probe topology in a transverse view of the MS is given in Fig. 12.

The T&P method can't be used for measuring the SA reconstruction efficiency, because of the lack of a good probe samples in data; so no further corrections are typically applied for these muons.

The measured reconstruction efficiency scale factors are typically found to be very close to one, within a few percent, and are determined with accuracy of per–mille.

2.3.1.1 *Tag and probe with* $J/\psi \to \mu^+\mu^-$*: an example performance measurement*

The main challenge in the J/ψ T&P analysis is the background subtraction which is achieved by a fit to the di–muon invariant mass spectrum; the method has been described in [68, 69, 70].

In the sample of probes one can distinguish those reconstructed as a muon (*matched*) and those not reconstructed as muons (*unmatched*). The reconstruction efficiency is obtained as the ratio of the number of events in the mass peak of the matched distribution to the total number of events in the mass peak. A binned max-

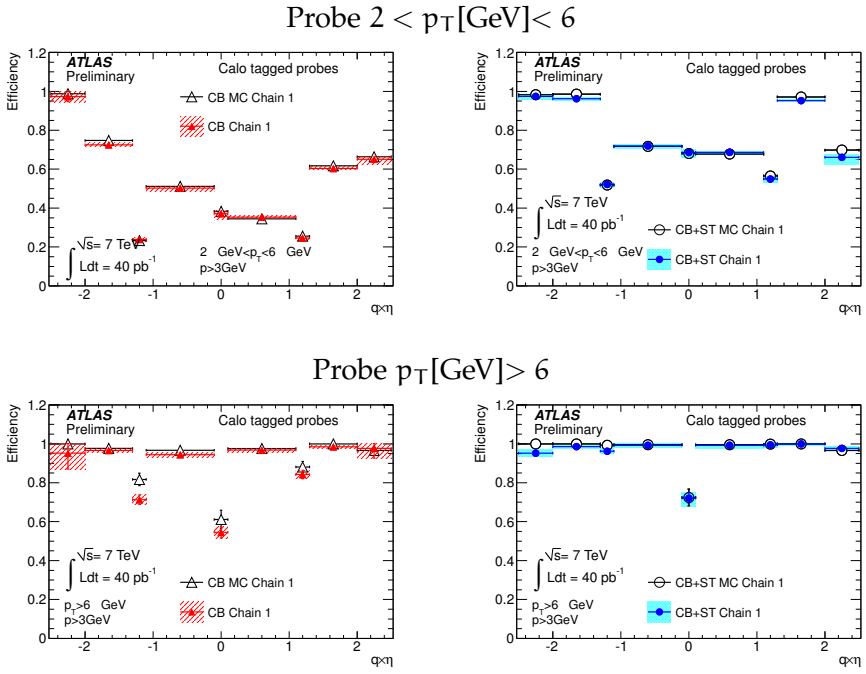

Figure 15: Efficiency for CB and CB+ST muons of chain 1 as a function of p_T in the barrel for data and MC [68, 69, 70] from the $J/\psi \to \mu\mu$ T&P analysis. The error bars represent the statistical uncertainties while the band around the data points represents the statistical and systematic uncertainties added in quadrature.

imum log–likelihood fit was performed simultaneously on the two distributions, with the following parametrization:

$$\begin{aligned} \text{Matched:} \quad f_M(m) &= N_{Tot}\,\epsilon\,G(m|\mu_M,\sigma_M) + P_M(m) \\ \text{Unmatched:} \quad f_U(m) &= N_{Tot}(1-\epsilon)\,G(m|\mu_U,\sigma_U) + P_U(m)\,, \end{aligned}$$

where m is the T&P invariant mass, $G(m|\mu,\sigma)$ is a Gaussian distribution with mean μ and standard deviation σ, used to describe the signal peak, and $P(m)$ is a polynomial function, used to describe the background shape. The main parameters extracted from the fit are the number of tag and probe pairs in the signal peak N_{Tot} and the muon reconstruction efficiency with respect to the reconstructed ID tracks ϵ. The mean and width of the two Gaussian distributions are forced to be the same and a second–order polynomial is used for the background shape modeling.

The systematic uncertainties on the measurement are dominated by the background and signal modeling and several fit variants have been tested in order to probe the stability of the fit results. As a further check the analysis is repeated using calorimeter–tagged probes, instead of simple ID tracks, which lead to a reduced dependency on the background subtraction.

As an illustration, Fig. 13 shows an example of T&P mass fit in the barrel region ($0.1 < |\eta| < 1.1$) for the analysis with ID probes (top) and CT probes (bottom) and the corresponding turn–on efficiency curve as a function of the muon p_T for chain 1.

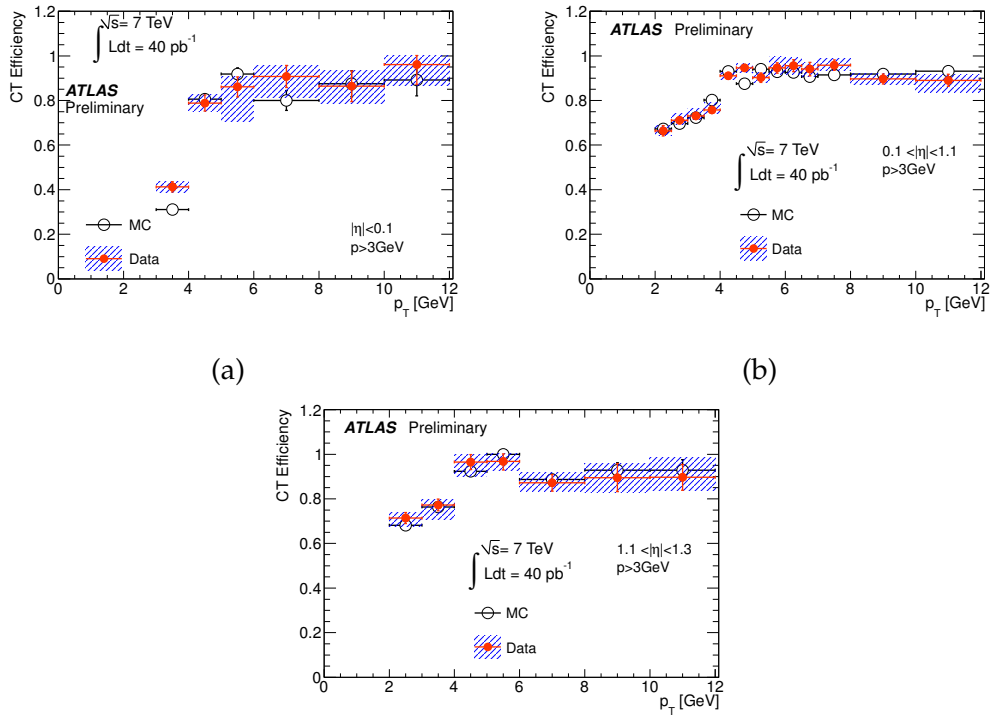

Figure 16: Calorimeter tagging efficiency as a function of p_T in three $|\eta|$ regions from the $j/\psi \to \mu\mu$ T&P analysis; the efficiency measured in data is compared to the simulation. The error bars are the statistical uncertainties while the band around the data points represents the statistical and systematic uncertainties added in quadrature.

Examples of scale factors for the chain 1 CB and CB+ST muons are shown in Fig. 14 in bins of muon $|\eta|$ and transverse momentum. The scale factors obtained with CT and ID probes are presented; they are found to be statistically consistent. It can be observed also that the uncertainty in the measurement obtained using the CT probe is smaller than the corresponding result derived with ID probes; this improvement arise due to lower background contamination in the sample of calorimeter tagged probes.

Due to the toroidal magnetic field of the ATLAS MS, muons with positive (negative) charge are bent towards larger (smaller) η. At a given η for low p_T muons there is a strong charge dependency arising from the CB track requirements.

However, as long as the ATLAS detector is symmetric with respect to $\eta = 0$, the efficiency depends only on $q \times \eta$, where q is the muon charge. Fig. 15 shows the reconstruction efficiency for CB muons of chain 2 as a function of $q \times \eta$ for probes with 2 GeV$< p_T <$ 6 GeV. A strong asymmetry between positive and negative $q \times \eta$ is observed for CB muons. The dependence is well reproduced in the simulation.

The same strategy used for measuring the muon reconstruction efficiency with ID probes can be applied to determine the efficiency for tagging a muon using the calorimeter. The calorimeter muon tagging efficiency is presented in Fig. 16; the simulation reproduces well the measured efficiency in data.

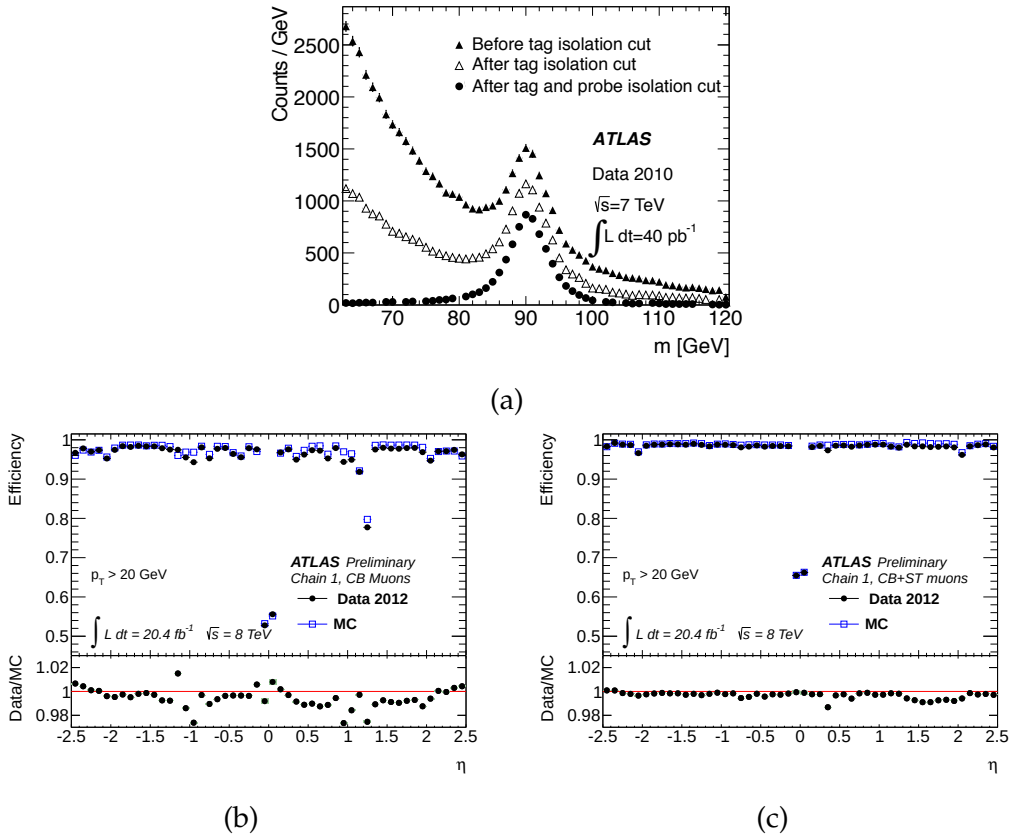

Figure 17: $Z \to \mu\mu$ tag and probe invariant mass distribution obtained without isolation cuts, with isolation cut on the probe only and on both the tag and the probe (a). Efficiency for CB (b) and CB+ST (c) muons of chain 1 with respect to the inner tracking efficiency as a function of the pseudorapidity of the muon for $p_T > 20$ GeV [71]. The panel at the bottom shows the ratio between the measured and predicted efficiencies.

2.3.1.2 *Tag and probe with* $Z \to \mu^+\mu^-$

The T&P with Z boson is designed to be as independent as possible from the background subtraction procedure; a track based isolation cut is applied to both the tag muon and the probe track, the effect of the isolation cut on the background in the T&P selection is shown in Fig. 17 (a).

The sample purity, as estimated from MC simulations, is 99.3% with a low contamination from $Z \to \tau\tau$, $W \to \mu\nu$, $W \to \tau\nu$, $c\bar{c}$, $b\bar{b}$ and $t\bar{t}$. The backgrounds normalization and shape are estimated with simulations and subtracted bin by bin from the tag and probe invariant mass distribution.

Thanks to the large available statistics and low background contamination, the muon identification efficiency is measured in $p_T \times \phi \times \eta$ bins to better match the ATLAS MS geometry layout. An example of the results is shown in Fig. 17 (b) for chain 1 CB muons and Fig. 17 (c) for CB+ST muons integrated over ϕ and p_T; excellent agreement is found between data and simulations. Systematic uncertainties on the efficiency measurement are due to background normalization and muon p_T resolution [71].

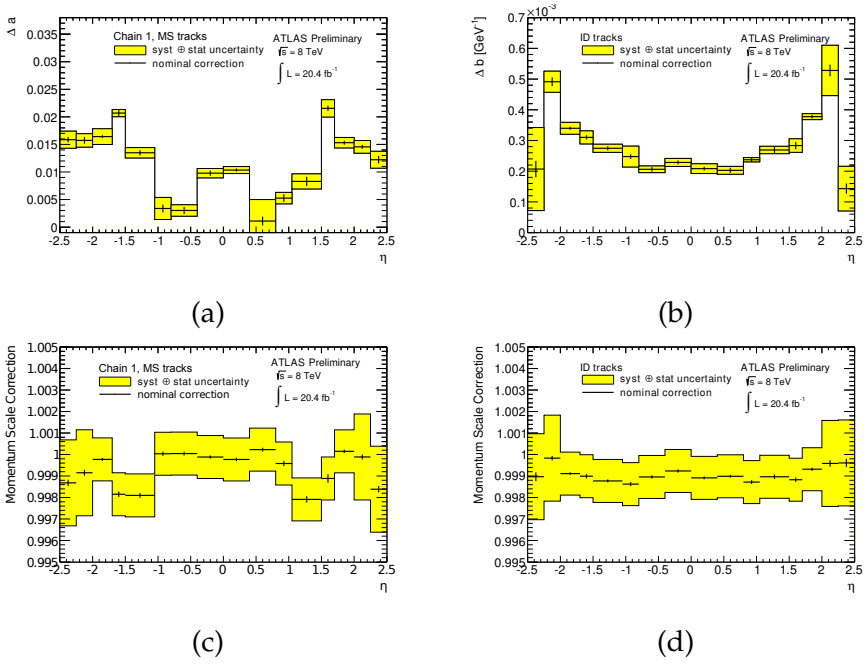

Figure 18: Fitted values and full uncertainty envelope for the Δa and Δb corrections of the MS (a) and ID (b) resolutions; the scale corrections for the MS (c) and the ID (d) are shown at the bottom.

2.3.2 *Muon momentum resolution and energy scale*

The muon momentum corrections are derived by a data–driven procedure using a fit to the di–muon Z boson invariant mass; for the most recent analysis the results are checked with data samples enriched of low–p_T muons by studying the $j/\psi \to \mu^+\mu^-$ and $\Upsilon \to \mu^+\mu^-$ invariant mass spectrum.

The "corrected" muon momentum for the ID, $p_T^{Cor,ID}$, and for the MS, $p_T^{Cor,MS}$, can be parametrized according to

$$p_T^{Cor,ID} = p_T^{ID} s^{ID}(\eta)(1 + \Delta a^{ID}(\eta) G(0,1) + \Delta b^{ID}(\eta) G(0,1) p_T^{ID}) \quad (25)$$

$$p_T^{Cor,MS} = p_T^{MS} s^{MS}(\eta)(1 + \Delta a^{MS}(\eta) G(0,1) + \Delta b^{MS}(\eta) G(0,1) p_T^{MS}) \quad (26)$$

where the original momentum in the MC simulation (p_T^{ID} and p_T^{MS}) are modified in various η regions by multiplicative corrections ($s^{ID}(\eta)$ and $s^{MS}(\eta)$), independent for ID and MS, by a Δa term, to correct the effect of residual mismodeling of multiple scattering in the ID and MS, and by a Δb term, related to intrinsic resolution mismodeling (e.g., simulation of chamber misalignments). The value of Δa^{ID} and Δb^{MS} are fixed to zero according to studies based on data and MC simulations.

The Z mass lineshape in data is fit by the Monte Carlo Z mass template with an iterative procedure: a set of MC templates are obtained by changing the muon p_T according to Eq. 26, the best fit parameters are derived corresponding to the best data–MC χ^2 obtained among the MC template variations. The procedure is independently performed for the ID and MS mass distributions; the correction for

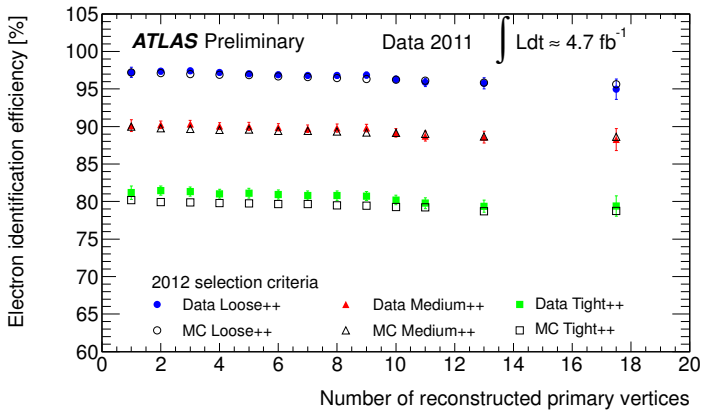

(a)

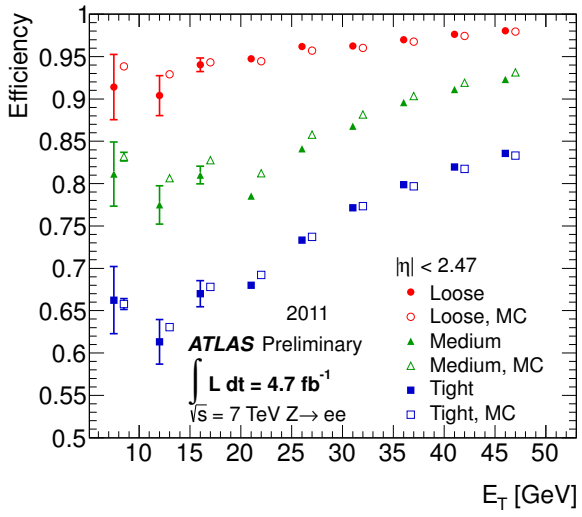

(b)

Figure 19: Pile–up dependence of the electron reconstruction efficiency (a) and efficiency as a function of the electron transverse energy (b) [72].

the combined p_T measurement is derived as a weighted average value of ID and MS corrected measurements.

The best fit value for the parameters Δa, Δb, s^{MS} and s^{ID} are given in Fig.18 (a-d) along with the envelope due to systematic uncertainties on their determination.

2.4 ELECTRON AND PHOTON IDENTIFICATION

The electron reconstruction is based on a combination of ID and ECAL measurements in the central region ($|\eta| < 2.47$) while it uses the ECAL measurements only outside the inner tracking volume ($2.5 < |\eta| < 4.9$).

The full electron reconstruction is seeded by electromagnetic (EM) cluster deposits in the ECAL, i.e. groups of calorimeter cells with energy deposits above threshold; the tracks identified in the tracking volumes are extrapolated to the ECAL and matched to the EM cluster based on a ΔR criterion. If the EM cluster is

found in the forward region, no tracking information is available; the EM cluster reconstruction is optimized taking into account the calorimeter noise and using a variable number of EM cells, *topological clusters*, in contrast to the reconstruction of central electrons where a fixed number of EM cells is used [73].

The electron identification uses a cut based identification. It consists in a set of cuts to the EM cluster and track quality as well as track–cluster matching criteria; they are designed to improve the electron fake rate rejection power by a factor of 500 (*Loose*), 5000 (*Medium*) and 50000 (*Tight*) as determined from Monte Carlo simulations of the 2010 detector operation; during the 2011 three more working points were introduced *Loose++*, *Medium++* and *Tight++* with reduced pile–up sensitivity but with similar fake rejection power of the Loose, Medium and Tight working points. The exact definition of the cuts used for the electron identification can be found in Ref. [73].

The electron performance in simulations is corrected to reproduce the performance observed in data; this is done mainly by using the tag and probe method at the j/ψ and Z resonances and cross checking the results with a sample of $W \to e\nu$; the basic ideas and experimental challenges are the same as discussed in Sec. 2.3 for the measurement of the muon performance. Separate data to MC corrections are delivered for the reconstruction, identification and trigger electron efficiencies binned in η–E_T. The main systematic uncertainties are driven by the background subtraction procedure.

Some examples of electron identification efficiencies are given in Fig. 19, where they are shown as a function of the number of reconstructed primary vertices and of electron transverse energy for the 2011 data taking. The electron ID efficiency is typically between 80%, for the tightest working point, and 97%, for the looser working point; the efficiency degradation due to pile–up is found to be of the order of $1-2\%$.

The electron energy scale is corrected to account for the residual miscalibration of the simulation by rescaling the electron energy as $E \to E(1+\alpha)$; the α parameter is estimated in several η regions to account for the ECAL inhomogeneities. The energy corrections are derived using a data driven method which exploits the Z mass lineshape; the E_T dependence of the corrections are investigated by using the j/ψ mass peak position as a reference for low E_T electrons.

As for the electron reconstruction, the photon identification exploits the electromagnetic shower shape information to distinguish prompt photons from background photons [74], mainly $\pi^0 \to \gamma\gamma$. The default photon identification method relies on a set of cuts on discriminant variables with an overall estimated efficiency of about 85% and a background rejection factor of the order of 5000. The photon efficiency is determined in data, and compared to Monte Carlo simulations, with three in situ methods based on the $Z \to \ell\ell\gamma$ ($\ell = \mu/e$) events, a Monte Carlo extrapolation from a $Z \to ee$ sample and using an inclusive sample of photon candidates.

2.5 RECONSTRUCTION OF JETS AND HADRONIC τ DECAYS

The standard jet reconstruction in ATLAS is seeded by calorimeter topological clusters which are used as input to the anti–k_t algorithm with radius parameter $R = 0.4$ or $R = 0.6$.

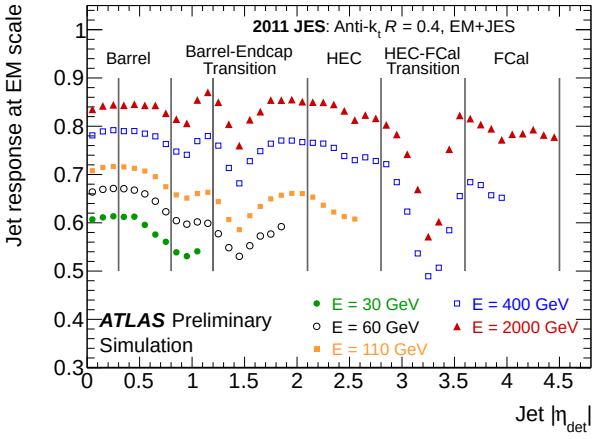

Figure 20: Jet energy response at the EM scale as a function of the jet pseudorapidity in various energy regimes [75].

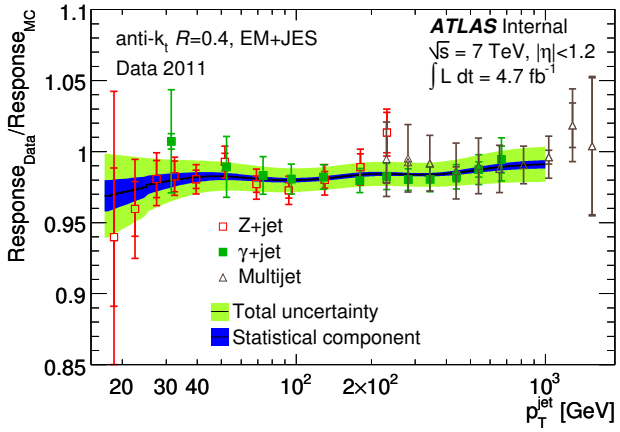

Figure 21: Ratio of jet energy response in data and simulation derived from the combination of the in situ methods described in the text after the Monte Carlo calibration; the individual response ratios for each in situ method are superimposed [75].

Clusters are reconstructed and their energy is estimated based on the electromagnetic calorimeter response (EM jets); alternatively, jets can be corrected by a "local weighting procedure" (Local Cluster Weighting, LCW) which uses the information carried by the shower envelope in the calorimeter to classify the jet as hadronic or electromagnetic and takes into account the non containment of particles produced in the shower development.

A jet energy calibration procedure is then applied in data and simulation [75]; it is based on two steps: first a Monte Carlo based calibration is used, then several in situ methods are adopted to cross validate the MC calibration and to derive residual corrections.

The Monte Carlo calibration is based on a comparison between the jet energy scale (JES) at detector level with the energy of the jet from the Monte Carlo truth; in order to define the truth level jets as close as possible to the detector level, neu-

trinos and muons are not passed to the clustering algorithm. The MC calibration naturally correct for

- pile–up: the jet energy scale is corrected on event by event base to take into account in–time and out–of–time pile–up by using the number of reconstructed vertices and the mean number of interactions per bunch crossing;
- primary vertex position: a jet by jet correction is applied to the jet four momentum in order to ensure that the jet direction is defined at the nominal primary vertex.

The jet energy response at the EM scale is given by the ratio $E_{jet}^{EM}/E_{jet}^{truth}$, being E_{jet}^{EM} the energy measured in the ECAL and E_{jet}^{truth} derived from the Monte Carlo. The response at the EM scale is shown in Fig. 20 as a function of the jet pseudorapidity for jets with energy from 30 GeV to 2 TeV.

The residual energy scale mismatch between data and simulations is taken into account by data driven corrections obtained as a function of the jet transverse momentum; these corrections are derived by exploiting the jet balance technique between a jet and a well measured object, like a leptonically decaying Z boson or a photon, or using multijet topologies. The results of the in situ calibrations are combined by using a weighted average based technique [76].

The results of the in situ calibration are presented in Fig. 21 including the combined data–to–MC response ratio. The experimental signatures exploited in the jet balance method are sensitive to complementary kinematic regimes of the recoiling jet; at low and intermediate jet p_T (15–100 GeV) the Z+jet signature provides the most important contribution, at intermediate p_T (100–600 GeV) the combination is dominated by the γ+jet balance, while the high p_T region ($p_T >$ 700 GeV) is mainly covered by the multijets balance method. The calibration uncertainties are provided as a full list of 49 parameters (nuisance parameters, NP), often reduced to an effective set of 12, that can be propagated into the analyses.

The modeling of a few other effects needs to be evaluated; therefore further dedicated studies are performed in order to cover the residual intrinsic uncertainties affecting the Monte Carlo calibration even after the in situ corrections are applied. The following sources of systematic uncertainties are identified.

- Flavor and topology. The jet balance method, especially in the low p_T region, probes mostly the energy response to quark initiated jets; a comparison of quark jets and gluon jets response can be performed using MC simulations using events with different expected quark and gluon composition.
- B–jets. Jets produced in b–quark fragmentation are expected to have a slightly different response because of the undetected energy of neutrinos or leptons from heavy flavors decays. An additional uncertainty, between 1.5% to 3%, is assigned for such jets based on studies using simulation and checked with data samples with enhanced fraction of heavy flavor jets.
- Close–by jets. The Monte Carlo calibration and, to a large extent, the jet balance method probes isolated jets; an additional study to take into account the JES dependence on close–by jets has been performed by comparing the data and the simulation for jets built from Inner Detector tracks, “track jets”,

and the standard jets (built from topological clusters) when one additional near–by jet with $p_T > 7$ GeV is present.

- Pile–up. The pile–up interactions shift the energy response. To study the jet energy "offset" introduced by the pile–up the JES is studied in simulation as a function of the number of reconstructed primary vertices and as a function of the average interactions per bunch crossing. As the Monte Carlo samples are already simulated with the same pile–up conditions of the data, the residual non–closure observed in the JES corrections are treated as an additional systematic.

- Monte Carlo non–closure. In the calibrations the used Monte Carlo samples are derived with specific simulation configurations. Possible systematic effects, for instance occurring when using different simulation configuration, are evaluated by comparing the jet response in various samples. This leads to a negligible effect in the central region and a maximum of about 3% in the forward region.

The jet energy resolution (JER) is well described by simulation, therefore no further corrections are applied to the MC samples; however, an uncertainty on the JER is used to cover all the residual data–to–MC discrepancies; it is propagated through the analyses by oversmearing the jet energy in simulation.

The τ lepton identification is based in the reconstruction of its leptonic decay modes, $\tau \to \mu\overline{\nu}_\mu\nu_\tau$, or by its hadronic decays. The identification of leptonically decaying τ leptons, τ_ℓ, rely substantially on the lepton and missing transverse energy reconstruction. On the other hand, hadronically decaying τ, τ_h, can be reconstructed using standard jet algorithms because the hadrons produced by the τ_h are typically well collimated; however, τ–jets have a peculiar hadron content, therefore a specific calibration is required. The τ_h candidates are reconstructed by the anti–k_t algorithm with radius parameter $R = 0.4$ using topological clusters as input in the LCW calibration scheme. The τ_h decays are categorized, according to the number of associated track found in the Inner Detector, as 1–prong (one reconstructed track) and as multi–prong (more than one reconstructed track); because the τ_h reconstruction makes use of tracking information, its acceptance is limited to the ID tracking volume $|\eta| < 2.5$. The details of the τ energy scale and identification performance are described in Ref. [77, 78].

2.6 MISSING TRANSVERSE ENERGY RECONSTRUCTION

The missing transverse energy (E_T^{miss}) determination is based on a full event reconstruction of all physics objects and the calorimeter objects, named soft terms (ST), not associated to any physics object; in each collision the total (true) transverse energy is zero, thus the reconstructed E_T^{miss} can be defined as the (signed) sum of the transverse energy components of each object

$$\begin{aligned} E_T^{miss} &= E_T^{miss,\mu} + E_T^{miss,e} + E_T^{miss,\gamma} + E_T^{miss,\tau} + \\ &\quad + E_T^{miss,jets} + E_T^{miss,calo\,\mu} + E_T^{miss,ST}\,, \end{aligned} \tag{27}$$

with

$$E_T^{miss,ST} = E_T^{miss,softjets} + E_T^{miss,CellOut} . \quad (28)$$

In Eq. 27 several contributions, listed below, can be identified.

- $E_T^{miss,\mu}$ and $E_T^{miss,calo\,\mu}$. For isolated muons the muon term, $E_T^{miss,\mu}$, is calculated from the parameters of the combined muon track and the muon energy deposit in the calorimeter, $E_T^{miss,calo\,\mu}$, is ignored to avoid double counting. In regions with limited MS coverage the muon parameters are measured from the ID track. If the muon is produced inside a jet (like in heavy flavor decays) its energy can not be easily resolved from the jet energy, and its calorimetric energy deposit is measured with limited precision. In this case the double counting of the muon energy deposit in the calorimeter is avoided by computing $E_T^{miss,\mu}$ with the kinematics of the muon reconstructed in the MS.

- $E_T^{miss,e}$ and $E_T^{miss,\gamma}$. The electron and photon terms, $E_T^{miss,e}$ and $E_T^{miss,\gamma}$, are determined from the electromagnetic energy clusters as described in Sec. 2.4.

- $E_T^{miss,\tau}$. The τ term is calculated using tight τ identification [78] calibrated in the LCW scheme.

- $E_T^{miss,jets}$. The jet term takes into account all the jets with transverse momentum greater than 20 GeV calibrated in the LCW+JES scheme.

- $E_T^{miss,softjets}$. The soft jets term takes into account jets with low transverse momentum, $7 < p_T[\text{GeV}] < 20$, clustered with the anti–k_t algorithm with $R = 0.6$ and calibrated in the LCW scheme.

- $E_T^{miss,CellOut}$. The CellOut term takes into account all the residual calorimetric topological clusters not associated to any physics objects; a further correction is applied to include soft particles not clustered in the calorimeters but which are reconstructed in the Inner Detector.

The missing transverse energy description in data and simulation, as far as the absolute scale and resolution are concerned, can be studied in a sample of $Z \to \ell\ell$ (with $\ell = e, \mu$) where no genuine missing transverse energy is expected apart from a small contribution due to heavy flavor semileptonic decays in jets which are expected to contribute as $\sim 10^{-4}$ to the total event rate.

In principle all the components of Eq. 27 are subject to scale and resolution systematic uncertainties of the corresponding physics objects; however it is quite common to consider only the systematic uncertainties related to the final state under consideration according to the effective event topology.

The $E_T^{miss,ST}$ term is further studied with dedicated methods using a sample of $Z \to \mu\mu$ events [79]; a 5% uncertainty is derived for the E_T^{miss} energy scale and a 2% uncertainty on the resolution in order to cover the residual mismodeling in simulation.

2.7 FLAVOR TAGGING

Currently, two main classes of b–tagging algorithms are used in ATLAS, one exploits the large lifetime of b–hadrons and the other relies to the reconstruction of "soft" (low p_T) muons from weakly decaying b–hadrons.

Lifetime based b–tagging algorithms aim at identifying topologies where b–hadrons decay inside jets leading to characteristic signatures which can be observed with the charged tracks reconstructed in the Inner Detector. Two main strategies are used by these algorithms. The most inclusive approach consists in characterizing the internal jet structure with the impact parameters (transverse and longitudinal) of the tracks associated to the primary vertex and then building a statistical discriminator which encodes this information into flavor weights [80]. A more exclusive approach is based on the explicit reconstruction of secondary vertices inside the jets [81]. In both methods, the tracks inside the jets used by the algorithms undergo a specific selection intended to reduce the rate of fake tracks from material interactions and long lived light flavored particles, like K_s and Λ; this track selection is based on cuts on the number of precision hits in the ID (measured by the Pixel or by the SCT) as well as transverse and longitudinal impact parameter cuts.

The most commonly used lifetime algorithms are:

- SV0. It reconstructs secondary vertices inside jets; the most commonly used outputs of this algorithm are the hadron decay length in the transverse plane and the invariant mass of the charged tracks stemming from the secondary vertex (SV0 mass).

- JetFitterCombNN. It combines into a neural network the input variables used in the JetFitter[2] and the IP3D[3] algorithms; the neural network output provides the probability for a jet to be light flavored (p_u), charm flavored (p_c) or to be beauty flavored (p_b), which are further combined to make two discriminant variables

$$\begin{aligned} \text{discriminant against light jets:} \quad & \log(p_b/p_u) \quad \text{(CombNN)} , \\ \text{discriminant against charmed jets:} \quad & \log(p_b/p_c) \quad \text{(CombNNc)} . \end{aligned}$$

- MV1. It combines the IP3D, the SV1[4] and the JetFitterCombNN algorithms weight by using a neural network; the MV1 weight derived from this combination provides the best discriminating power between light and b–jets.

2 The JetFitter algorithm uses the full topological information from the decay chain of heavy flavors, including the collinearity of vertices from b–hadrons and subsequent c–hadrons decays by using a Kalman filter; the algorithm combines the topological information (summarized by the number of two–track vertices, the number of single track vertices and the total number of tracks associated to two–track vertices) to the secondary vertex information (given in terms of invariant mass, energy fraction of tracks associated to the secondary vertex and vertex decay lengths); this information is combined into a single discriminant determined as output of an artificial neural network.

3 It builds jet weights using a likelihood ratio technique based on the discriminating power encoded in the transverse and longitudinal impact parameter significance.

4 It exploits properties associated to the reconstructed secondary vertex combined in a likelihood ratio discriminant; these includes the invariant mass of the tracks from the secondary vertex, their energy fraction (calculated with respect to all tracks of the jet) and the number of two–tracks vertices.

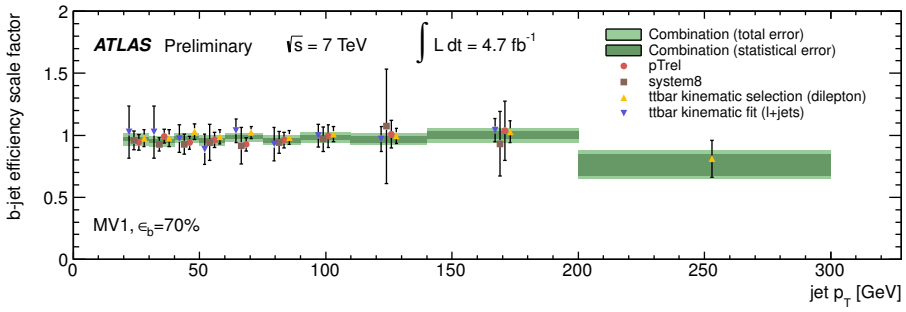

Figure 22: B–tagging scale factors derived from the di–jets (pTrel and system8) and $t\bar{t}$ (kinematics selection and kinematic fit) methods described in the text. The combination of the methods is also shown as a green band.

A complementary approach is used by algorithms based on soft muon tagging (SMT); low p_T muons inside jets are explicitly reconstructed as Combined muons with the purpose of identifying candidate decay or decay chains of b–hadrons with a good suppression of fake muons rate. The main limitation of such algorithm is the small signal efficiency due to the low (direct or indirect) decay rate of b–hadrons into muons which is $\sim$ 20%; it is used in specific analyses where the additional information of the muon measurement can be exploited.

For each b–tagging algorithm few cut thresholds (working points or operating points) are defined, corresponding to different mistagging rate and b–tagging efficiencies as estimated from Monte Carlo samples. For each working point the b–tagging efficiency description in simulation is corrected in bins of p_T and η to match the observed efficiency in data. The b–tagging efficiency in data is measured by using two kinds of control samples; di–jet samples with enhanced contribution of b-jets are exploited in the pTrel [82] and system8 [83] methods, while $t\bar{t}$ samples [84] (selected using a dilepton or a lepton+jet signature) are used by the tag–counting kinematic selection and the kinematic fit methods. The b–tagging efficiency scale factors used to correct the simulations are combined by a weighted average procedure; the preliminary combination [85] for the 2011 data taking is shown in Fig. 22; the calibration extends up to transverse momentum of 300 GeV.

Separate scale factors are derived for mistagged charm and light jets, as discussed in Ref. [86], by using samples with an enriched content of charm and light jets.

Part II

B–JETS PRODUCED IN ASSOCIATION WITH A Z BOSON IN ATLAS: DIFFERENTIAL CROSS SECTION MEASUREMENTS AND COMPARISON WITH THEORY

3

STATUS OF THE MEASUREMENTS OF B–JETS PRODUCTION IN ASSOCIATION WITH A Z BOSON

Measurements of heavy flavors production in association with a Z gauge boson has attracted the interest of the Tevatron and LHC experimental communities in the last decade; in particular, the Z+b production cross section has been measured at Tevatron and with the early LHC data. These measurements are statistically limited and don't allow to challenge significantly the available theoretical predictions.

As discussed in the introduction of this thesis, the associated production of a massive vector boson and b–jets is the main irreducible background to Higgs production in association with a vector boson, when the Higgs boson decays into a $b\bar{b}$ pair, and to signatures predicted in many BSM scenarios.

Cross section measurements of Z+b and Z+bb production are also intrinsically interesting because they provide an experimental ground for testing the predictions of QCD calculations with massive quarks, namely quarks with mass comparable with their transverse momentum.

In this context, the Z+b production is of particular interest because it is produced copiously and has low background contamination compared to similar measurements, such as $W + b$.

In this chapter the status of the Z+b measurements is summarized. The Tevatron results are illustrated in Sec. 3.1 and the first LHC measurements are introduced in Sec. 3.2.

While the analysis presented in this thesis was under finalization, two new results have been published by the CMS experiment [87, 88]. These results are briefly introduced in Chap. 6 and discussed in comparison with the results of the data analysis of this work.

3.1 CROSS SECTION FOR Z BOSON PRODUCTION IN ASSOCIATION WITH B–JETS AT TEVATRON

The first measurements of Z production in association with b–jets has been performed at the Tevatron collider [89] by the D$\emptyset$ experiment about ten years ago. The main analysis challenge was the background suppression, mainly Z+jets; this was achieved by using a b–tagging algorithm based on the reconstruction of a secondary vertex inside jets. Fig. 23 shows a comparison between the data and the signal prediction plus the estimated backgrounds after the event selection; the jet–p_T (left) is observed to be similar for light and b–jets, while the transverse decay length significance (right), L_{xy}/σ_{xy}, has a clear discrimination potential between the mistagged jets and the signal, as expected. The signal and backgrounds determination is based on a resolution of a two–equation system with the number of light+charm jets and b–jets as unknown; the relative amount of light and charm jets is estimated with Monte Carlo simulation. The results of this analysis are pre-

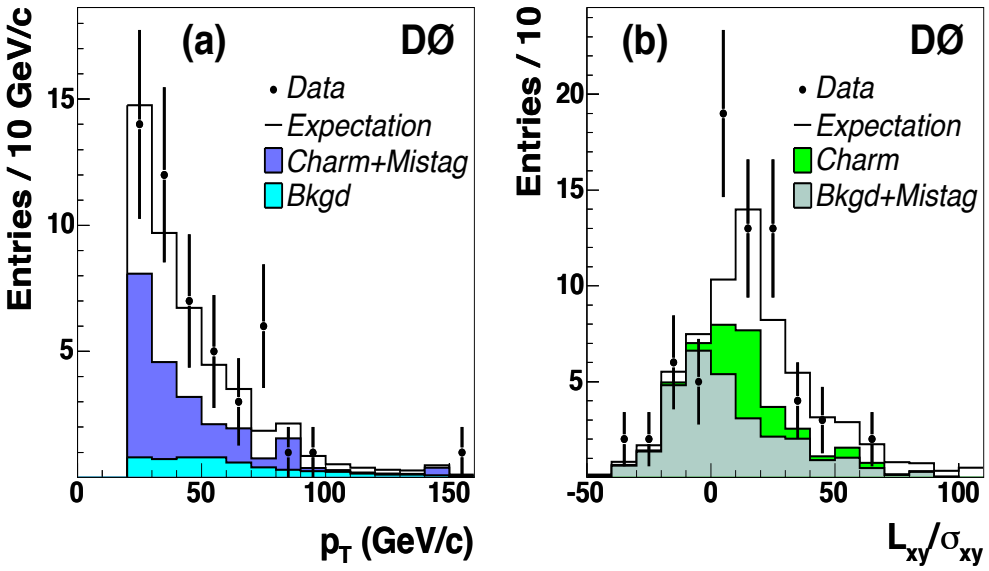

Figure 23: Transverse momentum (left) and transverse impact significance (right) of b–jets candidates selected in events with a Z boson decaying into electron or muon pairs in the first observation of Z+b production by the DØ experiment.

sented in terms of the cross section ratio $\sigma(Z+b)/\sigma(Z+jet)$ and compared to a NLO calculation obtained with the MCFM generator:

$$\text{Data: } \frac{\sigma(Z+b)}{\sigma(Z+\text{jets})} = 0.023 \pm 0.004(\text{stat.})^{+0.002}_{-0.003}(\text{syst.}) ,$$

$$\text{NLO QCD (MCFM): } \frac{\sigma(Z+b)}{\sigma(Z+\text{jets})} = 0.018 \pm 0.004 .$$

The uncertainty on this first measurement is of about 21% and it is dominated by the statistical error, ~ 17%; the theoretical error of the NLO calculation is also considerable, ~ 22%. Within the large uncertainties, the data and the NLO prediction are found to be consistent.

The first Z+b differential cross section measurements has been published in 2009 by the CDF Collaboration at Tevatron [90]. In addition of being the first differential Z+b measurement, this analysis introduces a new method for measuring the flavor fractions of jets produced with the Z boson; it is based on a fit to the invariant mass of tracks originating from the secondary vertex reconstructed inside the jets, Fig. 24. The idea of fitting a flavor sensitive observable for measuring the signal yield and for estimating the Z+jets background has been also adopted by the DØ experiment, is currently widely used at LHC and, in particular, is the same strategy used for the measurement described in Chap. 4.

The differential Z+b cross section measurements of the CDF experiment is summarized in Fig. 25; it is presented as the ratio of the Z+b cross section to the inclusive Z cross section, $\sigma(Z)$. The cross section ratio is measured as a function of the b–jet transverse energy and rapidity; furthermore the jet multiplicity and the b–jet multiplicity are determined; the Z boson kinematic is characterized by measuring its transverse momentum. The experimental error is dominated by the

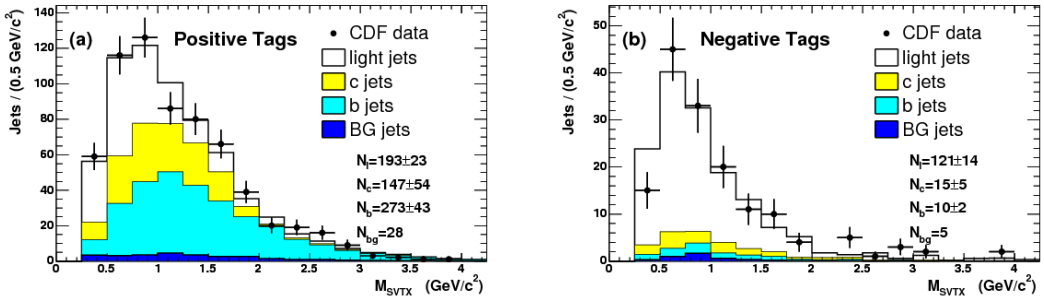

Figure 24: Fit to the invariant mass of tracks produced in the displaced secondary vertex reconstructed inside b–tagged jets in the CDF experiment. The sample is split into two categories: "positive tag" (left), where the secondary vertex is reconstructed in the same hemisphere as the jet, and "negative tag", where the secondary vertex is reconstructed in the hemisphere opposite to the jet, (right). The shapes of the distributions are predicted by simulation.

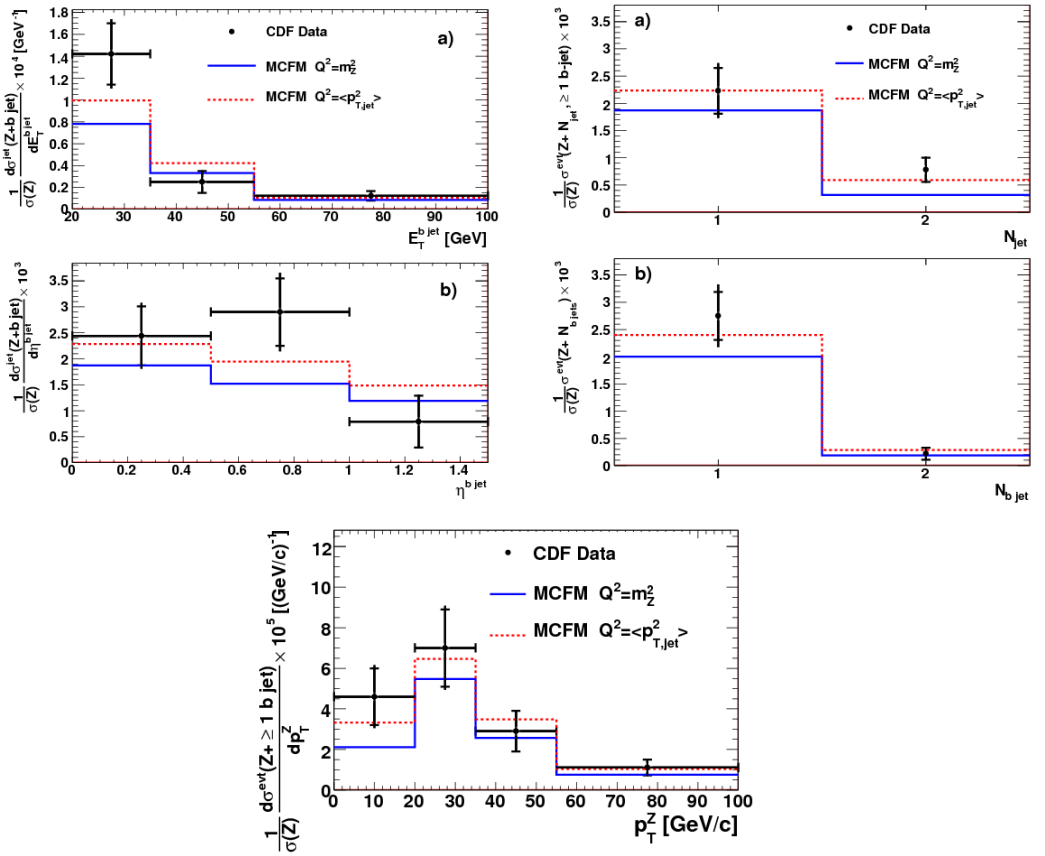

Figure 25: Differential cross section ratio $\sigma(Z+b)/\sigma(Z)$ measured by the CDF experiment as a function of the b–jet transverse energy (a, left), b–jet pseudorapidity (b, left), in jet multiplicity (a, right) and b–jet multiplicity (b, right), and as a function of the Z p_T (bottom). The data are compared to two NLO predictions obtained with the MCFM generator.

statistical uncertainty. The results are compared to NLO QCD predictions derived with MCFM with two different settings for the factorization and renormalization scales:

$$\begin{aligned} 1) \qquad \mu_F = \mu_R &= M_Z \,, \\ 2) \qquad \mu_F = \mu_R &= \sqrt{\langle p_{T,\,jet}^2 \rangle} \,. \end{aligned}$$

The inclusive measurements results are:

$$\begin{aligned} \text{Data: } \frac{\sigma(Z+b)}{\sigma(Z)} &= (3.32 \pm 0.53(stat.) \pm 42(syst.)) \times 10^{-3} \,, \\ \text{NLO QCD (MCFM): } \frac{\sigma(Z+b)}{\sigma(Z)} &= (2.3 \div 2.8) \times 10^{-3} \,. \end{aligned}$$

The uncertainties on the data is dominated by the statistical error which is of about 16%. These results are comparable in precision with the early DØ measurement. As for the differential analysis, the NLO calculation is presented for two choices of the factorization and renormalization scales. The prediction obtained with the scale setting $\mu_F = \mu_R = M_Z$ provides a lower cross section ratio value, 2.3×10^{-3}, whereas the scale choice $\mu_F = \mu_R = \langle p_{T,\,jet}^2 \rangle$ provides a prediction, 2.8×10^{-3}, which is closer to the data. In the same data analysis, other predictions have been tested; in particular a calculation obtained with the ALPGEN generator is found to underestimate the measurement by about a factor two. The statistical uncertainty on the differential measurement is too large to constrain the modeling of the studied distributions.

The most recent DØ measurement of the $\sigma(Z+b)/\sigma(Z+jets)$ ratio [91] is based on a data sample with integrated luminosity of about 10 fb^{-1}; it uses a fit to a flavor discriminant based on a combination of a neural network output and the secondary vertex mass to improve the statistical separation of the flavor components. The analysis results are:

$$\begin{aligned} \text{Data: } \frac{\sigma(Z+b)}{\sigma(Z+jets)} &= 0.0196 \pm 0.0012(stat.) \pm 0.0013(syst.) \,, \\ \text{NLO QCD (MCFM): } \frac{\sigma(Z+b)}{\sigma(Z+jets)} &= 0.0206^{+0.0022}_{-0.0013} \,. \end{aligned}$$

This is the most precise measurement of Z+b production at Tevatron; the statistical and systematic uncertainties are comparable in size, about 6%. In the same analysis, a differential cross section ratio $\sigma(Z+b)/\sigma(Z+jets)$ is determined as a function of the b–jet and Z transverse momentum, the b-jet pseudorapidity and a first measurement of the azimuthal angular correlation between the Z and the b–jet, $\Delta\phi$. These distributions are shown in Fig. 26 and are compared to a few calculations including multileg event generators and a NLO QCD prediction. These results exhibit some discrimination power between the various theoretical predictions; in particular, it is shown that the fixed order NLO calculation obtained with the MCFM generator is not satisfactory in describing the Z transverse momentum and the $\Delta\phi$ distributions.

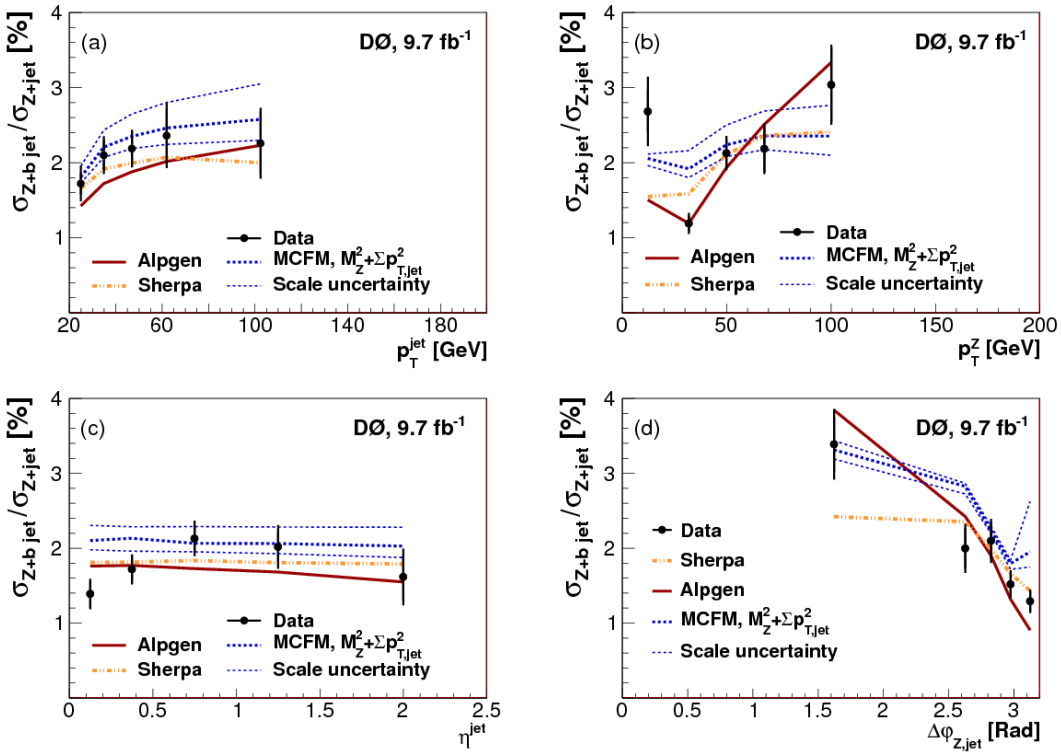

Figure 26: Differential measurements of the ratio $\sigma(Z+b)/\sigma(Z+jet)$ by the DØ experiment.

3.2 CROSS SECTION FOR Z BOSON PRODUCTION IN ASSOCIATION WITH B–JETS AT LHC

The first measurement of the Z+b cross section at LHC has been performed by the ATLAS Collaboration [92]. This analysis uses about 36 pb^{-1} of integrated luminosity collected during the 2010 data taking. The signal determination is based on a template fit to the SV0 mass distribution (see Chap. 2); the fit is shown in Fig. 27 (left). The measured cross section is compared to a few theory calculations, including the NLO MCFM prediction corrected for non perturbative effects.

Shortly after, a similar measurement has been published by the CMS Collaboration [93]. The analysis exploits a larger data sample, corresponding to an integrated luminosity of 2.2 fb^{-1}; the signal extraction is based on the same strategy used by ATLAS (Fig. 27 right). The cross section is then derived for the production of a Z+b and Z+bb final states; as usually the data are compared to the NLO prediction of MCFM and to other calculations based on leading order multileg generators.

As described in the following chapters, the ATLAS analysis using the 2011 dataset has been substantially updated and improved compared to the results shown in this section.

The results of the measurements from ATLAS and CMS are summarized in Tab. 7. The two experiments use a different cross section definition, a per–jet cross section in ATLAS and a per–event cross section in CMS, and a slightly different fiducial phase space.

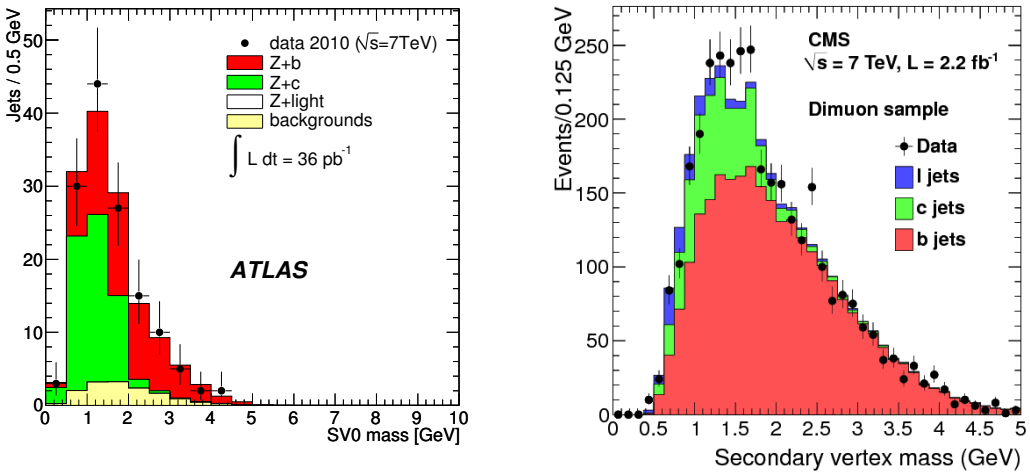

Figure 27: Fit to the invariant mass of tracks associated to the secondary vertex reconstructed inside the b–tagged jets in the ATLAS (left) and CMS (right) Z+b analyses. The shapes of the distributions are predicted by simulation.

$\sigma(Zb) \times N_{b-jets} \cdot BR(Z \to \ell\ell)$ [pb] ($\sqrt{s} = 7$ TeV)		
	Data	NLO QCD
ATLAS [92]	$3.55^{+0.82}_{-0.74}(stat.)^{+0.73}_{-0.55}(syst.) \pm 0.12(lumi.)$	3.88 ± 0.58
CMS [93]	$5.84 \pm 0.08(stat.) \pm 0.72(syst.)^{+0.25}_{-0.55}(theory)$	3.97 ± 0.47

Table 7: Main results of the first Z+b cross section measurements in ATLAS and CMS.

4

ASSOCIATED PRODUCTION OF A Z BOSON AND B–JETS: SIGNAL EXTRACTION

The strategy for the measurement of the $Z + b$ integrated and differential cross sections is described in this chapter and in the next one. The measurement procedure consists in a first step based on the study of detector (or reconstruction) level objects, where the candidate signal events in data are selected and the backgrounds are estimated and subtracted. In a second phase, explained in Chap. 5, the *detector level signal* is converted into a *particle level cross section* and the systematic uncertainties are evaluated.

The measurement uses data collected with the ATLAS detector at the Large Hadron Collider running at center of mass proton–proton energy of $\sqrt{s} = 7$ TeV in the data taking period between April and November 2011.

In this chapter the detector level analysis chain is presented starting in Sec. 4.1, where a general description of the methodology is provided together with the introduction of the observables at reconstruction level; the signal selection criteria are presented in Sec. 4.2 along with a description of the simulated Monte Carlo samples used for the background estimation and, more generally, to interpret the data. The method implemented for the multijets background evaluation is presented in Sec. 4.3; the data yields, the Monte Carlo predictions and the multijet contamination are summarized in Sec. 4.4. The final detector level $Z + b$–jet yield (briefly, b–yield) is determined with a flavor sensitive fit procedure described in Sec. 4.5.

4.1 ANALYSIS STRATEGY FOR THE DETECTOR LEVEL Z+B MEASUREMENT

The detector level Z+b analysis aims at identifying reconstructed b–jet production in association with a reconstructed e^+e^- or $\mu^+\mu^-$ pair from a Z decay for measuring the following yields:

- $N(Zb) \times N_{b\text{–jet}}$, number of b–jets produced in association with a Z boson;
- $N^\star(Zb) \times N_{b\text{–jet}}$, number of b–jets produced in association with a Z boson of transverse momentum $p_T \geqslant 20$ GeV;
- $N(Zb)$, number of events with at least one b–jet produced in association with a Z boson.

Corresponding to these signal definitions, several differential distributions are also measured.

- $N(Zb) \times N_{b\text{–jet}}$ signal: b–jet p_T, b–jet $|y|$ and $|y_{boost}(Z, b\text{–jet})| = |b\text{–jet}\, y + Z\, y|/2$ (indicated as $|y_{boost}(Z, b)|$).
- $N^\star(Zb) \times N_{b\text{–jet}}$ signal: $|\Delta y(Z, b\text{–jet})|$, $\Delta\phi(Z, b\text{–jet})$ and $\Delta R(Z, b\text{–jet})$ (indicated respectively as $|\Delta y(Z, b)|$, $\Delta\phi(Z, b)$ and $\Delta R(Z, b)$).

Distribution	Binning
b–jet p_T[GeV]	$\{20, 30, 50, 75, 110, 200, 500\}$
b–jet $\lvert y \rvert$	$\{0, 0.2, 0.4, 0.6, 0.8, 1.2, 1.6, 2.0, 2.4\}$
$\lvert y_{boost}(Z, b)\rvert$	$\{0.0, 0.2, 0.4, 0.6, 0.8, 1.2, 1.6, 2.0, 2.5\}$
$\lvert\Delta y(Z, b)\rvert$	$\{0.0, 0.2, 0.4, 0.6, 0.8, 1.2, 1.6, 2.0, 3.0, 5.0\}$
$\Delta\phi(Z, b)$[rad]	$\{0, 0.5, 1, 1.5, 2.0, 2.4, 2.8, 3, \pi\}$
$\Delta R(Z, b)$	$\{0, 1, 1.5, 2, 2.5, 3, 3.5, 4, 4.5, 6\}$
Z p_T[GeV]	$\{0, 20, 30, 40, 60, 80, 110, 200, 500\}$
Z $\lvert y \rvert$	$\{0.0, 0.2, 0.4, 0.6, 0.8, 1.2, 1.6, 2.0, 2.5\}$

Table 8: The measured differential distributions in the $Z + b$ analysis and the chosen binning.

- $N(Zb)$ signal: Z p_T and Z $|y|$.

These variables allow to investigate all the relevant kinematics features of the events of interest: from the transverse momentum measurement of the Z and b–jets to all the angular variables representing the distribution of the physics objects in space.

The binning for each differential distribution is shown in Tab. 8; it is dictated by the available statistics and resolution.

The basic analysis steps are the candidate signal selection and the background subtraction. The background are estimated with simulation or are statistically subtracted from data.

In this analysis, the dominating background contamination originates from events with a Z boson produced in association with a jet that is not a b–jet but, nevertheless, it passes the b–jet selection requirements. These special and dominating background events are either Z+light jets, where the jet (from a gluon or light quark) is accidentally reproducing features similar to those used to select b–jets, or Z+c–jets. The latter category of events is similar to the signal, due to presence of displaced secondary vertices from charmed hadrons weak decays.

According to an inclusive simulation of Z+jets events, the fractions of Z+light, Z+charm and Z+b are $(100 : 2 : 1)$; after applying a typical b–tagging selection one can expect that the relative fractions selected become $(40 : 30 : 30)$. The Z+light and Z+charm backgrounds cannot be handled by a pure subtraction of the fractions predicted by the simulation. Therefore a special fit of b–sensitive distributions is used to extract the b–jet yield in the total Z+jet selected signal; the fit method relies on the Monte Carlo only for the modeling of the flavor discriminating distributions.

The signal selection is a common ground for all the three kinds of measured b–yields. It is designed by the requirements of having a precise determination of leptons and jet reconstruction performance and small pile–up dependence. As a consequence the signal is defined within a *fiducial phase space* (or *fiducial volume*) at detector level.

The analysis is based on the Z boson decay modes $Z \to ee$ and $Z \to \mu\mu$; the two leptonic channels are studied separately at detector level and cross checked at particle level, but the main analysis results are obtained by combining the two channels already at detector level as described and justified in Sec. 4.5.

4.2 SIGNAL AND BACKGROUND PROCESSES

Selection	Description
Primary vertex definition	• Vertex with max $\left(\sum_{track} p_T\,(tracks)^2\right)$.
Primary vertex quality	• $\geqslant 3$ tracks assigned to event vertex.
Electron selection criteria	• Medium++. • $\lvert\eta(e)\rvert < 2.47$, $p_T(e) > 20$ GeV. • Transition region $1.37 < \lvert\eta(e)\rvert < 1.52$ excluded. • Electron track $\lvert z_0(e)\rvert < 1\,mm$, $\lvert d_0(e)\rvert/\sigma(d_0(e)) < 10$.
Muon selection	• Chain 1 Combined. • $\lvert z_0(\mu)\rvert < 1\,mm$, $\lvert d_0(\mu)\rvert/\sigma(d_0(\mu)) < 3$. • $\lvert\eta(\mu)\rvert < 2.4$, $p_T(\mu) > 20$ GeV. • Isolation: $\mathcal{I} < 0.1$.
$Z \to ee$ selection	• Two oppositely charged selected electrons. • No further e or μ in event (passing the same criteria). • $76 < M_{ee}[\,\text{GeV}] < 106$.
$Z \to \mu\mu$ selection	• Two oppositely charged selected muons. • No further e or μ in event (passing the same criteria). • No selected e with $\Delta R(e,\mu) > 0.1$. • $76 < M_{\mu\mu}[\,\text{GeV}] < 106$.
Event selection based on E_T^{miss}	• Pass "looser" E_T^{miss} cleaning. • $E_T^{miss} < 70$ GeV.
Jet selection	• Anti-k_t jets, built from topo-clusters, $R = 0.4$. • $p_T > 20$ GeV. • $\lvert y(\text{jet})\rvert < 2.4$. • $\Delta R(\text{jet, signal } \ell) > 0.5$. • If the JVF determination is available, require JVF > 0.75. • Pass "looser" jet cleaning requirements. • Jet not in LAr hole. • **B–tagging**: MV1 $\geqslant 0.404219$.

Table 9: Object and event selection criteria. The veto on the third lepton in the event refers to leptons passing all the selection requirements applied to the candidate leptons from $Z \to \ell\ell$. All the selection cuts are applied to physics objects with calibrated four–momentum.

The topology of a Z+b event consists of two high p_T same flavor leptons with opposite charge and invariant mass close to the Z boson peak, and by additional hadronic activity due to b–jet production; the candidate b-jets can be identified by means of their different structure compared to a gluon, a light quark or a charm quark jet by exploiting the distinctive signature of b-hadron weak decays inside the jet, leading to reconstructed displaced vertices and to characteristic distribution of the impact parameter of tracks.

All the background sources contribute to the signal selection because they produce a genuine two–leptons plus b-jets (*genuine* $\ell\ell$+*b*) signature or because they are misidentified in the detector as two–leptons plus b-jet candidates (*fake* $\ell\ell$+*b*) either due to leptons or b-jets misidentification. The main backgrounds for the Z+b selection belong to the fake $\ell\ell$+b category, and due to Z+light jets[1] or Z+charm (Z+c) jets production. Requiring at least two candidate b-jets the background composition changes significantly; in particular, the contribution of the $t\bar{t}$ background becomes important.

The $t\bar{t}$ background contributes to the signal by means of the decay chain $t\bar{t} \to WbWb \to \ell\nu b\ell\nu b$, therefore, it may produce exactly two same flavor high p_T leptons and two b–jets; however, because of the neutrinos from the leptonic W decays, the event exhibits a missing transverse energy much higher than the typical Z+b events. This feature can be exploited for an efficient suppression of this background.

Single top production in the tW–channel also produces a genuine $\ell\ell$+b signature in the decay mode $tW \to WbW \to \ell\nu b\ell\nu$; though, as for the $t\bar{t}$, it can be reduced exploiting the expected large missing transverse energy. Another sub–leading background contribution is due to single top production in s–channel and t–channel where the single top can be produced in association to a b-jet and the final state is characterized by two b–jets, with one of them misidentified as a lepton, and one high p_T lepton; these additional sources are suppressed compared to the tW–channel because of the small cross section and the low rate of leptons misidentification.

The di–boson production provides the largest non Z+jets background to the Z+b selection via the decays $ZZ(W^{\pm}) \to \ell\ell qq(qq')$, where q is a generic quark flavor, leading to both $\ell\ell$+b and fake $\ell\ell$+b backgrounds; these are irreducible backgrounds and can't be efficiently suppressed with specific topological cuts.

Other fake $\ell\ell$+b backgrounds are W+jets as well as $Z(\to \tau\tau) + jets$ contributing to the signal selection because either jets or τ are identified as electrons or muons. However, their contribution to the signal region can be safely neglected because of the small lepton misidentification rate and the relatively small production cross sections. The contribution to the Z+b candidates selection due to multijet production, where two jets are misidentified as leptons and at least one further jet being a genuine b–jet or a mistagged charm or light jet, is not a priori negligible because of the large cross section for jet production at LHC.

The signal and all backgrounds, but multijet production, are simulated with Monte Carlo programs interfaced with the detector simulation based on GEANT4 [94].

1 From here on Z+light indicates the associated production of a Z boson and a jet induced by a gluon, up quark, down quark or strange quark.

The generated samples for the signal and background sub-processes are listed, respectively, in Tab. 40 and Tab. 41 in App. B.

4.2.1 *Monte Carlo samples*

The Z+jets samples, including $Z \to ee$, $Z \to \mu\mu$ and $Z \to \tau\tau$ decays, are generated with ALPGEN [95] matrix element calculation using CTEQ61L PDF set [96] interfaced with HERWIG6.6 [47], for parton shower and hadronization, and with JIMMY [97], for the MPI and underlying event simulation. Double counting between parton jets produced in the matrix element and by the parton shower have to be removed in the Z+jets generation. The jets overlap removal is addressed with the MLM merging [42] algorithm.

In order to enhance the size of the signal sample, specific Z+bb events are generated with the ALPGEN matrix element in addition to the inclusive Z samples. The double counting of Z+bb events, which are produced also in the inclusive Z sample, is solved by implementing a Heavy Flavor Overlap Removal (HFOR) procedure based on a simple algorithm: as a first step the events in the inclusive Z sample where the b–quarks are produced by the ALPGEN matrix element are rejected, next the merging between the parton shower in the inclusive Z sample and the Z+bb matrix element in the other is emulated by retaining only the b-quark pairs from parton shower with $\Delta R(b, \bar{b}) < 0.4$ and b–quark pairs from matrix element with $\Delta R(b, \bar{b}) > 0.4$. All b–quarks produced in the underlying event are unaffected by the overlap removal procedure. All the Z+jets Monte Carlo samples are normalized to the inclusive Z production cross section evaluated at NNLO in perturbative QCD [98].

The $t\bar{t}$, Wt–channel and s–channel single top backgrounds are simulated with MC@NLO [99, 100] using CT10 NLO PDF set [96], while the single top production in the t–channel is simulated with the ACER MC [101] using a modified LO PDFs [102]; the di–boson backgrounds are generated with MC@NLO; the W+jets background is generated with ALPGEN matrix element calculation with CTEQ61L PDFs. All those samples are interfaced with HERWIG6.6 for parton shower and hadronization and JIMMY for the MPI, the only exception being the single top in the t–channel, generated with ACER MC, which is interfaced with PYTHIA6 [46] for parton shower, hadronization and MPI. The $t\bar{t}$ production cross section is normalized to the NNLO QCD calculation [103]; the single top as well as the di–boson cross sections are normalized to the MC@NLO predictions or to the ACER MC cross section; W+jets is normalized to NNLO QCD predictions [98].

The W+jets and $Z(\to \tau\tau)$+jets Monte Carlo samples are not used in the analysis apart from checking the level of these backgrounds in the selected data samples.

The data collected in the 2011 data taking is used; the average proton–proton interactions per bunch crossing in the collected data sample ranges between ~ 2 up to ~ 20 with a mean of 9.1 p–p interactions (more details are given in Sec. 2.1). The simulated samples are reweighted to reproduce the average multiplicity of p–p interactions per bunch crossing observed in data; therefore, the simulated hard scattering is accompanied by additional overlay of minimum bias interactions with the pile–up conditions in data.

Z decay channel	Trigger	Integrated luminosity [fb^{-1}]
$Z \to ee$	EF_2e12_medium	1.64
$Z \to ee$	EF_2e12T_medium	0.57
$Z \to ee$	EF_2e12Tvh_medium	2.37
$Z \to \mu\mu$	EF_mu18_MG	1.42
$Z \to \mu\mu$	EF_mu18_MG_medium	3.16

Table 10: Triggers used in the Z+b analysis and integrated luminosities collected during 2011 data taking periods.

4.2.2 *Event selection*

After requiring good detector conditions for all the detector subsystems the available integrated luminosity used for the Z+b cross section measurement amounts approximately to 4.6 fb^{-1}. It is collected with di–lepton and single lepton triggers; in the electron channel a di–electron trigger with 12 GeV threshold for the electron transverse energy is used while in the muon channel a single lepton trigger with a muon p_T threshold of 18 GeV is used. The triggers, along with the collected luminosity collected by each of them, are summarized in Table 10.

The electron triggers are found to be $\sim 97-98\%$ efficient with respect to two Medium electrons with $p_T > 20$ GeV selected offline [104]; while the muon trigger efficiency is $\sim 70\%$ in the barrel region and $\sim 90\%$ in the endcaps [105] with an expected 95% of the plateau efficiency reached already for muons with $p_T > 18.1$ GeV. The trigger decision is simulated in Monte Carlo samples and the trigger cuts are also applied on MC samples. Data-MC scale factors are used on Monte Carlo samples to correct for the residual mismodeling of the trigger decision simulation in MC; the scale factors for the electron triggers range between 0.99 and 1, while they are found consistent with one for the muon triggers.

The primary vertex in each event is identified as the vertex with the largest sum of track transverse momenta squared, $\sum p_T^2(\mathrm{track})$, where the sum is extended to all the charged tracks with $p_T > 400$ MeV associated to the vertex. Good proton–proton collision events are ensured by requiring that the primary vertex has at least three charged tracks with $p_T > 400$ MeV. It has been checked in simulation that these cuts are fully efficient on the signal selection while reducing the background from cosmic rays.

Candidate electrons are identified as Medium++ electrons (see Sec. 2.4) with $p_T > 20\,\mathrm{GeV}$ and $|\eta| < 2.47$, excluding the ECAL transition region $1.37 < |\eta| < 1.52$. The electron kinematics is defined either by the ID or by the calorimeter measurement; namely for a good quality track we benefit from the high resolution ID measurement, otherwise the calorimeter measurement is used. Fake electrons are produced in semi–leptonic decays of heavy flavors, kaons and pions or by photons, promptly produced or originating in $\pi^0 \to \gamma\gamma$ decays and converting in the ID into electron-positron pairs. Fake electrons produced in heavy flavor decays can be suppressed requiring $d_0(e)/\Delta d_0(e) < 10$ and $|z_0(e)| < 1$ mm (the definitions of $d_0/\Delta d_0$ and $|z_0(e)|$ are provided in App. A) as the electron tracks are expected

to be displaced from the primary vertex if the electrons are produced from heavy flavor decays.

Selection	Description
Electron track quality hits	• # Pixel + # SCT hits $\geqslant 4$.
Muon track quality hits	• At least one B-layer hit if B-layer hits are expected. • # Pixel hits + # dead Pixel sensors > 1. • # SCT hits + # dead SCT sensors > 5. • # Pixel holes + # SCT holes < 3. • if $\lvert\eta(\mu)\rvert < 1.9$ and # TRT hits + # TRT Outliers > 5, require TRT Outliers $< 90\%$ TRT hits + # TRT Outliers. • if $\lvert\eta(\mu)\rvert \geqslant 1.9$, require # TRT hits + # TRT Outliers < 5 or if # TRT hits + # TRT Outliers > 5, require TRT Outliers $< 90\%$ TRT hits + # TRT Outliers.

Table 11: List of hit requirements for tracks associated to a reconstructed Combined muon and to the electron tracks when the ID measurement is used to define the electron p_T.

Selected muons are good quality Combined muons with $p_T > 20\,GeV$ and $|\eta| < 2.4$. Fake muons are produced in heavy flavor, kaon and in pion semi–leptonic decays and in atmospheric air showers. The quality requirement on tracks associated to candidate muons along with the combined identification in the Inner Detector and in the Muon Spectrometer, already provide a good fake rejection that can be further improved by requiring $d_0(\mu)/\Delta d_0(\mu) < 3$ and $|z_0(\mu)| < 1$ mm, exploiting the large displacement with respect to the primary vertex of tracks associated to fake muons. To improve the muon purity an isolation criteria is used; in particular, a track based isolation method is adopted, using the variable

$$\mathcal{I} = \sum_{\{\text{track } |\Delta R(\text{track},\mu)<0.2\}} \frac{p_T(\text{track})}{p_T(\mu)} \quad , \; p_T(\text{track}) > 1\,GeV\,, \tag{29}$$

where the sum is extended to all the reconstructed tracks with $p_T(\text{track}) > 1$ GeV in a cone $\Delta R(\text{track}, \mu) = 0.2$ around the muon track; a muon is considered isolated if $\mathcal{I} < 0.1$.

Data to MC scale factors to correct for lepton identification mismodeling are applied in simulated samples as described in Sec. 2.3 and Sec. 2.4; their typical values are found to be $\sim 98\%$ for electrons and 97% muons for the leptons selected with the kinematic cuts previously described. Moreover, since simulation exhibit a better lepton p_T resolution than data, the electron and muon four momenta are smeared to reproduce the observed resolution in data. The lepton four momenta in simulation are also corrected to account for a residual energy scale mismatch with the data.

Leptonic Z boson decays into muon or electron pairs are identified in events with two opposite charge electrons or muons with invariant mass $76 < M_{\ell\ell}[GeV] < 106$. Only events with exactly two selected leptons are retained; however, in the muon

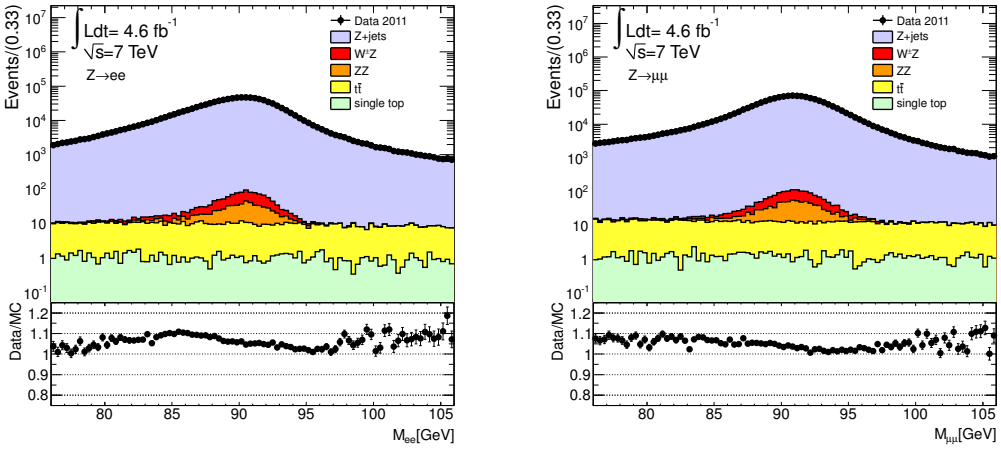

(a) (b)

Figure 28: Di–lepton invariant mass distributions for the electron (a) and muon (b) channel. The error bars on the data include the statistical uncertainty only, while the error bars of the ratio Data/MC is the sum in quadrature of the statistical uncertainty of the data and on the Monte Carlo simulations.

channel, if a muon associated to the Z decay is found close to a selected electron, specifically $\Delta R(e,\mu) < 0.1$, the electron is rejected, as it can be produced from bremsstrahlung from the muon and subsequent conversion of the photon, but the event is retained.

The lepton veto is found to be almost 100% efficient on a signal simulated sample with at least two selected same flavor leptons.

After the Z selection, 1126522 candidate events are observed in the electron channel and 1572428 in the muon channel, with predicted top and di–boson backgrounds, estimated from Monte Carlo, being less than $\sim 0.2\%$ and dominated by the diboson backgrouds ($\sim 0.1\%$) in both the channels; the multijets background is not estimated at this level of the selection.

The di–lepton invariant mass is shown in Fig. 28 for the electron (a) and muon (b) channel. The simulation underestimates slightly the observed data yield, by 6% in the electron channel and by 4% in the muon channel. The Z mass distribution in the electron channel suffers from a mismatch between the Monte Carlo and the data which is responsible for the peculiar shape of the data/MC ratio. In the muon channel the Z mass profile is much better modeled by the simulation compared to the electron channel.

The top background can be efficiently reduced making use of a cut on the missing transverse energy. To ensure that the E_T^{miss} is well measured, candidate events with the calorimeter not in ideal running conditions are rejected[2]. The missing transverse energy is calculated by using physics objects with four–momentum corrected to reproduce the energy resolution and energy scale observed in data. The selected events are required to have $E_T^{miss} < 70$ GeV; this cut reduces the $t\bar{t}$ background by a factor two, while retaining more than 99% of the selected events in the Z+jets simulated samples.

2 More details can be found in https://twiki.cern.ch/twiki/bin/viewauth/AtlasProtected/HowToCleanJets2011

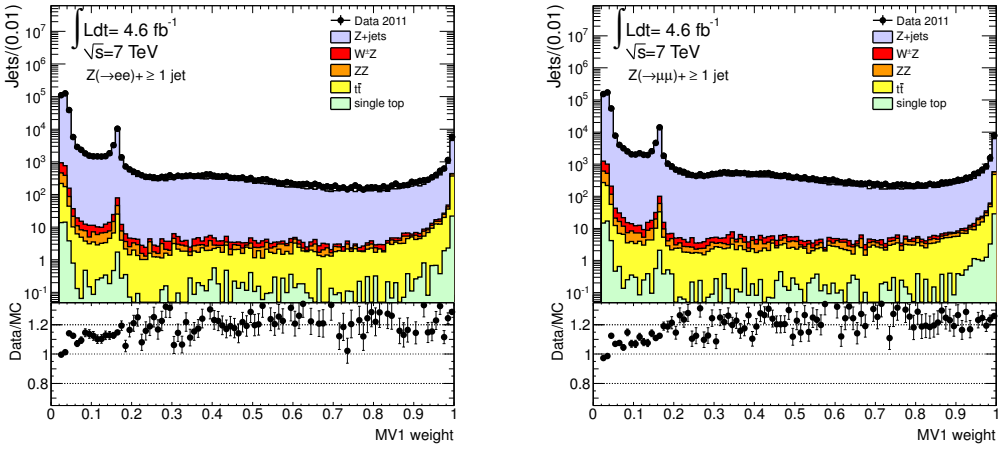

(a) (b)

Figure 29: MV1 weight distributions for the electron (a) and muon (b) channel after the lepton pair selection. The error bars on the data include the statistical uncertainty only, while the error bars on the ratio Data/MC are the sum in quadrature of the statistical uncertainty of the data and of the Monte Carlo simulations.

Jets are reconstructed with the anti-k_t clustering algorithm [106], as implemented in the FastJet package [107], with radius parameter $R = 0.4$ seeded by topological clusters. Jets, calibrated at the electromagnetic scale [76] (see also Sec. 2.5), are required to have $p_T > 20$ GeV, $|y| < 2.4$ and to be well separated from signal leptons by requiring $\Delta R(\ell, jet) > 0.5$ [3].

Jets originating from pile–up interactions are reduced using the jet–vertex–fraction (JFV) variable [108]. The JVF is computed according to the following definition

$$JVF(jet \mid PV) = \frac{\sum_{\{track \,|\, track \in jet \cap PV\}} p_T(track)}{\sum_{\{track \,|\, track \in jet\}} p_T(track)} \quad , \; p_T(track) > 400\,\text{MeV} \; , \quad (30)$$

with tracks passing some quality requirements. The sum at the denominator is extended over all tracks in the jet, while the sum at the numerator is evaluated for all tracks associated to both the jet and the primary vertex. To suppress jets from pile–up, jets are selected with $JVF > 0.75$, meaning that at least the 75% of the p_T–weighted number of tracks has to be associated to the primary vertex in the event; the jets without tracks useful for the calculation of the JVF are retained by the selection. The efficiency of the JVF cut is expected to be close to $98 - 99\%$ based on Monte Carlo simulations [108].

Badly measured jets or jets hitting the ECAL dead modules are rejected; these are a small subset of the selected sample, which has a negligible impact on the selected yield.

Candidate b–jets are selected by requiring the b–tagging algorithm output MV1, introduced in Sec. 2.7, to be above the threshold $MV1^{(75)} = 0.404219$. This threshold ensures an efficiency for b–jet identification of 75%, which is measured on

3 The cone $\Delta R(\ell, jet)$ provides a signal definition free from ambiguities related to double counting of the energy of leptons nearby jets and it is expected to be 91% (98%) efficient in the electron (muon) channel based on studies on simulated MC samples.

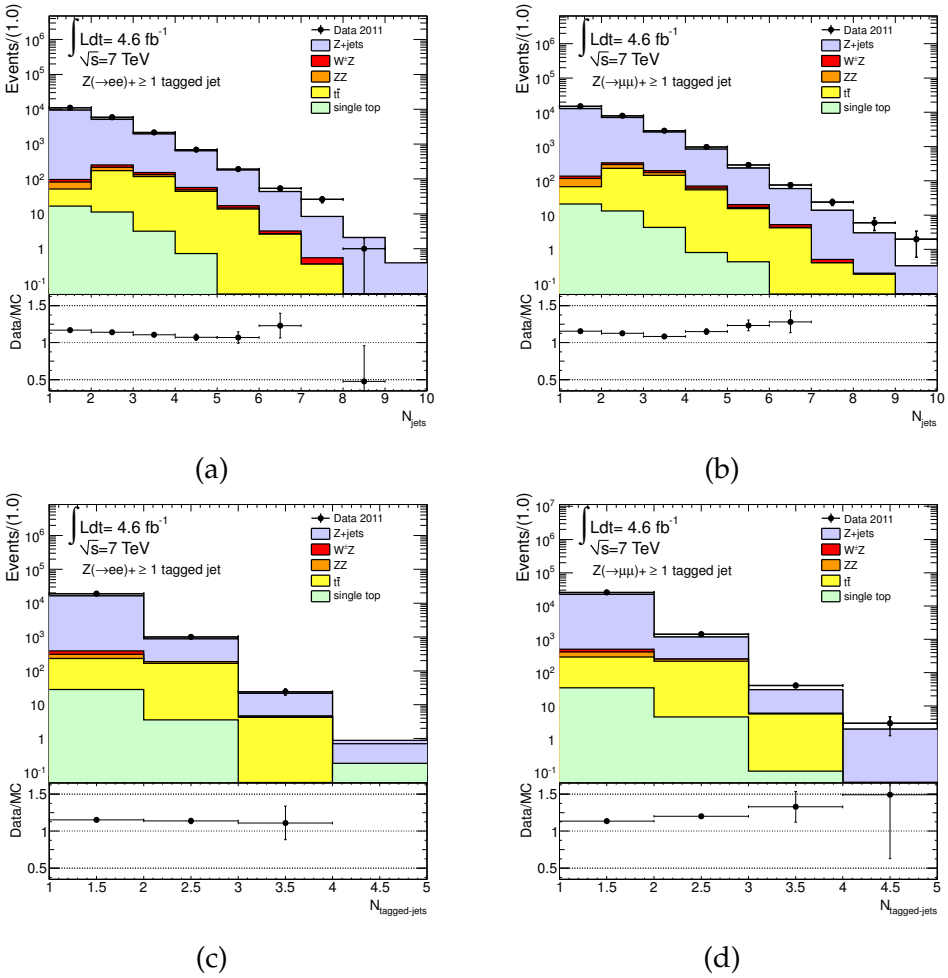

Figure 30: Inclusive jet and b–jet multiplicities in events with at least one b–tagged jet for the electron (a-c) and muon channel (b-d). The error bars on the data include the statistical uncertainty only, while the error bars on the ratio Data/MC is the sum in quadrature of the statistical uncertainty of the data and of the Monte Carlo simulations.

$t\bar{t}$ simulated samples [109]. Corresponding to the 75% b–tagging efficiency MV1 operating point, the expected mistag rate for light and charm jets are expected to be close to 1% and 50% respectively, based on the performance studies of Ref. [110, 111]. The MV1 weight distribution after the jet selection, but before the MV1 cut, in the electron and in the muon channel is shown in Fig. 29. The MC predictions underestimate the data, especially for high values of the MV1 weight.

After the b-tagging 20076 events are selected in the electron channel and 27062 in the muon channel corresponding to 21132 and 28569 b-tagged jets respectively; in the electron channel 1008 of them have at least two b–tagged jets, while in the muon channel there are 1415 candidates with two or more b-tagged jets; the total number of selected events with at least three b–tagged jets is 65; in the muon channel three events with four b–tagged jets are selected.

The inclusive jet multiplicity in events with at least one b–tagged jet is shown in Fig. 30 (a-b), while in Fig. 30 (c-d) the multiplicity of b–tagged jets is presented. The MC simulation underestimates the data in all the jet multiplicities bins.

The distributions of the b-jet p_T, b-jet $|y|$ and $|y_{boost}(Z, b)|$ are shown in Fig. 31 (a-c) and Fig. 32 (a-c) for the electron and the muon channel; the distributions are well modeled by the simulation which, on the other hand, underpredicts the total observed yield in data. The Z p_T and Z $|y|$ are shown in Fig. 31 (d-e) (electron channel) and Fig. 32 (d-e) (muon channel) for events with at least one b–tagged jet. Finally in Fig. 31 (f-h) (electron channel) and Fig. 32 (f-h) (muon channel) the angular correlation, $\Delta R(Z, b-jets)$, $\Delta\phi(Z, b-jets)$ and $\Delta y(Z, b-jets)$, between the Z boson and the b–tagged jets, are shown for events with a Z boson with transverse momentum larger than 20 GeV.

The multijet background is not taken into account in the simulated Monte Carlo samples, instead it is determined with a data driven method as described in the following section.

4.3 DATA–DRIVEN ESTIMATE OF THE BACKGROUND FROM MULTIJET EVENTS

The contamination from multijet events in the inclusive Zb selection is estimated with a data driven method. The motivations for this choice are the limited statistics of the available simulated background samples and the uncertainty on the modeling of the misidentification rate of jets as leptons.

The procedure is based on a few steps which will be detailed in the following sections.

- *Multijet enriched selection*. Special event selections are defined with features close to the signal selection but with an enhanced contribution of multijets events. These data are used to obtain the slope of a multijet discriminating.
- *Estimation of the multijet normalization*. The number of multijet events contributing to the nominal selection is estimated with a fit to the multijet discriminating variable. The di–lepton invariant mass in an enlarged region $[50, 200]$ GeV is used for this purpose.

The fit method used to normalize the multijet rate is common for the two leptonic channels. The shape of the invariant mass distribution, after all cuts are applied, can be modeled with

$$M(m_{\ell\ell}; N_{\overline{mj},\ell}, N_{mj,\ell}) = N_{\overline{mj},\ell}\, g_\ell(m_{\ell\ell}) + N_{mj,\ell}\, f(m_{\ell\ell})\,, \tag{31}$$

where the $g_\ell(m_{\ell\ell})$ represents the normalized distribution of the non multijet events and $f(m_{\ell\ell})$ is the normalized distribution for the multijet events. $N_{\overline{mj},\ell}$ and $N_{mj,\ell}$ are the number of events in the two components, for each lepton channel, $\ell = (e, \mu)$, which are left floating in the fit. The distribution of the non multijet background is estimated from MC simulations, relying on the simulated lineshape modeling and on the relative abundances of the various processes, which are summed in a single binned model (also referred to as template), $g(m_{\ell\ell})$, with unitary normalization.

The shape of the fake di–lepton invariant mass in multijet events is derived from the fit to data in a control region.

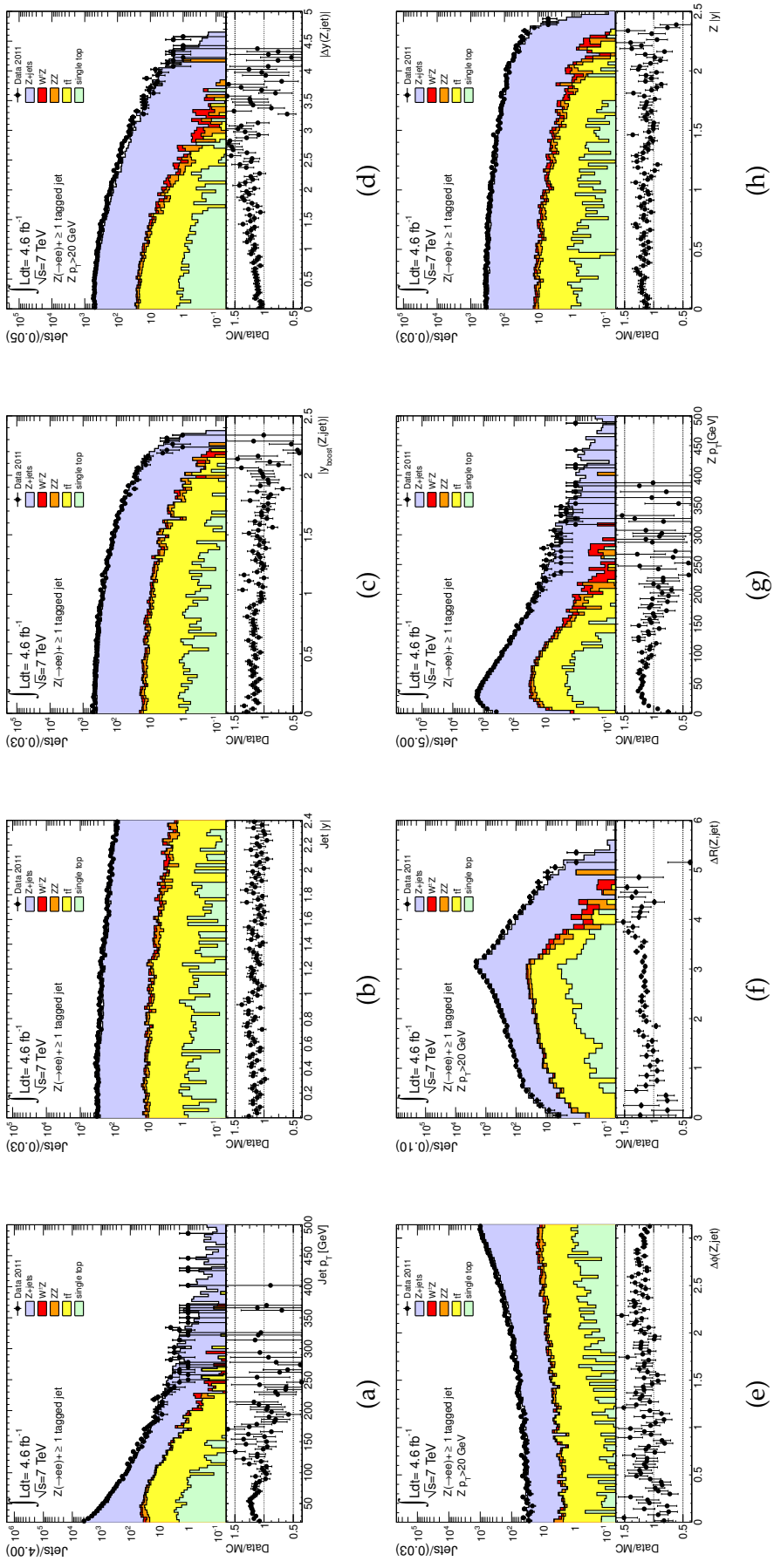

Figure 31: Distributions of the jet p_T (a), jet $|y|$ (b), $|y_{boost}(Z,jet)|$ (c), $|\Delta y(Z,jet)|$ (d), $\Delta\phi(Z,jet)$ (e), $\Delta R(Z,jet)$ (f), Z p_T (g) and Z $|y|$ (h) in the electron channel in events passing the (Z+b) selection. The jet p_T, jet $|y|$ and $|y_{boost}(Z,jet)|$ distributions are filled for each b–tagged jet; the angular correlation observables $|\Delta y(Z,jet)|$, $\Delta\phi(Z,jet)$ and $\Delta R(Z,jet)$ are filled on jet basis for events with a Z boson with $p_T > 20$ GeV, the Z p_T and the Z $|y|$ are instead filled per–event. The error bars on the data include the statistical uncertainty only, while the error bars on the ratio Data/MC is the sum in quadrature of the statistical uncertainty of the data and of the Monte Carlo simulations.

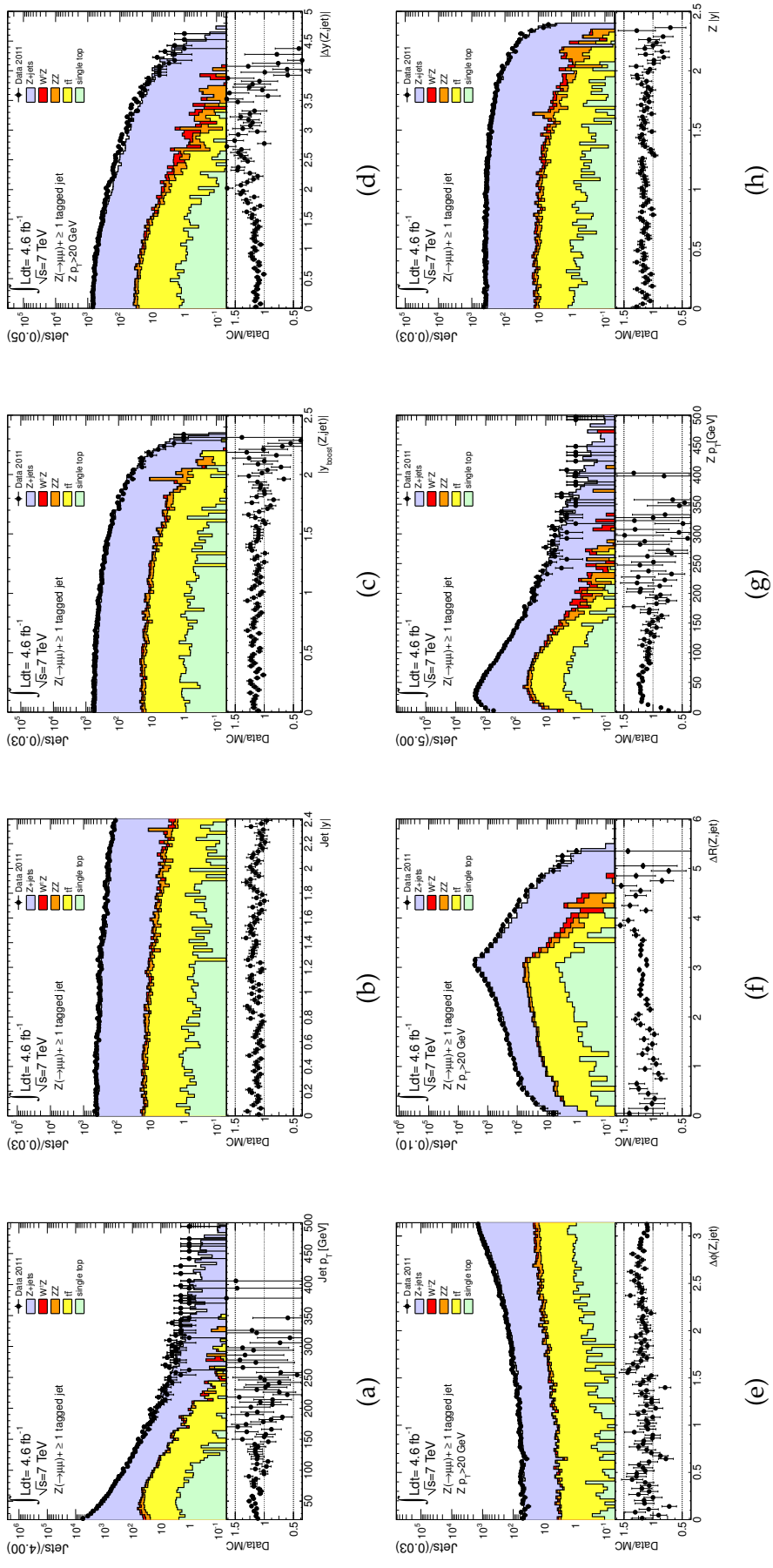

Figure 32: Distributions of the jet p_T (a), jet $|y|$ (b), $|y_{boost}(Z,jet)|$ (c), $|\Delta y(Z,jet)|$ (d), $\Delta\phi(Z,jet)$ (e), $\Delta R(Z,jet)$ (f), Z p_T (g) and Z $|y|$ (h) in the muon channel in events passing the (Z+b) selection. The jet p_T, jet $|y|$ and $|y_{boost}(Z,jet)|$ distributions are filled for each b–tagged jet; the angular correlation observables $|\Delta y(Z,jet)|$, $\Delta\phi(Z,jet)$ and $\Delta R(Z,jet)$ are filled on jet basis for events with a Z boson with $p_T > 20$ GeV, the Z p_T and the Z $|y|$ are instead filled per–event. The error bars on the data include the statistical uncertainty only, while the error bars on the ratio Data/MC is the sum in quadrature of the statistical uncertainty of the data and of the Monte Carlo simulations.

The selection of the background enriched control regions, the determination of the shape of the multijet background and the extraction of the multijet normalization are described in the following sections for the two lepton channels; besides relaxing the di–lepton invariant mass, the multijet control samples are defined by relaxing or inverting some lepton identification cuts and using more inclusive trigger cuts.

4.3.1 *Electron channel control regions*

A multijet enriched control region in the electron channel is obtained by applying all event and object selection requirements described in section 4.2.2, with few changes highlighted below leading to two kinds of di–lepton control samples.

1. The e^+e^- invariant mass range is extended to 70–120 GeV.
2. The impact parameter cuts on the electron track are removed.
3. Di–electron pairs are selected according to modified electron identification cuts
   - One candidate electron is a Medium++ and the other is not a Medium++ ($M, \overline{M}$ region).
   - Both the candidate electrons are Loose electrons but they fail the Medium++ requirement ($L_{\overline{M}}, L_{\overline{M}}$ region).

The selection was applied to events pre–selected online by a single electron trigger with a transverse energy threshold of 20 GeV (`EF_e20_medium`); this choice is a compromise between the possibility of having a sample of electrons not fully biased by the isolation applied by the trigger cut and the necessity of preserving the same offline p_T threshold as in the signal region definition in order to avoid a bias in the di–electron invariant mass. This trigger was unprescaled only in the first part of the 2011 data taking and it collected an integrated luminosity of 1.7 fb^{-1}. As an alternative, the unprescaled trigger `EF_2g20_loose` has been tried; however, a much lower statistics of events (up to a factor of 10) is obtained for the multijet enriched selections.

The e^+e^- invariant mass distribution obtained in the multijet control samples are studied in three different selections: inclusive di–lepton selection, di–lepton plus jets and di–lepton plus at least one b–tagged jet.

The same selection is applied to simulated samples of non multijet events from production of Z, top and pairs of gauge bosons that can contribute to the selection with real or fake leptons.

All the control regions and the di–lepton invariant mass fit in the invariant mass range $[70, 120]$ GeV are shown in Fig. 33. The data are well described by the sum of the various non multijet contributions, with total normalization adjusted to the data by the fit, and an exponentially decaying distribution, $f(m_{\ell\ell})$, with normalization and decay parameter, α_e, obtained from the fit to the data.

The reduced χ^2 is observed to be 0.5 and 2.2 and is typically closer to one for the fit performed in samples with reduced non multijet contamination. The fraction of multijet events is found to be between 79% and 96% with a larger multijet

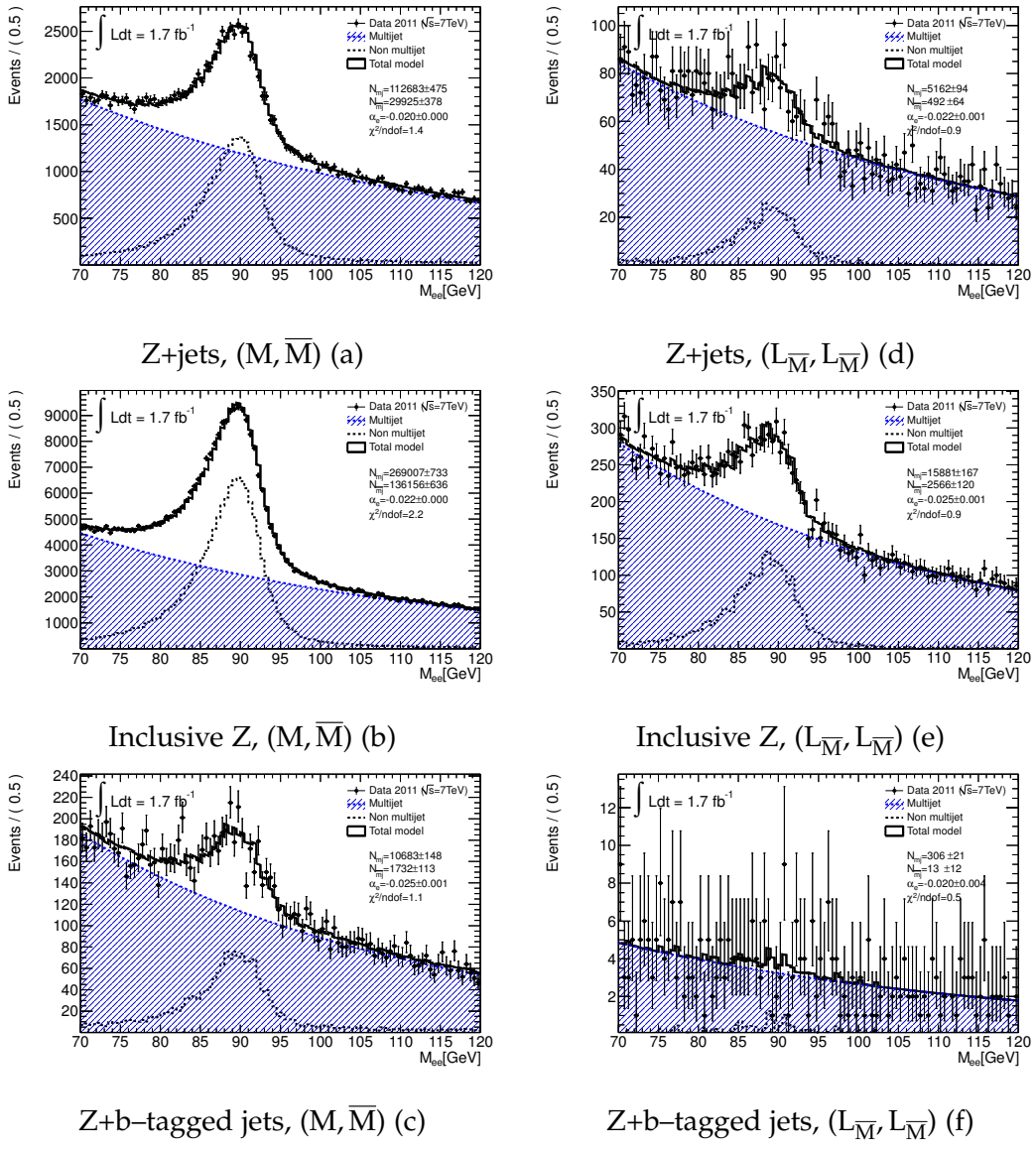

Figure 33: Invariant mass fit in the multijet enriched nominal control region for the electron channel corresponding to a Z+jets selection (a), in a wider control region corresponding to an inclusive Z selection (b), and in a region with a Z and one b-tagged jet (c). The fit results in a variation of the selections above with both electrons failing the Medium++ quality requirement but satisfying the Loose criterion: Z+jets (d), inclusive Z (e) and Z+b–tagged jets (f) selections.

Control region	α	$N_{\overline{mj}}$	N_{mj}	$N_{mj}[\%]$
Z+jets, $(M, \overline{M})$	-0.020 ± 0.001	29925 ± 378	112683 ± 475	79
Z+jets, $(L_{\overline{M}}, L_{\overline{M}})$	-0.022 ± 0.001	492 ± 64	5162 ± 94	91
Z, $(M, \overline{M})$	-0.022 ± 0.001	136156 ± 636	269007 ± 733	66
Z, $(L_{\overline{M}}, L_{\overline{M}})$	-0.025 ± 0.001	2566 ± 120	15881 ± 167	86
Z+b-jets, $(M, \overline{M})$	-0.025 ± 0.001	1732 ± 113	10683 ± 148	86
Z+b-jets, $(L_{\overline{M}}, L_{\overline{M}})$	-0.020 ± 0.004	13 ± 12	306 ± 21	96

Table 12: Electron channel. Results of the fit to the di–electron invariant mass in various multijet enriched control regions: decay constant and normalization of multijet and non multijet event samples. The notation (Q, Q') refers to the identification quality requirements satisfied by the two electrons in the pair.

Control region	Data	Z	$t\bar{t}$	Di–boson	Single–top	Total MC
Z+jets, $(M, \overline{M})$	142608	27307	441	523	398	28669
Z+jets, $(L_{\overline{M}}, L_{\overline{M}})$	5654.0	597.6	1.5	3.0	1.0	603
Z, $(M, \overline{M})$	405163	129318	522	621	476	130937
Z, $(L_{\overline{M}}, L_{\overline{M}})$	18447	3006	1.6	3.6	1.1	3012
Z+b-jet, $(M, \overline{M})$	12415	1236	186	196	178	1796
Z+b-jet, $(L_{\overline{M}}, L_{\overline{M}})$	319.0	27.2	0.7	1.0	0.7	29.6

Table 13: Electron channel. Composition, according to simulation, of the non multijet contribution to the selections for the various control regions. The notation (Q, Q') is defined in Tab. 12. The sum of the non multijet contributions predicted by the MC is consistent with the overall normalization from the fit to the data reported in Tab. 12.

component observed in the $(L_{\overline{M}}, L_{\overline{M}})$ di–lepton regions. In spite of the different acceptances of the two selections for multijets events, the slope parameter α_e is determinated with consistent values and for all kinds of selections. This confirms that the multijet background slope is measured to be stable against the lepton identification requirements and therefore it can be used to fit the multijet contribution in the signal region.

The results of the fit are summarized in Tab. 12, while Tab. 13 shows the contributions of non multijet events in the background enriched selections as predicted by the simulation. The sum of the expected yield from non multijet processes is in agreement with the result from the fit to the data within about 10%.

4.3.2 *Muon channel control regions*

The data for the multijet control region in the muon channel can be preselected by the same single muon triggers as done for the signal region defined in Sec. 4.2.2.

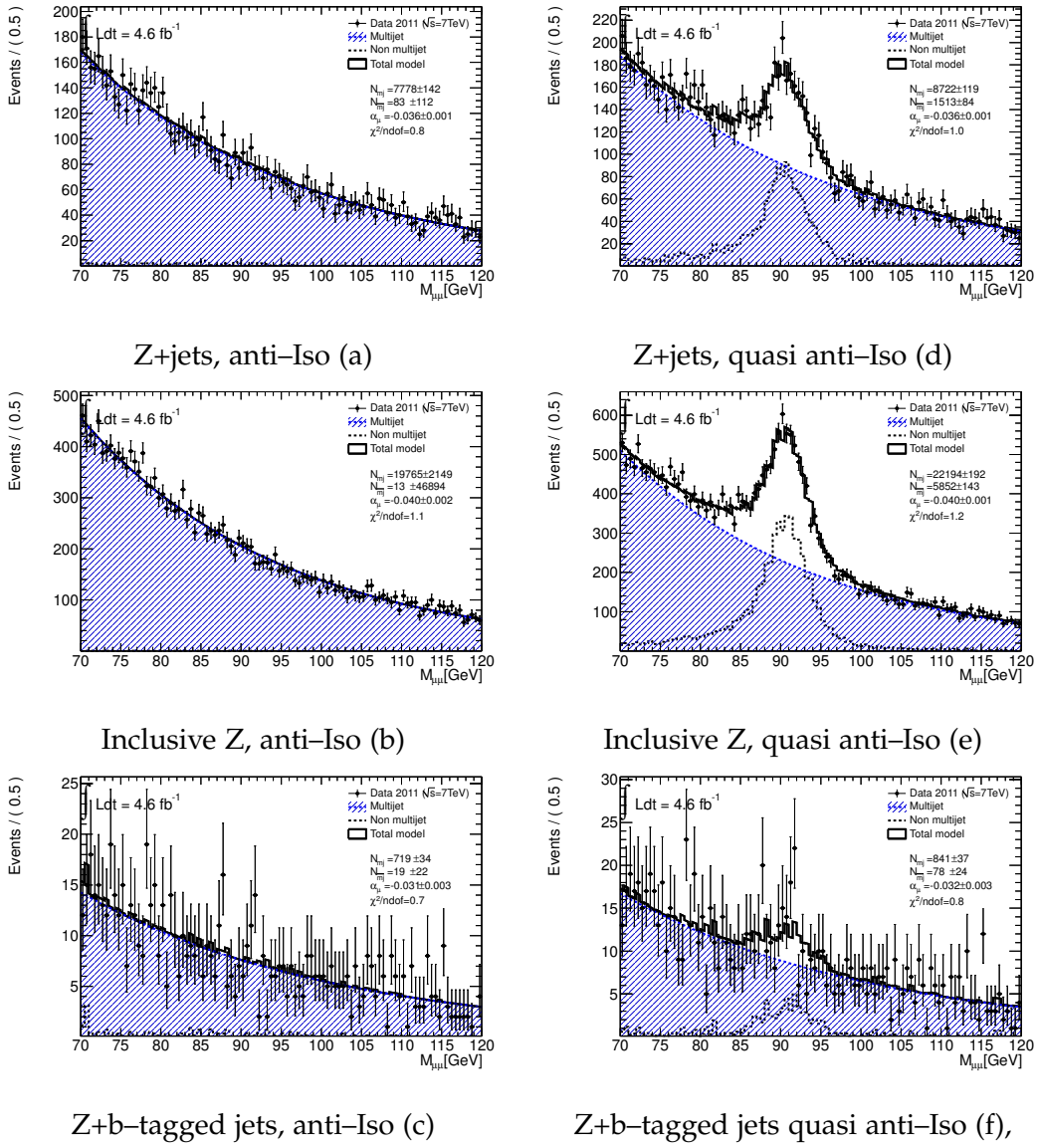

Figure 34: Invariant mass fit in the multijet enriched nominal control region for the muon channel corresponding to a Z+jets selection (a), in a wider control region corresponding to an inclusive Z selection (b), and in a region with a Z and a b–tagged jet (c). The fit results in a variation of the selections above based on quasi anti–isolated muons: Z+jets (d), inclusive Z (e) and Z+b-tagged jets (f) selections.

Control region	α	$N_{\overline{mj}}$	N_{mj}	$N_{mj}[\%]$
Z+jets, anti–Iso	-0.036 ± 0.001	83 ± 112	7778 ± 142	99
Z+jets, quasi anti–Iso	-0.036 ± 0.001	1513.4 ± 83.7	8722 ± 119	85
Z, anti–Iso	-0.040 ± 0.001	–	19752	99
Z, quasi anti–Iso	-0.040 ± 0.001	5852.1 ± 143.0	22167 ± 192	79
Z+b–jets, anti–Iso	-0.031 ± 0.002	18.6 ± 21.5	719.4 ± 34.1	97
Z+b–jets, quasi anti–Iso	-0.031 ± 0.002	77.8 ± 24.4	841.2 ± 36.9	92

Table 14: Muon channel. Results of the fit to the di–muon invariant mass in various multijet enriched control regions: decay constant and normalization of multijet and non multijet event samples.

Control region	Data	Z	$t\bar{t}$	Di–boson	Single–top	Total MC
Z+jets, anti–Iso	7861.0	30.5	9.6	0.2	1.7	42
Z+jets, quasi anti–Iso	10235.0	1140.4	26.9	3.7	5.5	1177
Z, anti–Iso	19778.0	90.0	10.3	0.2	2.2	103
Z, quasi anti–Iso	28045.0	4525.8	28.3	5.0	7.6	4567
Z+b-jets, anti–Iso	738.0	1.9	2.2	0.1	0.2	4.4
Z+b-jets, quasi anti–Iso	919.0	59.5	10.1	0.7	1.7	72

Table 15: Muon channel. Composition, according to simulation, of the non multijet contribution to the selections for the various control regions in the muon channel. The sum of the non multijet contributions predicted by the MC is consistent with the overall normalization from the fit to the data reported in Tab. 14.

In the muon channel, as in the electron channel, multijet enriched control regions can be obtained by relaxing or reversing some lepton identification cuts. The changes in event selection introduced for the definition of the multijet control regions in the muon channel are listed below.

1. The $\mu^+\mu^-$ invariant mass range is extended to 70–120 GeV.
2. The muons are not required to satisfy impact parameter cuts.
3. Candidate di–muon pairs are selected according to two isolation requirements using the isolation variable defined in Eq. 37.
   - Both the muons are anti–isolated, namely $\mathcal{I} > 0.1$ (anti–Iso region).
   - Both the muons are quasi anti–isolated, namely $\mathcal{I} > 0.01$ (quasi anti–Iso region).

As for the electron channel, the multijet control regions are studied for the inclusive di–lepton selection, for di–lepton plus jets and di–lepton plus at least one b–tagged jet.

Similarly to the electron channel, an exponentially decaying function provides a suitable description of the contribution to the di–muon invariant mass from multijet events as shown in Fig. 34. The distribution observed in data is fit, as in the electron channel, to the sum of the Monte Carlo templates for the non multijet processes with floating total normalization, and the exponential function with decay constant and normalization free in the fit. The reduced χ^2 is found to be between 0.7 and 1.2 and the slope parameter α_μ is observed to be well consistent across the regions anti–Iso and quasi anti–Iso. The fraction of multijet events exceed 97% in the selections with anti–isolated muons, while it is between 79% and 92% in the quasi anti–Iso region. The sum of the expected yield from non multijet processes is in agreement with the result from the fit to the data within about 10% as can be observed by a comparison of Tab. 14 and Tab. 15.

4.3.3 *Di–lepton invariant mass shape for multijet events*

The main result of the background control regions described so far is the universal shape of the multijet background. The determination of the multijet slope has been used in Eq. 31 to fit the normalization of the multijet background where all the nominal signal selection criteria are applied. However, when all the criteria of the nominal signal selection are applied, the very low level of the multijet background in the di–lepton invariant mass considered does not allow to evaluate in a reliable way the contamination from the multijet background. Therefore the fit to the invariant mass distribution is extended to a wider range of 50–200 GeV; in the lower edge of the range the multijet background can not be described by an exponential decaying function and a template must be derived from the multijet enriched regions. The templates for the multijet events are derived from data in the loose selections of each control region by subtracting the distribution of the non multijet events predicted by the simulation and normalized to the fit results presented in Sec. 4.3.1 and Sec. 4.3.2. The multijet invariant mass distributions derived with this procedure are presented in Fig. 35 for the electron channel and in Fig. 36 for the muon channel.

4.3.4 *Multijet background estimate*

The results of the fit to the wide invariant mass in the signal region, based on the multijet templates and on Monte Carlo simulation for the non multijet shape are reported in Fig. 37. In particular, these plots use the multijet templates from the Z+jets $(M, \overline{M})$ control region for the electron channel and the Z+jets anti–Iso control region for the muon channel. The total contamination of multijet events, $N_{mj,\ell}$, is found to be very small and, when integrated in the effective signal region (di–lepton invariant mass in the 76–106 range), it is found to be below 1% of the total yield and compatible with zero within one standard deviation. Repeating the fit with variations of the templates, based on different control regions, leads to statistically negligible differences in the value of $N_{mj,\ell}$.

The full list of results is given in Tab. 16, where $(\star)$ is used to label the estimates finally used in the analysis.

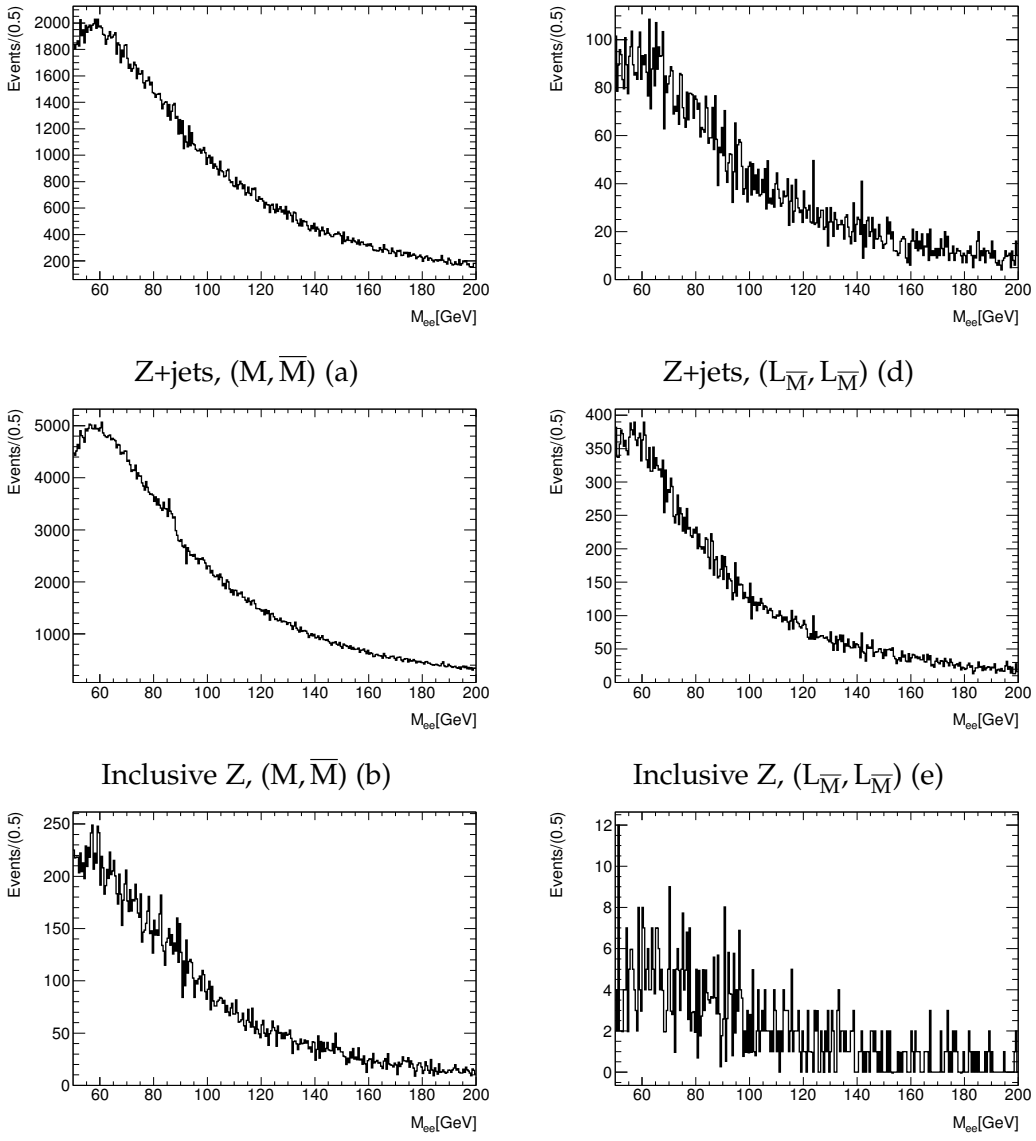

Figure 35: Electron channel. Multijet templates for the di–electron invariant mass distribution in the range 50–200 GeV corresponding to a Z+jets selection (a and d), an inclusive Z selection (b and e), and a Z and one b-tagged jet selection (c and f). The plots on the left are derived from the $(M, \overline{M})$ control region, by subtracting the non multijet contribution with normalization derived from data and shape from simulation. The plots on the right are derived from the $L_{\overline{M}}, L_{\overline{M}}$ control region.

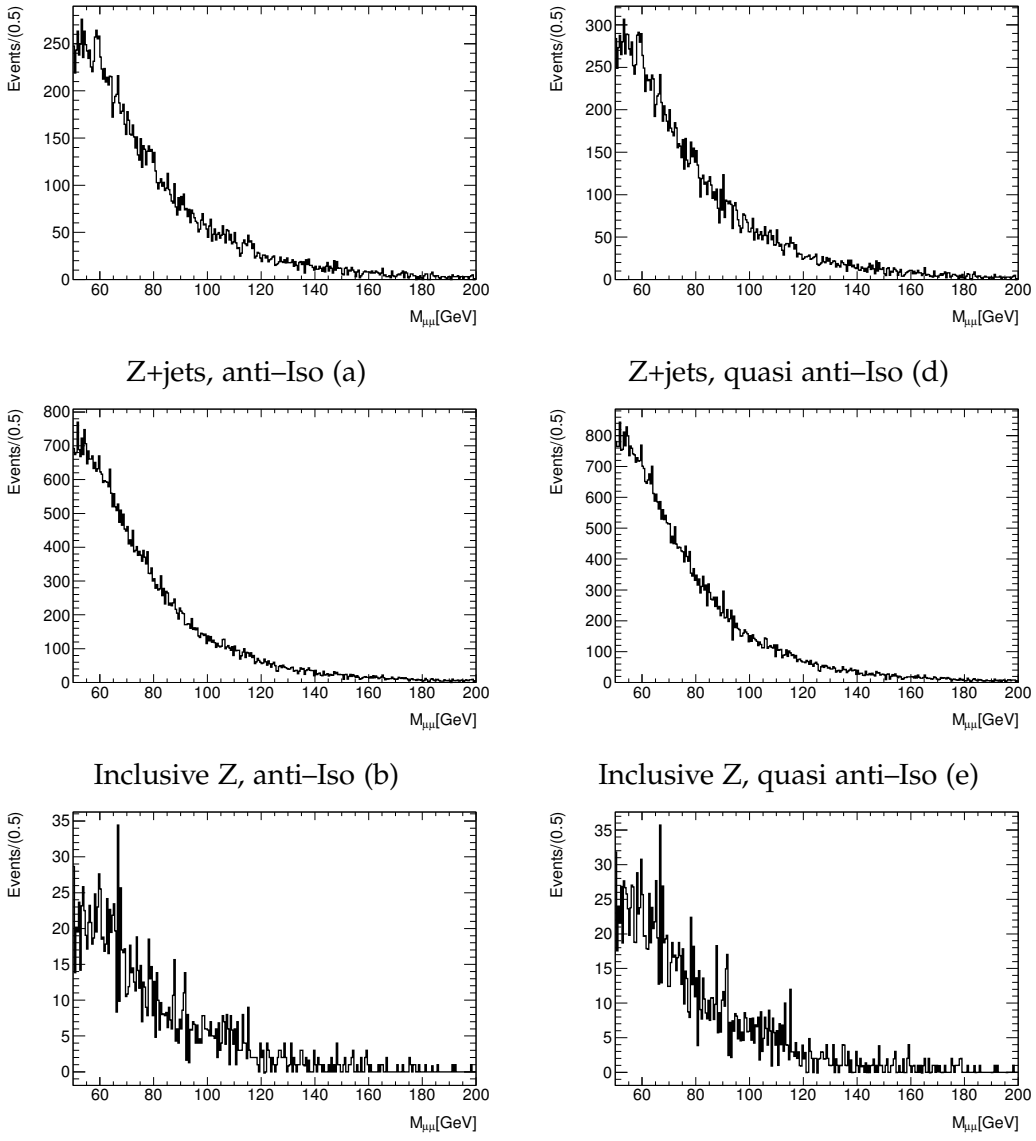

Figure 36: Muon channel. Multijet templates for the di–muon invariant mass distribution in the range 50-200 GeV corresponding to a Z+jets selection (a and d), an inclusive Z selection (b and e), and a Z and one b-tagged jet selection (c and f). The plots on the left are derived from the control region with the two muons both anti–isolated, by subtracting the non multijet contribution with normalization derived from data and shape from simulation. The plots on the right are derived from the quasi anti–isolated control region.

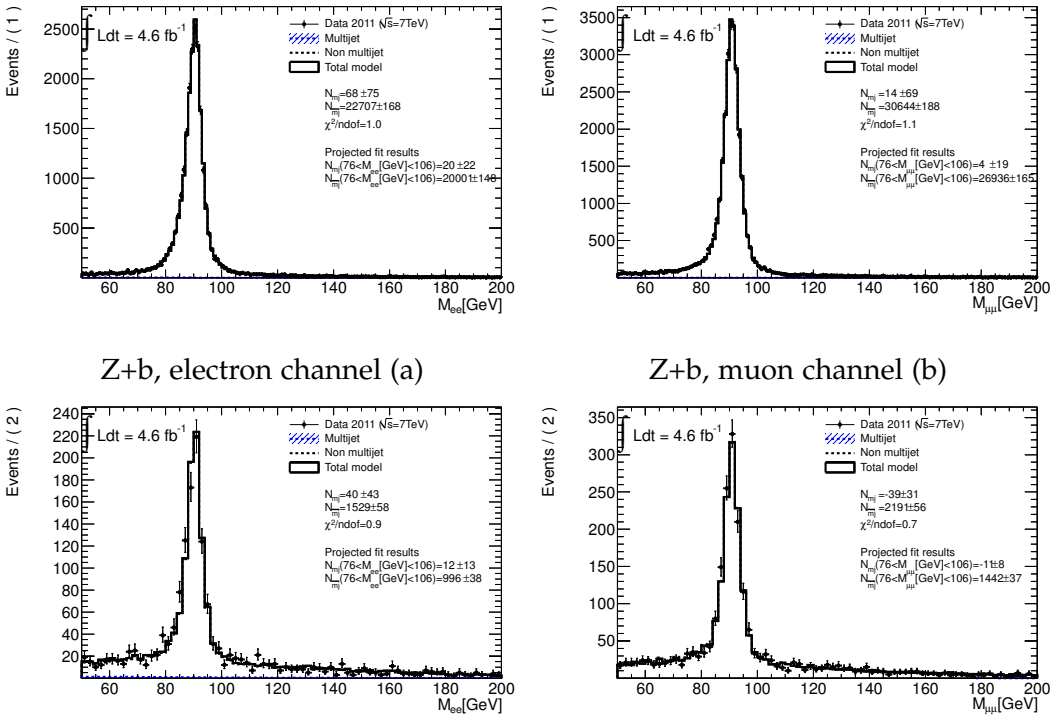

Z+b, electron channel (a)

Z+b, muon channel (b)

Z+bb, electron channel (c)

Z+bb, muon channel (d)

Figure 37: Extraction of the multijet background in the signal regions, corresponding to the nominal selection, from the fit to the di–lepton invariant mass: inclusive Z+b selection (a and b), and Z+bb selection (c and d). Plots on the left refer to the electron channel and plots on the right refer to the muon channel.

selection	CR for template	non multijet	multijet	non multijet	multijet
e-channel		wide mass range	wide mass range	signal wide range	signal mass range
$\geqslant 1$ b-tag	Z+jets $(M, \overline{M})$	22706.5 ± 168.1	67.6 ± 75.0	20001.1 ± 148.1	20.0 ± 22.1 $(\star)$
$\geqslant 1$ b-tag	Z+jets $(L_{\overline{M}}, L_{\overline{M}})$	22715.1 ± 167.5	58.1 ± 73.4	20008.7 ± 147.5	16.8 ± 21.3
$\geqslant 1$ b-tag	Z+$\geqslant$1 b-tag $(M, \overline{M})$	22692.5 ± 166.9	81.5 ± 72.5	19988.8 ± 147.1	24.5 ± 21.8
$\geqslant 1$ b-tag	Z+$\geqslant$1 b-tag $(L_{\overline{M}}, L_{\overline{M}})$	22698.7 ± 165.8	75.3 ± 69.7	19994.2 ± 146.0	23.5 ± 21.7
$\geqslant 2$ b-tags	Z+jets $(M, \overline{M})$	1529.0 ± 57.8	40.0 ± 43.0	995.6 ± 37.6	11.8 ± 12.7 $(\star)$
$\geqslant 2$ b-tags	Z+jets $(L_{\overline{M}}, L_{\overline{M}})$	1526.9 ± 57.1	42.1 ± 42.1	994.3 ± 37.2	12.2 ± 12.2
$\geqslant 2$ b-tags	Z+$\geqslant$1 b-tag $(M, \overline{M})$	1534.0 ± 55.5	35.0 ± 39.7	998.9 ± 36.1	10.5 ± 11.9
$\geqslant 2$ b-tags	Z+$\geqslant$1 b-tag $(L_{\overline{M}}, L_{\overline{M}})$	1527.7 ± 56.3	41.3 ± 41.1	994.8 ± 36.7	12.9 ± 12.8

selection	CR for template	non multijet	multijet	non multijet	multijet
μ-channel		wide mass range	wide mass range	signal wide range	signal mass range
$\geqslant 1$ b-tag	Z+jets, anti-Iso	30643.7 ± 188.2	14.4 ± 69.2	26936.0 ± 165.4	3.9 ± 18.9 $(\star)$
$\geqslant 1$ b-tag	Z+jets, quasi anti-Iso	30641.9 ± 188.3	16.7 ± 69.4	26934.5 ± 165.5	4.6 ± 19.1
$\geqslant 1$ b-tag	Z+$\geqslant$1 b-tag, anti-Iso	30647.5 ± 188.0	10.5 ± 68.7	26939.4 ± 165.3	2.9 ± 18.8
$\geqslant 1$ b-tag	Z+$\geqslant$1 b-tag, quasi anti-Iso	30643.9 ± 188.5	14.1 ± 70.1	26936.2 ± 165.7	4.0 ± 19.7
$\geqslant 2$ b-tags	Z+jets, anti-Iso	2191.2 ± 56.5	-39.2 ± 31.0	1442.5 ± 37.2	-10.7 ± 8.4 $(\star)$
$\geqslant 2$ b-tags	Z+jets, quasi anti-Iso	2191.2 ± 56.5	-39.2 ± 31.1	1442.5 ± 37.2	-10.8 ± 8.6
$\geqslant 2$ b-tags	Z+$\geqslant$1 b-tag, anti-Iso	2194.9 ± 56.6	-42.9 ± 31.1	1444.9 ± 37.3	-11.7 ± 8.5
$\geqslant 2$ b-tags	Z+$\geqslant$1 b-tag, quasi anti-Iso	2193.0 ± 56.9	-41.0 ± 31.8	1443.7 ± 37.5	-11.5 ± 8.9

Table 16: Estimates of the multijet background contamination in events passing the nominal selections Z+b and Z+bb in addition to the selection with a Z boson with one tagged jet and at least another non-tagged jet, for both lepton channels. The number of multijet events from the fit refers to the wide di-lepton invariant mass region and must be projected onto the signal mass range of the selection before being used. The values actually used in the following analysis (and set to zero in case of negative results) are flagged with $(\star)$.

The number of multijet events estimated in the signal region are propagated differentially in all the analysis bins of the distributions introduced in Sec. 4.1 by assuming a constant fraction of multijets compared to the data yields in all the bins. This hypothesis is cross checked with two methods as described in the following.

4.3.4.1 *Further checks on the differential estimation*

The relative fraction of multijet events in the signal region can be estimated directly by performing the fit to the di–lepton invariant mass distribution in each analysis bin. This procedure is affected by large statistical fluctuations in the multijet determination. However, within the errors, it leads to results consistent with the approach of assuming a constant relative contamination of the selection.

As further cross check of the assumption of constant multijet fraction in the signal region, the control regions can be used to derive the profile for all the distributions to be measured (listed in Sec. 4.1). Each distribution is derived from a suitable multijet enriched data sample (the $(L_{\overline{M}}, L_{\overline{M}})$ sample in the electron channel and the anti–Iso sample in the muon channel); the non multijet contribution

is normalized to the fit results shown in Sec. 4.3.1 and Sec. 4.3.2 and they are subtracted bin by bin; then the obtained distributions with a proper normalization can be interpreted as multijet probability densities, $\mathrm{pdf}(\mathrm{c.r.})$, which can be compared directly with the probability density functions derived from the data in the signal region, $\mathrm{pdf}(\mathrm{Data})$.

To quantify the suitability of the $\mathrm{pdf}(\mathrm{Data})$ used as baseline probability density function for the multijet description, corresponding to each distribution the variable

$$s(\mathbf{x}) = \frac{\mathrm{pdf}(\mathbf{x};\mathrm{c.r.}) - \mathrm{pdf}(\mathbf{x};\mathrm{Data})}{\sigma[\mathrm{pdf}(\mathbf{x};\mathrm{Data})]}\,, \tag{32}$$

where $\mathbf{x}$ indicates a set of binned data associated to a measured distribution and $\sigma[\mathrm{pdf}_{\mathrm{Data}}(\mathbf{x})]$ is the uncertainty on the multijet yield determined in the signal region from the fit shown in Tab. 16.

The values of $s(\mathbf{x})$ are shown in Fig. 38 for the electron channel (top) and for the muon channel (bottom); a systematic effect can be observed in all the distributions; it is most relevant for the Z transverse momentum, while it is typically smaller for the other distributions. On the basis of these results and considering the very small contribution of the multijet contamination in the signal region, this study is not used to derive a systematic uncertainty on the pdf choice.

4.3.4.2 *Summary*

In summary, given the results shown in Tab. 16, the estimate of the multijet background in each bin of the distributions for the Z+b candidate selection is performed as follows:

- for the electron channel, the results from the Z+jets $(\mathrm{M}, \overline{\mathrm{M}})$ control region are used;
- for the muon channel, the results from the Z+jets anti–Iso control region are used;
- for both channels the ratio between the multijet events and the total number of selected events is assumed to be constant in all analysis bins and equal to the ratio observed in the total sample, namely:

  electron channel: $0.10\% \pm 0.11\%$

  muon channel: $0.015\% \pm 0.070\%$

  combined channel: $0.051\% \pm 0.087\%$
- the multijet contamination is extracted in all bins of each distribution using the determination of the percentage contamination in the whole sample (see Tab. 42–49 where the absolute contamination of multijet events is listed along with all other backgrounds).

4.4 FINAL DATA YIELD AT RECONSTRUCTION LEVEL

The output of the event and jet selection to be used as input for the next step of the analysis, the b–yield extraction from the flavor fit, is summarized in Tab. 17

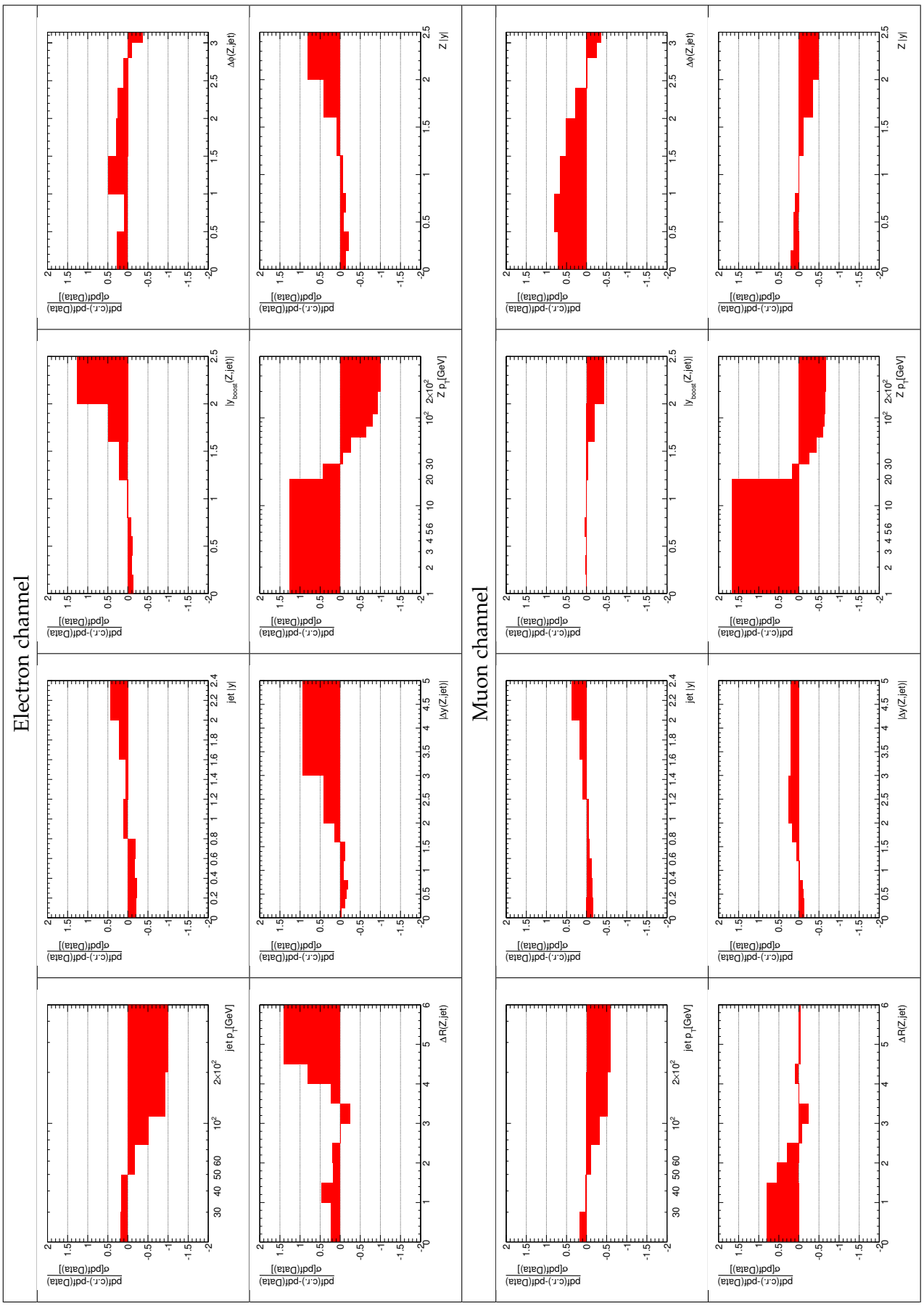

Figure 38: Comparison of the multijet pdf in the electron channel (top) and in the muon channel (bottom). The comparison is presented in terms of the difference of the two pdfs weighted by the uncertainty on the multijet yield in the signal region as derived from the fit shown in Tab. 16.

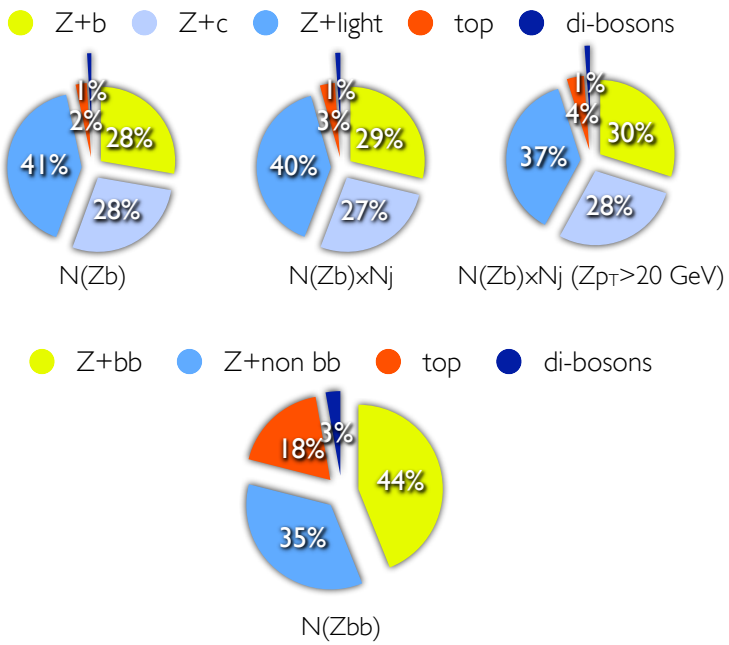

Figure 39: Monte Carlo predictions for the inclusive b-jet selection in association with one Z boson, for events with at least one b–tagged jet and for events with at least two b–tagged jets.

and represented in Fig. 39. The predictions from simulation are corrected for all the known mismodeling of reconstruction and identification algorithms.

The dominant backgrounds are due to Z+light and Z+charm, $\sim 65\% \div 69\%$, with the Z+c contribution being of the same order of the expected signal yield; the other backgrounds are predicted to be very small, at most 5%, with a slight dominance of the top ($t\bar{t}$+single top) background. In the sample with at least two b–tagged jets the expected relative signal yield increases, up to 44%, and becomes larger than the Z+jets background; at the same time the top background increases significantly by a factor $\sim 5 \div 9$. The di–boson contribution to all the selected signal samples is rather small, 3% at most; the multijet background has been measured to be the smaller background considered in the analysis, being of sub–percent level, as pointed out in Sec. 4.3.

4.5 FLAVOR FIT

The detector level selection detailed in Tab. 9 is used to select a sample of events with a Z boson candidate and at least one b–tagged jet (passing the MV1 cut at 75% efficiency) as described in Sec. 4.2.2. The number of b–jets, N_b, and the number of events with a Z boson and a b–jet, N_{Zb}, are extracted from the data using a fit procedure sensitive to the jet flavor.

The (binned) data can be fit by using an extended maximum likelihood fit based on a model defined in terms of binned probability density functions (pdfs), called *templates*, which are built from Monte Carlo simulations and provided separately for b–jets ($F_b(\{x\})$), charm–jets ($F_c(\{x\})$) and light–jets ($F_l(\{x\})$); in addition, the back-

Selection	Z+jets			Top	Di–boson	Multijet	Total	Data
	Z+b	Z+c	Z+l				Expectation	
Electron channel								
$N(Zb)$	4828	4874	7144	435	176	20	17477	20076
$N(Zb) \times N_{tag.-jets}$	5285	4983	7297	623	203	21	18402	21132
$N^{\star}(Zb) \times N_{tag.-jets}$	4459	4185	5520	569	185	18	14936	17563
$N(Zbb)$	413	365		172	25	-	975	1033
Muon channel								
$N(Zb)$	6586	6594	9767	563	248	4	23762	27062
$N(Zb) \times N_{tag.-jets}$	7185	6739	9983	794	281	4	24986	28568
$N^{\star}(Zb) \times N_{tag.-jets}$	6004	5660	7490	736	255	4	20149	23680
$N(Zbb)$	541	396		224	36	-	1296	1461

Table 17: Summary of selected data and estimated sample composition with the Monte Carlo simulation or with the data driven method of Sec. 4.3 for the multijet events. $N(Zb)$ is the number of selected events; $N(Zb) \times N_{tag.-jets}$ is the number of selected b–tagged jets; $N^{\star}(Zb) \times N_{tag.-jets}$ is the number of selected b–tagged jets corresponding to events where the Z p_T is greater than 20 GeV; $N(Zbb)$ is the number of selected events with at least two b–tagged jets.

ground pdf ($F_{bkg}(\{x\})$) is determined by combining the top, the di–bosons and the multijets with a suitable fraction as derived from MC predictions (top and di–bosons) or from the data (multijet). The statistical model used to describe the data is

$$\begin{aligned} F(\{x\}; N_b, N_c, N_l, N_{bkg}) &= N_b \cdot F_b(\{x\}) + N_c \cdot F_c(\{x\}) \\ &\quad N_l \cdot F_l(\{x\}) + N_{bkg} \cdot F_{bkg}(\{x\}) \,, \end{aligned} \tag{33}$$

where N_b, Nc and N_l are the b–jet, charm–jet and light–jet yields to be determined from the fit; the background normalization, N_{bkg}, is fixed to the Monte Carlo predictions (top and di–bosons) or to the data driven determination (multijet). The fit is concretely implemented in the RooFit [112] framework.

An assignment of the jet flavor, *truth labeling*, for the simulated jets used to build the probability density functions $F_b(\{x\})$, $F_c(\{x\})$ and $F_l(\{x\})$, is needed to properly determine the signal yield at detector level. For each b–tagged jet, the jet flavor is recursively defined by using an angular matching criterion between the jet axis and the direction of a stable b–hadron or final state charm or light partons in the MC truth record as described below.

1. If a stable b–hadron with $p_T > 5$ GeV is found with $\Delta R(jet,b\text{–hadron}) < 0.3$, the jet is labeled as a b–jet.

2. If the jet is not a b–jet and a final state charm parton with $p_T > 5$ GeV and with $\Delta R(jet,charm) < 0.3$ is found, the jet is labeled as a charm jet (or c–jet).

3. If the jet is not a b–jet nor a c–jet and a final state light parton with $p_T > 5$ GeV and with $\Delta R(\text{jet,light}) < 0.3$ is found, the jet is considered a light jet.

The exact list of stable b–hadrons used in the truth labeling is provided later in Chap. 5 and it is the same used to define the signal at particle level.

The flavor composition for the non Z+jets backgrounds is not needed; a dedicated procedure is used to define the multijet component of the $F_{bkg}(\{x\})$ pdf as explained in Sec. 4.5.2; the multijet component is included in the final results provided in Sec. 4.5.3 but, given its extremely low contribution, it is not taken into account in the optimization study concerning the flavor fit illustrated in the next section.

4.5.1 *Flavor fit optimization*

Ideally the data distribution **D** exploited in the likelihood template fit should have a good sensitivity to the jet flavors in order to minimize the statistical uncertainty in the signal yield extraction. The most interesting *flavor sensitive* distributions studied[4] are the SV0 mass [113], two combinations of the JetFitterCombNN algorithm output, $\log(p_b/p_u)$ and $\log(p_b/p_c)$, also indicated as CombNN and CombNNc respectively, the MV1 weight and the JetFitter mass; all of them are introduced in Sec. 2.7.

The modeling of the flavor discriminant distributions used in the flavor fit is crucial in order to avoid bias in the signal yield extraction. The ability to model all the flavor discriminants rely on the Monte Carlo description of the b–hadron decay chains.

A specialized generator used to simulate b–hadrons decay, EvtGen (see Sec. 1.2.3.2), has been developed in the last decade and validated with B–factories data [50]; EvtGen is expected to provide the best available simulation of b–hadron decays. Therefore, a truth level reweighting using EvtGen is applied to the nominal analysis sample Alpgen+Herwig+Jimmy in the same way as Ref. [114], in order to correct the distribution of the number of charged tracks multiplicity in the signal Monte Carlo; the correction is propagated to detector level variables, including the flavor discriminants under study.

The validity of the CombNNc discriminant shape as determined from the reweighted simulation is studied with a sample of data enriched in b–jets by selecting $t\bar{t}$ events. In this control sample the CombNNc distribution in data is compared to the simulation and a correcting function is obtained; therefore this function is used to derive a systematic uncertainty on the CombNNc shape modeling as also described in Sec. 5.4. As an illustration of this study, in Fig. 40 the ratio of the data to the nominal simulation and the ratio between the corrected and the uncorrected simulation for CombNNc are reported; more details on the CombNNc templates validation are given in Ref. [115].

To check the sensitivity to the jet flavor separation a fit to the inclusive jet sample is performed by using the discriminants SV0 mass, JetFitter mass, MV1, CombNN and CombNNc with three free parameters, N_b, N_c and N_l. The electron and the

4 The initial study was reported in https://indico.cern.ch/event/184029/contribution/0/material/slides/0.pdf

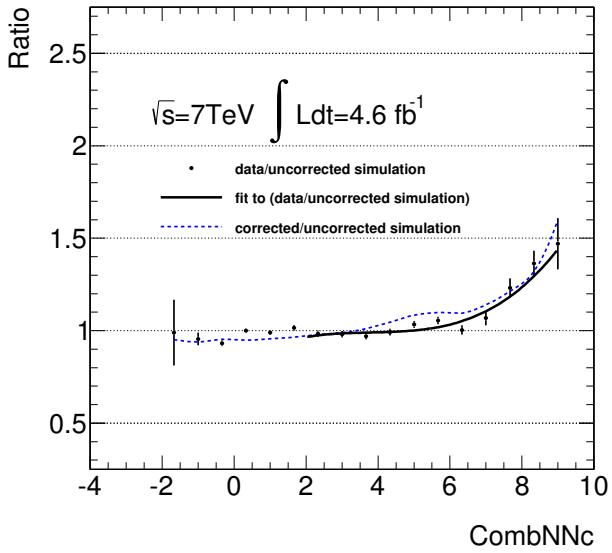

Figure 40: Ratio of data to the uncorrected simulation, and the derived correcting function (black line), and the ratio between the EvtGen corrected and the uncorrected simulation as a function of CombNNc. The corrected simulation is used as default choice for the analysis results; the correcting function is used to modify the MC CombNNc template for the evaluation of the systematic uncertainty on the CombNNc modeling.

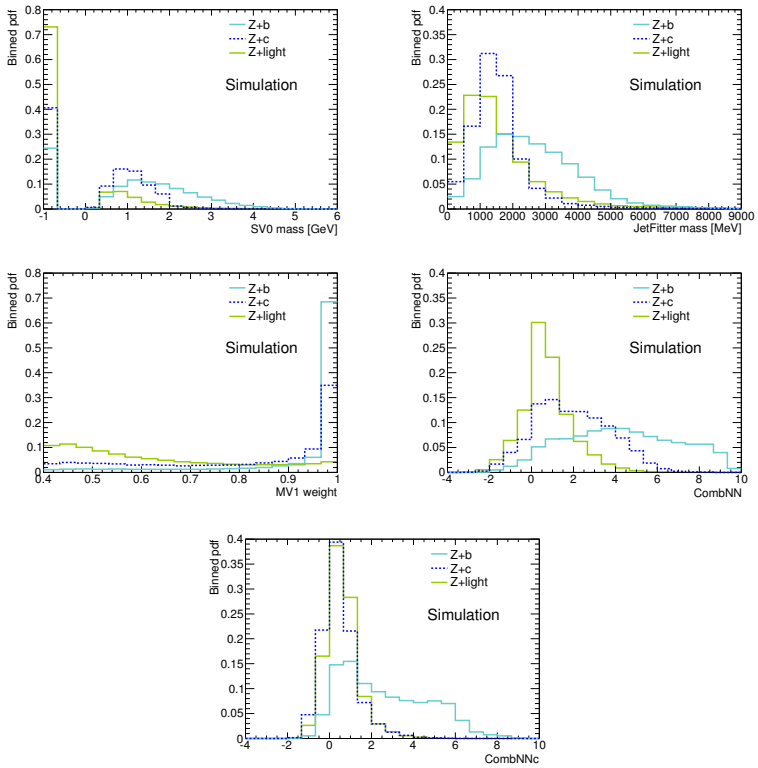

Figure 41: Template shapes for the five flavor sensitive observables SV0 mass, JetFitter mass, MV1, CombNN and CombNNc.

muon channels are combined at reconstruction level in a single dataset both in data and in simulation. The flavor templates for each variable are shown in Fig. 41.

The light and charm probability density functions for the CombNNc distribution are almost degenerate, thus a sensitive statistical separation light–to–charm jets can't be achieved with this discriminant; instead, the separation between the signal and the Z+jets background is maximum with CombNNc.

In order to overcome the degeneration of charm–jets and light–jets in the CombNNc distributions while preserving a good statistical precision on N_b, a multidimensional fit combining CombNNc with the other discriminants is performed using the following combinations:

- (SV0 mass,CombNNc);
- (JetFitter mass,CombNNc);
- (MV1 weight,CombNNc);
- (CombNN,CombNNc).

The light–charm degeneration is found to be solved with the two–dimensional fit approach but there is no significant gain in the statistical precision on the signal yield extraction; thus a simple fit method is used as default based on the CombNNc distribution with combined template for the charm–jets and light–jets; this fit method relies on the Monte Carlo predictions of the light–to–charm jets ratio; however, this is shown to be well predicted by using the full flavor separation provided by the fit to the SV0 mass, Jet Fitter mass, MV1 and CombNN distributions. For example the fit to the number of b–tagged jets in the combined lepton channel obtained with the CombNN discriminant is shown in Fig. 42; this result can be compared with the MC estimate of the number of light and charm jets also reported in Tab. 17; the Monte Carlo simulation predicts very well the ratio of charm and light fraction observed in data, therefore, justifying the nominal fit method adopted in the analysis.

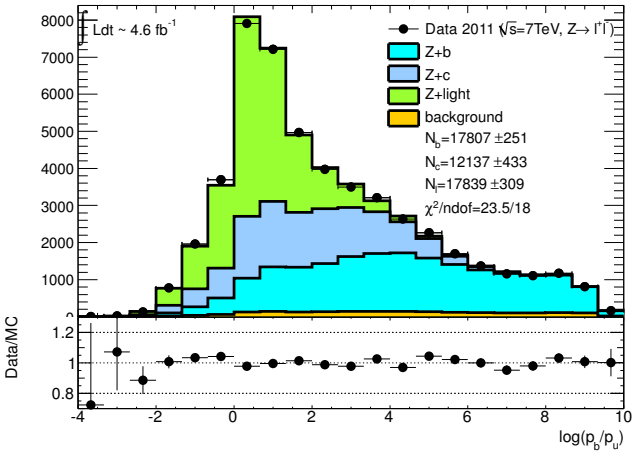

Figure 42: Fit to the distribution of $\ln(pb/pu)$ (CombNN) for b–tagged jets in the combined lepton channel with free normalization for light, charm and b–jet contributions.

Yields	Estimation
N_c fit	12137 ± 433
N_l fit	17839 ± 309
N_c/N_l fit	0.680 ± 0.027
N_c MC	11722
N_l MC	17280
N_c/N_l MC	0.678

Flavor discriminant	Uncertainty [%]			Correlation		
D=1, 3 flavors	ΔN_b	ΔN_c	ΔN_l	$\rho(N_b, N_c)$	$\rho(N_b, N_l)$	$\rho(N_l, N_c)$
SV0 mass	1.7	4.0	2.0	-0.61	0.11	-0.69
JetFitter mass	1.4	3.6	3.5	-0.18	-0.24	-0.80
MV1 weight	2.2	5.3	1.9	-0.86	0.60	-0.81
CombNN	1.5	4.2	1.8	-0.67	0.36	-0.78
CombNNc	1.2	13.4	4.4	0.10	-0.22	-0.97
D=2, 3 flavors	ΔN_b	ΔN_c	ΔN_l	$\rho(N_b, N_c)$	$\rho(N_b, N_l)$	$\rho(N_l, N_c)$
(SV0 mass,CombNNc)	1.2	2.7	1.8	-0.27	-0.10	-0.70
(JetFitter mass,CombNNc)	1.2	3.8	2.7	-0.13	-0.13	-0.85
(MV1 weight,CombNNc)	1.2	2.4	1.3	-0.39	-0.06	-0.50
(CombNN,CombNNc)	1.2	2.6	1.4	-0.36	-0.08	-0.55
D=1, 2 flavors	ΔN_b	ΔN_{c+l}	-	$\rho(N_b, N_{c+l})$	-	-
COMBNNc	1.2	0.8	-	-0.48	-	-

Table 18: Summary of the fit optimization studies; the statistical uncertainties on the fitted yields of b–jets, charm–jets and light–jets (ΔN_b, ΔN_c and ΔN_l) is shown for each one–dimensional fit method using three free parameters (D=1, 3 flavors), two–dimensional fit methods (D=2, 3 flavors) and for the one–dimensional fit to CombNNc with combined charm and light templates (D=1, 2 flavors). The correlation coefficients among the free parameters are also provided.

The fit optimization studies are summarized in Tab. 18 where the statistical uncertainty of the fitted parameters along with the parameter correlations are reported.

4.5.2 *Derivation of the multijet templates*

A template for the b–flavor discriminant CombNNc in multijet background events must be determined from data and used as input for the b-jet yield extraction. The sample used to derive the CombNNc distribution is based on the selection of the multijet enriched control region with the additional requirement that one jet is tagged as b-jet. In the muon case, both leptons are anti-isolated; in the electron channel, both leptons are failing the Medium++ criterion; the residual non multijet contribution is estimated with the MC simulations and it is subtracted bin by bin from the CombNNc distribution.

The CombNNc data distributions obtained from the multijet enriched samples for both lepton channels are shown in Fig. 43 (a,b). Different control regions have been used for checking the stability of the template shape; a comparison of the CombNNc shapes for the multijets background derived in alternative control sam-

ples is shown in Fig. 43 (c,d). In the muon channel the CombNNc profiles are in good agreement in the two control regions whereas some tensions are observed in the electron channel due to the different flavor composition of the two control samples. However, the variation of the measured signal yield obtained interchanging the multijet templates in the fit is observed to be much smaller than one per mille.

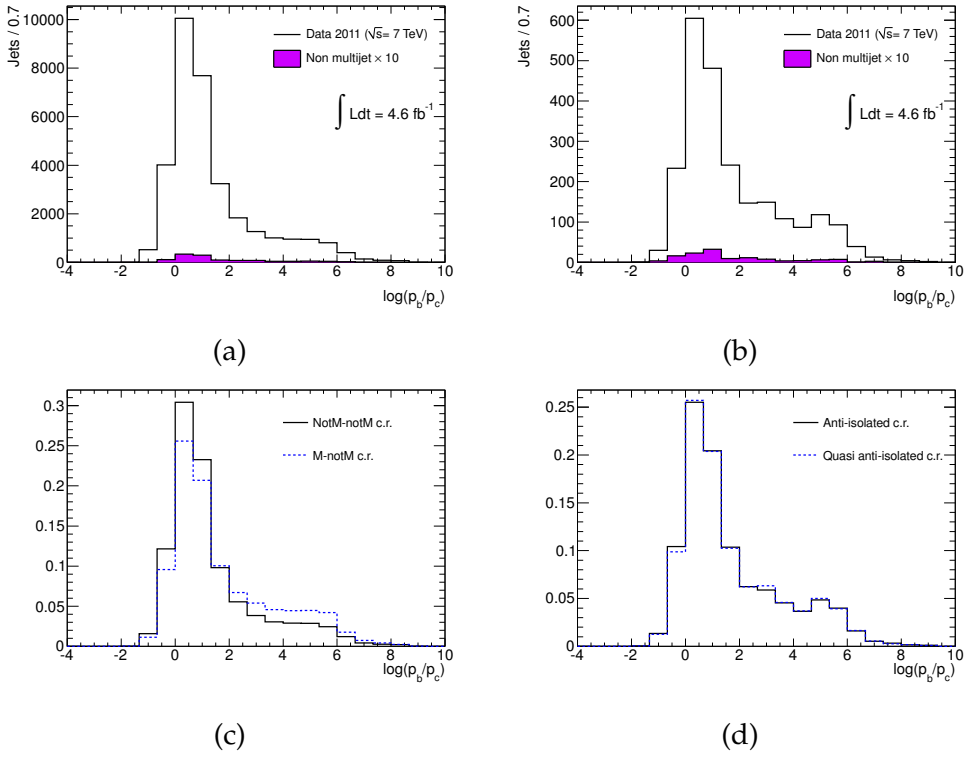

Figure 43: The CombNNc template from multijet events, as obtained from a modified control region demanding at least one tagged jet, for the electron (a) and muon (b) channel. The alternative multijet templates are compared at the bottom for the electron channel (c) and the muon channel (d).

4.5.3 *Final yield extraction*

The signal yield extraction is performed following a two parameter (N_b and N_{c+l}) fit to the CombNNc distribution as explained in Sec 4.5.1. For the jet–level observables, all tagged jets from data and MC simulations enter the flavor templates; for event–level distributions, the leading (in p_T) tagged jet is used in the flavor templates. The templates are derived independently in all the analysis bins in order to fully account for the dependence of the template shape on the kinematics.

For the central results, the electron and muon channels are first combined for each distribution simply by adding together the two sets of data, flavor templates and backgrounds. The procedure has been shown to improve the statistical preci-

sion and to be robust against statistical fluctuations in the evaluation of the systematic effects.

The combined data are compared to the Monte Carlo prediction after the template fit results have been used to alter the normalization of the b–jets and charm+light–jets templates, for all of the differential bins of the analysis, from Fig. 45 to Fig. 52. The fit performed on the full analysis samples used for the extraction of $N(Zb) \times N_{b\text{–jet}}$, $N^{\star}(Zb) \times N_{b\text{–jet}}$ and $N^{\star}(Zb) \times N_{b\text{–jet}}$ are reported in Fig. 44.

The data yields, the corresponding expectations for Z+light, Z+charm, Z+b and various background processes and, finally, the quality of the fit for the tagged $|\Delta y(Z, jet)|$ distribution is reported in Tab. 19; the results are presented separately for the electron channel, the muon channel and the channel combination. Similar information for all the distributions are provided in App. C.

The statistical uncertainty on the signal yield varies from 1.2% and reaching $\sim$ 16%–20% only in kinematic tails like for jet $p_T > 200$ GeV.

The MC model describes well the shape of the CombNNc discriminant observed in the data as shown by the values of the reduced χ^2 of the fit reported in App. C and from Fig. 45 to Fig. 52. In particular, the maximum value of χ^2/ndof is found to be 2.1 corresponding to a p–value of about 1%.

The percentage of Z+jets (light+charm–jets) background is observed to be typically uniform across the analysis bins. Its fitted contribution is shown from Fig. 45 to Fig. 52 by separating the light–jets (shown in light green) and charm–jets (shown in azure) components, which are overall normalized according to the fit results but with their relative contributions estimated by Monte Carlo predictions. The Z+jets background is observed to populate mostly the lower side of the CombNNc distribution, resulting in a very good discrimination of the signal.

As discussed in Sec. 4.2.2, the impact of the non Z+jets background is overall small, being about 10% of the signal in the integrated analysis samplings. However, in some phase space regions it becomes more significant; for example, this is the case for the intermediate b–jet p_T region (75–110 GeV) where the background reaches more than the 24% of the signal and for the low $\Delta R(Z, b)$ or $\Delta\phi(Z, b)$ where it can be larger than 30% of the fitted b–yields; on the other hand these phase space regions are not very populated by the signal, the uncertainty on the b–yield extraction can be as large as 10%, and the background have a small impact on the final results, as discussed in Sec. 5.4.

After the EvtGen based correction to the Alpgen+Herwig+Jimmy sample, the overall variation of the number of candidate b-jets extracted from the flavor fit was found to be about of 4-5% leading to a decrease of the number of b-jets, independently of the values of jet transverse momentum and rapidity.

4.5.4 *Fit quality*

The signal extraction at detector level is based on a extended maximum likelihood binned template fit; the b–yield values determined from this procedure are expected to be affected by a bias proportional to $1/N$ being N the number of observed events [116]. The bias affecting the N_b estimation is studied by using a toy Monte Carlo method based on RooFit and described in this section.

$\lvert\Delta y(Z,jet)\rvert$	[0-0.2]	[0.2-0.4]	[0.4-0.6]	[0.6-0.8]	[0.8-1.2]	[1.2-1.6]	[1.6-2]	[2-3]	[3-5]
Combined channel									
Total data	4783	4802	4526	4286	7492	5597	3926	4749	1082
Pre fit N_b	1321	1282	1221	1145	1953	1405	924	1013	198
Pre fit N_{charm}	1249	1272	1183	1092	1809	1322	869	884	166
Pre fit N_{light}	1493	1447	1466	1344	2280	1746	1259	1512	465
$t\bar{t}$	197.2	196.2	178.4	158.2	241.9	152.4	65.63	37.48	1.74
Single top	9.601	10.46	12.27	9.538	13.42	10.29	5.318	4.922	0.408
Dibosons	55.1	52.17	48.02	54.62	76.53	57.11	38.33	46.85	10.63
Multijets	2.431	2.447	2.38	2.205	3.844	2.94	1.98	2.349	0.498
Fitted N_b	1835 ± 65	1812 ± 63	1832 ± 62	1631 ± 61	3016 ± 82	2032 ± 67	1491 ± 57	1658 ± 62	304 ± 29
Fitted N_{c+l}	2684 ± 69	2731 ± 69	2453 ± 66	2431 ± 66	4141 ± 87	3342 ± 76	2325 ± 63	2999 ± 72	765 ± 36
Reduced χ^2	0.79	1.8	0.67	0.56	2.1	0.97	1.4	0.52	1.5
p–value	0.6945	0.0287	0.8216	0.9067	0.0090	0.4812	0.1399	0.9315	0.1026
Electron channel									
Total data	2021	2038	2006	1843	3209	2477	1640	1931	398
Pre fit N_b	572	549	521	491	830	604	397	419	76
Pre fit N_{charm}	535	549	512	472	761	563	369	369	55
Pre fit N_{light}	653	627	640	555	981	740	517	628	179
$t\bar{t}$	86.78	84.93	77.28	68.95	104.9	68.12	27.84	15.81	0.704
Single top	4.668	4.868	4.938	3.586	6.471	4.185	1.794	3.124	0.352
Dibosons	22.33	21.54	20.52	22.09	32.51	23.83	18.75	18.81	4.178
Multijets	2.021	2.038	2.005	1.843	3.209	2.477	1.641	1.93	0.397
Fitted N_b	790 ± 42	768 ± 41	794 ± 41	738 ± 41	1309 ± 54	897 ± 45	680 ± 38	688 ± 40	105 ± 17
Fitted N_{c+l}	1117 ± 45	1157 ± 45	1107 ± 44	1009 ± 43	1754 ± 57	1482 ± 51	909 ± 41	1203 ± 46	287 ± 22
Reduced χ^2	0.74	0.63	1.1	0.82	1.8	0.87	1.2	0.63	1
Muon channel									
Total data	2762	2764	2520	2443	4283	3120	2286	2818	684
Pre fit N_b	749	733	701	654	1123	801	526	595	122
Pre fit N_{charm}	714	723	671	619	1048	758	500	516	111
Pre fit N_{light}	840	819	826	789	1299	1005	742	884	286
$t\bar{t}$	110.4	111.2	101.1	89.21	137	84.3	37.78	21.67	1.036
Single top	4.933	5.587	7.33	5.951	6.951	6.105	3.524	1.798	0.056
Dibosons	32.77	30.63	27.5	32.53	44.01	33.28	19.59	28.05	6.45
Multijets	0.41	0.411	0.374	0.363	0.635	0.464	0.339	0.418	0.101
Fitted N_b	1046 ± 49	1043 ± 48	1041 ± 47	899 ± 46	1707 ± 62	1134 ± 50	809 ± 42	968 ± 48	198 ± 23
Fitted N_{c+l}	1567 ± 53	1574 ± 52	1343 ± 49	1418 ± 50	2387 ± 66	1861 ± 56	1416 ± 48	1797 ± 56	478 ± 29
Reduced χ^2	1.9	2.3	0.82	1.6	1.2	0.59	1.5	0.65	1

Table 19: Summary of the fit results in the electron and muon channel together with their combination in bins of $\lvert\Delta y(Z,jet)\rvert$; for each analysis bin the estimation of the backgrounds and of the signal are presented. For the combined channel the χ^2 probability (p–value) is also reported.

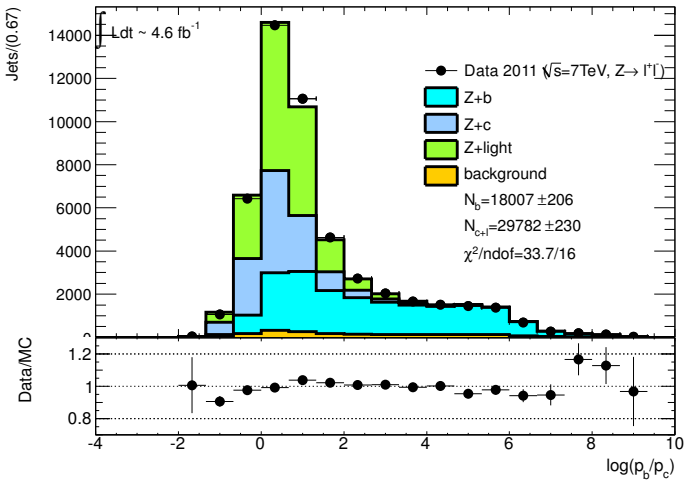

(a)

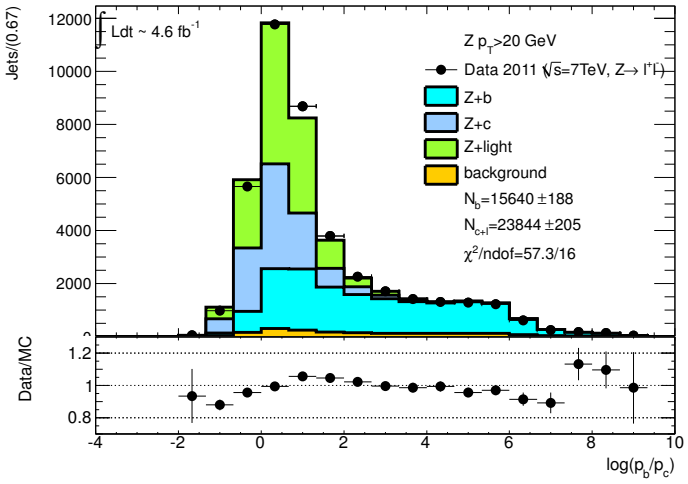

(b)

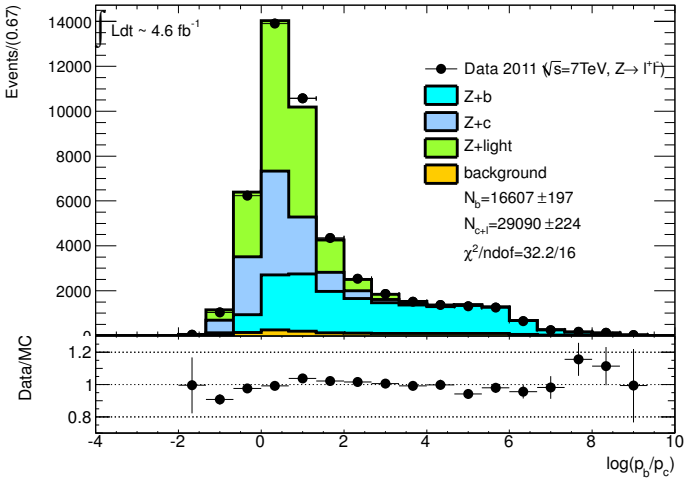

(c)

Figure 44: Flavor fit results in the inclusive sample of tagged jets (a), for the data sample with a selected Z boson with $p_T > 20$ GeV (b) and for the event level yield extraction using the leading b–tagged jets (c).

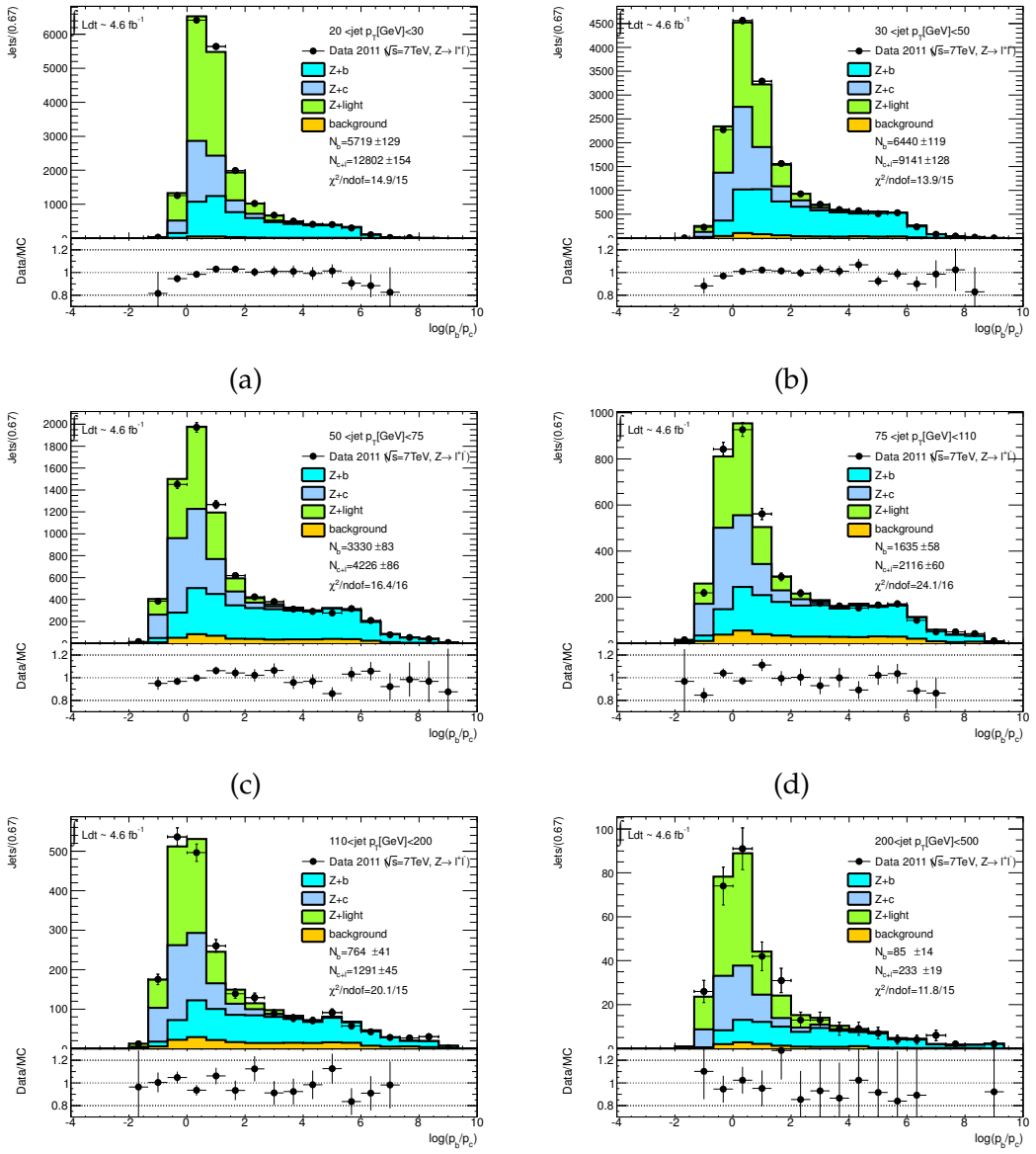

Figure 45: Flavor fit results in the bins 20 $\leqslant$b-jet p_T[GeV]$<$ 30 (a), 30 $\leqslant$b-jet p_T[GeV]$<$ 50 (b), 50 $\leqslant$b-jet p_T[GeV]$<$ 75 (c), 75 $\leqslant$b-jet p_T[GeV]$<$ 110 (d), 110 $\leqslant$b-jet p_T[GeV]$<$ 200 (e) and 200 $\leqslant$b-jet p_T[GeV]$\leqslant$ 500 (f).

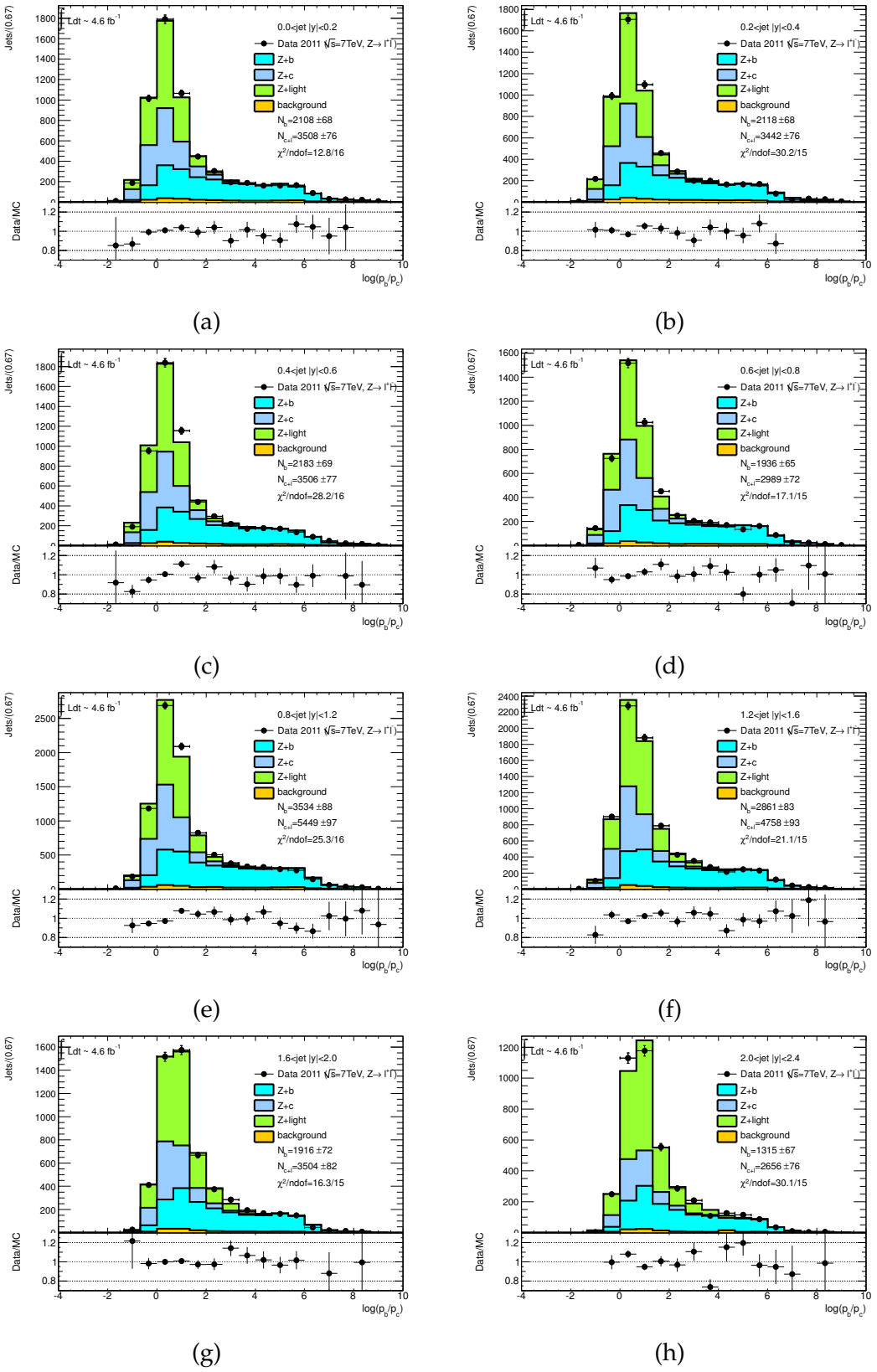

Figure 46: Flavor fit results in the bins $0 \leqslant$b-jet $|y| < 0.2$ (a), $0.2 \leqslant$b-jet $|y| < 0.4$ (b), $0.4 \leqslant$b-jet $|y| < 0.6$ (c), $0.6 \leqslant$b-jet $|y| < 0.8$ (d), $0.8 \leqslant$b-jet $|y| < 1.2$ (e), $1.2 \leqslant$b-jet $|y| < 1.6$ (f), $1.6 \leqslant$b-jet $|y| < 2.0$ (g) and $2.0 \leqslant$b-jet $|y| \leqslant 2.4$ (h).

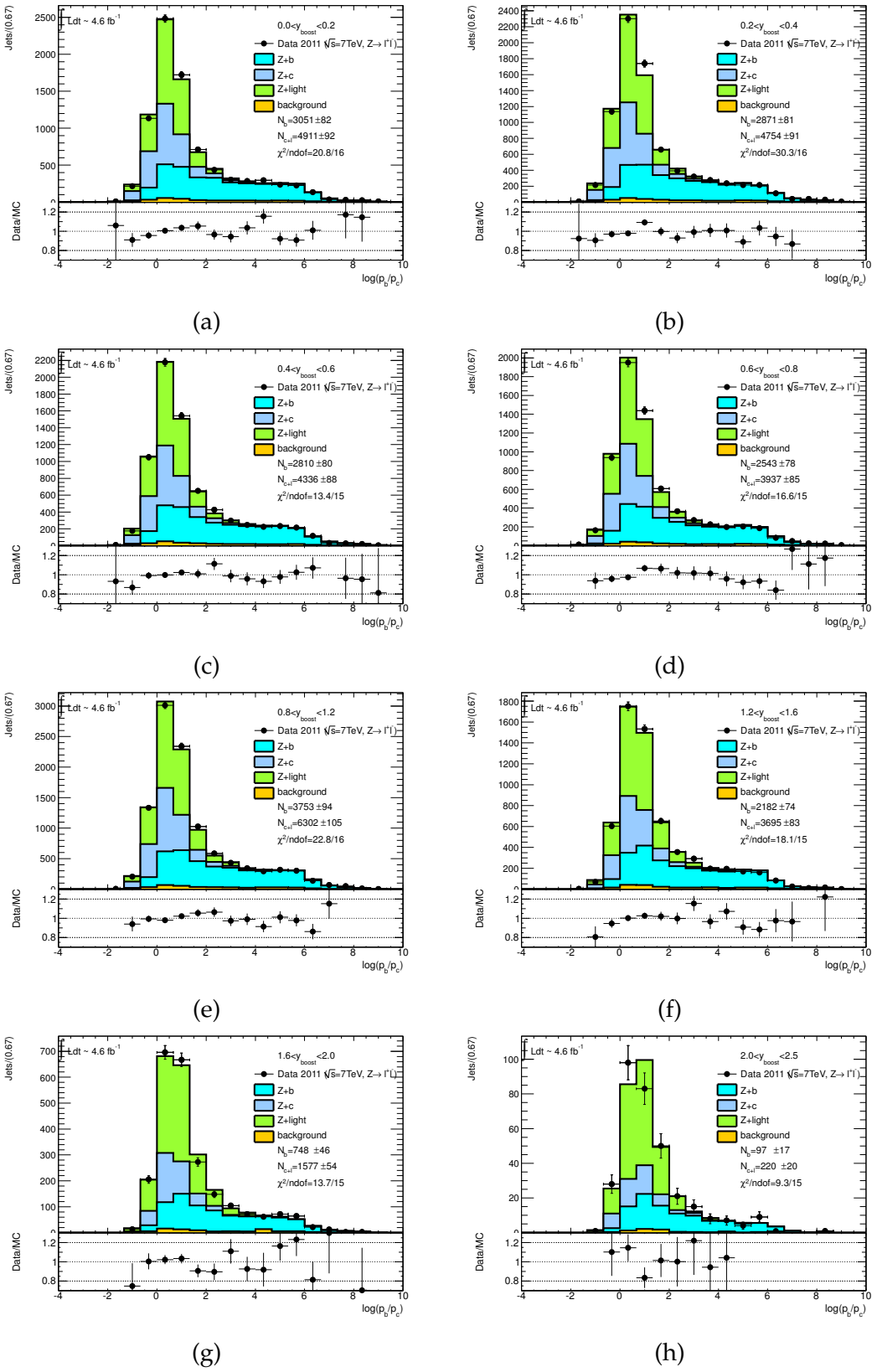

Figure 47: Flavor fit results in the bins $0 \leqslant |y_{boost}(Z, b-jet)| < 0.2$ (a), $0.2 \leqslant |y_{boost}(Z, b-jet)| < 0.4$ (b), $0.4 \leqslant |y_{boost}(Z, b-jet)| < 0.6$ (c), $0.6 \leqslant |y_{boost}(Z, b-jet)| < 0.8$ (d), $0.8 \leqslant |y_{boost}(Z, b-jet)| < 1.2$ (e), $1.2 \leqslant |y_{boost}(Z, b-jet)| < 1.6$ (f), $1.6 \leqslant |y_{boost}(Z, b-jet)| < 2.0$ (g) and $2.0 \leqslant |y_{boost}(Z, b-jet)| < 2.5$ (h).

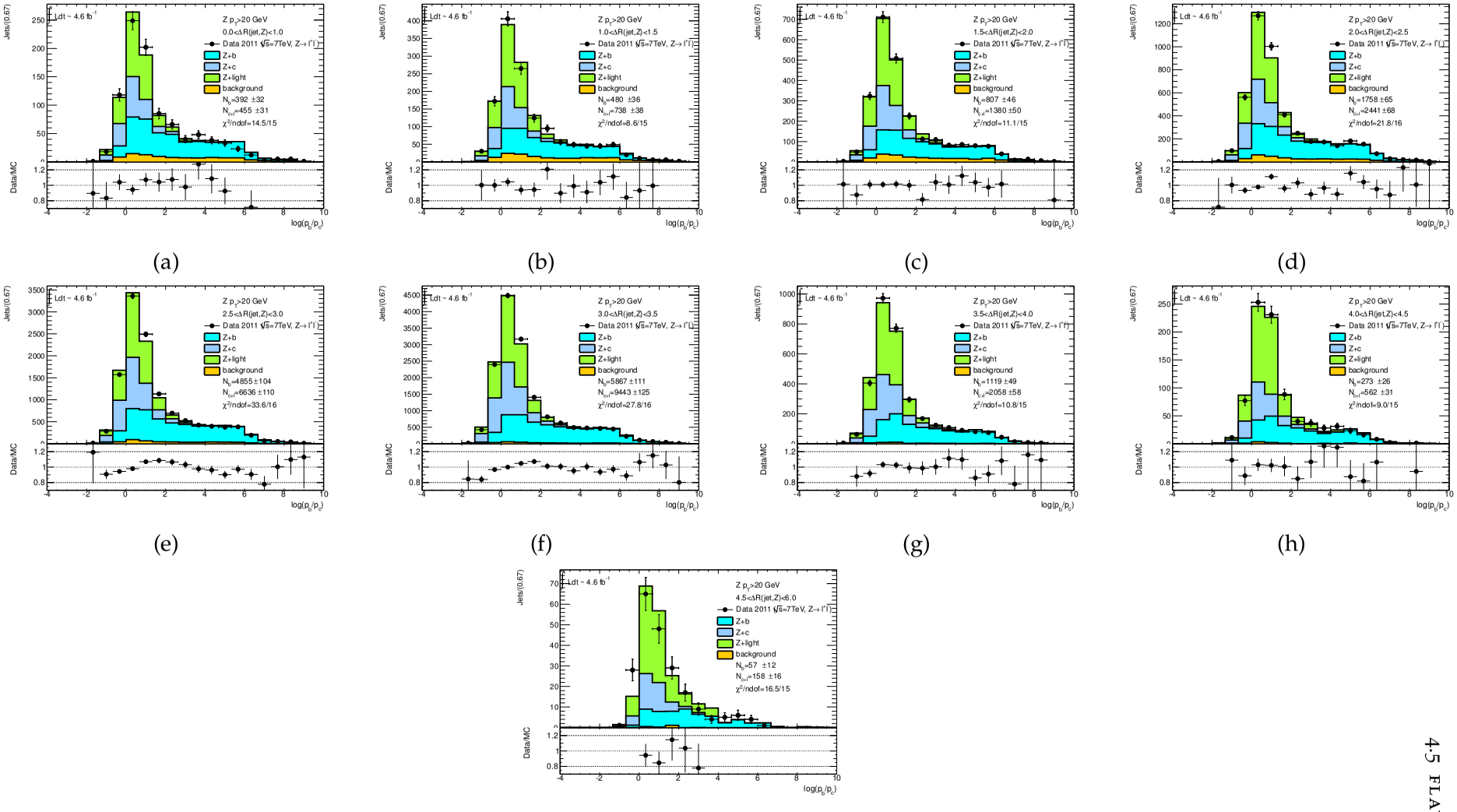

Figure 48: Flavor fit results in the bins $0.0 \leqslant \Delta R(Z, b-jet) < 1.0$ (a), $1.0 \leqslant \Delta R(Z, b-jet) < 1.5$ (b), $1.5 \leqslant \Delta R(Z, b-jet) < 2.0$ (c), $2.0 \leqslant \Delta R(Z, b-jet) < 2.5$ (d), $2.5 \leqslant \Delta R(Z, b-jet) < 3.0$ (e), $3.0 \leqslant \Delta R(Z, b-jet) < 3.5$ (f), $3.5 \leqslant \Delta R(Z, b-jet) < 4.0$ (g), $4.0 \leqslant \Delta R(Z, b-jet) < 4.5$ (h) and $4.5 \leqslant \Delta R(Z, b-jet) \leqslant 6.0$ (i).

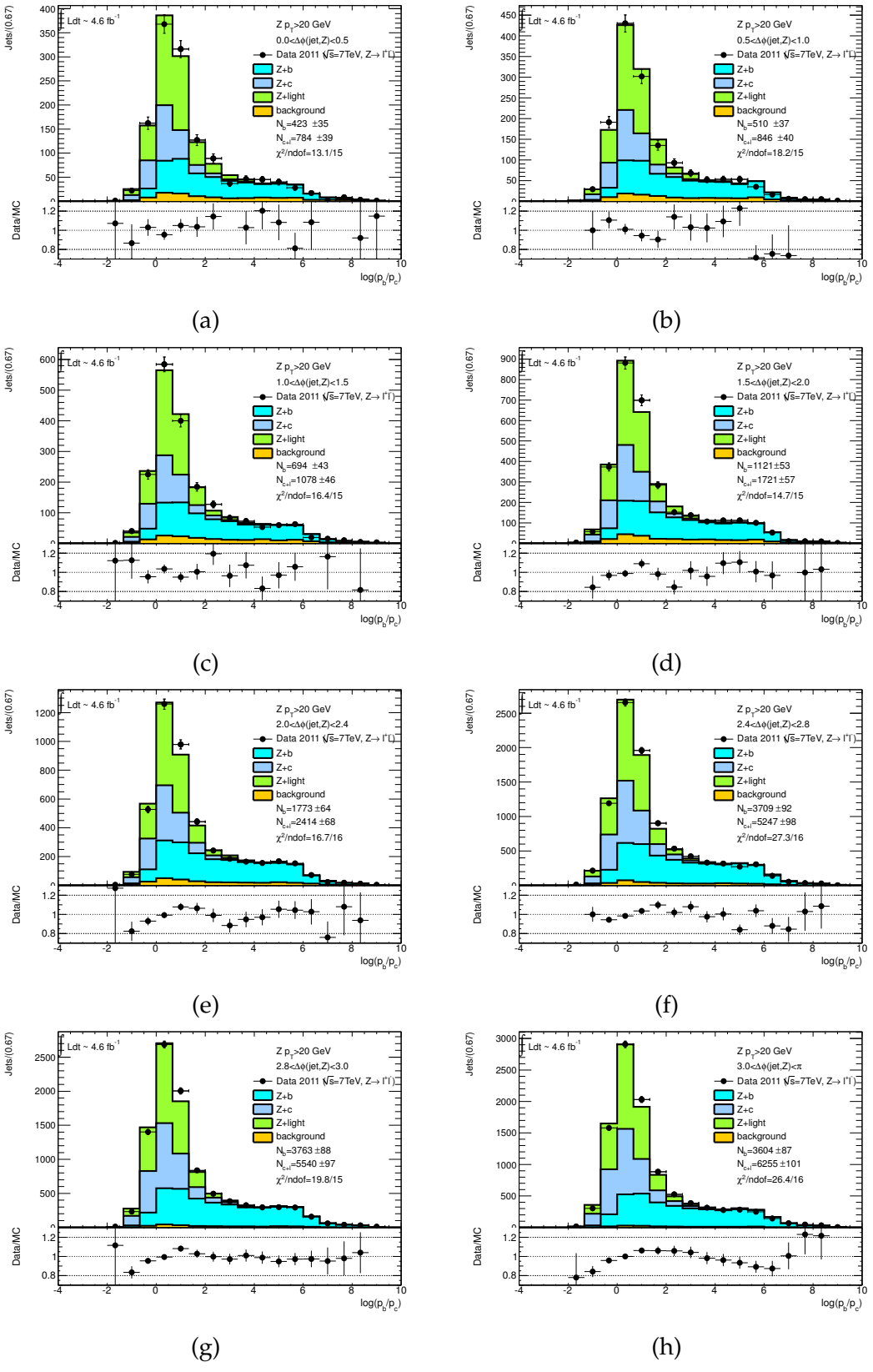

Figure 49: Flavor fit results in the bins $0 \leqslant \Delta\phi(Z, b-\text{jet}) < 0.5$ (a), $0.5 \leqslant \Delta\phi(Z, b-\text{jet}) < 1.0$ (b), $1.0 \leqslant \Delta\phi(Z, b-\text{jet}) < 1.5$ (c), $1.5 \leqslant \Delta\phi(Z, b-\text{jet}) < 2.0$ (d), $2.0 \leqslant \Delta\phi(Z, b-\text{jet}) < 2.4$ (e), $2.4 \leqslant \Delta\phi(Z, b-\text{jet}) < 2.8$ (f) $2.8 \leqslant \Delta\phi(Z, b-\text{jet}) < 3.0$ (f) and $3.0 \leqslant \Delta\phi(Z, b-\text{jet}) \leqslant \pi$ (h).

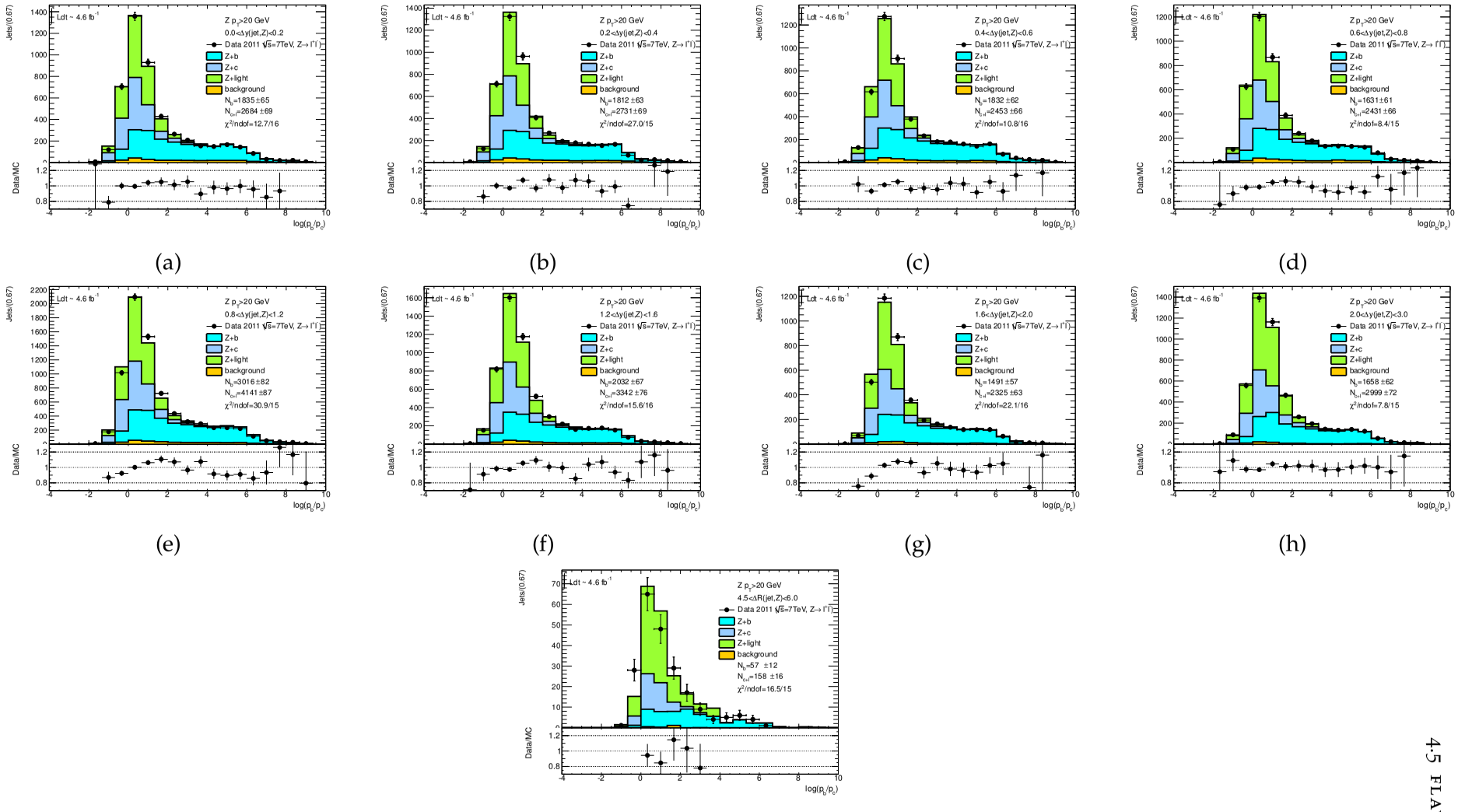

Figure 50: Flavor fit results in the bins $0.0 \leqslant \Delta y(Z, b-jet) < 1.0$ (a), $1.0 \leqslant \Delta y(Z, b-jet) < 1.5$ (b), $1.5 \leqslant \Delta y(Z, b-jet) < 2.0$ (c), $2.0 \leqslant \Delta y(Z, b-jet) < 2.5$ (d), $2.5 \leqslant \Delta y(Z, b-jet) < 3.0$ (e), $3.0 \leqslant \Delta y(Z, b-jet) < 3.5$ (f), $3.5 \leqslant \Delta y(Z, b-jet) < 4.0$ (g), $4.0 \leqslant \Delta y(Z, b-jet) < 4.5$ (h) and $4.5 \leqslant \Delta y(Z, b-jet) \leqslant 6.0$ (i).

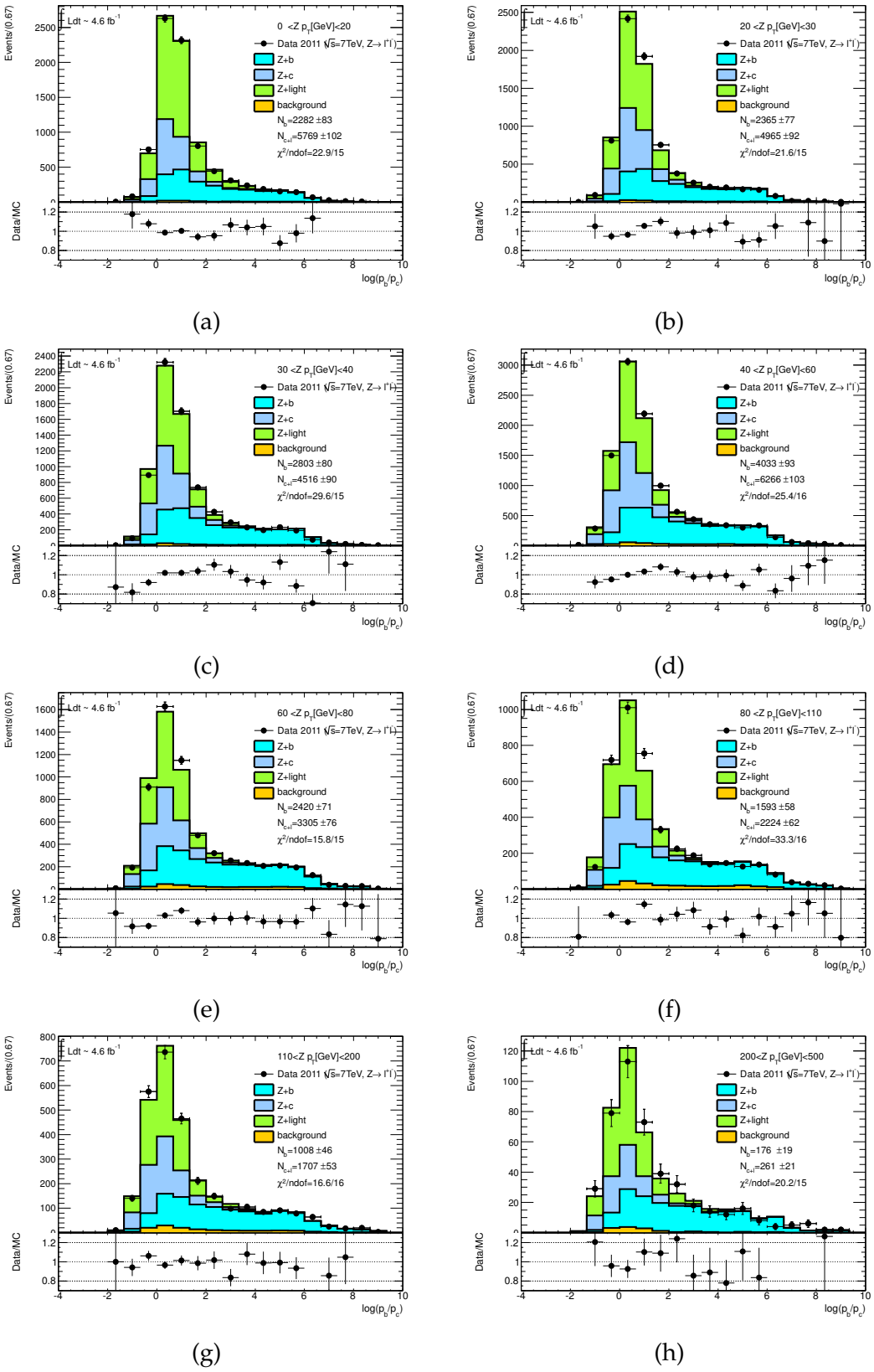

Figure 51: Flavor fit results in the bins $0 \leqslant Z\ p_T[\text{GeV}] < 20$ (a) $20 \leqslant Z\ p_T[\text{GeV}] < 30$ (b), $30 \leqslant Z\ p_T[\text{GeV}] < 40$ (c), $40 \leqslant Z\ p_T[\text{GeV}] < 60$ (d), $60 \leqslant Z\ p_T[\text{GeV}] < 80$ (e), $80 \leqslant Z\ p_T[\text{GeV}] < 110$ (f), $110 \leqslant Z\ p_T[\text{GeV}] < 200$ (g) and $200 \leqslant Z\ p_T[\text{GeV}] < 500$ (h).

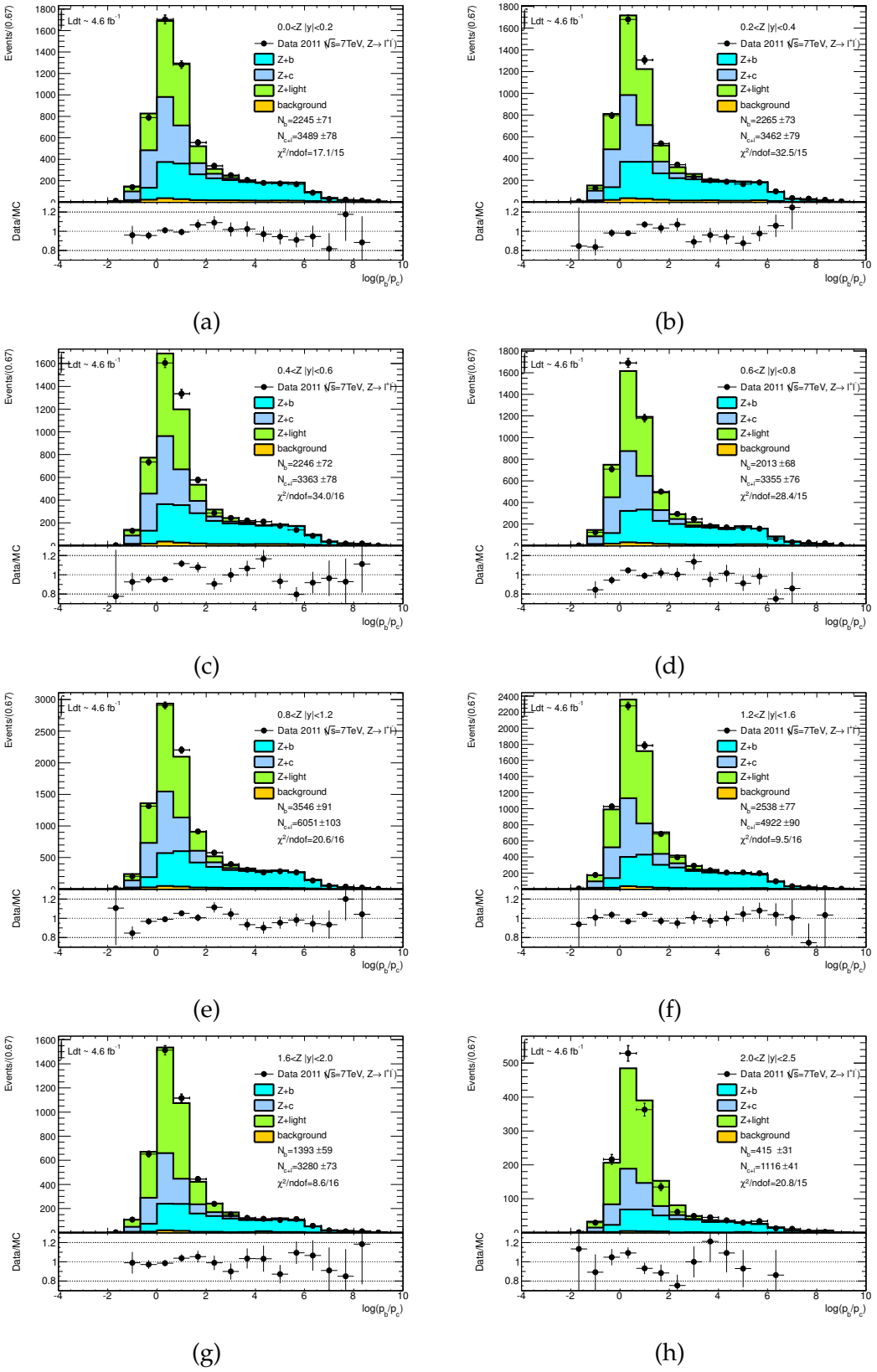

Figure 52: Flavor fit results in the bins $0 \leqslant |Zy| < 0.2$ (a) $0.2 \leqslant |Zy| < 0.4$ (b), $0.4 \leqslant |Zy| < 0.6$ (c), $0.6 \leqslant |Zy| < 0.8$ (d), $0.8 \leqslant |Zy| < 1.2$ (e), $1.2 \leqslant |Zy| < 1.6$ (f), $1.6 \leqslant |Zy| < 2.0$ (g) and $2.0 \leqslant |Zy| < 2.5$ (h).

An analysis bin is characterized by a data distribution $\mathbf{D}_{bin}$, by charm+light–jet template F_{c+l}, and by a b–jet template F_b. A set of pseudo–data $\mathbf{D}_{bin}^{(pseudo)}$ can be generated according to the measured values N_b and N_{c+l}, from the fit to $\mathbf{D}_{bin}$, using the Monte Carlo templates F_{c+l} and F_b; the total number of entries in $\mathbf{D}_{bin}^{(pseudo)}$ is fluctuated according to a Poisson distribution with average given by the total expected data in the bin. The templates F_{c+l} and F_b can be then used to fit the pseudo–data distribution of CombNNc; thus the value $N_b^{(toy)}$ fitted for each pseudo–experiment can be used to define the *pull* (p_{N_b}) of the N_b parameter

$$p_{N_b} = \frac{N_b^{(toy)} - N_b}{\Delta N_b^{(toy)}} , \tag{34}$$

where $\Delta N_b^{(toy)}$ is the statistical uncertainty on $N_b^{(toy)}$ as determined from the fit to the pseudo–data; the pull is expected to have mean zero, implying an unbiased N_b determination, and unitary width, meaning a correct estimation of ΔN_b.

The procedure is repeated and the distribution of p_{N_b} is built for each analysis bin; simultaneously the corresponding pull for the charm+light yield N_{c+l} can be obtained; a Gaussian fit to the p_{N_b} distributions can be performed in order to extract the mean and width of the pull in all the analysis bins. Finally, if a substantial bias is observed, for each bin the central values N_b and its uncertainty ΔN_b might be corrected according to

$$N_b \pm \Delta N_b \rightarrow [N_b + \Delta N_b \times mean(p_{N_b})] \pm \Delta N_b \times \sigma(p_{N_b}) . \tag{35}$$

The pull mean and width for all the analysis bins are summarized in Fig. 53 and Fig. 54 respectively. Typically a small negative shift of the pull mean is observed, interpreted as a negative bias in the N_b determination, which, as expected, tends to be larger in bins populated by a low number of observed events; it reaches values close to 0.08 for $\Delta R(Z, b) > 4.5$ but it is typically found to be ~ 0.02. The corresponding pull widths are observed to be very close to 1 in all the analysis bins, deviating at most by 0.2.

The effect of the bias in the fit procedure is judged to be comfortably small, therefore the fitted b–yields are not corrected for it.

4.5.5 *Comparison of extracted yields with* ALPGEN

The fit results on the entire selected data sample are reported in Tab. 20 along with the ALPGEN predictions at detector level normalized to the inclusive Z prediction at NNLO in perturbative QCD as described in Sec. 4.2.2. The light+charm fitted yields in data are found to be about $2-3\%$ deviation higher than the ALPGEN+HERWIG+JIMMY predictions; the b–yields observed in data are observed to be 50% higher than the predicted. A more complete comparison taking into account all the systematic uncertainty in data it is provided in Chap. 6.

The fit results are shown at the reconstruction level for all the differential observables in Fig. 55 and they are compared to the ALPGEN predictions.

A first raw comparison of the observed distributions in data and the ALPGEN predictions can be made by a χ^2 test [117], taking into account only the statistical

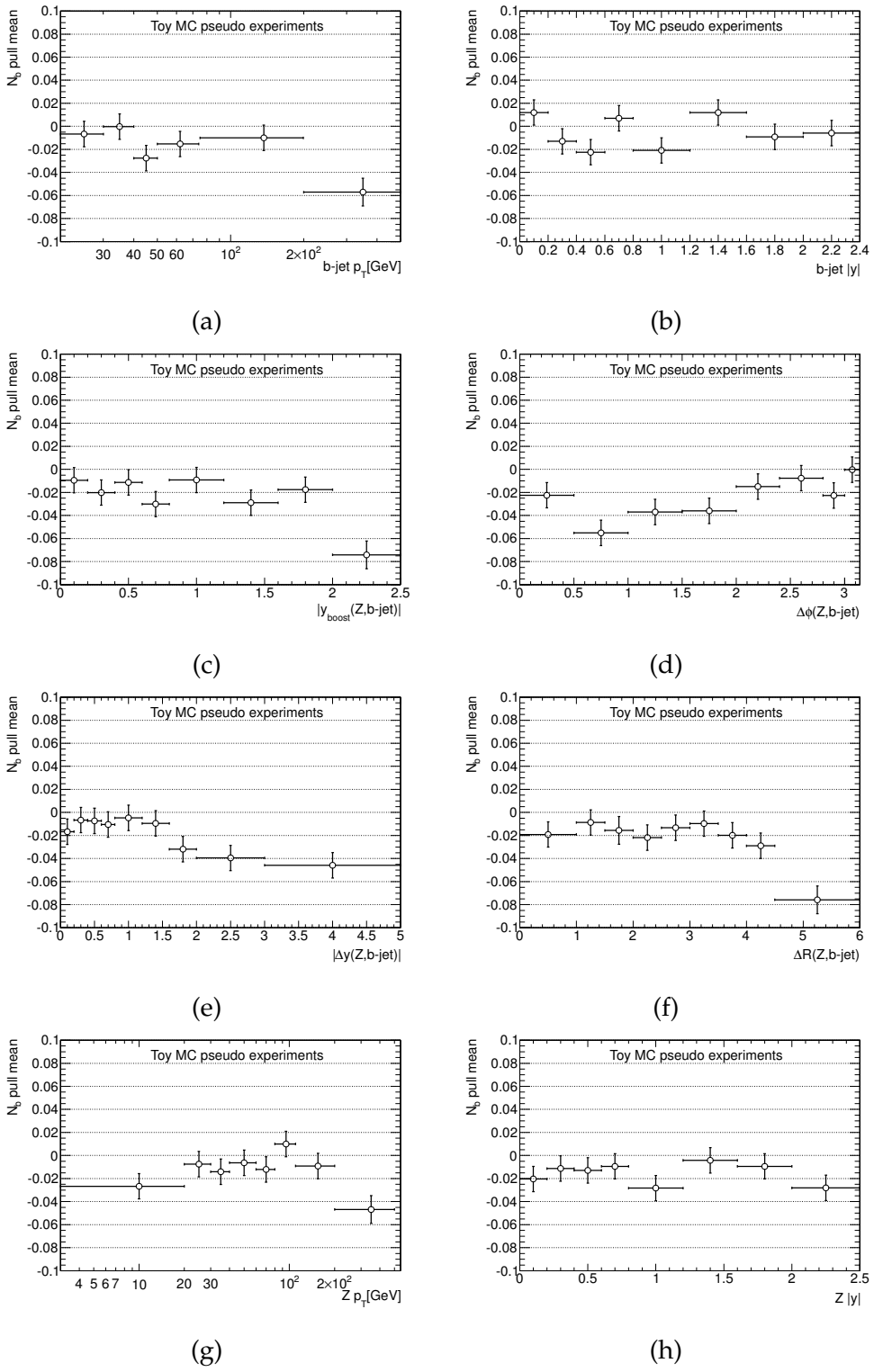

Figure 53: Pull mean as a function of the b–jet p_T (a), b–jet |y| (b), $|y_{boost}(Z,b\text{–jet})|$ (c), $\Delta\phi$(Z,b–jet) (d), $|\Delta y(Z,b\text{–jet})|$ (e), ΔR(Z,b–jet) (f), Z p_T (g) and Z |y| (h).

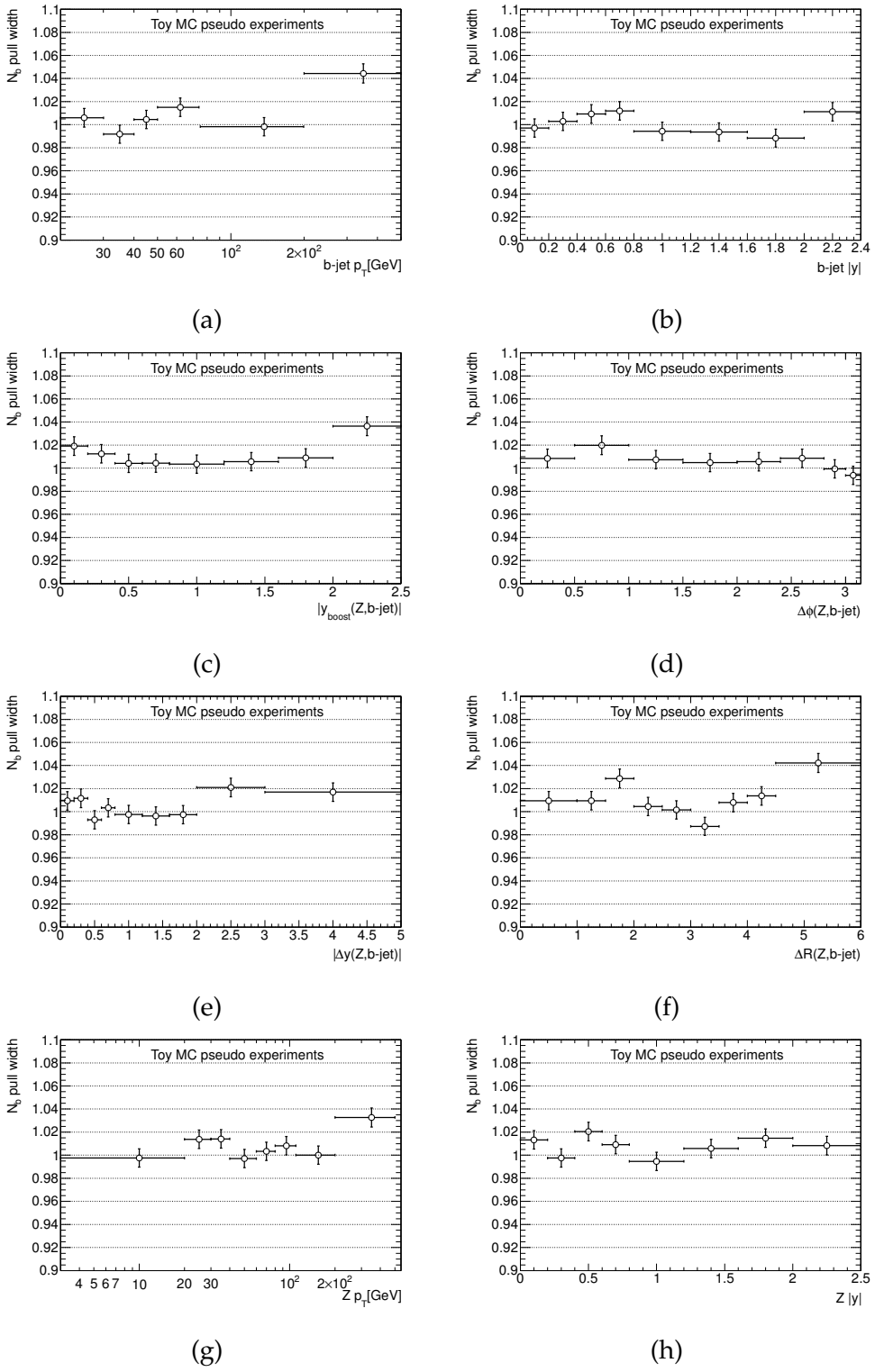

Figure 54: Pull width as a function of the b–jet p_T (a), b–jet $|y|$ (b), $|y_{boost}(Z,b\text{–jet})|$ (c), $\Delta\phi(Z,b\text{–jet})$ (d), $|\Delta y(Z,b\text{–jet})|$ (e), $\Delta R(Z,b\text{–jet})$ (f), Z p_T (g) and Z $|y|$ (h).

Sample	Post–fit N_b	Post–fit N_{c+l}	Pre–fit N_b	Pre–fit N_{c+l}
$N(Zb) \times N_{b\text{–jet}}$	18007 ± 206	29782 ± 230	12470	29002
$N^{\star}(Zb) \times N_{b\text{–jet}}$	15640 ± 188	23844 ± 205	10463	22855
$N(Zb)$	16607 ± 197	29090 ± 224	11414	28379

Table 20: Comparison of integrated detector level yields fitted in data and predicted by the ALPGEN+HERWIG+JIMMY generator at detector level normalized to the inclusive Z prediction at NNLO in QCD as described in Sec. 4.2.2.

Distribution	NDOF	χ^2		p–value	
		Z+non b	Z+b	Z+non b	Z+b
jet p_T	5	0.52	0.43	0.99	0.99
jet $\lvert y \rvert$	8	11.85	24.36	0.11	10^{-3}
$\lvert y_{boost}(Z, jet) \rvert$	8	7.85	30.31	0.35	10^{-4}
$\lvert \Delta y(Z, jet) \rvert$	9	77.06	16.80	10^{-13}	0.03
$\Delta\phi(Z, jet)$	8	29.79	37.56	10^{-4}	10^{-6}
$\Delta R(Z, jet)$	9	35.64	40.87	10^{-5}	10^{-6}
Z p_T	8	2.84	7.32	0.90	0.40
Z $\lvert y \rvert$	8	0.95	6.35	1.00	0.50

Table 21: χ^2 compatibility test between the measured b and $c + l$ (also referred to as "Z+non b") yields in data and the ALPGEN predictions at detector level for all the measured differential distributions.

uncertainty on the fitted yields in data. This test is expected to be approximate because it does not take into account all the systematic uncertainties uncorrelated or not fully correlated among the analysis bins and between the data and the ALPGEN calculation.

The results are summarized in Tab. 21 by the χ^2 and the p–value of each test.

For the Z+b yields the most inclusive observables, Z p_T and Z $\lvert y \rvert$, are typically well described by the predictions and the χ^2 test provides a p–value of 40% and 50% respectively; the same conclusions hold for the b–jet p_T ; the angular correlations between the Z boson and the b–jet ($\Delta\phi(Z, b)$, $\lvert \Delta y(Z, b) \rvert$ and $\lvert \Delta R(Z, b) \rvert$) and $\lvert y_{boost}(Z, b) \rvert$ show a rather large disagreement between tha data and the calculations; the p–value can be as small as 10^{-6}.

The measured charm plus light ($c + l$) jet yields are well described by the simulation, better than the corresponding Z+b distributions; the only exceptions are $\lvert \Delta y(Z, c + l) \rvert$, $\Delta\phi(Z, c + l)$ and $\Delta R(Z, c + l)$ which are inconsistent between data and simulation.

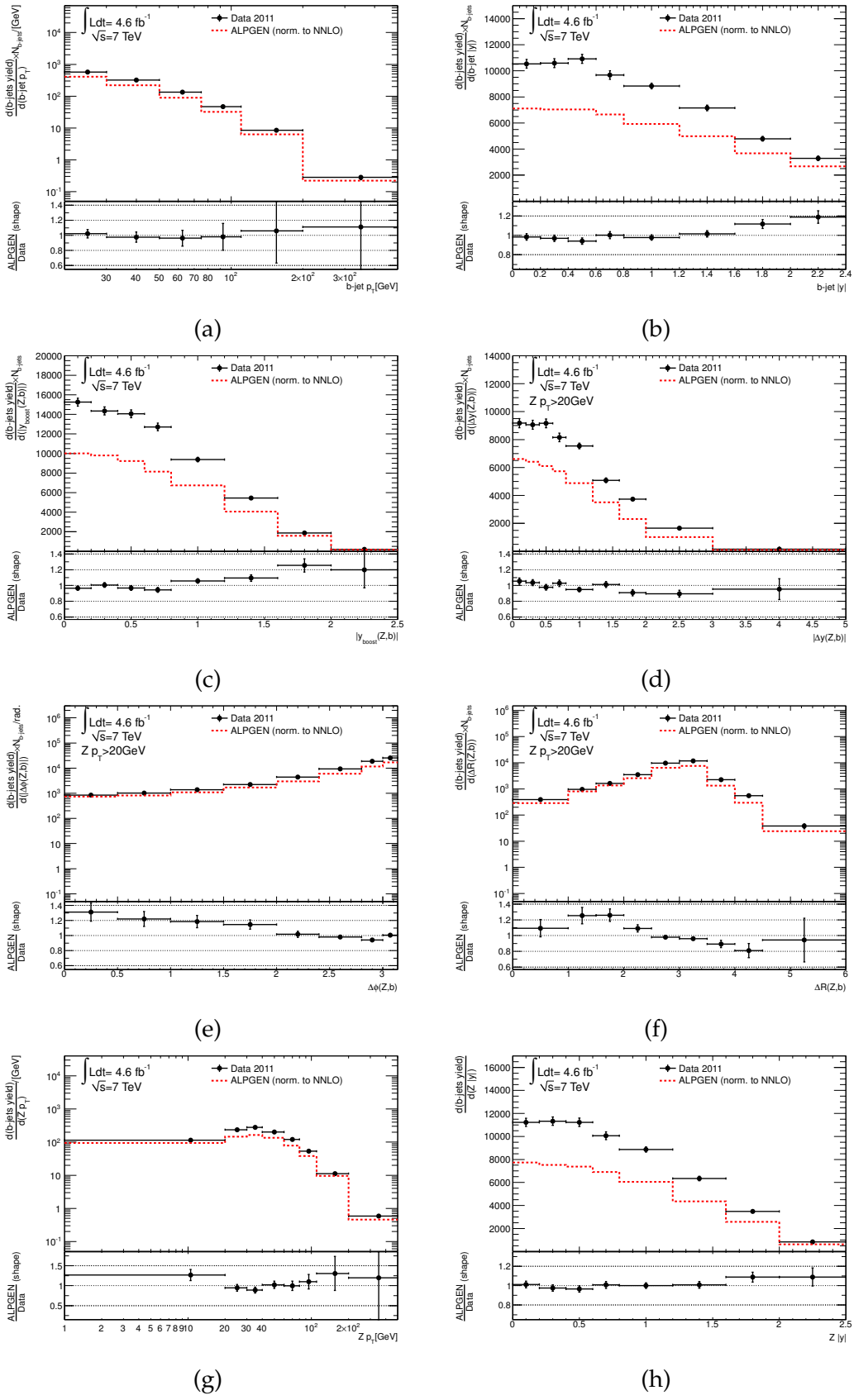

(a) (b) (c) (d) (e) (f) (g) (h)

Figure 55: B–jet yields. Distribution of the detector level yields as a function of the variables b–jet p_T(a), b–jet |y| (b), $|y_{boost}(Z,b)|$ (c), $|\Delta y(Z,b)|$ (d), $\Delta\phi(Z,b)$ (e), $\Delta R(Z,b)$ (f), Z p_T (g) and Z |y| (h). The reconstructed level data (points) are compared to the ALPGEN model (dashed line). Only the statistical uncertainty on the data points is shown here.

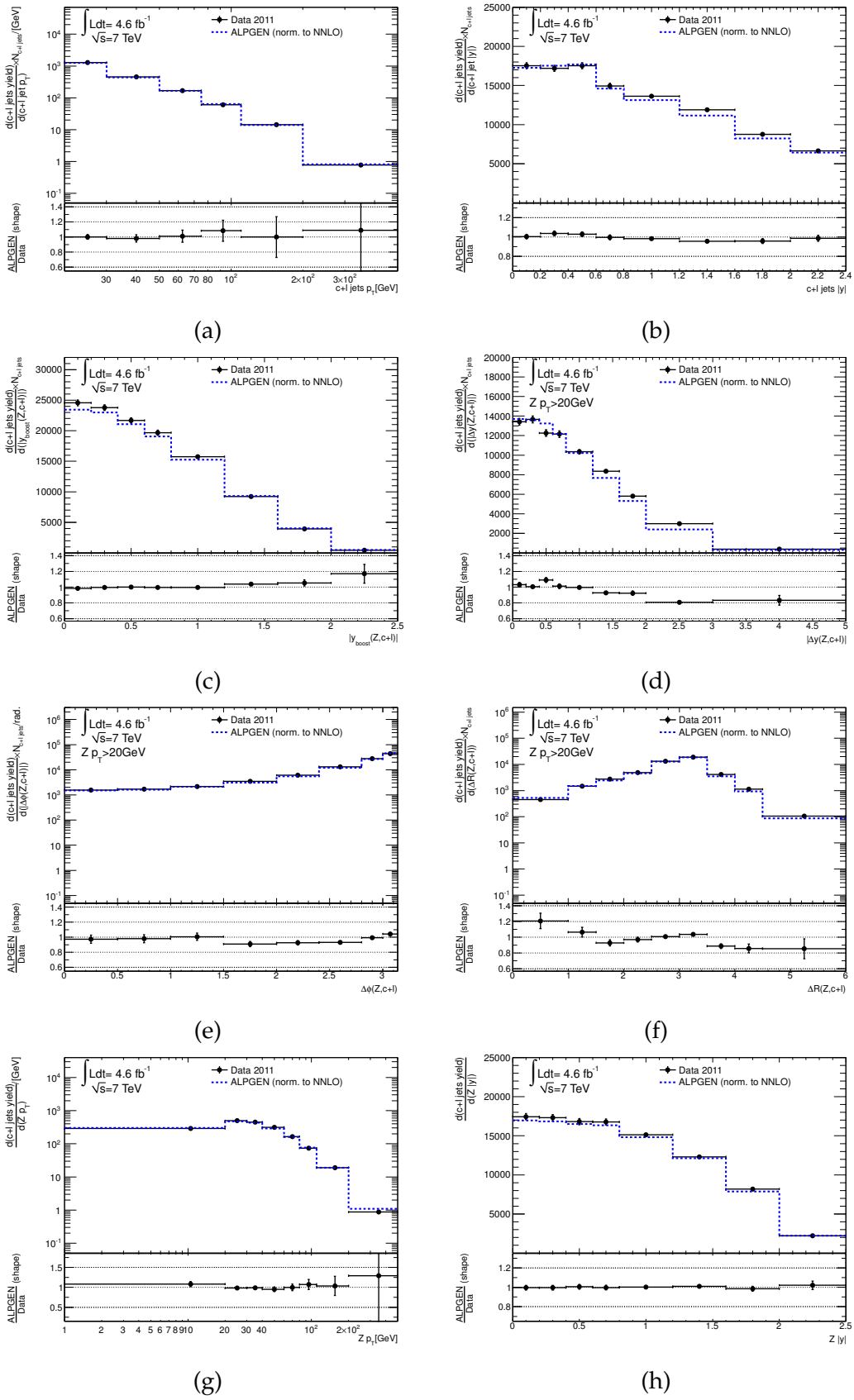

Figure 56: Charm plus light jets yields. Distribution of the detector level yields as a function of the variables $c + l$–jet p_T(a), $c + l$–jet $|y|$ (b), $|y_{boost}(Z, c + l)|$ (c), $|\Delta y(Z, c + l)|$ (d), $\Delta\phi(Z, c + l)$ (e), $\Delta R(Z, c + l)$ (f), Z p_T (g) and Z $|y|$ (h). The reconstructed level data (points) are compared to the ALPGEN model (dashed line). Only the statistical uncertainty on the data points is shown.

5

CROSS SECTION MEASUREMENT AND SYSTEMATIC UNCERTAINTIES

The analysis described in Chap. 4 lead to the selection of events with a Z decaying into muon or electron pairs and at least one b–jet reconstructed in the ATLAS detector. Several differential distributions of events and jet properties have been extracted from data and compared with the reference MC samples of the signal simulation.

Here the steps leading to the derivation of integrated and differential cross section measurements corresponding to jet or event yields selected in the analysis are described.

The notation that will be used for the various cross sections is reminded here and summarized in Tab. 22[1]:

- $\sigma(Zb) \times N_{b\text{–jet}}$, the cross section for b-jet produced in association with a Z boson; this is measured also as a function of b–jet p_T, b–jet $|y|$ and $|y_{boost}(Z, b\text{–jet})|$;
- $\sigma^{\star}(Zb) \times N_{b\text{–jet}}$, the cross section for b-jet produced in association with a Z boson of transverse momentum $p_T \geqslant 20$ GeV; the corresponding differential cross sections are functions of $|\Delta y(Z, b\text{–jet})|$, $\Delta\phi(Z, b\text{–jet})$ and $\Delta R(Z, b\text{–jet})$;
- $\sigma(Zb)$, the cross section for the production of events with at least one b–jet in association with a Z boson; the corresponding differential cross sections are functions of Z p_T and Z $|y|$.

The precise definition of the particle leve cross section that is measured is described in Sec. 5.1; the procedure to correct for detector effects the data yields resulting from the selection is presented in Sec. 5.2. The results of the integrated cross sections are presented in Sec. 5.3.

The systematic uncertainties of the measurements are presented in Sec. 5.4.

5.1 PARTICLE LEVEL SIGNAL DEFINITION

The result of the Z+b selection at detector level must be corrected for detector effects in order compare the data to theory predictions not interfaced with a detector simulation. This approach allows also to compare the measurements with theory predictions which will be available in the future and with other experimental results.

The existing generators are capable to predict the final state of the primary interaction up to the level of stable hadrons, leptons and photons. In order to reduce the model dependence and systematic uncertainties in the data–theory comparison, these truth particles are clustered into jets, dressed leptons and isolated photons according to procedures similar to the reconstruction algorithms adopted in the experiments.

1 The binning used for the particle level analysis is the same introduced in Sec. 4.1.

Distribution	Description	Input yields	Range
b–jet p_T[GeV]	-	$N(Zb) \times N_{b\text{–jet}}$	$[20, 500]$
b–jet $\lvert y \rvert$	-	$N(Zb) \times N_{b\text{–jet}}$	$[0, 2.4]$
$\lvert y_{boost}(Z, b) \rvert$	$\left\lvert \frac{b\text{–jet}\lvert y \rvert + Z\lvert y \rvert}{2} \right\rvert$	$N(Zb) \times N_{b\text{–jet}}$	$[0.0, 2.5]$
$\lvert \Delta y(Z, b) \rvert$	$\lvert b\text{–jet}\lvert y \rvert - Z\lvert y \rvert \rvert$	$N^{\star}(Zb) \times N_{b\text{–jet}}$	$[0.0, 5.0]$
$\Delta\phi(Z, b)$[rad]	-	$N^{\star}(Zb) \times N_{b\text{–jet}}$	$[0, \pi]$
$\Delta R(Z, b)$	$\sqrt{\Delta y(Z, b)^2 + \Delta\phi(Z, b)^2}$	$N^{\star}(Zb) \times N_{b\text{–jet}}$	$[0, 6]$
Z p_T[GeV]	-	$N(Zb)$	$[0, 500]$
Z $\lvert y \rvert$	-	$N(Zb)$	$[0.0, 2.5]$

Table 22: Summary of the measured differential distributions; the detector level yields used as input and the range are also provided.

Theory predictions formulated in terms of complex physics objects (jets, dressed leptons and isolated photons) built out of the final state particles (hadrons, leptons and photons) are referred to as *particle level predictions*. On the other hand, in the simulations used by the experiments the complete set of particles in the final state are injected into a GEANT4 based simulation for a detailed emulation of the response of the experimental apparatus to them. The simulation can then be used to correlate particle level observables to reconstruction level observables built from simulated tracks and energy clusters as in the case of data. The situation is represented schematically in Fig. 57.

The *unfolding procedure* consists in converting the reconstructed observables in data into the particle level observables by reverting the detector response emulated in the simulation.

Several studies performed in the past years [118] have been used as starting point to guide the $Z + b$ signal definition at particle level.

The signal is defined in a fiducial kinematic region with the aim of avoiding large extrapolations from the detector acceptance to the entire phase space. The cuts defining the fiducial cross section are given in Tab. 23; they are applied to leptons and b–jets defined at particle level as described in the following.

Leptons. Leptons (electrons and muons) produced in $Z \to \ell\ell$ decays are *dressed* with photon radiation produced in a cone $\Delta R(\ell, \gamma) < 0.1$ around them; this procedure corresponds to the redefinition of the lepton four–momentum according to the relation

$$p_\ell^{(dressed)} = p_\ell^{(bare)} + \sum_\gamma p^{(\gamma)} \quad , \quad \{\gamma \,|\Delta R(\gamma, \ell) < 0.1\}, \tag{36}$$

where $p_\ell^{(bare)}$ is the four–momentum of the lepton after QED final state radiation and $p_\ell^{(dressed)}$ is the four–momentum which defines the lepton kinematics at particle level.

Z boson. The candidate Z boson four–momentum is defined by adding the four–momentum of the (dressed) selected leptons; in events with more than

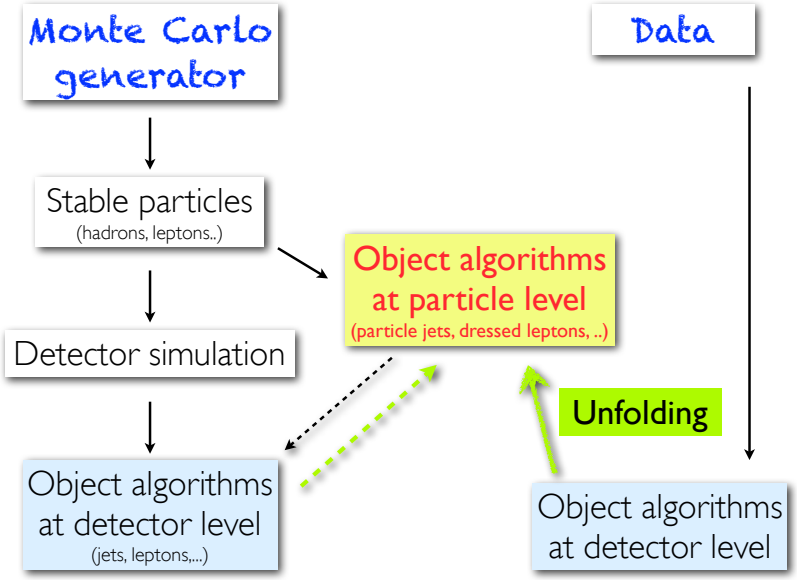

Figure 57: A schematic representation of the building blocks entering in the unfolding procedure.

Selection	Description
Lepton dressing	Dressed leptons are constructed using all photons in a cone $\Delta R < 0.1$ around any stable (status=1) muon or electron.
Lepton selection	The two highest p_T dressed, same flavor leptons are then used. They are required to have $p_T > 20$ GeV, $\|\eta\| < 2.5$, be opposite charge and have a dilepton mass $76 < M[\text{GeV}] < 106$. Z p_T> 20 GeV when measuring the angular correlations $\Delta\phi(Z, b)$, $\|\Delta y(Z, b)\|$ and $\Delta R(Z, b)$.
Jet Selection	All other stable particles (including muons and neutrinos) are passed to the jet finder (the Antikt4TruthWZ collection is used). Jets are required to have $p_T > 20$ GeV and $\|y\| < 2.4$. Any jets within $\Delta R < 0.5$ of a signal lepton are discarded.
Jet flavor	Jets matched to a weakly-decaying b-hadron with $p_T > 5$ GeV based on a simple $\Delta R < 0.3$ matching are labelled as b–jets. If no b–hadron is found, the same criteria are applied using charm quarks. If still no match is found, the jet is labelled as a light flavor jet. When constructing jet observables (e.g., $\Delta R(b, b)$), the two leading b-jets are used.

Table 23: Object and event selection criteria used for particle level events.

Meson	Valence quarks	Lifetime [ps]	PdgID
B^0	$d\bar{b}$	1.5	511
B^+	$u\bar{b}$	1.6	521
B_s^0	$s\bar{b}$	1.5	531
B_c^+	$c\bar{b}$	0.5	541

Baryon	Valence quarks	Lifetime [ps]	PdgID
Σ_b^-	-	-	5112
Λ_b^0	udb	1.4	5122
Ξ_b^-	dsb	1.56	5132
Ξ_{bc}^0	-	1.49	5142
Σ_b^0	-	-	5212
Σ_b^+	-	-	5222
Ξ_b^0	usb	1.49	5232
Ξ_{bc}^+	-	-	5242
Ω_b^-	ssb	1.1	5332

Table 24: Stable b-hadrons used in the particle level b-jet definition reported along with their lifetime, the particle data group identifier PdgID as well as the quark composition as predicted by the quark model.

two selected leptons the two with the leading p_T are used. Consistently with the detector level analysis, the Z boson transverse momentum is required to be greater than 20 GeV when $\Delta\phi(Z, b)$ is measured. This cut ensures that the Z boson has a well defined ϕ coordinate determination; the same cut is also applied for the $\Delta R(Z, b)$ and, for consistency, for the $|\Delta y(Z, b)|$ measurements.

Jets. Jets are defined by the anti–k_t clustering algorithm with radius 0.4 using as input all particles with lifetime $\tau > 15$ ps including leptons and neutrinos. Ambiguities from overlapping leptons and jets are resolved, like for the detector level analysis, by requiring $\Delta R(\ell, jet) > 0.5$.

Jet flavor. A b–jet is defined as a particle level jet which matches a weakly decaying b–hadron (B) with $p_T > 5$ GeV based on a simple angular matching criterion $\Delta R(jet, B) < 0.3$. The list of weakly decaying b–hadrons is provided in Tab. 24 along with the b–hadron lifetime from [5], quark composition (as predicted by the quark model) and the Particle–data–group identifier (PdgID).

Other lepton definitions at particle level have been studied, including the *born lepton* whose four–momentum, $p_\ell^{(born)}$, is defined before any QED final state radiation:

$$p_\ell^{(born)} = p_\ell^{(bare)} + \sum_\gamma p^{(\gamma)} \,. \tag{37}$$

A comparison of the different lepton definitions is summarized in Tab. 25, where the ratios of the number of particle level Z+b events selected in a signal Monte Carlo sample using the born, the dressed and the bare lepton definitions are reported as a function of the Z p_T; the ratios are provided separately for the electron and muon channels as well as for the channel combination.

The three lepton definitions differ in terms of total number of selected events by a few percents; in the electron channel the differences between bare and dressed is of the order of 6% but it reaches values larger than 10% at high p_T; in the muon channel, due to the larger muon mass, the differences between bare and dressed leptons are very much suppressed being below 4% for Z p_T as large as 500 GeV. For the dressed leptons instead this ratio is slightly more than 2% and it is almost independent of the lepton kinematics. More detailed studies have been reported in [115].

Bins	e-channel		μ-channel		e-μ combined	
Z p_T [GeV]	Dressed/Bare	Dressed/Born	Dressed/Bare	Dressed/Born	Dressed/Bare	Dressed/Born
(0,20)	1.041 ± 0.010	0.976 ± 0.010	1.013 ± 0.010	0.974 ± 0.011	1.027 ± 0.007	0.975 ± 0.007
(20,30)	1.044 ± 0.008	0.978 ± 0.008	1.013 ± 0.009	0.977 ± 0.009	1.029 ± 0.006	0.978 ± 0.006
(30,40)	1.058 ± 0.007	0.976 ± 0.008	1.016 ± 0.008	0.975 ± 0.008	1.037 ± 0.005	0.975 ± 0.006
(40,60)	1.057 ± 0.006	0.977 ± 0.006	1.021 ± 0.006	0.974 ± 0.006	1.039 ± 0.004	0.975 ± 0.004
(60,80)	1.079 ± 0.008	0.972 ± 0.008	1.026 ± 0.008	0.969 ± 0.009	1.052 ± 0.006	0.970 ± 0.006
(80,110)	1.075 ± 0.009	0.968 ± 0.010	1.029 ± 0.010	0.967 ± 0.011	1.051 ± 0.007	0.967 ± 0.007
(110,200)	1.087 ± 0.011	0.973 ± 0.011	1.033 ± 0.013	0.971 ± 0.013	1.059 ± 0.008	0.972 ± 0.009
(200,500)	1.121 ± 0.027	0.969 ± 0.030	1.029 ± 0.033	0.961 ± 0.035	1.074 ± 0.021	0.965 ± 0.022

Table 25: QED FSR corrections for the $Z + b$ selection as a function of the Z transverse momentum as predicted by ALPGEN .

5.2 UNFOLDING THE DETECTOR EFFECTS

Given a binned measured distribution it is possible to transform it into a particle level distribution by subtracting the contamination of *fake* signal events, dividing the yields by the efficiency and correcting for bin migration induced by resolution effects. The determined observable is thus free from detector effects. The same procedure, with the exception of the bin migration correction, is applied for the measurement of an integrated cross section. Contamination from fake signal, efficiency and bin to bin migration probabilities are estimated with high statistics signal simulated samples. In this analysis the signal Monte Carlo sample ALPGEN+HERWIG+JIMMY is used (Tab. 40 in App. B). The simulated events are processed to check at the same time if they pass a truth–based particle level selection, corresponding to the signal definition, and the data–like reconstruction level selection. Particle level physics objects are then correlated to detector level reconstructed objects.

Jets passing the detector level selection and tagged as b–jets are considered true b–jets if they satisfy the same matching criterion with weakly decaying b–hadrons applied to particle level b–jets.

Jets selected at detector level are *matched* to the particle level jets by requiring $\Delta R(\mathrm{jet}^{\mathrm{particle}}, \mathrm{jet}^{\mathrm{detector}}) < 0.4$. For event based observables this *reco–to–particle* jet matching applies to leading p_T b–tagged jet which is required to match a particle level b–jet.

The fake contamination originates because truth level objects migrate from outside the fiducial region into the fiducial region at reconstruction level. This is due to resolution effects and inefficiencies in the reco–to–truth matching; therefore the fake signal has to be subtracted from the detector level yield. The fake rate is defined as

$$\text{Fake rate: } f = \frac{N(\mathrm{reco\text{–}all}) - N(\mathrm{reco\text{–}match})}{N(\mathrm{reco\text{–}all})} , \tag{38}$$

where $N(\mathrm{reco\text{–}all})$ is the total number of reconstructed objects and $N(\mathrm{reco\text{–}match})$ is the number of objects reconstructed and matching a particle level object.

The so called fake correction is introduced as a multiplicative correction to the detector level yields, called *purity*, and defined as

$$\text{Purity: } P = \frac{N(\mathrm{reco\text{–}match})}{N(\mathrm{reco\text{–}all})} = 1 - f . \tag{39}$$

The detector level efficiency is taken into account from the unfolding procedure with a correction estimated as *truth efficiency*, estimated with the MC signal samples, which is defined as

$$\varepsilon = \frac{N(\mathrm{truth\text{–}match})}{N(\mathrm{truth\text{–}all})} , \tag{40}$$

where $N(\mathrm{truth\text{–}match})$ is the number of particle level objects matched to detector level objects and $N(\mathrm{truth\text{–}all})$ is the total yield selected at particle level.

The correction factors $C(Zb \times N_{\text{b–jet}})$, $C^{\star}(Zb \times N_{\text{b–jet}})$ and $C(Zb)$, used to determine the integrated cross sections, combine the corrections for detector efficiency with respect to the truth and the fake contamination at detector level:

$$C(Zb \times N_{\text{b–jet}}) = \varepsilon^{-1}_{Zb \times N_{\text{b–jet}}}(\mathrm{truth}) \times P_{Zb \times N_{\text{b–jet}}} , \tag{41}$$

$$C(Zb \times N^{\star}_{\text{b–jet}}) = \varepsilon^{-1}_{Zb \times N^{\star}_{\text{b–jet}}}(\mathrm{truth}) \times P_{Zb \times N^{\star}_{\text{b–jet}}} , \tag{42}$$

$$C(Zb) = \varepsilon^{-1}_{Zb}(\mathrm{truth}) \times P_{Zb} . \tag{43}$$

$$\tag{44}$$

The breakdown of the correction factors in terms of truth efficiency and purity is shown in Tab. 26, separately for the electron channel, the muon channel and for their combination. The truth efficiencies in the electron channel are observed to be smaller than the efficiencies in the muon channel by 10%; for the electron channel they vary between 28.40% and 29.86%, while in the muon channel between 38.69% and 40.08%; the large efficiencies are observed in the $Zb \times N^{\star}_{\text{b–jet}}$ selection where a harder p_T spectrum for the signal jets is expected. The purities are consistent

	e-channel		μ-channel		e-μ combined	
C	ε[%]	P[%]	ε[%]	P[%]	ε[%]	P[%]
$C(Zb \times N_{b\text{–jet}})$	28.40	92.10	38.69	91.89	33.54	91.98
$C(Zb \times N^{\star}_{b\text{–jet}})$	29.86	93.48	40.49	93.45	35.16	93.46
$C(Zb)$	29.33	92.38	40.08	92.08	34.69	92.21

Table 26: Breakdown of the correction factors in terms of truth efficiency and purity for the electron channel, the muon channel and their combination.

among the leptonic channels with values around 93.5% in the $Zb \times N^{\star}_{b\text{–jet}}$ selection while they are slightly lower for the $Zb \times N_{b\text{–jet}}$ and Zb signal definitions, but greater than 90%.

The procedure used to unfold detector effects for the differential b–yields is based on the Bayesian unfolding algorithm [119] of the RooUnfold [120] implementation available with the Root framework.

In the Bayesian approach the detector level results are corrected to particle level by constructing with the Monte Carlo signal simulation a set of prior probability densities and conditional probabilities of observing detector yields given the predicted truth yields in the simulated sample. The prior is defined as the truth particle level prediction. The conditional probabilities are defined based on a *generalized efficiency* for each analysis bin k, computed as the product $\varepsilon\, P^{-1}$ as discussed previously, and a *migration matrix*, which defines the probability to have a particle level object, belonging to a given bin i, reconstructed in a bin j, for all combinations of i and j.

The detector level yields are effectively migrated from the reco bins to the truth bins according to the migration probabilities stored in the migration matrices. The efficiency corrections are then applied to the migrated yields. Before correcting for the migration and efficiency effects with the unfolding procedure, the detector level b–yields are modified according with the fake correction as described for the integrated cross sections.

The statistical uncertainty on a specific unfolded bin is calculated according with the statistical uncertainty of the detector level bin and taking into account the bin to bin correlation introduced by the migration effects from truth level to detector level bins.

The migration matrices of each differential distribution are shown in Fig. 58 normalized to the corresponding total number of reconstructed true and matched objects.

The bin by bin migration is observed to be very small for all the studied distributions with the exception of the b–jet p_T, where the first bin presents a substantial migration, up to $\sim 25\%$ of the particle level jets migrating toward the second bin of reconstructed p_T; the Z p_T exhibits a maximum migration of about $\sim 6\%$ while for all the other observables the migration is typically below 5%.

The purity for all the analysis bins is shown in Fig. 59; it is typically above 90% with some exceptions, like the first b–jet p_T bin where it falls below 80%, but suddenly increases above 95% already in the second bin; a similar raise in the purity,

but less pronounced, is observed for the Z p_T while for the other distributions the purity is in general more uniform across the bins.

The efficiency in all the analysis bins is shown in Fig. 60 for the channel combination. It reaches a plateau at ~ 45% for Z $p_T >$ 100 GeV like also observed for the b–jet p_T distribution; the truth efficiency can be as low as 25% as in the last Z $|y|$ bin, because the truth level extrapolation on the lepton pseudorapidity, and this effect is also observed in the other angular distributions which are correlated with the Z $|y|$.

5.3 INTEGRATED CROSS SECTION

The fit results converted into particle level yields, as described in Sec. 5.2, and corrected with the measured integrated luminosity [121] $\int Ldt = 4.6\ fb^{-1}$, for the 2011 data taking, are used to determine the integrated cross sections:

$$\sigma(Zb \times N_{b\text{–jet}}) = \frac{C(Zb \times N_{b\text{–jet}})}{\int Ldt} N(Zb \times N_{b\text{–jet}}) , \quad (45)$$

$$\sigma(Zb \times N^{\star}_{b\text{–jet}}) = \frac{C(Zb \times N^{\star}_{b\text{–jet}})}{\int Ldt} N(Zb \times N^{\star}_{b\text{–jet}}) , \quad (46)$$

$$\sigma(Zb) = \frac{C(Zb)}{\int Ldt} N(Zb) , \quad (47)$$

$$(48)$$

by using the detector level yields $N(Zb \times N_{b\text{–jet}})$, $N(Zb \times N^{\star}_{b\text{–jet}})$ and $N(Zb)$ of Tab. 20 and the correction factors of Tab. 26.

The results for the integrated cross sections are reported in Tab. 27 including the statistical uncertainties; they are shown separately for the leptonic channels and for their combination. The two leptonic channels in the per–jet cross sections are statistically consistent within 1.6–1.7 statistical standard deviations while the per–event cross section are different by 2.2 standard deviations. However, a more significant comparison among the channels would require the inclusions of the uncorrelated systematic uncertainties which are not taken into account here and are introduced in Sec. 5.4.

σ[pb]	e–channel	μ–channel	e–μ combined
$\sigma(Zb \times N_{b\text{–jet}})$	5.51 ± 0.10	5.30 ± 0.081	5.39 ± 0.06
$\sigma^{\star}(Zb \times N_{b\text{–jet}})$	4.64 ± 0.08	4.46 ± 0.07	4.54 ± 0.054
$\sigma(Zb)$	4.96 ± 0.09	4.71 ± 0.07	4.82 ± 0.06

Table 27: Integrated Z+b cross sections shown separately for the electron channel, muon channel and their combination.

The results of the differential cross sections are shown in Chap. 6 along with a discussion of the comparison with the theory predictions.

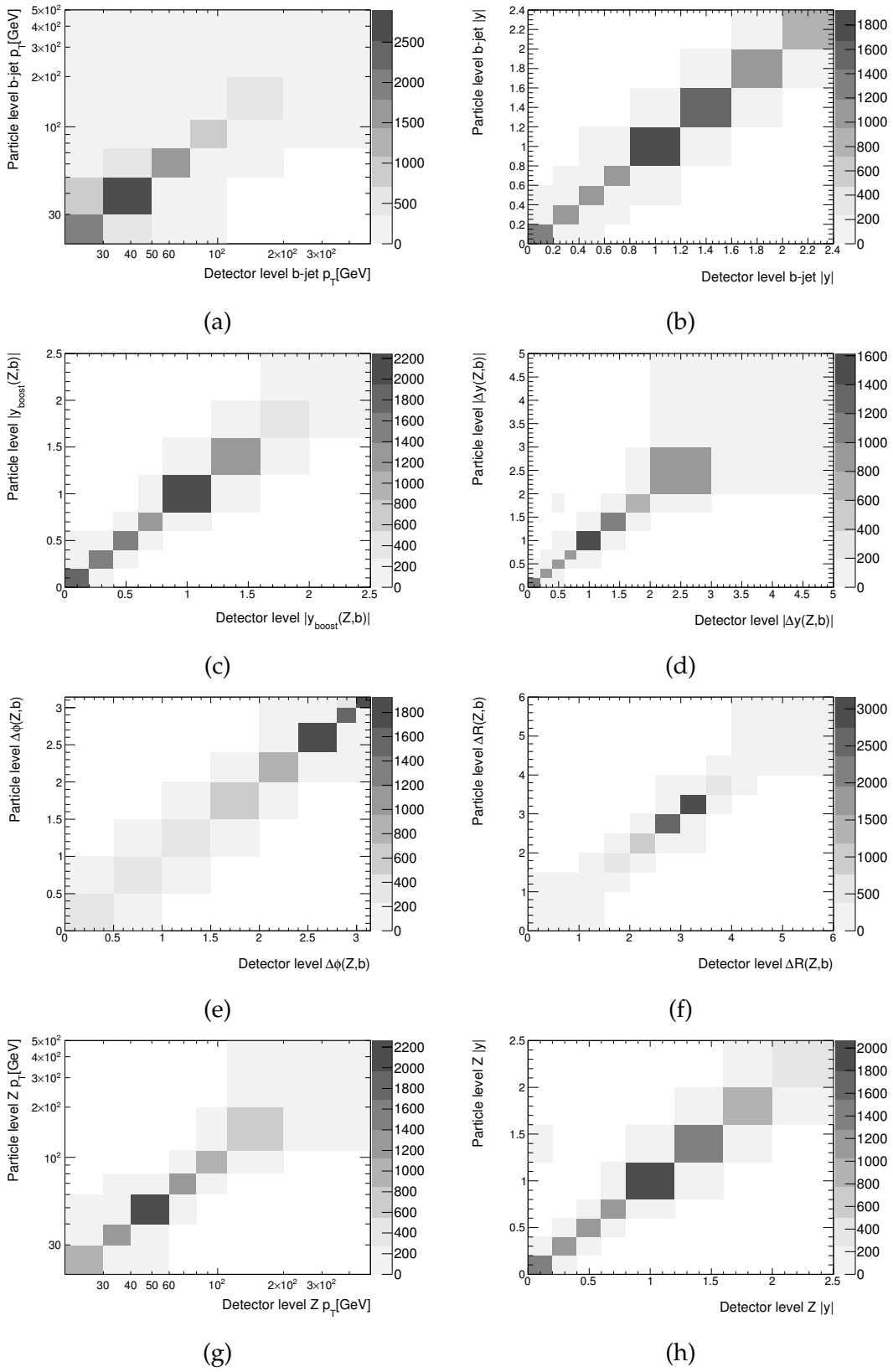

Figure 58: Migration matrices of the distribution of the b–jet p_T (a), b–jet |y| (b), $y_{boost}(Z,b)$ (c), $|\Delta y(Z,b)|$ (d), $\Delta\phi(Z,b)$ (e), $\Delta R(Z,b)$ (f), Z p_T (g) and Z |y| (h).

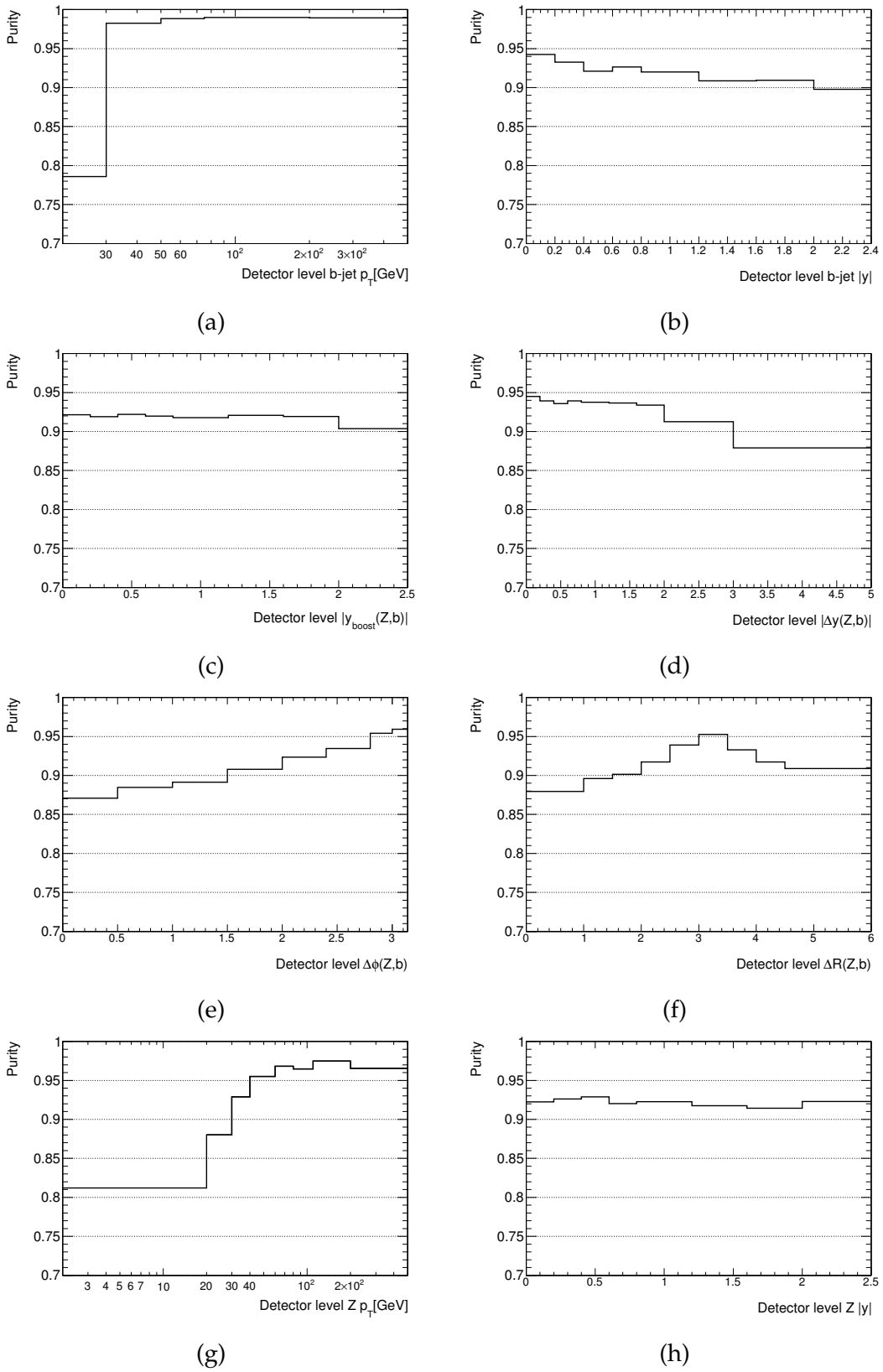

Figure 59: Purity of the distribution of the b–jet p_T (a), b–jet $|y|$ (b), $y_{boost}(Z,b)$ (c), $|\Delta y(Z,b)|$ (d), $\Delta\phi(Z,b)$ (e), $\Delta R(Z,b)$ (f), Z p_T (g) and Z $|y|$ (h).

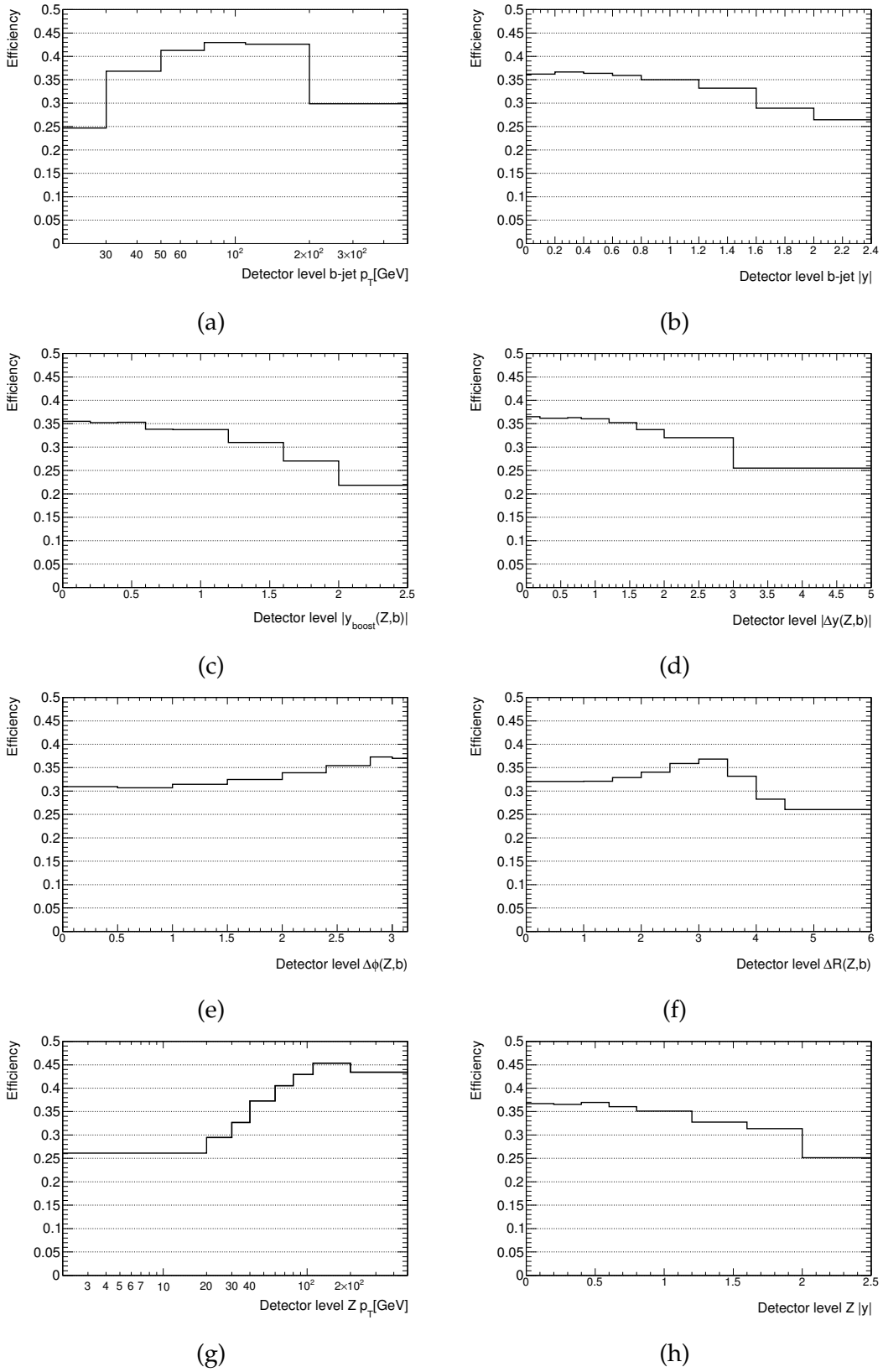

Figure 60: Truth efficiency of the distribution of the b–jet p_T (a), b–jet $|y|$ (b), $y_{boost}(Z,b)$ (c), $|\Delta y(Z,b)|$ (d), $\Delta\phi(Z,b)$ (e), $\Delta R(Z,b)$ (f), Z p_T (g) and Z $|y|$ (h).

5.4 SYSTEMATIC UNCERTAINTIES

Systematic effects can lead to uncertainties on the detector level signal yield extraction as well as on the unfolding and can affect both experimental procedures in a correlated way. The biggest uncertainties arise from the b–jet CombNNc template shape modeling, b–tagging efficiency and jet energy scale uncertainties. The main systematic uncertainty sources are listed in Tab. 28 indicating whether the uncertainty affects the fit, the unfolding or both; a special treatment is needed for the E_T^{miss} calculation which is correlated with all other physics objects, therefore the effects of its variation has to be considered for each systematics affecting the kinematic of leptons and jets.

Source	Affect the fit	Affect the unfolding
Template shapes	✓	✗
b–tagging efficiency	✓	✓
jet energy scale and resolution	✓	✓
Underlying physics model	✓	✓
Lepton ID and trigger	✗	✓
Monte Carlo statistic	✓	✓

Table 28: Short list of the systematic effects on the $Z + b$ cross section measurements indicating whether the systematic uncertainties affect the signal fit, the unfolding or both.

In the following subsections all the studied uncertainties are presented and their effect is discussed.

5.4.1 *Template shapes uncertainty*

As described in Chap. 4 the fit procedure used to extract the signal yield at detector level is sensitive to the modeling of the b–hadron decay properties which are used by the JetFitterCombNN algorithm; as discussed in Sec. 4.5 the nominal signal Monte Carlo sample is reweighted according to the track multiplicity of b–hadron decay chains as predicted by the EvtGen generator which is expected to provide the best available description of b–hadron decays.

An alternative reweighting of the signal MC samples is obtained from data using a control sample dominated by $t\bar{t}$, which is expected to provide a b–jet purity of about 90%.

The observed variation of the fitted b–yield when using the Alpgen+Herwig+Jimmy prediction for the CombNNc b–jet template corrected with this data driven reweighting function instead of using the default correction based on the EvtGen generator is found to be between 4.8% and 4.9% for the integrated cross sections. This difference, evaluated in each analysis bin, is assigned as systematic uncertainty due to the b–decay modeling; it is the dominant systematic uncertainties.

The modeling of light and charm jets templates is validated by comparing the nominal Monte Carlo generator Alpgen+Herwig+Jimmy with Sherpa. The two

generators are found to provide a similar description of the CombNNc for light and charm distributions; from this comparison two correction functions are derived and applied to the nominal light and charm jets templates. The effect of reweighting the charm and light jets templates is found to be typically smaller than 1% on the fitted b–yield leading to a negligible effect on the uncertainty affecting the measured cross sections.

5.4.2 *Effects of the Monte Carlo statistical fluctuation in the flavor fit*

The flavor templates used in the fit procedure is based on the assumption that flavor templates are not affected by statistical uncertainties. The finite statistics of the Monte Carlo simulation can actually lead to a small distortion of the CombNNc shapes, thus changing the fit results.

The effect of the finite Monte Carlo statistics is studied by using a toy–MC method. For each analysis bin 5000 pseudo experiments are generated; in each of them a new set of Monte Carlo templates is build by fluctuating the original CombNNc distributions, for both the light+charm and b–jets, according to the statistical uncertainty in each CombNNc bin; a Gaussian approximations is adopted for emulating the fluctuations in all the CombNNc bins. For each pseudo–experiment a fit to the original data with the distorted MC templates is performed and the number of fitted b–jets is stored. From this procedure the distribution of the fitted number b–jets in the pseudo experiments normalized to the nominal fit result, $N_b^{\mathrm{toy\,s.}}/N_b$, can be defined; it is expected to follow a Gaussian distribution with average 1 and with width as large as the relative statistical uncertainty due to the Monte Carlo statistics.

The resulting uncertainty is found to be around 0.35%–0.5% of the statistical uncertainty in the differential analysis bins as well as on the integrated cross sections.

5.4.3 *Effects of the Monte Carlo statistical fluctuation in the unfolding procedure*

In the derivation of the integrated and differential cross sections the procedure used to unfold the detector effects can be affected by the finite Monte Carlo sample size, either by a distortion of the migration matrix or via statistical errors on the efficiency and purity corrections. These effects are taken into account with a toy–MC ensemble test where the correlation between the simulated events used to built the migration matrix and the efficiency and purity corrections are taken into account by using a binomial statistics.

For a given differential distribution in each experiment, the particle level yield is modified by allowing the population of each bin, $N_i(\mathrm{truth\text{–}all})$, to be a value extracted from a Poisson distribution with mean equal to the original Monte Carlo prediction. Correspondingly, the population of each bin of the unfolding matrix, $M_{ij}^{(\mathrm{toy\,s.})}$, is defined by extracting it from a binomial distribution with number of trials equal to $N_i(\mathrm{truth\text{–}all})$ and success probability equal to the originally predicted efficiency $M_{ij}\varepsilon_i(\mathrm{truth})$ for reconstructing in a detector level bin j the objects belonging to bin i at truth level. Finally, the number of fake signal events or jets in a given analysis bin is extracted from a binomial distribution with number of trials equal to the expected number or reconstructed objects in that bin and suc-

cess probability equal to the fake signal rate predicted in the same bin. In each toy experiment the reconstruction level results in data have been processed with a simulated variation of efficiency, purity and migration matrix. For each bin of the unfolded distribution the ratio of the yield to the nominal result of the analysis is estimated and distributions of these ratios for all bins are produced. The distributions over 5000 pseudo experiments have a Gaussian behavior with mean equal to one and the sigma of the distribution is used as an estimate of systematic uncertainty from the MC statistics.

The derived systematic uncertainty due to the finite Monte Carlo statistics in the unfolding is found to be smaller than 0.9% for the integrated cross sections and to be smaller than a third of the statistical uncertainty for the differential bins.

5.4.4 *Model dependence*

The unfolding and the flavor fit are performed with the signal Monte Carlo simulation provided by ALPGEN+HERWIG+JIMMY event generator interfaced with the full detector simulation; thus, to some extended, the unfolded particle level yields retain some dependence on the underlying ALPGEN+HERWIG+JIMMY model. This *model dependence* is evaluated with the following checks:

- hard double parton interactions,
- gluon splitting,
- charm–light jets ratio,
- jet transverse momentum modeling,
- unfolding non closure;

they are described in the follow.

5.4.4.1 *Double parton interactions*

Jets from DPI are typically produced at high rapidity and have a softer transverse momentum spectrum compared to the jets coming from Z+jets events in single parton interactions. Accordingly, the uncertainty on the total DPI rate predicted by the simulation induces a variation of the b–jet kinematics in the simulation; this leads to a distortion of the CombNNc template, thus changing the fit results, and a modification of the truth efficiency, thus affecting the unfolding procedure.

The DPI rate in JIMMY is checked with a comparison using the ATLAS data coming from three previous measurements: the effective area parameter, σ_{eff} (Fig. 61 (a)), regulating the total hard double parton interactions rate [122], the inclusive Z boson cross section [37] and the b–jets cross section [123]. These three ingredients are connected with the Z+b DPI cross section according to the equation

$$\sigma(Z+b)_{DPI} = \frac{\sigma(Z)\cdot\sigma(b)}{\sigma_{eff}}\ ; \tag{49}$$

therefore, using the measured values of $\sigma(Z)$ and $\sigma(b)$ with suitable phase space extrapolations, the cross section of b–jets production in association with a Z boson

from DPI, $\sigma(Z+b)_{DPI}$, can be predicted. A comparison of this prediction with the cross section estimate based on the JIMMY generator is shown in Fig. 61 (b-e) from Ref. [115].

The DPI fraction in the ALPGEN+HERWIG+JIMMY calculation is varied by 50% as found necessary in order to cover the differences observed between the JIMMY DPI and the estimation provided by $\sigma(Z+b)_{DPI}$.

The uncertainty introduced by the DPI variation can be as large as 3% for the integrated cross section but it is found to be significantly smaller, 1.2%, for $\sigma^{\star}(Zb \times N_{b\text{–jet}})$ and increases up to $\sim 5\%$ at high b–jet rapidity.

5.4.4.2 *Gluon splitting*

B–quark pair production at small opening angle in the signal Monte Carlo is modeled by gluon splitting in $b\bar{b}$ in the parton shower evolution. It is poorly constrained with experimental data, thus is assumed to be known within a factor two. Correspondingly, it is scaled up and down in the simulation by a factor two in the fit and in the unfolding as it is expected to induce a distortion of the CombNNc templates and to change the truth efficiency.

The gluon splitting uncertainty is observed to be of order 1% and almost uniform across the analysis bins.

5.4.4.3 *Other checks*

As described in Sec. 4.5, the charm–light jet ratio in the simulated signal MC sample is an important input to the flavor fit procedure where the light and charm jet CombNNc templates are combined. This MC prediction is checked in data with a fit procedure capable in discriminating light and charm jets; the measured charm to light ratio is found to agree very well with the MC prediction (see Sec. 4.5), therefore no systematic uncertainties are assigned.

The CombNNc templates are correlated to the jet transverse momentum; for a reliable description of the templates, the jet transverse momentum has to be well described by the simulation. A reweighting procedure on the jet p_T distribution of the MC Z+jet sample is adopted based on a data–MC comparison for the selected candidate signal events. The reweighting leads to a small change on the jet p_T distribution, which is already well modeled by the simulation, and a negligible effect on the signal yield extraction, of order 10^{-5}. Based on this study, no additional systematic error is added to the analysis results.

A further cross check is performed by a particle level comparison of the ALPGEN+HERWIG+JIMMY predictions with SHERPA. The differences between the two generators are propagated through the detector level predictions of the simulated ALPGEN+HERWIG+JIMMY sample. This reweighted ALPGEN+HERWIG+JIMMY sample is then used to set–up a toy MC pseudo experiment, where the nominal detector level predictions of ALPGEN is unfolded by using the reweighted sample and it is compared to the nominal truth level predictions. The deviation of the unfolded MC yields compared to the nominal particle level predictions are used to infer the residual non closure effects on the measurement; typically this uncertainty is found to be of about 0.1%–0.3% but it reaches $\sim 3\%$ in the first b–jet p_T bin.

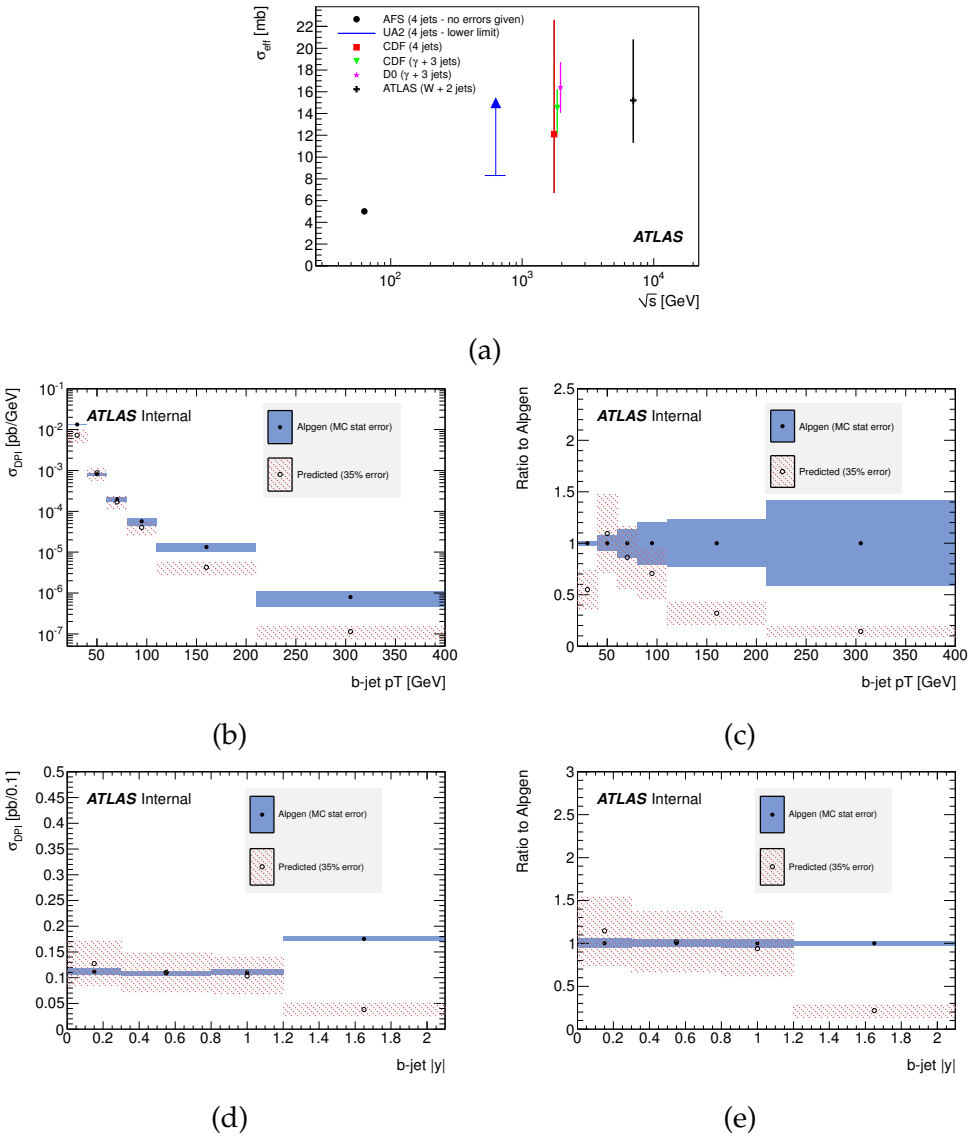

Figure 61: σ_{eff} [122] extracted in different processes and experiments (a) and comparison of the "predicted" DPI cross section, obtained by combining σ_{eff} and the ATLAS measurements [37] and [123], with the DPI cross section from the ALPGEN+HERWIG+JIMMY generator (b-e).

5.4.5 *Uncertainties from physics object reconstruction*

As widely discussed in Sec. 4.2.2, the simulated Monte Carlo sample is corrected for all the known detector mismodeling effects in order to reproduce the same physics object performance observed in data. Every mismodeling correction is known up to some uncertainty leading to biases in the estimated reconstruction efficiency as well as to distortion of the kinematics of simulated events altering the bin migration probabilities. These *object performance uncertainties* can affect the unfolding and the fit in a correlated way or can lead to variation of the unfolded yields only.

In the following sub–sections all the known uncertainties related to the physics object reconstruction in ATLAS are highlighted.

5.4.5.1 *Lepton identification and trigger*

As described in Sec. 4.2.2 the lepton reconstruction in the simulated samples is corrected to match the observed energy resolution and scale as well as to reproduce the identification efficiency measured in the data. Moreover, the data sample used in the analysis is selected online with single or dilepton triggers; therefore the emulation of the trigger efficiency in the MC samples must be corrected to reproduce the efficiency in data. All the studies used to constrain the lepton performances in the simulation are based on tag–and–probe methods as introduced in Sec. 2.3.

The systematic effects related to lepton reconstruction and trigger concern the unfolding only; specifically, they change the signal selection efficiency and induce variations on the nominal bin by bin migration. Thus for each systematic variation a new set of migration matrices, efficiencies and purities corrections are obtained for each distribution or for the integrated sample and the nominal signal yields are unfolded to particle level with the new set of matrices and corrections.

The upward and downward uncertainties on the electron energy resolution ($\texttt{EER}\uparrow$ and $\texttt{EER}\downarrow$) have a very small impact on the cross sections, typically of order $\sim 1‰$ or smaller, and are determined with a considerable statistical error. The electron energy scale uncertainties ($\texttt{EES}\uparrow$ and $\texttt{EES}\downarrow$) tend to give slightly larger effects, about few per–mille, on the differential distributions while they are found to be of order $\sim 1‰$ on the integrated cross sections. Another small uncertainty comes from the electron trigger scale factor measurement; this is observed to be smaller than $\sim 2‰$ for the integrated cross section and increase up to $6‰$ in bins of the differential cross sections. The dominant uncertainty related to the electron reconstruction performance comes from the uncertainty on the identification efficiency which is slightly larger than 1% in most of the analysis bins and it is found to vary at per–mille level across the analysis bins.

As for the electrons, the muon reconstruction performance is measured using in situ methods with an high accuracy typically of the order of a few per–mille. The uncertainty due the Combined muon p_T resolution is derived by varying independently the p_T resolution of the MS and of the ID measurements within their uncertainties leading to four independent variations; the resulting uncertainties on the analysis range from $\sim 0.1‰$ and $\sim 0.2‰$ for the integrated cross sections and is found to be typically of order $\sim 1‰$ for the bins of the differential distributions. The muon energy scale uncertainty has an impact similar to the p_T resolution un-

certainty. The muon trigger efficiency affects the cross section determination by an uncertainty of $\sim 0.3‰$ and it is found to be almost independent on the analysis bin. The muon reconstruction efficiency uncertainty has similar feature as the trigger uncertainty and a comparable size; it is 3.5‰ in average and reaches $\sim 1\%$ in some bins of the differential distributions.

5.4.5.2 *Jet energy scale and resolution*

Effects of jet energy mis–measurements induce distortions of the Monte Carlo CombNNc templates as well as variations of the truth efficiencies, purities and migration matrices.

The jet energy scale is determined with high precision (0.8%–2.4%) in the central region with slightly degrated experimental accuracy at high rapidity and low jet transverse momentum. The JES uncertainty is propagated through the full analysis chain by using a reduced set of twelve nuisance parameters determined from the calibration analysis of Ref. [75] as discussed in Sec. 2.5. Six of them, referred in Tab. 29 as "EffectiveNP", parametrize the experimental errors on the in situ measurements used to correct the simulation; two uncetainties are associated with data statistical uncertainties and Monte Carlo modeling (EtaIntercalibration_TotalUnc1 and EtaIntercalibration_TotalUnc2); other two NPs, Pileup_OffsetMu and Pileup_OffsetNPV, encode the pile–up modeling uncertainty in terms of average interactions per bunch crossing and number of reconstructed primary vertices; an additional uncertainty, SingleParticle_HighPt is derived from single hadron response measurements [76]; the last one, RelativeNonClosure_MCTYPE, is introduced to cover all the residual Monte Carlo non closure effects.

As explained in Sec. 2.5 the nuisance parameters derived from the combination of the in situ JES calibrations are supplemented by additional topology and flavor related uncertainties; these are observed to be typically the most relevant uncertainties in the $Z + b$ analysis being between 0.5% and 1.3%.

Name	Brief description	Size [%]
EffectiveNP $(1, ..., 6)$	Effective nuisance parameters	0.1–1.7
EtaIntercalibration_TotalUnc $(1, 2)$	Data statistic and MC modeling	0.4–1.7
Pileup_OffsetMu	Pile–up, average interactions per bunch crossing	0.3%–0.5
Pileup_OffsetNPV	Pile–up, number of primary vertices	< 0.1
SingleParticle_HighPt	High p_T uncertainty	< 0.1
RelativeNonClosure_MCTYPE	Monte Carlo non closure effects	0.2
FlavAndTopo_CloseByJets	Close–by jets	0.6–0.7
FlavAndTopo_FlavorComposition	Quark/gluon fraction	0.7
FlavAndTopo_FlavorResponse	Quark flavors response	0.4
FlavAndTopo_Bjets	B–jets response	1.2
Total	Total JES uncertainty from sum in quadrature	2–3

Table 29: Breakdown of the jet energy scale systematic uncertainties for the integrated cross sections.

The relative effects due to the JES uncertainties on the integrated cross sections are summarized in Tab. 29; it is found to be in total about 2%–3% but it can reach $\sim$ 10% in some differential bins with a substantial contribution from the fit variations.

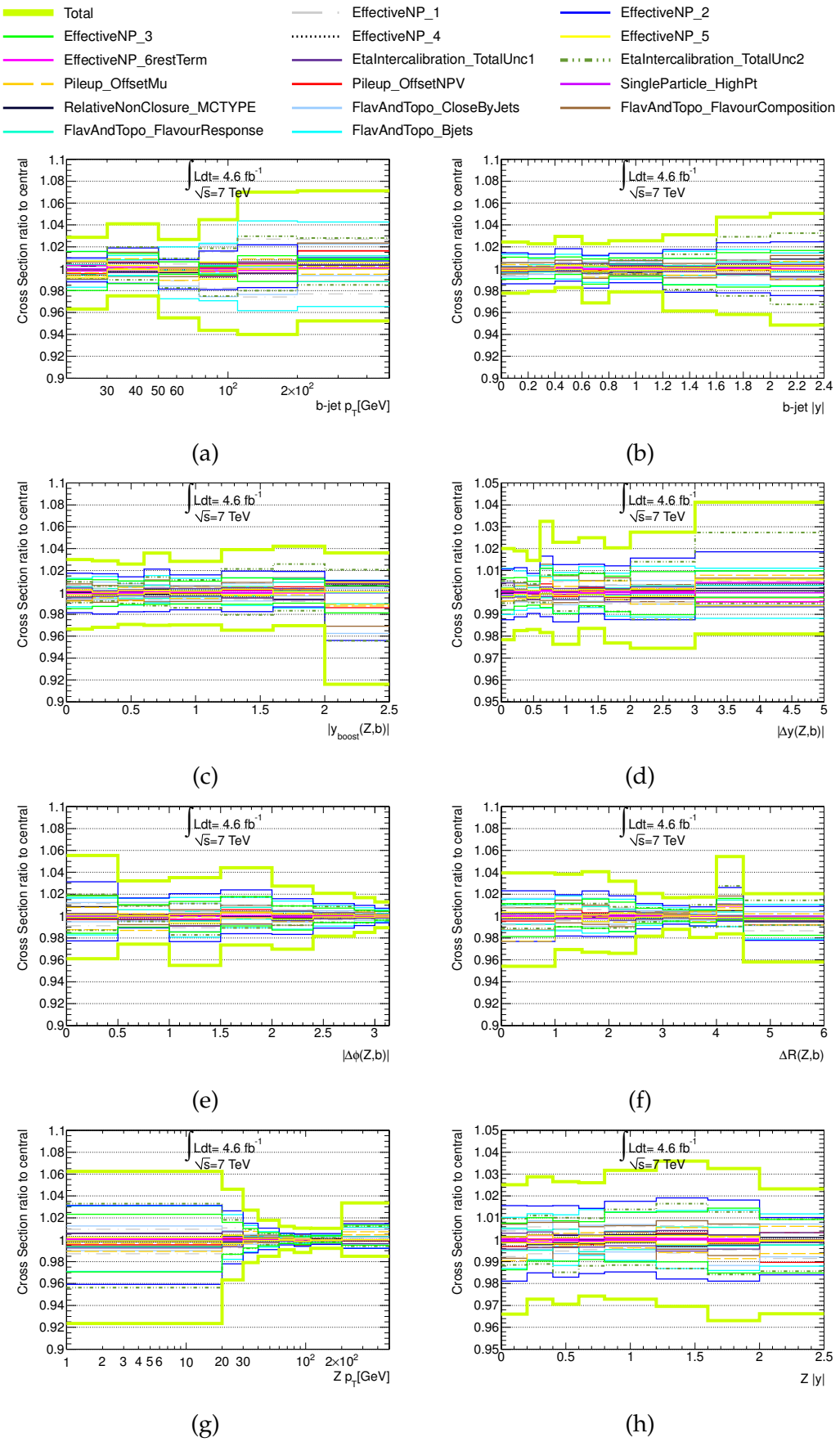

Figure 62: Jet energy scale uncertainties breakdown for the distribution of the b–jet p_T (a), b–jet $|y|$ (b), $y_{boost}(Z,b)$ (c), $|\Delta y(Z,b)|$ (d), $\Delta\phi(Z,b)$ (e), $\Delta R(Z,b)$ (f), Z p_T (g) and Z $|y|$ (h).

The jet energy resolution uncertainty is derived by oversmearing the jet energy in simulated MC samples as explained in Sec. 2.5; its effect on the cross section uncertainties is found to be very small, below 0.5%, is spite of the rather large effect 6% in the first b–jet p_T bin.

5.4.5.3 *B–tagging, charm tagging and mistag rate*

As described in Sec. 2.7, the b–tagging efficiency, the mis–tag rate as well as the charm mis–tag rate mismodeling in simulation are corrected with the application of data–to–simulation scale factors; these scale factors are found to be slightly dependent on the jet transverse momentum and pseudorapidity therefore are expected to impact the fit in addition to the unfolding; specifically, all the flavor tagging scale factors affect the fit while only the b–tagging scale factor uncertainties need to be propagated also into the unfolding; unlike the JES and JER uncertainties, the b–tagging scale factor uncertainties do not induce any bin migration effects.

The flavor tagging scale factors used in this analysis are derived from the combination of the dijet and $t\bar{t}$ calibrations. The calibration related uncertainties have several sources expressed in terms of a set of uncorrelated parameters, *eigenvectors* (EV), by performing the diagonalization of the covariance matrix. The sources of experimental errors on the light and charm mis–tagging efficiencies are combined into two separate global uncertainties.

In average the mistag rate and charm tagging efficiency have a small impact on the cross section, smaller than 0.6%, which grows up to about 1% with increasing jet rapidity. The b–tagging efficiency uncertainty is found to be typically smaller than 4%, increasing for high p_T b–jet up to more than 15% due to the limited data statistic in the $t\bar{t}$ calibration, which dominates the calibration combination accuracy at high p_T.

5.4.6 *Other systematic uncertainties*

Other small systematic uncertainties are introduced by the missing transverse energy cut, the z–vertex reweighting, pile–up conditions description and background normalization uncertainty.

The uncertainties on the E_T^{miss} determination are expected to have a very small impact on the measured cross sections due to the large selection efficiency of the signal. Most of the uncertainties affecting the E_T^{miss} calculation are already taken into account when performing jet and lepton energy scale and resolution variations. As explained in Sec. 2.6, an additional contribution to the E_T^{miss} definition arises from soft calorimetric terms which contribute to the E_T^{miss} uncertainty with other energy scale and resolution variations; the resolution uncertainty leads to changes of the cross sections which are typically smaller than 0.5‰ while the uncertainty due to the energy scale reach values up to 2.5‰ but its average value is less than 1‰.

The mismodeling of the distribution of the z–coordinate of the primary vertex in simulation is corrected with a reweighting procedure based on truth particle level vertex information; the uncertainty on the analysis results related to its residual mismodeling is conservatively estimated by performing the unfolding with the

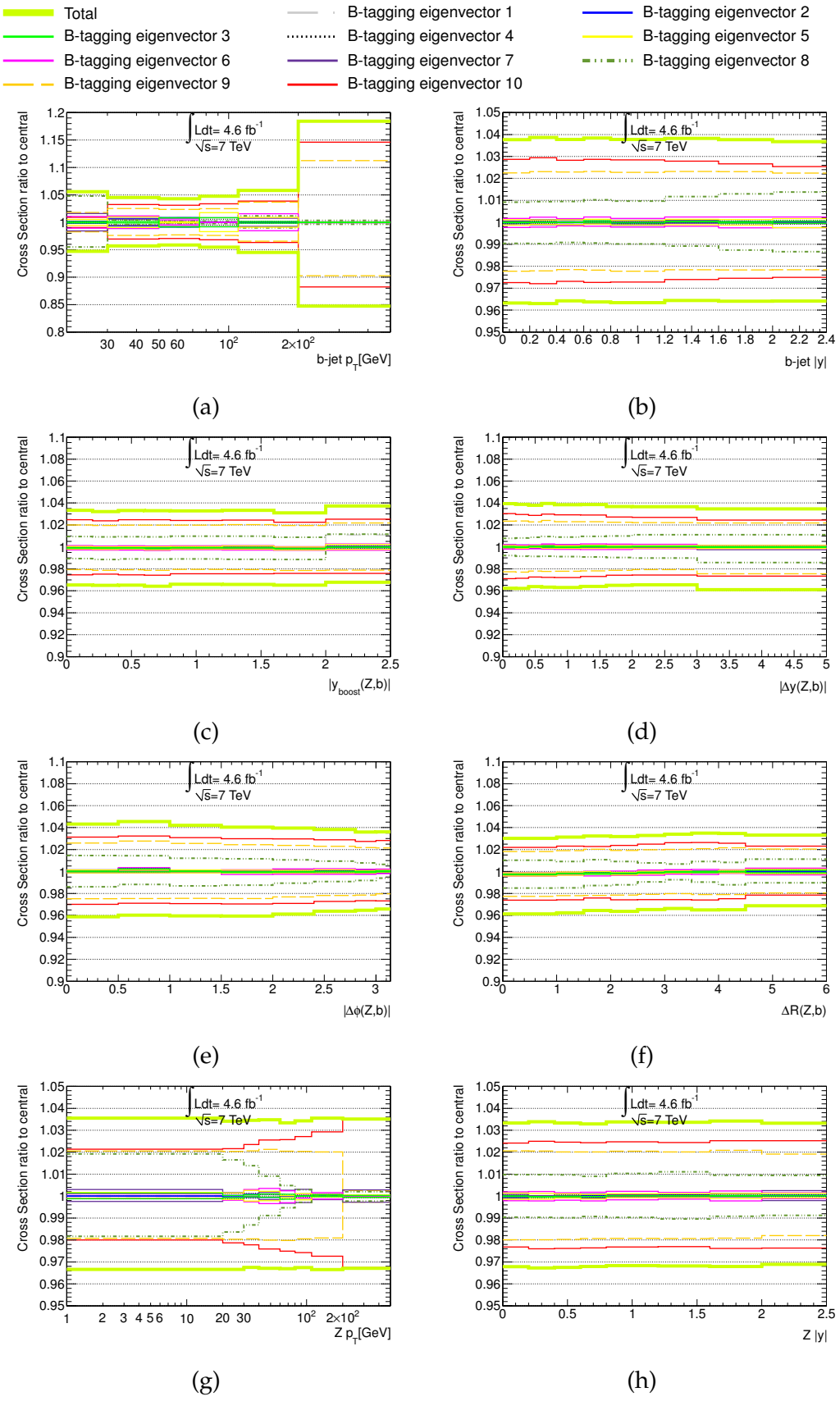

Figure 63: B–tagging scale factor uncertainties breakdown for the distribution of the b–jet p_T (a), b–jet |y| (b), $y_{boost}(Z,b)$ (c), $|\Delta y(Z,b)|$ (d), $\Delta\phi(Z,b)$ (e), $\Delta R(Z,b)$ (f), Z p_T (g) and Z |y| (h).

MC simulation without the z–vertex reweighting; this uncertainty affects both the fit and the unfolding and correlation is properly taken into account. The observed variation of the cross section amounts to a few per–mille.

The pile–up in the Monte Carlo samples is simulated to reproduce the same conditions observed in data; an uncertainty is derived by varying the pile–up in simulation in order to cover the residual observed difference in the number of primary vertices reconstructed in data and simulation; the pile–up misdescription in the simulation can change both the fit results and the unfolded yields, thus it is fully propagated into the analysis chain and the correlations between the fit and the unfolding are taken into account.

A small fit specific uncertainty is due to background normalization in the CombNNc distribution. For the small multijet background the normalization uncertainty is provided from a data–driven method as explained in Sec. 4.3 while the other backgrounds are normalized with the NLO QCD cross sections which are varied conservatively by 10%. The average uncertainty is about 1% and increases up to ~ 3% in specific phase space regions where the fraction of top background is high, e.g. high jet p_T.

5.4.7 *Summary of the systematic uncertainties*

The full list of the systematic uncertainties for all the differential and integrated cross sections are provided in App. D. The total systematic uncertainties are estimated by combining in quadrature about one hundred of contributions; the total systematic error on the integrated cross sections is calculated to be between 7.1% and 7.9%; the dominant systematics are typically uncorrelated across the differential bins with some exceptions leading to an increase of the total uncertainty up to about 20%, like for b–jet $p_T >$ 200 GeV. The systematic uncertainties on the differential cross sections are presented in Fig. 64 after combining the JES and the b–tagging efficiency scale factors uncertainties. It is observed that usually the total uncertainty in differential analysis bins is dominated by systematic errors while the statistical uncertainty becomes relevant only in few bins in kinematic tails.

Sources	$\Delta\sigma(Zb) \times N_{b\text{–jet}}$[%]	$\Delta\sigma^{\star}(Zb) \times N_{b\text{–jet}}$[%]	$\Delta\sigma(Zb)$[%]
b–template shape	4.92	4.90	4.82
jet energy scale	3.02	2.11	2.89
b–tagging efficiency	3.70	3.71	3.29
Model dependence	2.80	1.27	3.05
Monte Carlo statistics	1	0.95	1.04
Others	1.97	2.94	2.46
Total systematic	7.73	7.31	7.67
Statistical	1.14	1.20	1.19

Table 30: Summary of systematic uncertainties for the measured integrated cross sections; the statistical uncertainty is also reported as a reference.

In Tab. 30 a summary of the systematic uncertainties on the three integrated cross sections $\sigma(Zb) \times N_{b\text{–jet}}$, $\sigma^{\star}(Zb) \times N_{b\text{–jet}}$ and $\sigma(Zb)$ is shown, including the dominant systematics due to b–template shape, JES, b–tagging efficiency scale factors, model dependence and the Monte Carlo statistical uncertainty; all the other systematic uncertainties (indicated as "Others") are combined in a single nuisance parameter; as a reference the total systematic uncertainty as well as the statistical uncertainty are also shown. The asymmetric uncertainties are symmetrized in Tab. 30 whereas they are reported as asymmetric variations in App. D.

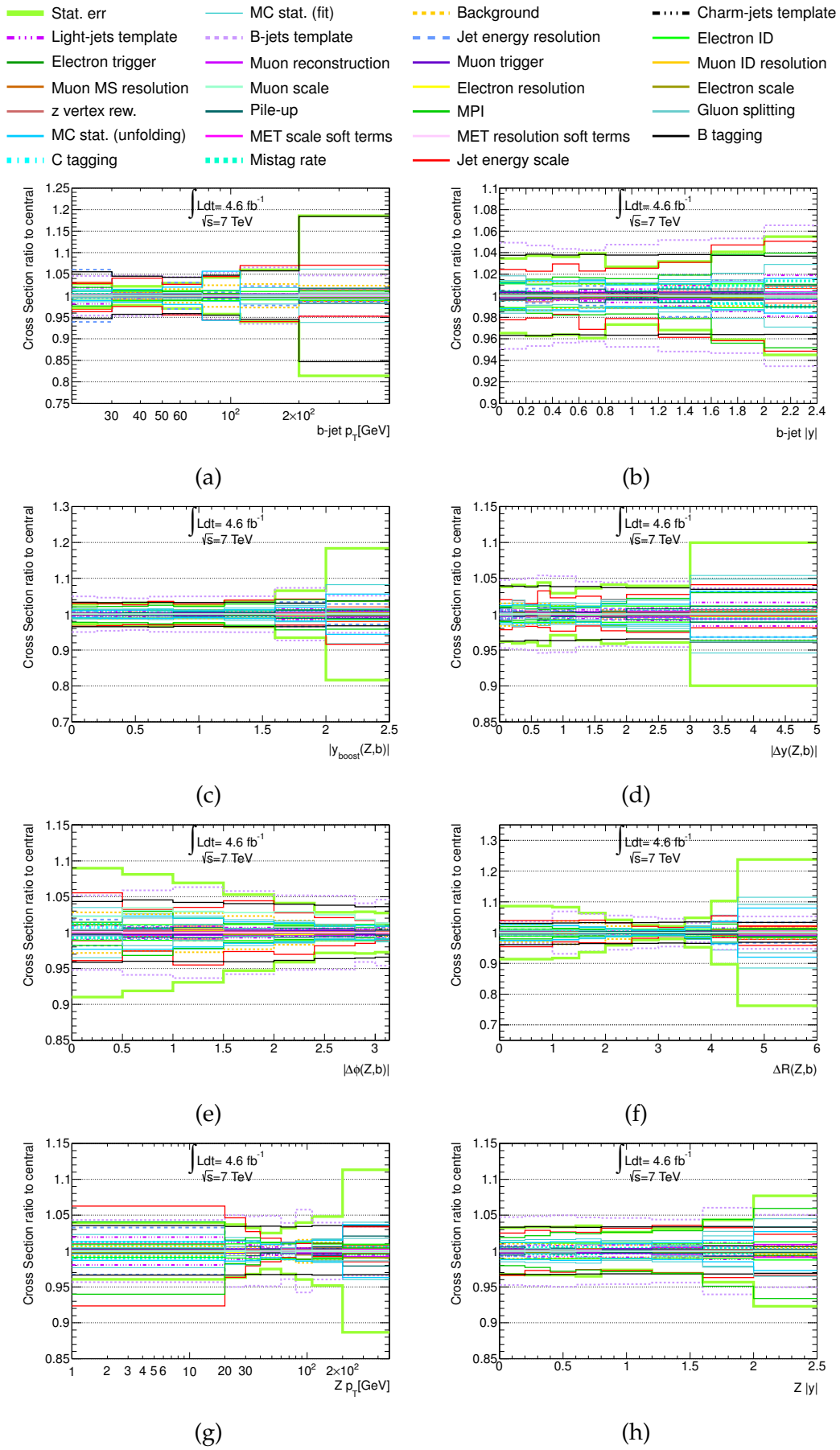

Figure 64: Breakdown of all the systematic uncertainties for the b–jet p_T (a), b–jet $|y|$ (b), $y_{boost}(Z,b)$ (c), $|\Delta y(Z,b)|$ (d), $\Delta\phi(Z,b)$ (e), $\Delta R(Z,b)$ (f), Z p_T (g) and Z $|y|$ (h). The JES and b–tagging uncertainties are shown as two single uncertainty sources determined by adding in quadrature all their sub–components shown separately in Fig. 62 and Fig. 63.

6 ANALYSIS RESULTS AND THEORY PREDICTIONS

In Chap. 4 and Chap. 5 all the steps concerning the measurement of the cross sections for the production of a Z boson and at least one b–jet have been presented; in particular, the definition of the particle level observables has been detailed in Sec. 5.1.

A similar data analysis with minor differences in the signal yield extraction procedure and in the unfolding method (see Ref. [115]), leads to the measurement of the Z production in association with at least two b–jets for the inclusive cross section as well as for the following differential distributions:

- the invariant mass of the b–jet pair, $M(b, b)$;
- ΔR between the two b–jets, $\Delta R(b, b)$;
- Z p_T and Z $|y|$ in events with at least two b–jets.

A summary of the $Z + bb$ data analysis procedure, extensively discussed in Ref. [115], is reported in Sec. 6.1.

All the measured cross sections for the Zb and Zbb final states are finally compared to the theory predictions in Sec. 6.5 and in Sec. 6.6 where the interpretation of the results is also discussed.

The particle level theory calculations exploited here are obtained with the generators aMC@NLO [124], Alpgen+Herwig+Jimmy [43, 47, 97], and Sherpa [49] which are introduced in Sec. 6.2; moreover, the parton level generator Mcfm [125, 126, 127] is used to perform a calculation which afterwards is corrected for non perturbative QCD effects and QED final state radiation as explained in Sec. 6.3.

All the results shown in this chapter are obtained for the combination of the two Z boson decay channels and presented per single leptonic decay mode of the Z boson.

6.1 CROSS SECTION FOR THE ASSOCIATED PRODUCTION OF A Z BOSON AND AT LEAST TWO B–JETS

The measurement of the cross section for the production of a Z boson, decaying into a charged lepton pair, with at least two b–jets is based on the same detector level selection described in detail in Sec. 4.2.2.

The signal yield extraction at detector level is performed from the data sample with at least two b–tagged jets; the CombNNc weights for the two b–tagged jets with the highest p_T are added to build a single discriminant $\sum$CombNNc, used to fit the $Z + bb$ yield and the non–$Z + bb$ events.

The $Z + bb$ fit procedure shares other common features with the $Z + b$ signal fit. The non–Z+jets background contribution is dominated by $t\bar{t}$ and it is estimated by Monte Carlo simulation. As for the $Z + b$ fit, the simulated signal samples provided

Distribution	Description	Binning
$\Delta R(b,b)$	$\sqrt{\Delta y(b,b)^2 + \Delta\phi(b,b)^2}$	$\{0.4, 1.15, 1.9, 2.4, 2.8, 3.2, 5.0\}$
$M(b,b)$[GeV]	-	$\{10, 45, 85, 115, 165, 350\}$
Z p_T[GeV]	-	$\{0, 20, 40, 60, 80, 110, 250\}$
Z $\lvert y\rvert$	-	$\{0, 0.2, 0.4, 0.6, 0.8, 1.2, 1.6, 2.5\}$

Table 31: Measured particle level distributions in events with associated production of a Z boson and at least two b–jets; the two leading p_T jets are used to define the observables $\Delta R(b,b)$ and $M(b,b)$.

by the ALPGEN+HERWIG+JIMMY (also indicated as ALPGEN+HJ in this chapter) generator are reweighted by using the EVTGEN generator in order to ensure a reliable description of the charged track multiplicity in b–hadron decays at truth level.

The method used to unfold the integrated $Z + bb$ yields is based on a global correction factor, as defined for the corrections applied to the $Z + b$ integrated yields in Sec. 5.2 but requiring at least one more b–jet both at detector and particle level; the signal at particle level and the truth–reco matching are defined on the basis of the two b–jets leading in p_T.

The differential cross sections are obtained from the detector level yields corrected bin–by–bin with factors accounting for efficiency and purity. The measured differential cross sections and their binning are summarized in Tab. 31.

The uncertainty is dominated by the statistical error which is 3.8% for the integrated measurement and reaches almost 20% in some analysis bins.

The systematic uncertainty treatement is exactly the same described in Sec. 5.4 for the $Z + b$ cross section. The dominant systematic uncertainties are consistently found to be due to the modeling of the CombNNc shape description, from $\sim$ 5% to $\sim$ 20%, the b–tagging scale factor uncertainty, from $\sim$ 6% to $\sim$ 15%, and to the jet–energy–scale determination, $\sim$ 5%.

6.2 THEORETICAL DESCRIPTION OF B–JET PRODUCTION IN ASSOCIATION WITH A Z BOSON

The theoretical prediction for the production of a boson in association with b–jets is a highly non trivial task as noticed since the first attempts of calculating the NLO perturbative QCD corrections for the benckmark process of the Higgs production in association with two b–jets in hadron–hadron collisions. Shortly later, the first NLO calculation for the cross section of Z boson production in association with b–jets have been made available from a few authors [126, 127].

For the calculation of the cross section for b–jets production in association with a Z boson, two main approaches have been investigated in parallel, which here are referred to as the *four flavor number scheme*, 4FNS, and the *five flavor number scheme*, 5FNS; a more rigorous classification has been recently summarized in Ref. [128].

In the 4FNS the b–quarks are produced by hard initial state gluon splitting (described by the QCD matrix element) leading to a final state with at least two b–quarks as represented by the Feynman diagram of Fig. 65 (a). The matrix ele-

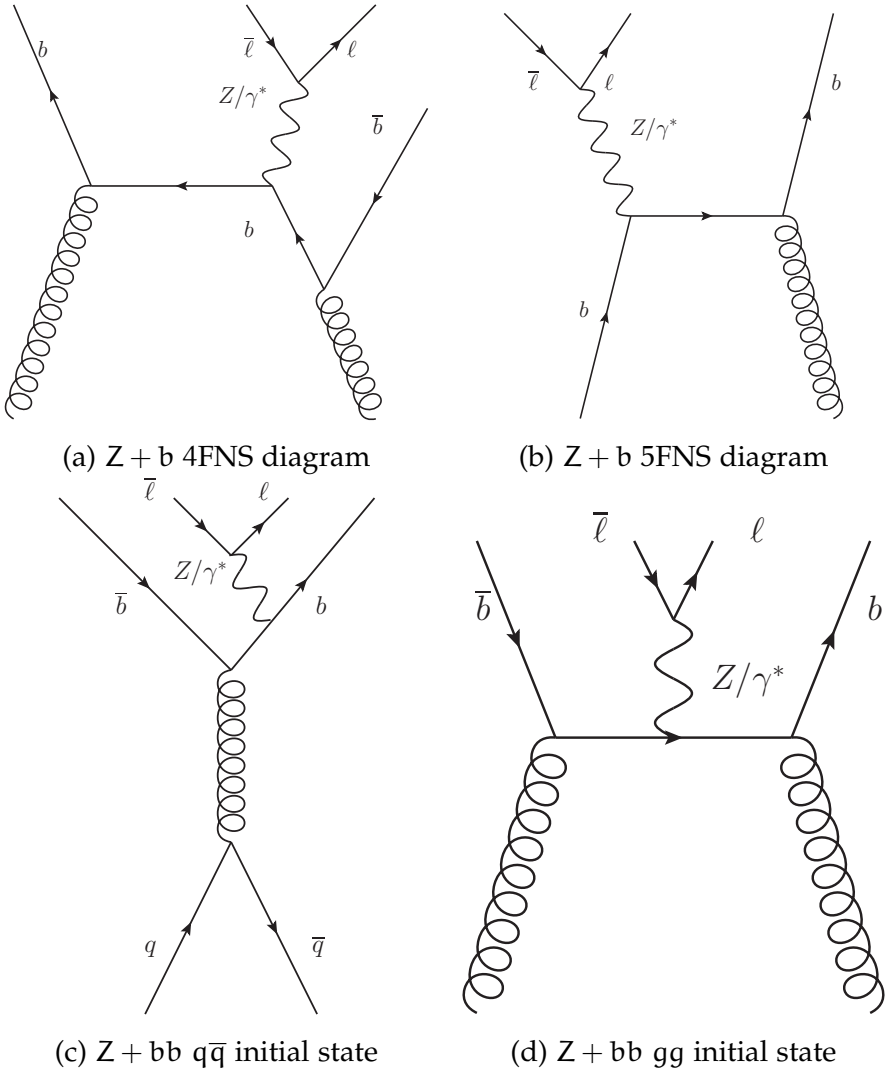

(a) Z + b 4FNS diagram (b) Z + b 5FNS diagram

(c) Z + bb $q\overline{q}$ initial state (d) Z + bb gg initial state

Figure 65: Representative Feynman diagrams for Z + b (top) and Z + bb (bottom) production including the leading tree–level diagram for Z + b production in the 4FNS (a) and 5FNS (b) as described in the text. Notice that the diagram in (a) is the same as in (d) but with the latter producing two b–quarks inside the acceptance.

ment can be defined in the massive b–quark approximation or in the simplified assumption of massless quark. On the other hand, in the 5FNS the b–quark parton distribution funtion is calculated from the gluon density DGLAP evolution above the b–quark mass threshold and describing the b–quark as a massless parton (zero mass variable flavor number scheme, ZM–VFN) or taking the b–quark as massive (general mass variable flavor number scheme, GM–VFN) but generating it only above the b–quark mass scale. Correspondingly, the b–quark can be taken as massless or massive in the QCD matrix element calculation. An example of Feynman diagrams for the Z + b production in 5FNS is presented in Fig. 65 (b). The production of b–quark pair in association with a Z boson is dominated by two distinct production modes shown in Fig. 65 (c-d) with quark pairs $q\overline{q}$ or gluon pairs gg in the initial state where, in particular, the $q\overline{q}$ initial state includes $b\overline{b}$ if the 5FNS is

adopted. The processes in Fig. 65 (c-d) also contribute to the Z+b production with 2 b–quarks in the final state, with one b–quark outside the acceptance or with the two quarks merged in a single parton jet.

Physical observables involving jet production are sensitive to non perturbative (NP) effects. As discussed in Sec. 1.2, reliable theory predictions have to include both perturbative as well as non perturbative effects. Of particular importance for the measurement discussed here are the following NP effects:

- hard double parton interactions (hard DPI, or simply DPI), additional b–jets produced in a secondary parton–parton interaction in the same proton–proton collision where a Z boson is produced in the primary interaction;
- underlying event (UE), additional hadronic activity from the protons remnants leading to additional production of hadrons[1];
- fragmentation–hadronization (also referred to as hadronization for semplicity), mapping the parton level predictions into final states defined in terms of physical hadrons.

The data cross sections are corrected for all the pile–up effects by the unfolding procedure, therefore there is no need to simulate the data pile–up conditions in the particle theory predictions introduced in this chapter.

Similarly to the data analysis, all the theory predictions are interfaced with FastJet for defining jets using as input final state particles for particle level predictions (aMC@NLO, Alpgen+Herwig+Jimmy and Sherpa) or partons for parton level calculations (Mcfm). Hadron level b–jets are defined on the same foot of the data by using the hadron list provided in Tab. 18.

The same fiducial cuts applied to the particle level observables summarized in Sec. 5.2, are also used for the theory predictions. Most of the calculations provide a simulation of soft and collinear QED radiation out of the leptons from Z decays, therefore, dressed leptons can be used to define the fiducial phase space; when the QED FSR are not simulated, like for the Mcfm prediction, a correction factor is applied to the calculations, as specified in Sec. 6.3.1.

6.2.1 *Predictions based on leading order multileg matrix element merged to a parton shower*

The definition of a prediction based on a leading order multileg matrix element (briefly multileg prediction) has been already introduced in Sec. 1.2. Two multileg predictions for $Z + b$ and $Z + bb$ cross sections have been obtained with the two generators Alpgen+Herwig+Jimmy and Sherpa.

The prediction provided by the Alpgen+Herwig+Jimmy generator has been already partially introduced in Sec. 4.2.2. It is based on a 4FNS calculation implemented in alpgen , where the QCD matrix element provides a calculation at leading order for the production of a Z boson plus up to five partons; therefore the

1 The separation between the "underlying event" and the hard DPI is not a well defined task from an experimental point of view and is weakly significative in Monte Carlo studies but it is introduced in view of the discussion presented in Sec. 6.3.1, which provides a good insight into the understanding of the theory predictions for the Zb and Zbb observables.

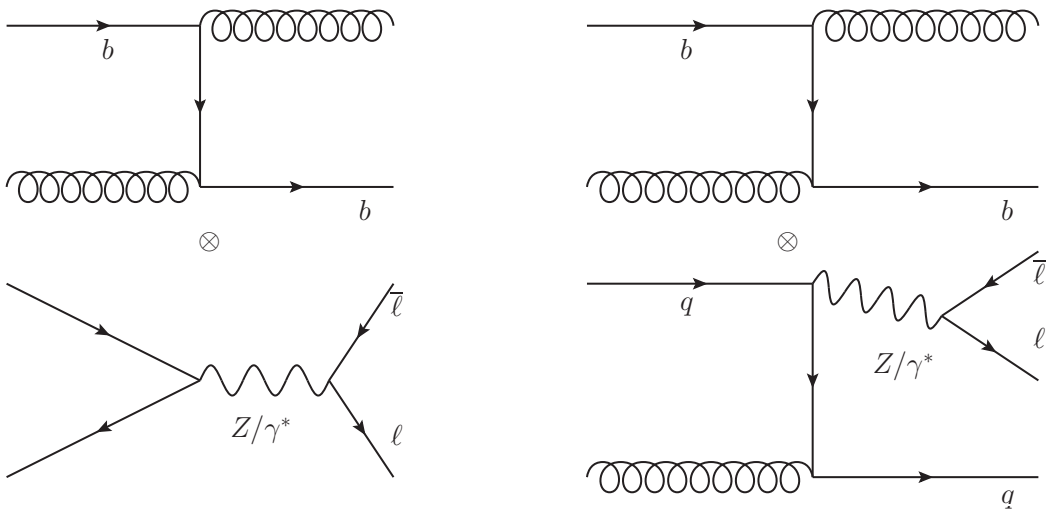

Figure 66: Feynman diagrams representing the Z production in association with a b–quark from a double parton scattering as described in the text.

calculation includes up to three extra partons generated in $Z + bb$ events, as well as Z produced with five light partons from the matrix element. Furthermore the calculation includes, through the interface of ALPGEN matrix element with the JIMMY generator, the contributions where the b–quarks are produced from hard double parton interactions in events with a Z, Z+jets and $Z + bb$ generated from the primary parton scattering. The parton level calculation is interfaced with the HERWIG parton shower. The factorization and renormalization scales (μ_F and μ_R) are set on an event basis to $\mu_F = \mu_R = \sqrt{m_Z^2 + p_{T,Z}^2}$. The prediction is fully defined at hadron level as it uses the hadronization model implemented in HERWIG. As described in Sec. 4.2.2, the ALPGEN+HERWIG+JIMMY prediction uses the CTEQ61L PDF set [96]; the MLM merging [42] procedure provides the overlap removal between parton jet production from matrix element and from parton shower while the HFOR algorithm is used to perform the overlap removal between the heavy flavors generated from the Z+light samples and the $Z + bb$ samples. The MLM merging scale, μ_Q, is set event by event to $\mu_Q = min(20, \text{jet–}p_{T_{min}}[\text{GeV}])$, where jet–$p_{T_{min}}$ is the transverse momentum of the softest jet clustered in the event. The b–quarks are treated as massive in the matrix element calculation as well as in the parton shower evolution. The final state QED radiation is taken into account by interfacing the event generation with PHOTOS [129].

The ALPGEN+HERWIG+JIMMY predictions are presented in the comparison with data without normalizing them to the NNLO inclusive Z cross section as instead done in Chap. 4.5.

Another multileg prediction has been obtained by using the SHERPA generator interfaced with CT10 next–to–leading order PDFs. The SHERPA generator provides an inclusive high statistics Z sample which includes the $Z + b$ as well as the $Z + bb$ signal; the calculation is performed in 5FNS treating the b–quarks as massive partons both in the QCD matrix element as well as in the parton shower evolution; the QCD matrix element is calculated for up to four partons produced in association with the Z boson. As for the ALPGEN+HERWIG+JIMMY prediction the factorization

and renormalization scales are set to $\mu_F = \mu_R = \sqrt{m_Z^2 + p_{T,Z}^2}$ event by event. SHERPA has a built–in model for the hadronization [130], and uses AMISIC to simulate the multiple parton interactions, including hard DPI, leading to a complete particle level calculation for the $Z + b$ and $Z + b\bar{b}$ observables. The overlap between the parton jets produced in the matrix element and the parton shower is resolved with the CKKW merging using $\mu_Q = \sqrt{30/E_{CM}[\text{GeV}]}$ as merging scale, being E_{CM} the proton–proton center of mass energy. Final state QED radiation is simulated with a built–in SHERPA model.

The ALPGEN+HERWIG+JIMMY and SHERPA calculations are expected to provide a very good description of the signal kinematic distributions in several phase space configurations and kinematic tails due to the high parton multiplicity reached by the QCD matrix element calculation. However they are not expected to provide a good estimation of the total event rate because the virtual QCD corrections are missing in the multileg QCD amplitudes at leading order.

6.2.2 *Next–to–leading order QCD calculations*

The MCFM program implements a NLO calculation of the cross section for Z+b and Z+bb production in hadron collisions. These predictions are available since the nineties and have been historically the first predictions for cross section of vector boson plus heavy flavors with a NLO accuracy. Therefore it has been used as benchmark theory calculation for the early measurement at Tevatron and LHC.

MCFM allows to derive parton level predictions without parton shower. The next–to–leading order QCD matrix element calculation for the $Z + b$ and the $Z + b\bar{b}$ final states are defined in the 5FNS. The b–quark is treated as a massless parton with the only exception of the sub–process with a $b\bar{b}$ pair in generation but only one b–quark produced inside the acceptance or with the two b–quarks merged in a single parton jet.

The MCFM predictions have been obtained with three different parton distribution function families, namely MSTW2008 (the nominal PDF set), CT10 and NNPDF2.3. For all the calculations, the factorization and the renormalization scales are set according to $\mu_F = \mu_R = \sqrt{M_Z^2 + p_{T,Z}^2}$.

Being defined at parton level, the MCFM calculation has to be corrected for non perturbative effects including hard DPI; futhermore the MCFM calculation do not account for the leptons QED FSR, thus it requires and additional correction as described in the following section.

Two predictions for the Z+b and Z+bb cross sections at NLO are obtained with the MCFM generator. For the Z+bb cross section prediction, the event generation is performed with the MCFM process ID 51 at NLO (see the MCFM manual [131]). The Z+b cross section calculation is more involved; the complete prediction is obtained by combining four sub–processes:

- 261 NLO; calculates the cross section for producing only one b–quark in the final state; it includes the virtual QCD corrections to the born process $gb \to Zb$ (a born level diagram is shown in Fig. 65 (a)) as well as the real contribution due to the tree level process $gb \to Zbg$ (Fig. 67 (a));

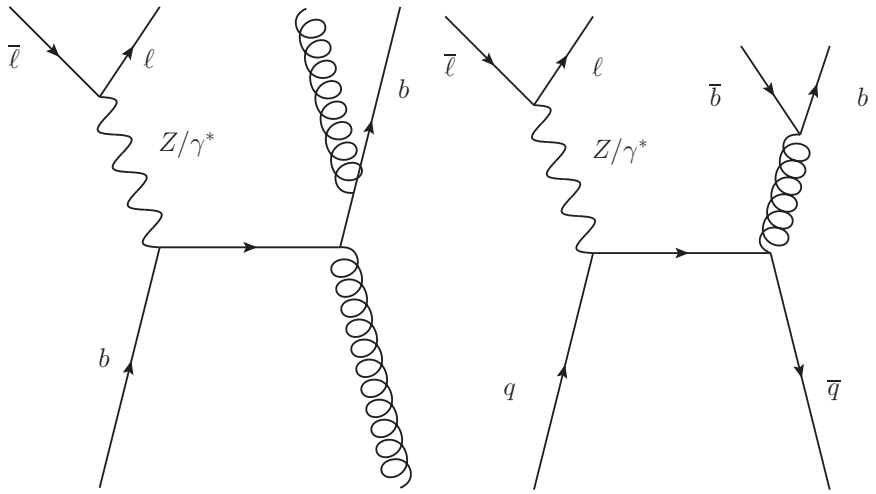

(a) $Z + bg$ diagram (b) Gluon splitting diagram

Figure 67: Feynman diagrams for the real correction to the born level $Z + b$ production in 5FNS (a) and gluon splitting (b).

- 266 REAL; includes contributions to the same final states produced by the gb→Zbg but with other initial states;
- 263 LO; provides events corresponding to the processes $gg \to Zb\overline{b}$ (Fig. 65 (d)) and $q\overline{q} \to Zb\overline{b}$ (Fig. 67 (b)) where one b–quark is outside the acceptance or the two b–quarks are merged into a single parton jet; the b–quark mass effects are retained in this calculation; typically b–quarks merged into a single parton jet are expected to be produced via gluon splitting (Fig. 67 (b));
- 50 LO; generates the same subprocess as for 263 LO but populating the phase space with two b–quarks well separated and both inside the acceptance; as for the previous process, the b–quark mass effects are taken into account in the QCD matrix element.

In recent years a new calculation has been publishes for the $Z + b$ and $Z + bb$ final states [124]. This is made available through the aMC@NLO framework, where the NLO event generator can be easily interfaced with parton shower and particle level MC generators like HERWIG, HERWIG++, PYTHIA or PYTHIA8.

For this analysis two next–to–leading order QCD calculations have been obtained with the aMC@NLO generator interfaced with HERWIG++ for parton shower, hadronization and for multiple parton interactions.

A next–to–leading order QCD prediction in 5FNS is obtained in the massless b–quark approximation for the matrix element calculation, while retaining the b–quark mass in the parton–shower; the QCD matrix element is calculated with the MSTW2008 NLO PDF set [29]. This prediction is based on a NLO matrix element calculation for the production of a Z boson in association with one b–quark; therefore it is accurate at NLO for the $Z + b$ observables, whereas it is effectively only leading order for the $Z + bb$ cross section.

In the aMC@NLO framework a NLO calculation in 4FNS with massive b–quarks have been also performed using the the MSTW2008 NLO PDF with four active

flavors. The matrix element calcuations provide a full $Z + bb$ final state with no kinematic cuts applied to the b–quarks, thus can be used to describe the $Z + b$ and the $Z + bb$ observables preserving, the NLO accuracy for both.

As for the ALPGEN+HERWIG+JIMMY and SHERPA predictions, the aMC@NLO calculation is defined at particle level; however, the prediction have been obtained by generating a more exclusive matrix elements leading to a missing hard DPI contribution for the following cases:

- the 5FNS calculation, does not include the DPI contribution from events with a production of Z with no hard partons generated by the QCD matrix element;
- the 4FNS calculation, does not include the DPI contribution in events where the Z is produced without additional partons or when it is produced in association with hard light partons.

Therefore, in order to fully account for all the signal DPI cross section an additive correction has been applied to the aMC@NLO predictions, which is obtained from the ALPGEN+HERWIG+JIMMY generator as explained in Sec. 6.3.1.

The final state QED radiation is simulated with the HERWIG++ generator.

6.3 NON PERTURBATIVE EFFECTS AND FINAL STATE QED RADIATION

The NLO theory predictions derived with the aMC@NLO and MCFM generators need to be supplemented with additional corrections in order to be properly compared to the data; the corrections applied to the aMC@NLO are derived with the ALPGEN+HERWIG+JIMMY generator. The full non perturbative corrections applied to the MCFM calculations are instead derived with dedicated studies using SHERPA, with the same configuration as described in Sec. 6.2, and PYTHIA, as described in the following. PYTHIA events are generated using a leading order matrix element calculation for the production of a quark in association with a Z boson in 5FNS which is interfaced with the PYTHIA parton shower; the calculation is performed usign the CTEQ5L PDF set. The non perturbative effects are simulated with the PYTHIA built–in models [46] and the PERUGIA 2011 tune [132] is used.

The QED FSR are not taken into account by the MCFM prediction, therefore a correction is derived by using the QED FSR simulation in ALPGEN+HERWIG+JIMMY based on PHOTOS.

6.3.1 *Corrections to* aMC@NLO

The particle level events generated with the aMC@NLO generator for the 5FNS and for the 4FNS predictions are based on a Z+jet (5FNS) or $Z + bb$ (4FNS) matrix element calculations; therefore, they do not fully take into account the additional contribution due to hard DPI production in events with a Z boson or with the Z boson produced in association with light partons. An additive correction is derived by using the inclusive sample from the ALPGEN+HERWIG+JIMMY Monte Carlo by selecting signal events where the b–quarks are produced from the secondary interactions generated by JIMMY. This DPI cross section has to be properly scaled before

	Generator	Cross section [pb]	
		UE	DPI
$\sigma(Zb)$	SHERPA +AMISIC	0.116 ± 0.008	0.149 ± 0.008
$\sigma(Zb)$	aMC@NLO+HERWIG++	0.106 ± 0.048	-
$\sigma(Zb)$	JIMMY	-	0.1861 ± 0.0035
$\sigma(Zb) \times N_{b\text{–jet}}$	SHERPA +AMISIC	0.144 ± 0.008	0.160 ± 0.008
$\sigma(Zb) \times N_{b\text{–jet}}$	aMC@NLO+HERWIG++	0.120 ± 0.050	-
$\sigma(Zb) \times N_{b\text{–jet}}$	JIMMY	-	0.1938 ± 0.0036
$\sigma(Zb)^{\star} \times N_{b\text{–jet}}$	SHERPA +AMISIC	0.102 ± 0.008	0.071 ± 0.007
$\sigma(Zb)^{\star} \times N_{b\text{–jet}}$	aMC@NLO+HERWIG++	0.069 ± 0.047	-
$\sigma(Zb)^{\star} \times N_{b\text{–jet}}$	JIMMY	-	0.047 ± 0.002
$\sigma(Zbb)$	SHERPA +AMISIC	0.0274 ± 0.0025	0.0120 ± 0.0019
$\sigma(Zbb)$	aMC@NLO+HERWIG++	0.016 ± 0.012	-
$\sigma(Zbb)$	JIMMY	-	0.005 ± 0.0006

Table 32: Underlying event and DPI contributions to the observed total cross sections separated into the two components discussed in the text; the uncertainty is statistical only.

being added to the Z+jet and Z+bb aMC@NLO samples. The normalization factors to be applied are:

$$\text{5FNS aMC@NLO:} \quad c_{DPI}^{5FNS} = \frac{\sigma(Z,\text{Inc.}) - \sigma(Z+\text{jets})}{\sigma(Z,\text{Inc.})} = 0.77\,,$$

$$\text{4FNS aMC@NLO:} \quad c_{DPI}^{4FNS} = \frac{\sigma(Z,\text{Inc.}) - \sigma(Z+bb)}{\sigma(Z,\text{Inc.})} = 0.99\,,$$

where $\sigma(Z,\text{Inc.})$ is the inclusive Z cross section, $\sigma(Z+\text{jets})$ is the cross section for the Z boson production in association with at least one quark generated by the matrix element, and $\sigma(Z+bb)$ is the cross section for Z boson production in association with at least one b–quark generated from the matrix element; all of them are estimated with the ALPGEN generator.

The hard double parton interaction rate determined using the JIMMY generator, has been validated with the prediction derived with SHERPA, which is artificially decomposed in terms of underlying event and hard DPI. The UE correction has been estimated as the difference between the full particle level predictions in SHERPA with and without generating the hadrons from the underlying interactions in events where the hard scattering produces Z+b or a Z+bb final state. The DPI cross section is estimated by the signal event yield obtained from events where no b–quarks are generated from the matrix element or from the parton shower.

An additional check of the UE correction is performed by dedicated event generations, with limited statistics, using the aMC@NLO generator in the 4FNS set–up interfaced with HERWIG++ with or without simulating the underlying event.

	SHERPA			PYTHIA		
Observable	$\langle C_j^{F,H} \rangle$	$\langle C_j^{U+D} \rangle$	$\langle C_j^{NP} \rangle$	$\langle C_j^{F,H} \rangle$	$\langle C_j^{U+D} \rangle$	$\langle C_j^{NP} \rangle$
$\sigma(Zb) \times N_{b\text{–jet}}$	0.850	1.078	0.916 ± 0.006	0.847	1.065	0.902 ± 0.021
$\sigma(Zb)^\star \times N_{b\text{–jet}}$	0.871	1.050	0.915 ± 0.008	0.870	1.034	0.900 ± 0.003
$\sigma(Zb)$	0.862	1.076	0.928 ± 0.008	0.858	1.063	0.912 ± 0.029
$\sigma(Zbb)$	0.742	1.103	0.818 ± 0.021	0.758	1.084	0.822 ± 0.095

Table 33: Breakdown of the non perturbative effect corrections as described in the text; the uncertainty shown on the averaged corrections C^{NP} are statistical only.

The JIMMY hard DPI cross sections have been found to range from 0.071 pb to 0.16 pb for the $Z + b$ observables and to be of about 0.005 pb for the integrated $Z + bb$ cross section. As expected, the DPI cross section is smaller for $\sigma(Zb)^\star \times N_{b\text{–jet}}$ observables, where the Z boson p_T must be greater than 20 GeV, and for the $\sigma(Zbb)$ cross section, because the softer p_T spectrum of the DPI jets compared to jets from the primary interaction.

A comparison between the JIMMY and the SHERPA DPI cross sections is presented in Tab. 32 for each measured integrated observable, namely for $\sigma(Zb) \times N_{b\text{–jet}}$, $\sigma(Zb)^\star \times N_{b\text{–jet}}$, $\sigma(Zb)$ and $\sigma(Zbb)$. The two generators are relatively consistent, considering the poor knowledge of this process. The DPI contribution estimated from SHERPA is found to be smaller than the JIMMY DPI cross section for the most inclusive observables, $\sigma(Zb) \times N_{b\text{–jet}}$ and $\sigma(Zb)$, by up to 4.2 statistical standard deviations; the SHERPA DPI and the JIMMY DPI for the per–jet cross section $\sigma^\star(Zb) \times N_{b\text{–jet}}$ are instead found to differ by 3.2 standard deviations, being the JIMMY DPI cross section estimated to be larger. Finally, for the $\sigma(Zbb)$ cross section the SHERPA prediction is found to be larger by a factor two compared with the JIMMY prediction but consistent within 3.5 standard deviations.

The UE correction estimated with SHERPA and HERWIG++ are observed to be in good agreement whithin the large statistial uncertainty on the prediction of the latter generator.

Both the UE and the DPI corrections are positive; the former produces an overlay of hadrons in the event which can be clustered inside the hard jets moving more jets in the fiducial region; the latter adds a production mechanism for the Z+b and Z+bb final states.

The DPI corrections to the AMC@NLO predictions are derived differentially in all the analysis bins.

6.3.1.1 *Corrections to MCFM*

The MCFM predictions have to be corrected for QED final state radiation as well as non perturbative effects.

The QED FSR correction for the analysis bin j is given by

$$C_j^{FSR} = \frac{N_j(\text{dressed})}{N_j(\text{born})}\,, \tag{50}$$

where $N_j(\text{dressed})$ is the signal yield corresponding to dressed leptons used to define the Z boson, while $N_j(\text{born})$ is the yield obtained with born leptons. This ratio has been observed to be flat in all the analysis bins corresponding to a global QED FSR correction $\langle C_j^{FSR} \rangle = 0.9739 \pm 0.0023$ as derived from the ALPGEN+HERWIG+JIMMY samples, where the photon radiation is simulated using PHOTOS; the uncertainty on the QED FSR correction is due to the Monte Carlo statistics.

The effect of the fragmentation–hadronization and multiple parton interactions have been studied in detail by comparing a set of predictions determined using the SHERPA and PYTHIA generators for three kind of signal yields:

- N(F,H,U+D): fragmentation, hadronization as well as underlying event and DPI are simulated;
- N(F,H): fragmentation and hadronization are simulated but the underlying event and hard DPI are not;
- N(P): pure parton level prediction.

As already pointed out in Sec. 6.3.1, the UE and DPI corrections to the $Z + b$ and $Z + b\bar{b}$ observables lead to an increase of the cross section; their overall effect on an analysis bin j is estimated as the ratio:

$$C_j^{U+D} = \frac{N_j(F,H,U+D)}{N_j(F,H)} , \tag{51}$$

which is the ratio of signal yield with and without the underlying event and double parton interactions simulated.

The non perturbative correction factors to be applied bin by bin to the MCFM prediction are defined as the ratio of signal yield at particle level to the parton level prediction:

$$C_j^{F,H,U+D} \equiv C_j^{NP} = \frac{N_j(F,H,U+D)}{N_j(P)} , \tag{52}$$

which takes into account also the yield variation due to fragmentation as well as hadronization effects besides the underlying event and multiple parton interactions. Fragmentation and hadronization induce a degradation of the original quark momentum which is shared among a number of hadrons out of the non perturbative transition; these hadrons are in general not expected to be all clustered by the jet algorithm leading to a decrease of the cross section when moving from the parton level to the particle level. Moreover, by comparing Eq. 51 and Eq. 52 the hadronization correction for the bin j can be derived as:

$$C_j^{F,H} = \frac{C^{NP}}{C^{U+D}} . \tag{53}$$

The average of the correction factors defined in Eq. 51, Eq. 52 and Eq. 53 are summarized in Tab. 33 for all the measured integrated cross sections; the uncertainty is shown only for the factors $\langle C_j^{NP} \rangle$ and is determined by the finite Monte Carlo statistics.

The average non perturbative corrections $\langle C_j^{NP} \rangle$ calculated with SHERPA and PYTHIA, reported in Tab. 33, are determined with a statistical precision better than

1% for SHERPA and with precision of order ~ 2% for PYTHIA and are found to be well consistent within the statistical uncertainties; the factors $\langle C_j^{NP} \rangle$ are observed to be smaller than one, indicating a dominance of hadronization corrections, being of order ~ 0.9 for $Z + b$ observables and of ~ 0.8 for $Z + b\bar{b}$.

In Fig. 68 the non perturbative corrections C_j^{NP} are shown for each distribution for the Z production in association with at least one or two b–jets. The correction factors C_j^{NP} are found to be usually constant across the analysis bins but a significant dependence has been observed on the b–jet p_T and on the kinematic variables correlated with it; for example, the correction factor C_j^{NP} is found to vary by 22% for the b–jet p_T distribution and by more than 40% in bins of $M(b, b)$; the corrections factors C_j^{U+D} are also shown for reference.

The nominal value for C_j^{NP} is derived by averaging the correction factors obtained with the SHERPA and PYTHIA generators.

The differences observed bin–by–bin between the SHERPA and PYTHIA generators are used to asses a systematic uncertainty on the C_j^{NP} factors due to the model depencence of the corrections, σ_{model}.

As described in Sec. 5.4 the hard DPI cross section predicted by JIMMY is found to agree with the ATLAS measurement [122] within 50% of the total predictions; this comparison is used to define a range of variation for the DPI rate to estimate an uncertainty on the unfolded data due to unknown fraction of heavy flavor produced from DPI. The same argument applys to the MPI corrections of the MCFM calculation; a 50% error is then used as an additional uncertainty in the C_j^{NP} corrections, σ_{DPI}.

Additional sources of uncertainties on the C_j^{NP} factors arise from the limited Monte Carlo statistics in the calculation of the correction factors for the non perturbative effects, $\sigma_{MC\ stat.}$, and for the QED FSR, σ_{FSR}. The former uncertainty is tipically subleading with some exceptions in low statistics bins, like for b–jet $p_T > 200$ GeV, where the low statistics in the PYTHIA sample induces a significant error, of order 20%; the latter is instead well determined given the high statistics of the MC sample user for the calculation.

The total uncertainty, σ_{total}, on the correction factors is found to be typically of a few percent.

The non perturbative corrections are summarized in Tab. 34; all the uncertainty sources are also separately presented in terms of absolute errors on C_j^{NP}.

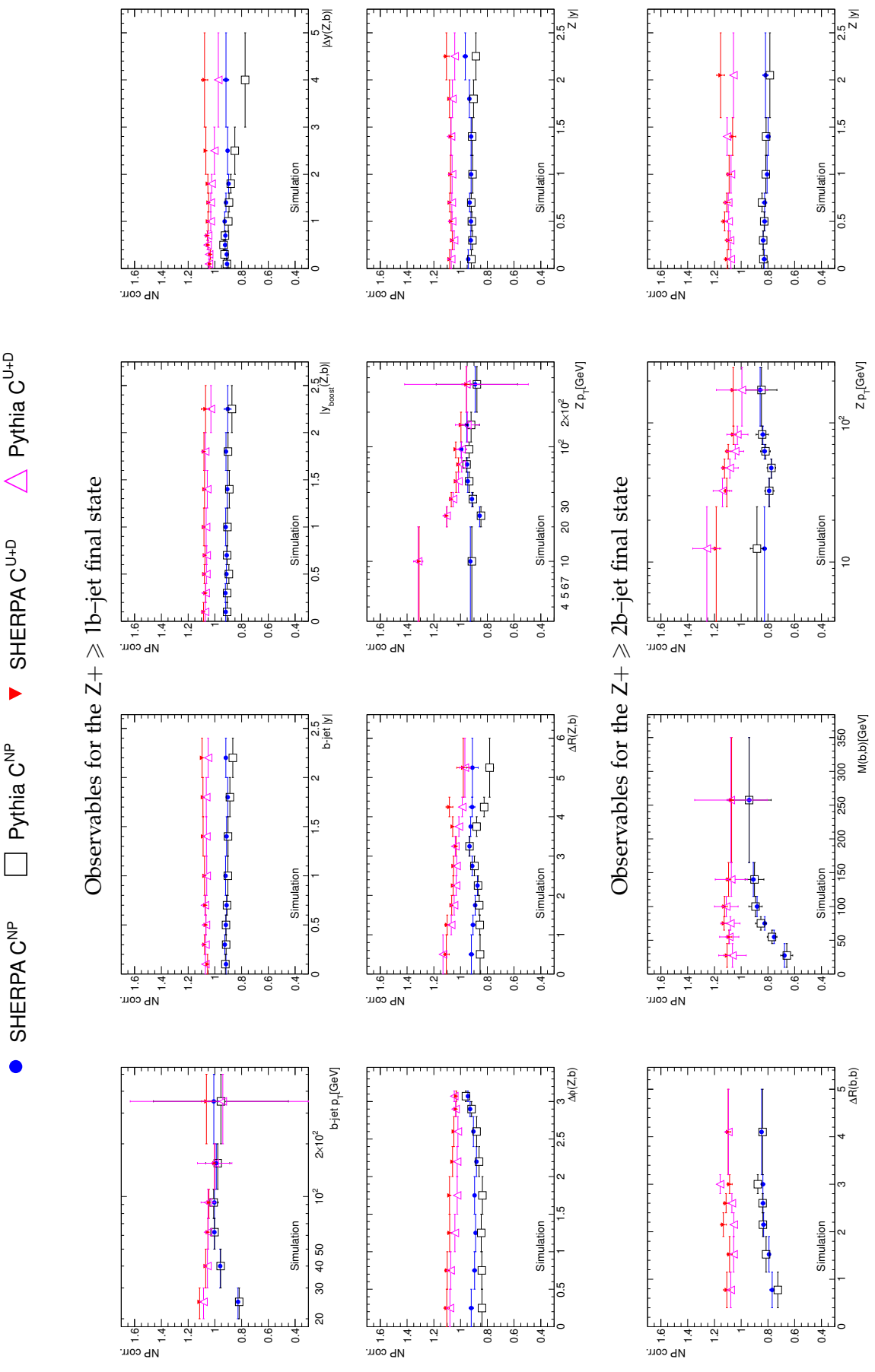

Figure 68: Non pertubative corrections in all the differential bins of the $Z+b$ and $Z+bb$ analyses as determined from the SHERPA and PYTHIA generators; the factors C_j^{U+D} and C_j^{NP} are shown separately and the uncertainty is statistical only.

Observables for the Z+ ⩾ 1b–jet final state															Observables for the Z+ ⩾ 2b–jets final state							
variable	[min, max]	C^{NP}	$\sigma_{MC\ stat.}$	σ_{model}	σ_{FSR}	σ_{DPI}	σ_{total}	variable	[min, max]	C^{NP}	$\sigma_{MC\ stat.}$	σ_{model}	σ_{FSR}	σ_{DPI}	σ_{total}	variable	[min, max]	C^{NP}	$\sigma_{MC\ stat.}$	σ_{model}	σ_{FSR}	σ_{DPI}	σ_{total}
b–jet p_T [GeV]	[20, 30]	0.8014	0.0033	0.0044	0.0019	0.0319	0.0324	$\Delta\phi(Z, b)$	[0.00, 0.50]	0.8565	0.0097	0.0391	0.0020	0.1045	0.1120	$\Delta R(b, b)$	[0.40, 1.15]	0.7278	0.0096	0.0209	0.0017	0.0043	0.0235
b–jet p_T [GeV]	[30, 50]	0.9336	0.0053	0.0020	0.0022	0.0106	0.0122	$\Delta\phi(Z, b)$	[0.50, 1.00]	0.8454	0.0088	0.0268	0.0020	0.0750	0.0801	$\Delta R(b, b)$	[1.15, 1.90]	0.7820	0.0084	0.0105	0.0018	0.0026	0.0138
b–jet p_T [GeV]	[50, 75]	0.9768	0.0094	0.0009	0.0023	0.0019	0.0100	$\Delta\phi(Z, b)$	[1.00, 1.50]	0.8441	0.0073	0.0204	0.0020	0.0556	0.0598	$\Delta R(b, b)$	[1.90, 2.40]	0.8131	0.0089	0.0023	0.0019	0.0028	0.0098
b–jet p_T [GeV]	[75, 110]	0.9803	0.0176	0.0027	0.0023	0.0014	0.0181	$\Delta\phi(Z, b)$	[1.50, 2.00]	0.8432	0.0055	0.0287	0.0020	0.0292	0.0413	$\Delta R(b, b)$	[2.40, 2.80]	0.8167	0.0090	0.0018	0.0019	0.0035	0.0100
b–jet p_T [GeV]	[110, 200]	0.9585	0.0441	0.0055	0.0023	0.0012	0.0445	$\Delta\phi(Z, b)$	[2.00, 2.40]	0.8485	0.0042	0.0099	0.0020	0.0086	0.0139	$\Delta R(b, b)$	[2.80, 3.20]	0.8341	0.0087	0.0187	0.0020	0.0100	0.0229
b–jet p_T [GeV]	[200, 500]	0.9555	0.2467	0.0258	0.0023	0.0016	0.2480	$\Delta\phi(Z, b)$	[2.40, 2.80]	0.8687	0.0028	0.0112	0.0021	0.0033	0.0122	$\Delta R(b, b)$	[3.20, 5.00]	0.8215	0.0095	0.0037	0.0019	0.0078	0.0130
b–jet $\lvert y\rvert$	[0.00, 0.20]	0.8947	0.0040	0.0021	0.0021	0.0080	0.0094	$\Delta\phi(Z, b)$	[2.80, 3.00]	0.8994	0.0029	0.0051	0.0021	0.0010	0.0063	$M(b, b)$ [GeV]	[10, 45]	0.6502	0.0228	0.0082	0.0015	0.0044	0.0247
b–jet $\lvert y\rvert$	[0.20, 0.40]	0.8967	0.0040	0.0044	0.0021	0.0085	0.0106	$\Delta\phi(Z, b)$	[3.00, π]	0.9280	0.0030	0.0073	0.0022	0.0024	0.0085	$M(b, b)$ [GeV]	[45, 65]	0.7420	0.0187	0.0070	0.0018	0.0119	0.0233
b–jet $\lvert y\rvert$	[0.40, 0.60]	0.8933	0.0040	0.0001	0.0021	0.0095	0.0105	$\Delta R(Z, b)$	[0.00, 1.00]	0.8636	0.0115	0.0315	0.0020	0.0502	0.0604	$M(b, b)$ [GeV]	[65, 85]	0.8166	0.0208	0.0142	0.0019	0.0093	0.0269
b–jet $\lvert y\rvert$	[0.60, 0.80]	0.8874	0.0041	0.0017	0.0021	0.0087	0.0100	$\Delta R(Z, b)$	[1.00, 1.50]	0.8586	0.0086	0.0250	0.0020	0.0310	0.0408	$M(b, b)$ [GeV]	[85, 115]	0.8640	0.0251	0.0055	0.0020	0.0048	0.0262
b–jet $\lvert y\rvert$	[0.80, 1.20]	0.8875	0.0031	0.0083	0.0021	0.0106	0.0140	$\Delta R(Z, b)$	[1.50, 2.00]	0.8524	0.0062	0.0147	0.0020	0.0247	0.0295	$M(b, b)$ [GeV]	[115, 165]	0.8813	0.0350	0.0044	0.0021	0.0036	0.0356
b–jet $\lvert y\rvert$	[1.20, 1.60]	0.8831	0.0034	0.0051	0.0021	0.0153	0.0166	$\Delta R(Z, b)$	[2.00, 2.50]	0.8488	0.0042	0.0020	0.0020	0.0107	0.0118	$M(b, b)$ [GeV]	[165, 350]	0.9159	0.0805	0.0003	0.0022	0.0008	0.0806
b–jet $\lvert y\rvert$	[1.60, 2.00]	0.8722	0.0038	0.0084	0.0021	0.0272	0.0288	$\Delta R(Z, b)$	[2.50, 3.00]	0.8807	0.0025	0.0081	0.0021	0.0021	0.0090	Z p_T [GeV]	[0, 20]	0.8542	0.0285	0.0226	0.0020	0.0350	0.0506
b–jet $\lvert y\rvert$	[2.00, 2.40]	0.8683	0.0045	0.0255	0.0021	0.0429	0.0501	$\Delta R(Z, b)$	[3.00, 3.50]	0.9088	0.0024	0.0003	0.0021	0.0018	0.0037	Z p_T [GeV]	[20, 40]	0.7729	0.0178	0.0072	0.0018	0.0030	0.0196
$\lvert y_{boost}(Z, b)\rvert$	[0.00, 0.20]	0.8895	0.0034	0.0051	0.0021	0.0151	0.0165	$\Delta R(Z, b)$	[3.50, 4.00]	0.8786	0.0056	0.0221	0.0021	0.0125	0.0261	Z p_T [GeV]	[40, 60]	0.7594	0.0166	0.0041	0.0018	0.0012	0.0172
$\lvert y_{boost}(Z, b)\rvert$	[0.20, 0.40]	0.8907	0.0035	0.0068	0.0021	0.0153	0.0172	$\Delta R(Z, b)$	[4.00, 4.50]	0.8460	0.0115	0.0436	0.0020	0.0374	0.0586	Z p_T [GeV]	[60, 80]	0.8161	0.0206	0.0084	0.0019	0.0007	0.0224
$\lvert y_{boost}(Z, b)\rvert$	[0.40, 0.60]	0.8808	0.0035	0.0089	0.0021	0.0146	0.0176	$\Delta R(Z, b)$	[4.50, 6.00]	0.8249	0.0256	0.0628	0.0019	0.4734	0.4783	Z p_T [GeV]	[80, 110]	0.8203	0.0277	0.0057	0.0019	0.0008	0.0283
$\lvert y_{boost}(Z, b)\rvert$	[0.60, 0.80]	0.8857	0.0037	0.0017	0.0021	0.0152	0.0159	Z p_T [GeV]	[0, 20]	0.8967	0.0088	0.0052	0.0021	0.0580	0.0589	Z p_T [GeV]	[110, 250]	0.8348	0.0673	0.0044	0.0020	0.0005	0.0674
$\lvert y_{boost}(Z, b)\rvert$	[0.80, 1.20]	0.8889	0.0029	0.0062	0.0021	0.0144	0.0161	Z p_T [GeV]	[20, 30]	0.8299	0.0055	0.0048	0.0020	0.0115	0.0138	Z $\lvert y\rvert$	[0.00, 0.20]	0.8093	0.0090	0.0034	0.0019	0.0028	0.0102
$\lvert y_{boost}(Z, b)\rvert$	[1.20, 1.60]	0.8756	0.0036	0.0074	0.0021	0.0170	0.0190	Z p_T [GeV]	[30, 40]	0.8874	0.0057	0.0028	0.0021	0.0037	0.0077	Z $\lvert y\rvert$	[0.20, 0.40]	0.8136	0.0093	0.0004	0.0019	0.0045	0.0105
$\lvert y_{boost}(Z, b)\rvert$	[1.60, 2.00]	0.8856	0.0056	0.0073	0.0021	0.0233	0.0251	Z p_T [GeV]	[40, 60]	0.9157	0.0065	0.0052	0.0022	0.0032	0.0091	Z $\lvert y\rvert$	[0.40, 0.60]	0.8046	0.0094	0.0019	0.0019	0.0021	0.0100
$\lvert y_{boost}(Z, b)\rvert$	[2.00, 2.50]	0.8651	0.0143	0.0154	0.0020	0.0221	0.0306	Z p_T [GeV]	[60, 80]	0.9284	0.0094	0.0015	0.0022	0.0036	0.0104	Z $\lvert y\rvert$	[0.60, 0.80]	0.8130	0.0098	0.0094	0.0019	0.0032	0.0141
$\lvert\Delta y(Z, b)\rvert$	[0.00, 0.20]	0.8862	0.0039	0.0004	0.0021	0.0027	0.0052	Z p_T [GeV]	[80, 110]	0.9403	0.0143	0.0283	0.0022	0.0039	0.0320	Z $\lvert y\rvert$	[0.80, 1.20]	0.7898	0.0076	0.0047	0.0019	0.0063	0.0111
$\lvert\Delta y(Z, b)\rvert$	[0.20, 0.40]	0.8952	0.0039	0.0079	0.0021	0.0028	0.0095	Z p_T [GeV]	[110, 200]	0.9124	0.0308	0.0158	0.0022	0.0053	0.0351	Z $\lvert y\rvert$	[1.20, 1.60]	0.7851	0.0092	0.0073	0.0019	0.0071	0.0139
$\lvert\Delta y(Z, b)\rvert$	[0.40, 0.60]	0.9051	0.0041	0.0055	0.0021	0.0030	0.0078	Z p_T [GeV]	[200, 500]	0.8616	0.1489	0.0065	0.0020	0.0088	0.1493	Z $\lvert y\rvert$	[1.60, 2.50]	0.7810	0.0118	0.0162	0.0018	0.0072	0.0214
$\lvert\Delta y(Z, b)\rvert$	[0.60, 0.80]	0.8988	0.0043	0.0017	0.0021	0.0031	0.0060	Z $\lvert y\rvert$	[0.00, 0.20]	0.9065	0.0039	0.0112	0.0021	0.0108	0.0162	Z $\lvert y\rvert$	[1.60, 2.50]	0.7810	0.0118	0.0162	0.0018	0.0072	0.0214
$\lvert\Delta y(Z, b)\rvert$	[0.80, 1.20]	0.8894	0.0034	0.0129	0.0021	0.0037	0.0140	Z $\lvert y\rvert$	[0.20, 0.40]	0.8930	0.0038	0.0058	0.0021	0.0105	0.0127								
$\lvert\Delta y(Z, b)\rvert$	[1.20, 1.60]	0.8818	0.0039	0.0112	0.0021	0.0042	0.0128	Z $\lvert y\rvert$	[0.40, 0.60]	0.8948	0.0039	0.0035	0.0021	0.0128	0.0140								
$\lvert\Delta y(Z, b)\rvert$	[1.60, 2.00]	0.8661	0.0048	0.0082	0.0020	0.0053	0.0111	Z $\lvert y\rvert$	[0.60, 0.80]	0.9017	0.0041	0.0056	0.0021	0.0127	0.0146								
$\lvert\Delta y(Z, b)\rvert$	[2.00, 3.00]	0.8547	0.0049	0.0264	0.0020	0.0107	0.0290	Z $\lvert y\rvert$	[0.80, 1.20]	0.8914	0.0032	0.0052	0.0021	0.0164	0.0176								
$\lvert\Delta y(Z, b)\rvert$	[3.00, 5.00]	0.8228	0.0120	0.0697	0.0019	0.0380	0.0803	Z $\lvert y\rvert$	[1.20, 1.60]	0.8936	0.0038	0.0037	0.0021	0.0207	0.0214								
								Z $\lvert y\rvert$	[1.60, 2.00]	0.8940	0.0052	0.0153	0.0021	0.0271	0.0316								

Table 34: Multiplicative correction factors applied to parton-level theory predictions from MCFM to account for the softening of the jet spectra due to fragmentation and hadronization and to the enhancement of the cross section due to multi-parton interactions (MPI). A constant QED multiplicative factor, correcting the born lepton definition in MCFM to the dressed definition used in the analysis, is included. The various sources of uncertainties (MC statistics, differences between PYTHIA and SHERPA in the modeling of NP-QCD effects, QED final state radiation (FSR) correction and uncertainties on the modeling of the double parton interaction from a comparison to data) are listed separately, along with their quadratic sum, σ_{total}.

Generators set–up					
Generator	b–quark mass	PDFs	HF scheme	Parton shower	FSR
ALPGEN+HERWIG+JIMMY	✓	CTEQ61L	4FNS	✓	✓
SHERPA	✓	CT10	5FNS	✓	✓
aMC@NLO 5FNS	✗	MSTW2008	5FNS	✓	✓
aMC@NLO 4FNS	✓	MSTW2008_NF4	4FNS	✓	✓
MCFM	✗	MSTW2008	5FNS	✗	✗

MCFM parameters

Electroweak parameters				
$G_F[GeV^{-2}]$	$M_W[GeV]$	$M_Z[GeV]$	$\alpha(M_Z)$	$\sin^2\theta_W$
1.16639×10^{-5}	80.398	91.187	calculated	calculated

Other parameters		
α_s	$m_b[GeV]$	$\Gamma_Z[GeV]$
0.12018	4.75	2.4952

Table 35: Summary of the theory calculations described in the text (top) and setting of the electroweak parameters (middle) and other relevant parameters (bottom) in the MCFM generator.

6.4 THEORETICAL UNCERTAINTIES AND A COMPARISON BETWEEN THEORY PREDICTIONS

The theory predictions described in the previous section can be characterized in terms of the flavor number scheme used in the QCD matrix element calculation (HF scheme), the treatment of b–quark mass effects, the availability of the parton shower simulation, and the simulation of the QED FSR. A summary of them is presented in Tab. 35.

Where possible a consistent treatment of the electroweak parameters and $\alpha_s(M_Z)$ is ensured. Anyway, as discussed later, the theory predictions are affected by large uncertainties, related to the μ_F and μ_R variations, while the exact choice of the electroweak parameters has a negligible impact on the results. The electroweak parameters choice for the MCFM calculations is provided in the middle of Tab. 35. Other parameters relevant for the calculation are presented at the bottom of Tab. 35.

A comparison of the theory predictions for integrated cross sections corresponding to the four measured observables $\sigma(Zb)$, $\sigma(Zb) \times N_{b\text{–jet}}$, $\sigma(Zb)^\star \times N_{b\text{–jet}}$ and $\sigma(Zbb)$ is summarized in Tab. 37. The next–to–leading order calculations derived with MCFM are shown with their statistical as well as systematic uncertainties; the systematic uncerainties are presented separately for each prediction obtained by changing the PDFs set. All other theory calculations are presented with their statistical uncertainty only. A breakdown of theoretical uncertainties in all the analysis

m_b [GeV]	$\Delta\sigma(Zb)$ [%]	$\Delta\sigma(Zbb)$ [%]
$m_b = 4$	$+6.0$	-0.4
$m_b = 4.25$	$+3.8$	-0.3
$m_b = 4.5$	$+1.9$	-0.1
$m_b = 4.75$	nominal	nominal
$m_b = 5$	-1.8	$+0.1$
$m_b = 5.25$	-3.5	$+0.2$
$m_b = 5.5$	-5.3	$+0.3$

Table 36: Effect of the m_b variations in the MCFM calculations for the cross sections $\sigma(Zb)$ and $\sigma(Zbb)$.

bins is presented if Fig. 69 for the MCFM predictions obtained with MSTW2008 parton distribution function set.

The systematic uncertainties on the MCFM calculation are defined as follows.

- Factorization and renormalization scales variations. As already described in Sec. 6.2, they are set as $\mu_F = \mu_R = \sqrt{M_Z^2 + p_{T,Z}^2}$ in the nominal MCFM calculations; the dependence of the cross sections from their settings is evaluated by varying by a factor of two independently both scales leading to eight possible combinations in addition to the nominal scale choice; the envelope of the cross section variations is then used to define a systematic uncertainty.
- Parton distribution functions and α_s. An uncertainty due to the parton density functions and α_s is defined following the prescriptions highlighted in Sec. 1.2.
- Uncertainty on the correction factors. It is mainly driven by the uncertainty of the QCD non perturbative corrections which are a combination of a statistical component araising from MC statistics, a term due to the comparison between SHERPA and PYTHIA generators and a contribution related to validation with data of hard double–parton–interactions as explained in Sec. 6.3; the uncertainty on the QED FSR correction is also propagated although it contributes at per–mille level.

The predictions for the $Z + b$ and $Z + bb$ cross sections can be sensitive to the choice of the b–quark mass, m_b, in the QCD matrix element calculations. A dedicated study of this effect is performed by interfacing the MCFM generator with a special PDF set, MSTW2008NLO_MBRANGE [133], which has the same setting as the nominal MSTW2008 PDFs but it provides also six additional PDFs derived from global fit with varied m_b value in input. The cross section variation due to the change of the m_b input value can be seen from Tab. 36, both for the $\sigma(Zb)$ and $\sigma(Zbb)$ cross sections. According to Ref. [133], a reliable estimate of the uncertainty due to the b–quark mass is then obtained by taking the cross section envelope in the range $m_b[\text{GeV}] \in [4.5, 5]$; the variations of $\sigma(Zb)$ and $\sigma(Zbb)$ are observed to be respectively of $\sim 1.8\%$ and $\sim 0.1\%$. These uncertainties are not taken into account in the MCFM predictions discussed in the following.

σ [pb]	PDF	MCFM	$\sigma_{stat.}$	σ_{α_s}	σ_{μ_F,μ_R}	σ_{PDFs}	$\sigma_{C^{NP}}$
$\sigma(Zb)$	MSTW2008	5.230	±0.033	$+0.106\ -0.142$	$+0.666\ -0.687$	$+0.121\ -0.099$	±0.109
$\sigma(Zb)\times N_{b-jet}$	MSTW2008	5.463	±0.036	$+0.122\ -0.147$	$+0.715\ -0.722$	$+0.116\ -0.097$	±0.111
$\sigma^{\star}(Zb)\times N_{b-jet}$	MSTW2008	4.331	±0.033	$+0.103\ -0.145$	$+0.376\ -0.449$	$+0.092\ -0.078$	±0.063
$\sigma(Zbb)$	MSTW2008	0.413	±0.008	$+0.010\ -0.022$	$+0.056\ -0.054$	$+0.007\ -0.006$	±0.007
$\sigma(Zb)$	CT10	4.854	±0.026	$+0.060\ -0.108$	$+0.550\ -0.651$	$+0.141\ -0.147$	±0.106
$\sigma(Zb)\times N_{b-jet}$	CT10	5.073	±0.030	$+0.063\ -0.112$	$+0.613\ -0.683$	$+0.131\ -0.136$	±0.110
$\sigma^{\star}(Zb)\times N_{b-jet}$	CT10	4.028	±0.031	$+0.051\ -0.087$	$+0.321\ -0.424$	$+0.105\ -0.107$	±0.059
$\sigma(Zbb)$	CT10	0.386	±0.004	$+0.018\ -0.013$	$+0.049\ -0.045$	$+0.015\ -0.015$	±0.006
$\sigma(Zb)$	NNPDF2.3	5.424	±0.019	$+0.069\ -0.089$	$+0.647\ -0.691$	$-0.089\ +0.089$	±0.109
$\sigma(Zb)\times N_{b-jet}$	NNPDF2.3	5.664	±0.032	$+0.071\ -0.088$	$+0.700\ -0.726$	$-0.079\ +0.079$	±0.113
$\sigma^{\star}(Zb)\times N_{b-jet}$	NNPDF2.3	4.491	±0.026	$+0.055\ -0.068$	$+0.361\ -0.444$	$-0.062\ +0.062$	±0.065
$\sigma(Zbb)$	NNPDF2.3	0.423	±0.009	$+0.016\ -0.011$	$+0.064\ -0.049$	$-0.006\ +0.006$	±0.007

σ [pb]	SHERPA	ALPGEN	aMC@NLO 5FNS	aMC@NLO 4FNS
$\sigma(Zb)$	3.7700 ± 0.0077	2.5811 ± 0.0068	4.679 ± 0.0036	3.394 ± 0.0018
$\sigma(Zb)\times N_{b-jet}$	4.2084 ± 0.0080	2.9240 ± 0.0072	5.010 ± 0.0037	3.906 ± 0.0020
$\sigma^{\star}(Zb)\times N_{b-jet}$	3.6429 ± 0.0073	2.3769 ± 0.0058	4.225 ± 0.0035	3.286 ± 0.0018
$\sigma(Zbb)$	0.4216 ± 0.0023	0.3169 ± 0.0018	0.314 ± 0.0009	0.485 ± 0.0007

Table 37: Comparison of the theory predictions at particle level. For the MCFM calculation the breakdown of the error into the various components is shown at the top for three choices of the PDF set. All the other calculations are shown at the bottom.

The leading order multileg predictions obtained with the ALPGEN+HERWIG+JIMMY and SHERPA generators are found to be in remarkable disagreement for the $Z+b$ observables with a 35% mismatch of the integrated cross sections. For the $Z+bb$ cross section the agreement between the two generators is found to improve by a 10%. The cross sections derived with SHERPA are always found to be larger than the corresponding obsevables calculated with ALPGEN+HERWIG+JIMMY.

The MCFM predictions are presented with the full uncertainty breakdown for three different PDF sets, namely MSTW2008, CT10 and NNPDF2.3. The dominant systematic uncertainty is due to the μ_F and μ_R variations consisting in about 13% both for $Z+b$ and $Z+bb$ cross sections with the exception of $\sigma(Zb)^{\star}\times N_{b\text{–jet}}$ which is affected by a $\sim$ 10% error. The uncertainties on the non perturbative and QED final state radiation corrections are found to be about 2%, thus they don't affect significantly the accuracy of the calculation. The uncertainties due to the PDFs errors are observed to be also much smaller than the scale uncertainty, being about 1.7%–2.3%, 2.6%–3.8%, and 1.3%–1.6% for MSTW2008, CT10 and NNPDF2.3, respectively.

The MCFM and 5FNS aMC@NLO calculations are expected to provide consistent cross section predictions for the $Z+b$ final state although aMC@NLO is interfaced with a parton shower and MCFM is corrected bin by bin for the non perturbative effects; for the $Z+bb$ cross section the 5FNS aMC@NLO calculation is only accurate at leading order while MCFM has a NLO accuracy. It can be observed from

Tab. 37 that for the most inclusive observables $\sigma(Zb)$ and $\sigma(Zb) \times N_{b\text{–jet}}$ the two calculations differ by about 10%; a proper comparison between the two predictions would need to take into account all the uncorrelated or not fully correlated systematic uncertainties. However, for the observable $\sigma^{\star}(Zb) \times N_{b\text{–jet}}$ MCFM and 5FNS–aMC@NLO are found to be different by less than 3%; this can be interpreted as a reduced sensitivity to the non perturbative effects and parton shower for the phase space region where Z $p_T > 20$ GeV.

Finally, it is interesting to compare the MCFM and 4FNS aMC@NLO calculations which are NLO accurate for both the $Z + b$ and $Z + bb$ cross sections. The MCFM prediction, which is derived in 5FNS, is higher than the 4FNS aMC@NLO calculation for all the $Z + b$ observables by 30%–50%. On the other hand the 4FNS aMC@NLO calculation is observed to predict the $Z + bb$ cross section higher than the MCFM generator and the two predictions differ by more than 6 statistical standard deviations.

It would be possible to provide a more quantitative comparison between the 5FNS and the 4FNS calculations with a proper treatment of the correlation between the uncertainties. For the MCFM predictions, as can be observed from Tab. 37, the most important theoretical uncertainty is due to the variations of factorization and renormalization scales.

The degree of correlation between the scale variations in the 5FNS and 4FNS computations is not a priori known. Therefore, a dedicated study by using the aMC@NLO generator is performed; the 4FNS and 5FNS predictions in the aMC@NLO framework are obtained for all the μ_F and μ_R variations. The results are presented in Tab. 38 for the integrated cross sections and in Fig. 70–71 for all the differential observables in the 4FNS and 5FNS, respectively.

The 4FNS prediction exhibits a large variation, up to $\sim 20\%$, due to the renormalization scale change; it is also observed that the uncertainty is typically asymmetric being larger in the upward variation of μ_R. The effect of varying the factorization scale is typically small, less than 1%, but increases in some regions, like high b–jet p_T. On the other hand, the change in the 5FNS calculation due to the μ_F and μ_R variations shows a very different pattern; the cross section predictions change by more than 5% due to the μ_F variations and the dominant contribution to the uncertainty envelope is driven by the scale setting with μ_F and μ_R varied in the opposite directions.

As reported in Tab. 38, the scale dependence of the cross sections obtained with the MCFM generator is similar to the 5FNS aMC@NLO but with a weaker sensitivity to μ_F; thus a slightly smaller total uncertainty is observed for the MCFM prediction.

The feature of the scales dependence in the 4FNS and 5FNS deserves more phenomenological studies in a future analysis.

The tensions among the various theoretical predictions are interpreted also in the next section where the calculations are compared to the measured cross sections.

μ_R/μ_R^0	μ_F/μ_F^0	$\sigma/\sigma^0 - 1.$			
		$\sigma(Zb)$	$\sigma(Zb) \times N_{b-jet}$	$\sigma^\star(Zb) \times N_{b-jet}$	$\sigma(Zbb)$
aMC@NLO 5FNS					
1	1	0.000	0.000	0.000	0.000
1	2	-0.065	-0.062	-0.061	-0.025
1	0.5	+0.056	+0.054	+0.054	+0.018
2	1	+0.062	+0.065	+0.059	+0.096
2	2	+0.002	+0.007	+0.003	+0.078
2	0.5	+0.117	+0.117	+0.110	+0.109
0.5	1	-0.058	-0.059	-0.056	-0.080
0.5	2	-0.124	-0.123	-0.120	-0.109
0.5	0.5	-0.002	-0.006	-0.002	-0.059
env. of all var.s UP		+0.117	+0.117	+0.110	+0.109
env. of all var.s DW		-0.124	-0.123	-0.120	-0.109
env. of one scale var.s DW		+0.062	+0.065	+0.059	+0.096
env. of one scale var.s DW		-0.065	-0.062	-0.061	-0.080
aMC@NLO 4FNS					
1	1	0.000	0.000	0.000	0.000
1	2	+0.003	+0.004	+0.005	+0.010
1	0.5	-0.003	-0.004	-0.004	-0.009
2	1	+0.169	+0.169	+0.174	+0.171
2	2	+0.168	+0.169	+0.175	+0.178
2	0.5	+0.171	+0.170	+0.175	+0.168
0.5	1	-0.136	-0.136	-0.140	-0.139
0.5	2	-0.131	-0.131	-0.134	-0.127
0.5	0.5	-0.141	-0.142	-0.147	-0.150
env. of all var.s UP		+0.171	+0.170	+0.175	+0.178
env. of all var.s DW		-0.141	-0.142	-0.147	-0.150
env. of one scale var.s UP		+0.169	+0.169	+0.174	+0.171
env. of one scale var.s DW		-0.136	-0.136	-0.140	-0.139
MCFM 5FNS					
1	1	0.000	0.000	0.000	0.000
1	2	-0.027	-0.030	-0.023	+0.017
1	0.5	+0.030	+0.033	+0.024	+0.001
2	1	+0.058	+0.080	+0.061	+0.090
2	2	+0.031	+0.045	+0.028	+0.094
2	0.5	+0.095	+0.121	+0.099	+0.068
0.5	1	-0.073	-0.099	-0.062	-0.097
0.5	2	-0.093	-0.119	-0.078	-0.057
0.5	0.5	-0.052	-0.073	-0.062	-0.087
env. of all var.s UP		+0.095	+0.121	+0.099	+0.094
env. of all var.s DW		-0.093	-0.119	-0.078	-0.097
env. of one scale var.s UP		+0.058	+0.080	+0.061	+0.090
env. of one scale var.s DW		-0.073	-0.099	-0.062	-0.097

Table 38: Relative variations of the aMC@NLO predictions in 5FNS (top) and 4FNS (middle) for all integrated cross sections as a function of changes in the renormalization μ_R and factorization μ_f scales. The dependency of the MCFM predictions on the scales is presented (bottom). The nominal factorization and renormalization scales are indicated as μ_F^0 and μ_R^0.

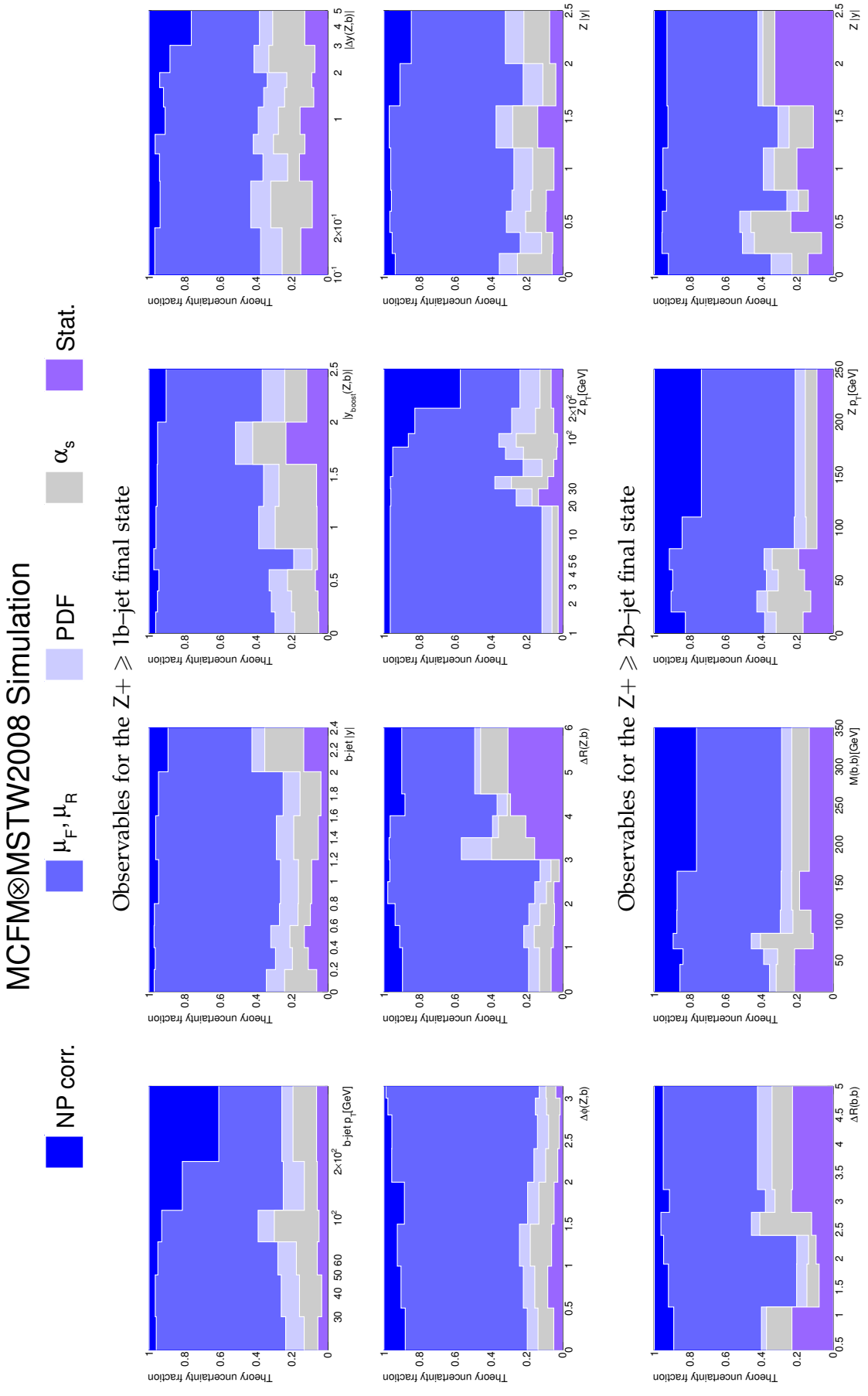

Figure 69: Breakdown of the theory uncertainties for the calculation performed by using the MCFM generator interfaced with MSTW2008 PDFs for all the differential distribution studied in the $Z+$ b and $Z+$ bb final states.

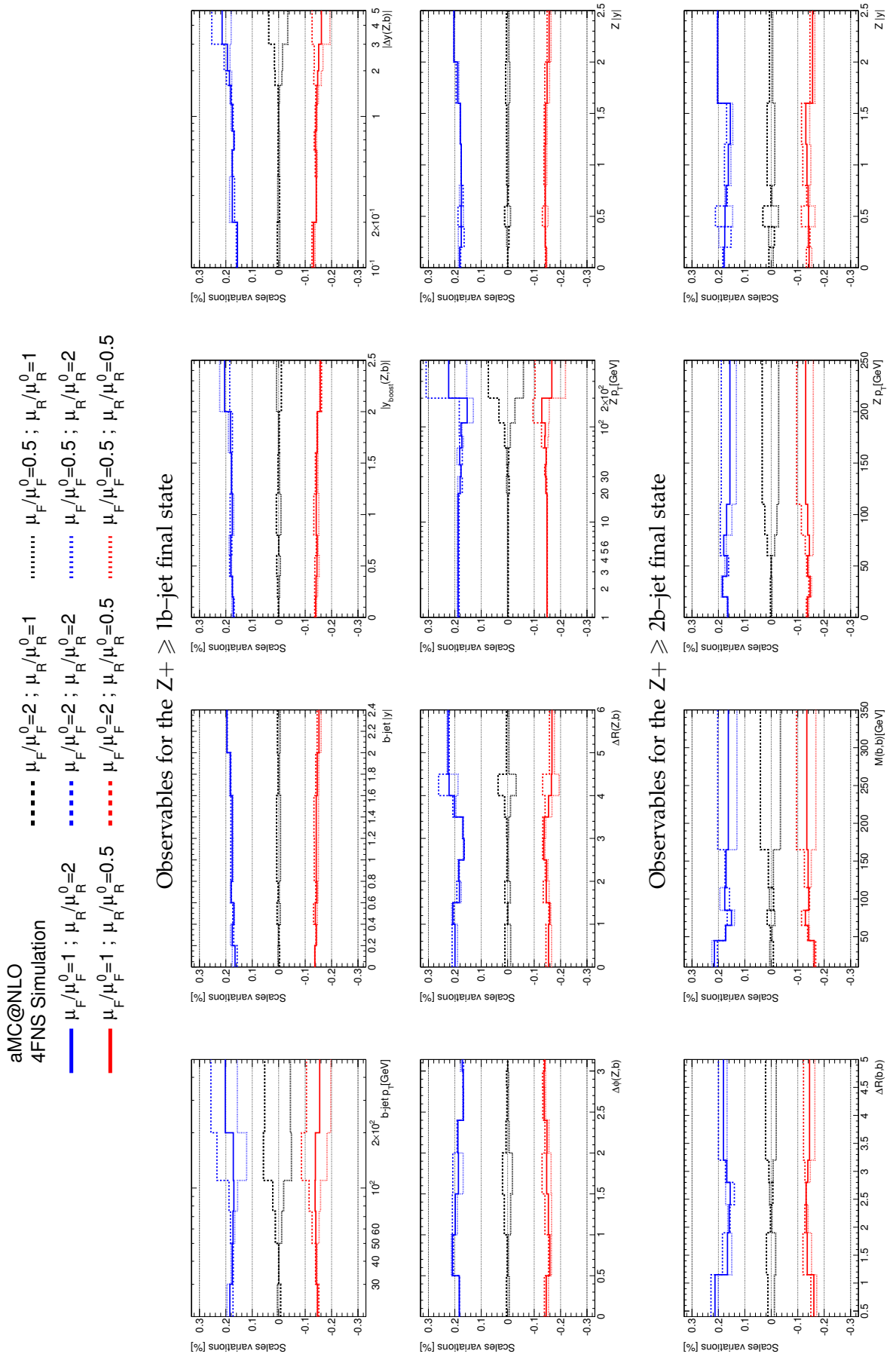

Figure 70: Percentual uncertainty of the 4FNS aMC@NLO predictions due to the variations of μ_F and μ_R. The effect of all possible scale settings are shown for each differential distribution corresponding to the $Z + b$ and $Z + bb$ cross sections.

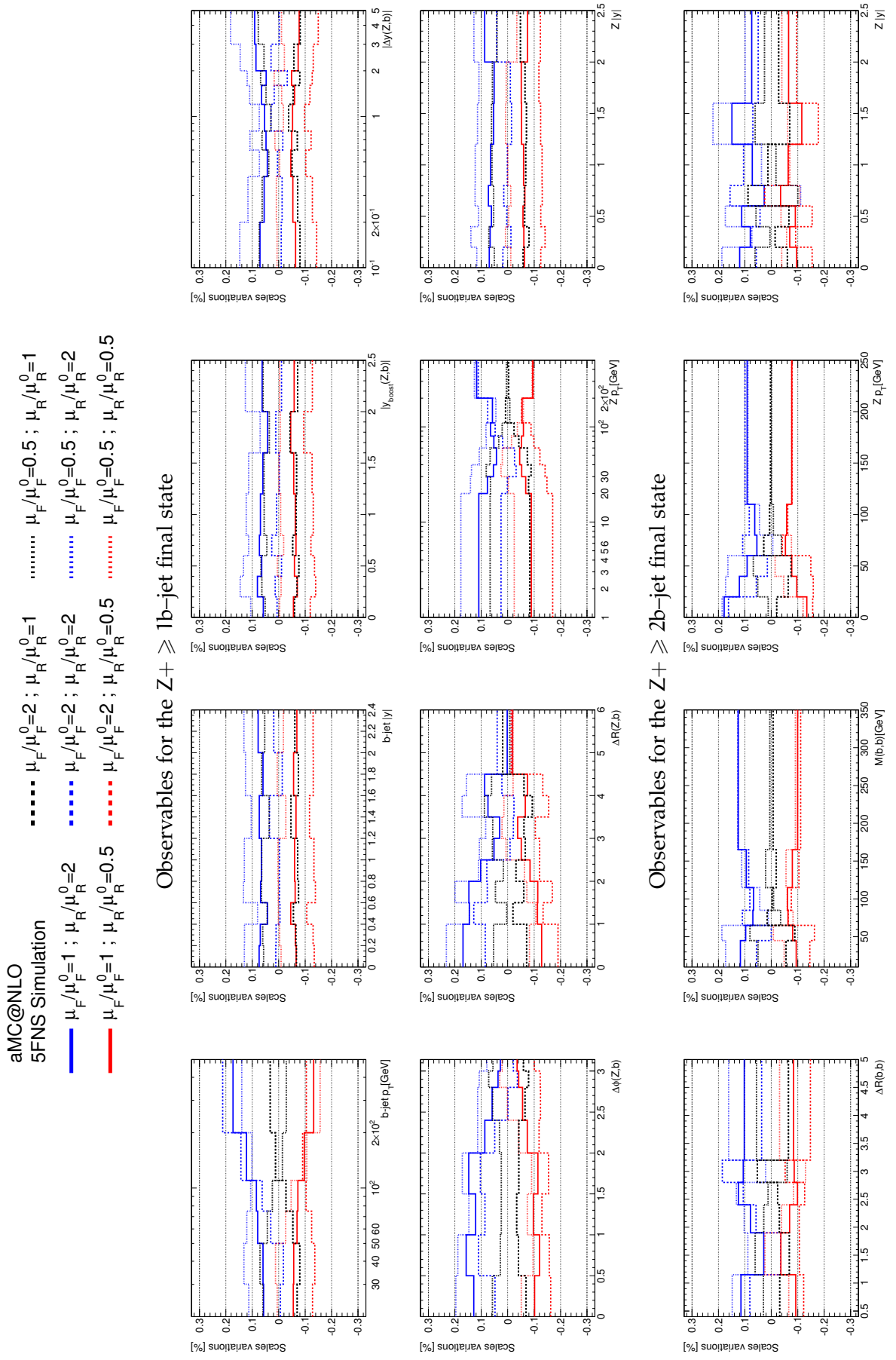

Figure 71: Percentual uncertainty of the 5FNS aMC@NLO predictions due to the variations of μ_F and μ_R. The effect of all possible scale settings are shown for each differential distribution corresponding to the $Z + b$ and $Z + bb$ cross sections.

6.5 INTEGRATED CROSS SECTIONS

The measured integrated cross sections are compared to the theory predictions discussed in Sec. 6.4 and Sec. 6.2.

The detector level yields in data and the predictions of the Monte Carlo generator ALPGEN+HERWIG+JIMMY were already compared in Chap. 4 where the generator signal yield was presented normalized to the NNLO QCD inclusive Z cross section calculation; however, in this section as for each prediction, the ALPGEN+HERWIG+JIMMY calculation is shown without applying any k–factor.

All the integrated cross sections are shown in Fig. 72 and Fig. 73 where the data are compared to the NLO and LO multileg calculations previously described, including the MCFM prediction obtained with three sets of parton distribution functions. The uncertainty on the data is obtained by combining in quadrature the total systematic uncertainty with the statistical error; the statistical error is presented as an azure band while, the sum in quadrature of the statistical and systematic uncertainties is shown as a green band; the central value of the measured cross section is presented as a vertical blu line. The uncertainty on the MCFM predictions are derived as described in Sec. 6.4 by combining in quadrature the envelope due to μ_F and μ_R variations as well as the PDFs uncertainties, and the errors related to α_s, QCD non perturbative corrections including the DPI uncertainty and QED final state radiation and errors related to it; the small statistical uncertainty on the MCFM calculations are shown with an inner bar while the outer bar is the total uncertainty obtained adding in quadrature the total systematic and the statistical errors; in the case of the NLO predictions from aMC@NLO the scale uncertainty has been evaluated as described in the previous section and it is shown combined to the statistical uncertainty. All the other calculations are presented without systematic uncertainties, only the statistical uncertainty is shown.

The per–jet cross sections $\sigma(Zb) \times N_{b\text{–jet}}$ and $\sigma^{\star}(Zb) \times N_{b\text{–jet}}$ are shown in Fig. 72; the next–to–leading order MCFM predictions (5FNS) are observed to predict well the observed jet–level cross sections measured in data; the maximum deviation between MCFM and the data is observed to be 1.2 standard deviation of the data cross section, specifically observed for the calculation performed using the CT10 for the $\sigma^{\star}(Zb) \times N_{b\text{–jet}}$ cross section. Also the 5FNS prediction obtained with the aMC@NLO generator describes well the data; on the other hand the 4FNS aMC@NLO calculation underpredict the measured cross section in data up to 3 data standard deviations consistently for the $\sigma(Zb) \times N_{b\text{–jet}}$ and $\sigma^{\star}(Zb) \times N_{b\text{–jet}}$ cross sections. The leading order multileg 4FNS ALPGEN+HERWIG+JIMMY cross sections are found to be smaller than the measurements by $\sim 50\%$, while the LO multileg predictions in 5FNS obtained with SHERPA are found to be much closer to the data cross section, underestimating the measurements by $\sim 20\%$.

A consistent picture is observed from the integrated cross section for the production of at least one b–jet in association with a Z boson shown in Fig. 73; the theory predictions exhibit the same kind of hierarchy of the jet–level cross sections and the data favor the 5FNS NLO calculation of MCFM and aMC@NLO; the next–to–leading order aMC@NLO calculation in 4FNS is observed to underestimate the data by 30%, as already observed for the per–jet cross sections, while the 5FNS NLO calculations are closer to the data, but the MCFM prediciton obtained with the NNPDF2.3 is ob-

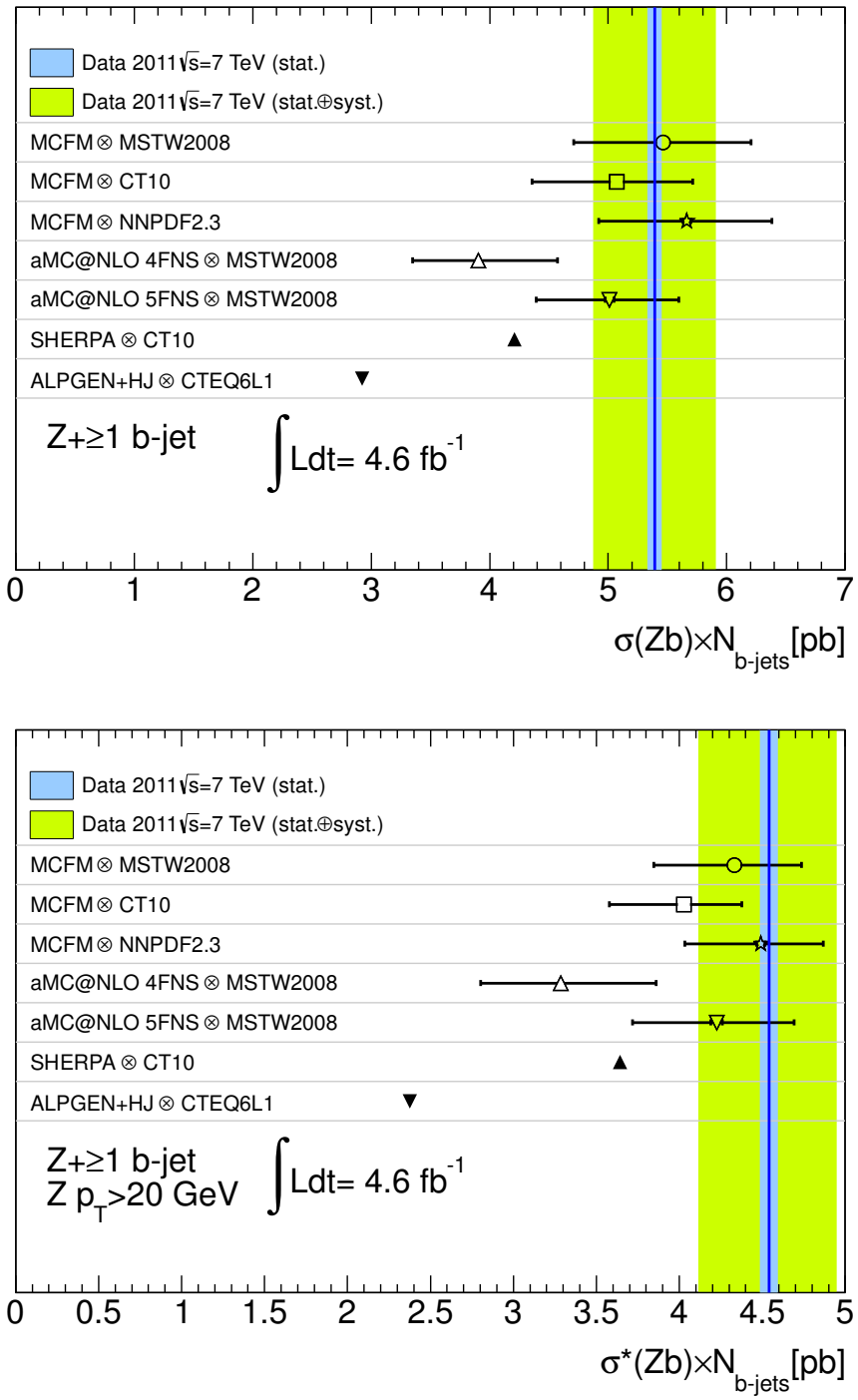

Figure 72: Per–jet cross sections $\sigma(Zb) \times N_{b\text{–jet}}$ (top) and $\sigma^*(Zb) \times N_{b\text{–jet}}$ (bottom); the data are presented displaying separately the statistical (azure bands) and the total uncertainties (green bands); the MCFM calculation is shown with its statistical error (inner bars) as well as the total uncertainty (outer bars); the aMC@NLO calculations are presented with the uncertainty due to the μ_R–μ_F variations (outer bars) combined in quadrature with the statistical error (inner bars); the LO multileg predictions are presented with their statistical uncertainty only.

served to overestimate the data by ~ 13%. The multileg predictions underestimate the data cross section both for the 4FNS implemented in ALPGEN+HERWIG+JIMMY and the 5FNS of the SHERPA generator, respectively by a ~ 50% and ~ 20%.

The measurement of the cross section for Z production in association with at least two b–jets is less precise, with a total uncertainty of about 15%. However, it shows a substantial agreement of the aMC@NLO prediction derived with the 4FNS, in spite of the poor description of the cross sections for the production of a Z and at least one b–jet; the aMC@NLO calculation in 5FNS underestimates the data by 40%, not surprisingly since it only provides a leading order accuracy for this final state. The MCFM calculation underestimates the data cross sections by about 20%–25% corresponding up to 1.9 data standard deviations. The multileg predictions from the ALPGEN+HERWIG+JIMMY underpredict the data cross section by 40% while the cross section calcuated with SHERPA is found to be closer to the data providing a cross section smaller by 20% with respect to the measurement as also observed for the $Z + b$ final state.

The measured integrated cross sections are also summarized in Tab. 39 and are compared to the theory predictions previously described.

The integrated cross section measurement and the comparison with the theory predictions are found to be consistent with the results previously reported by ATLAS [92] based on the limited statistics of the 2010 data. The CMS results [88] are consistent with the results in Tab. 39 showing that the fiducial $Z + b$ cross section is better described by predictions based on the 5FNS, while the two theoretical approaches 5FNS and 4FNS are both consistent with the data for the $Z + bb$ cross section. The current NLO calculations still exhibit a large dependence from the factorization and renormalization scales therefore also the aMC@NLO prediction obtained with the 4FNS is in agreement with the data taking into account the uncertainty on the calculation.

It can be noticed that lowering the renormalization scale (for example by a factor 2) like it was done for estimating the scale dependence of the prediction, reduces the data–theory discrepancy by about a factor two in the 4FNS. The impact on the 4FNS predictions of the scale choice is discussed exaustively in Ref. [128] along with the interplay between the *variable flavor number scheme* and the *fixed flavor number scheme*.

What can be clearly seen from the data is that the experimental precision is now accurate enough to challenge the implementation of the theory predictions and typically allows to choose the most suitable approach for a given observable or to reconcile the various predictions based on experimentally justified choice of configuration parameters for the calculation.

6.6 DIFFERENTIAL CROSS SECTIONS

All the measured particle level differential cross sections are shown from Fig. 59 to Fig. 64 for both for the $Z + b$ and the $Z + bb$ observables. Like in the case of the integrated cross sections, theory predictions are quoted with full error (MCFM), dominant error (scale variations for aMC@NLO) or statistical error only.

The b–jet p_T and the b–jet $|y|$ are presented in Fig. 59. The b–jet p_T is well described by all the calculations although the MCFM calculation provides a slightly

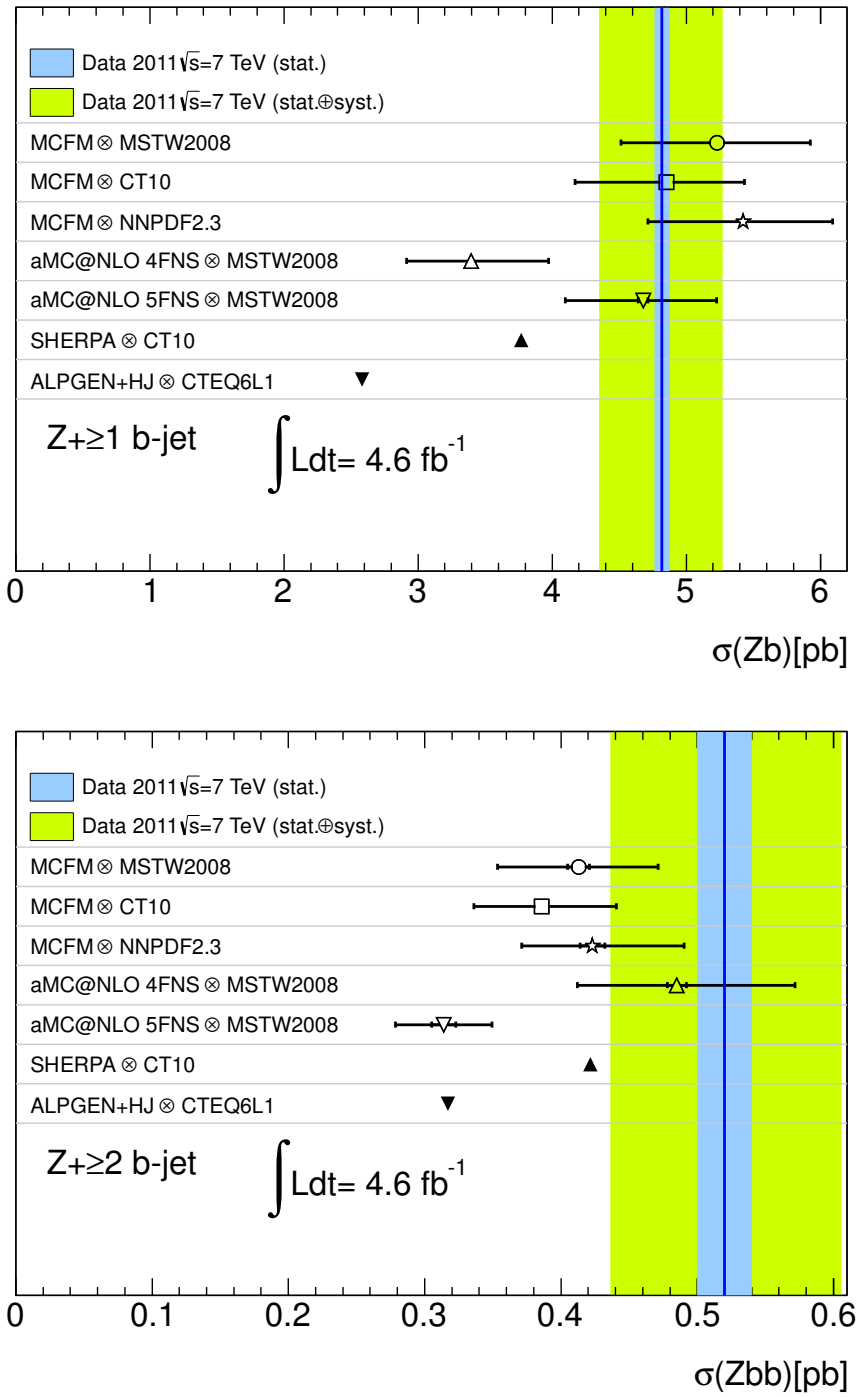

Figure 73: Per–jet cross sections $\sigma(Zb)$ (top) and $\sigma(Zbb)$ (bottom); the data are presented displaying separately the statistical (azure bands) and the total uncertainties (green bands); the MCFM calculation is shown with its statistical error (inner bars) as well as the total uncertainty (outer bars); the aMC@NLO calculations are presented with the uncertainty due to the μ_R–μ_F variations (outer bars) combined in quadrature with the statistical error (inner bars); the LO multileg predictions are presented with their statistical uncertainty only.

	$\sigma(Zb)$ [fb]	$\sigma(Zb) \times N_{b-jets}$ [fb]	$\sigma^{\star}(Zb) \times N_{b-jets}$ [fb]	$\sigma(Zbb)$ [fb]
Data	$4820 \pm 60^{+360}_{-380}$	$5390 \pm 60 \pm 480$	$4540 \pm 55 \pm 330$	$520 \pm 20^{+74}_{-72}$
MCFM(MSTW2008)	$5230 \pm 30^{+690}_{-710}$	$5460 \pm 40^{+740}_{-740}$	$4331 \pm 30^{+400}_{-480}$	$410 \pm 10^{+60}_{-60}$
MCFM(CT10)	$4850 \pm 30^{+580}_{-680}$	$5070 \pm 30^{+640}_{-710}$	$4030 \pm 30^{+350}_{-450}$	$386 \pm 5^{+55}_{-50}$
MCFM(NNPDF2.3)	$5420 \pm 20^{+670}_{-710}$	$5660 \pm 30^{+720}_{-740}$	$4490 \pm 30^{+380}_{-460}$	$420 \pm 10^{+70}_{-50}$
aMC@NLO (4FNS)	$3390 \pm 20^{+580}_{-480}$	$3910 \pm 20^{+660}_{-560}$	$3290 \pm 20^{+580}_{-460}$	$485 \pm 7^{+80}_{-70}$
aMC@NLO (5FNS)	$4680 \pm 40^{+550}_{-580}$	$5010 \pm 40^{+590}_{-620}$	$4220 \pm 40^{+460}_{-510}$	$314 \pm 9^{+30}_{-30}$
SHERPA	3770 ± 10	4210 ± 10	3640 ± 10	422 ± 2
ALPGEN	2580 ± 10	2920 ± 10	2380 ± 10	317 ± 2

Table 39: Measurement and theory predictions for the total fiducial cross-sections. The MCFM results are corrected for MPI, non-perturbative QCD effects and QED radiation effects. The statistical uncertainty is quoted first. For the data the second uncertainty is the total systematic; for MCFM the second uncertainty is the sum in quadrature of all theory uncertainties; and for aMC@NLO, the second uncertainty is the scale uncertainty.

harder spectrum. The b–jet $|y|$ is well described by the MCFM and 5FNS aMC@NLO calculations and reasonably well also by multileg generators, although for the latter a harder spectrum is observed, consistently for SHERPA and ALPGEN+HERWIG+JIMMY; the 4FNS aMC@NLO calculation does not describe well the distribution being about 70% below the data in most of the central region, while in the most forward region it becomes statistically consistent with the data.

The $|y_{boost}(Z, b)|$ distribution, presented in Fig. 60, shows the same features observed for the b–jet rapidity; namely the 4FNS aMC@NLO calculation isn't able to describe well the distribution, while all the other calculations are more accurate. The $|\Delta y(Z, b)|$ distribution is also reported in Fig. 60; a poor description from the MCFM and 4FNS aMC@NLO predictions is observed in the tail of $|\Delta y(Z, b)|$, while all the other calculations are tipically well behaving.

In Fig. 61 the $\Delta\phi(Z, b)$ and the $\Delta R(Z, b)$ distributions are shown. As already observed when comparing distributions of variables representing azimuthal separation between physics objects in data and NLO predictions [134] the limited multiplicity of the final state in the NLO calculation and the kinematic constraints prevent a proper description of the azimuthal shape. The disagreement is dramatic in the case of the fixed order MCFM prediction, but also rather large for the aMC@NLO MC. Multileg generators, allowing for multiple hard partons in the final state, are needed in order reproduce well the shape observed in data. The $\Delta R(Z, b)$ distribution is of course correlated with $\Delta\phi(Z, b)$ and, as expected, it highlights similar features.

The per–event $Z + b$ distributions, Z p_T and Z $|y|$, are presented in Fig. 62. The Z transverse momentum is clearly not very well described by all the predictions; typically, the NLO calculations provide a reasonable description of the intermediate p_T region (Z $p_T <$ 200 GeV) but tend to underpredict the measured cross section at high p_T; on the other hand the multileg generators are observed to predict a harder spectrum. The Z $|y|$ distribution is well predicted by the multileg generators; among the NLO caclulations the 5FNS aMC@NLO calculation provides a good

description of the data while the 4FNS aMC@NLO and MCFM tend to populate the central region more than observed in data.

The differential cross sections in events with at least two b–jets are measured with a tipical precision of 15%–30%, therefore they are not expected to provide a strong discrimination power between the generators. In addition, for these differential cross sections the 5FNS aMC@NLO calculation is not expected a priori to provide a good description of the data.

The $\Delta R(b,b)$ and $M(b,b)$ are shown in Fig. 63. The $\Delta R(b,b)$ is not well described by all the NLO calculations which underpredict the cross section for b–jets with small angular separation; on the other hand the multileg calculations provide a better prediction also in the low $\Delta R(b,b)$ regime. The modeling of the low $\Delta R(b,b)$ region in the NLO calculations points to a known problem of the state of art QCD predictions for final states with b–pairs. The calculation of the probability for a gluon to split in $b\bar{b}$ pair, which contributes to the $\Delta R(b,b)$ observation in the low value tail, is affected by technical and conceptual difficulties.

For the b–jets invariant mass $M(b,b)$ the multileg generators present a slightly softer spectrum, compared with the data while the NLO MCFM and the 4FNS aMC@NLO generators provide a slightly harder spectrum although they are statistically consistent with the data; among the NLO calculations the 4FNS aMC@NLO is observed to provide the best description of the $M(b,b)$ distribution.

The Z p_T and the Z $|y|$ distributions in events with at least two b–jets are presented in Fig. 64. They are found to be typically very well described by all the predictions given the current statistical uncertainties on the measurement.

As observed in Sec. 6.4 the predictions obtained with the MCFM generator, interfaced with the three PDFs sets MSTW2008, CT10 and NNPDF2.3, exhibit a relative offset, which can be as large as the total uncertainty on the data. It is interesting to understand whether the differences among these three predictions are enhanced in specific space space regions or if they provide different modeling of the differential distributions under consideration for the $Z+b$ and $Z+b\bar{b}$ final states. The measurement of the Z $|y|$ for the production of a Z boson in association with at least one or two b–jets is shown in Fig. 80 in comparison to the MCFM predictions obtained with MSTW2008, CT10 and NNPDF2.3 parton distribution functions; only the calculation performed with the MSTW2008 PDFs is shown with the full uncertainty band, while the other predictions are presented with their statistical uncertainty only. The complete set of distributions is provided in App. E for both the $Z+b$ and $Z+b\bar{b}$ observables. The Z $|y|$ in $Z+b$ events does not show any relative shape effects among the calculations but all of them mismodel the shape observed in data in the same manner; the Z $|y|$ in $Z+b\bar{b}$ events does not present the same kind of behavour within the current experimental uncertainty.

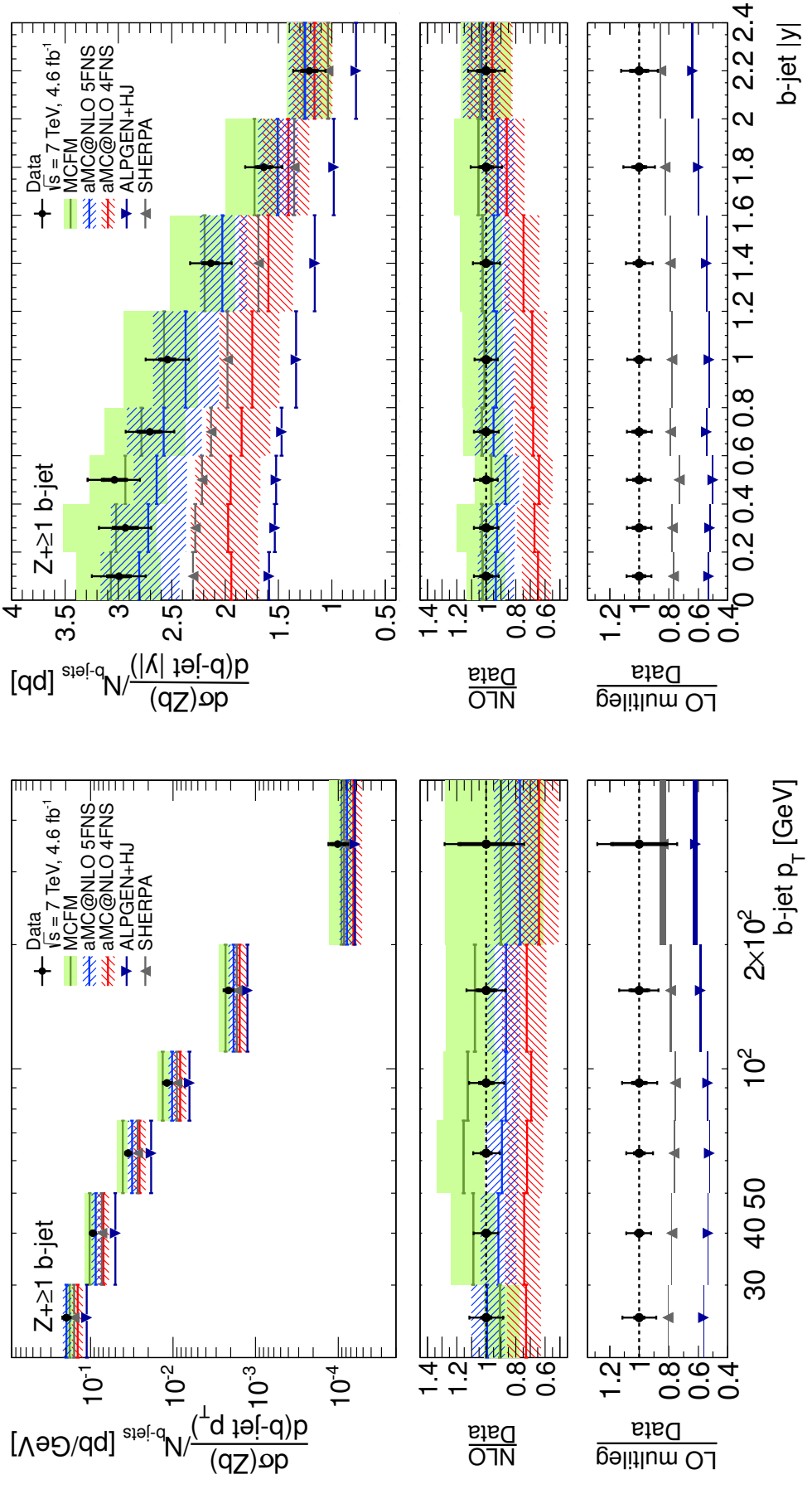

Figure 74: Differential cross section for the production of a Z boson in association with at least one b-jet as a function of the b-jet p_T (left) and of the b-jet |y| (right). The data points are presented along with their statistical (inner bars) and total uncertainty (outer bars); the MCFM calculation is shown with its total uncertainty (light green filled bands); the aMC@NLO calculations are presented with the uncertainty due to the μ_R–μ_F variations (red and blue shaded area) combined in quadrature with the statistical error; the LO multileg predictions are presented with their statistical uncertainty only.

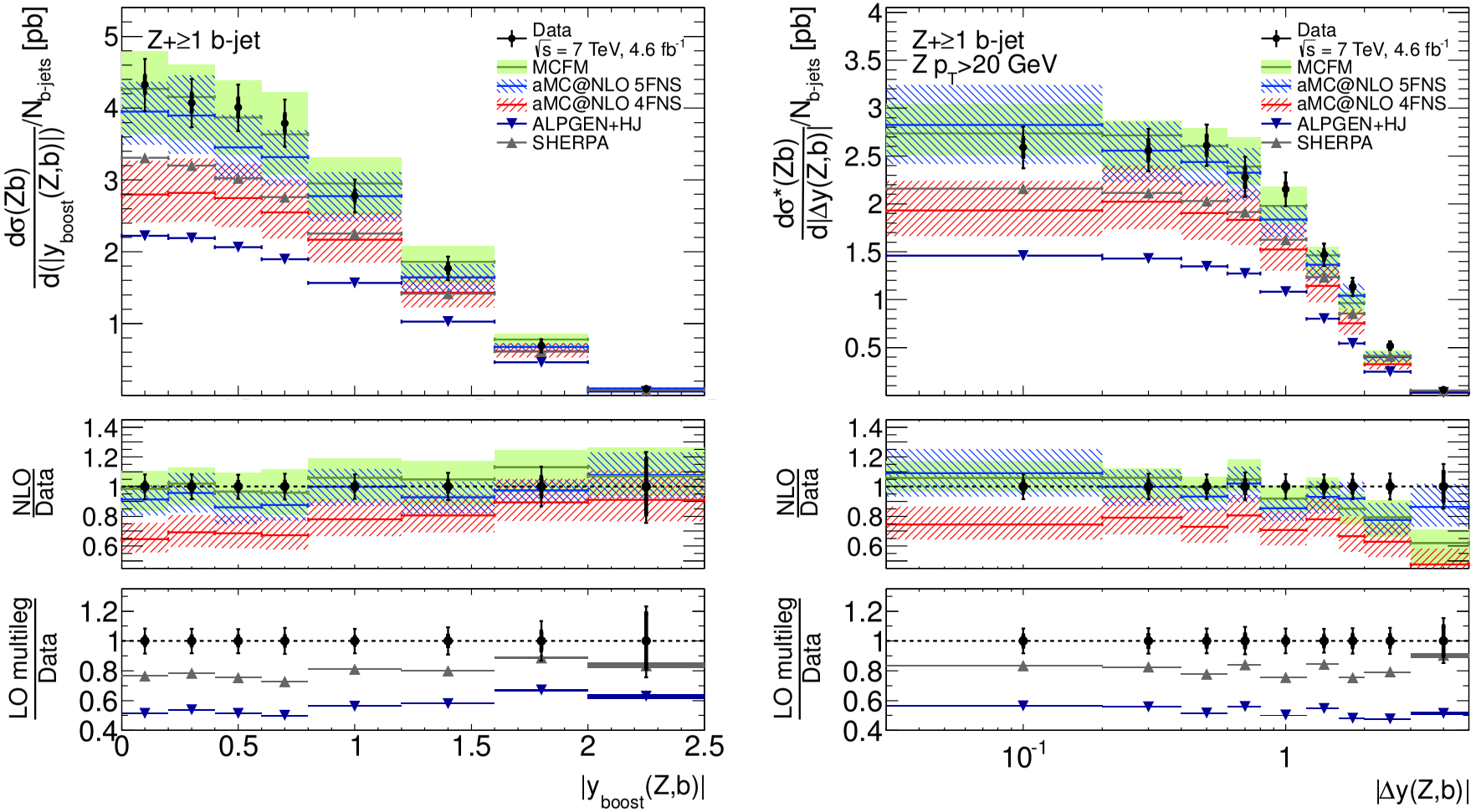

Figure 75: Differential cross section for the production of a Z boson in association with at least one b–jet as a function of $|y_{boost}(Z,b)|$ (left) and of the $|\Delta y(Z,b)|$ (right). The data points are presented along with their statistical (inner bars) and total uncertainty (outer bars); the MCFM calculation is shown with its total uncertainty (light green filled bands); the aMC@NLO calculations are presented with the uncertainty due to the μ_R–μ_F variations (red and blue shaded area) combined in quadrature with the statistical error; the LO multileg predictions are presented with their statistical uncertainty only.

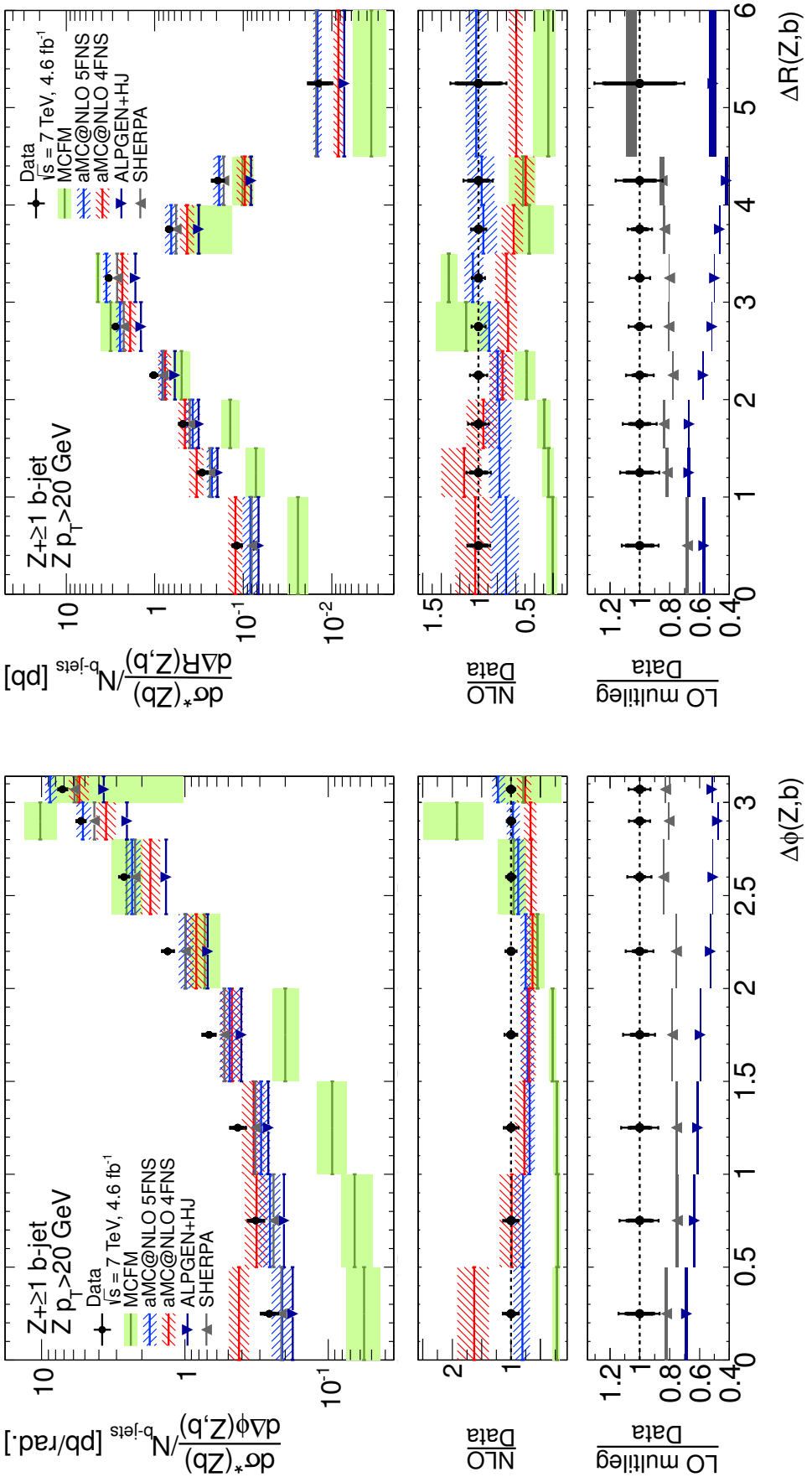

Figure 76: Differential cross section for the production of a Z boson in association with at least one b–jet as function of $\Delta\phi(Z,b)$ (left) and $\Delta R(Z,b)$ (right). The data points are presented along with their statistical (inner bars) and total uncertainty (outer bars); the MCFM calculation is shown with its total uncertainty (light green filled bands); the aMC@NLO calculations are presented with the uncertainty due to the μ_R–μ_F variations (red and blue shaded area) combined in quadrature with the statistical error; the LO multileg predictions are presented with their statistical uncertainty only.

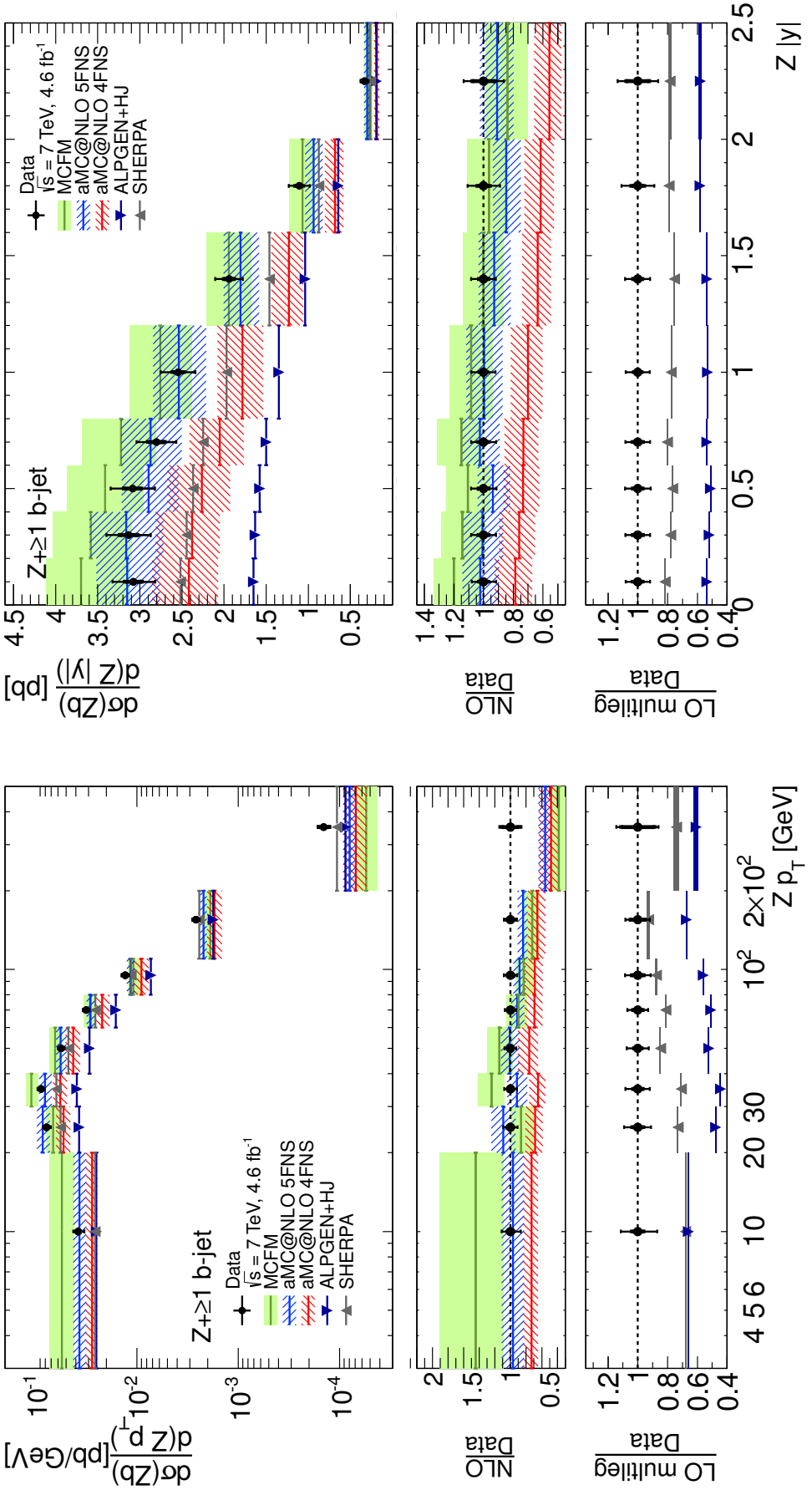

Figure 77: Differential cross section for the production of a Z boson in association with at least one b-jet as function of the Z p_T (left) and the Z |y| (right). The data points are presented along with their statistical (inner bars) and total uncertainty (outer bars); the MCFM calculation is shown with its total uncertainty (light green filled bands); the aMC@NLO calculations are presented with the uncertainty due to the μ_R–μ_F variations (red and blue shaded area) combined in quadrature with the statistical error; the LO multileg predictions are presented with their statistical uncertainty only.

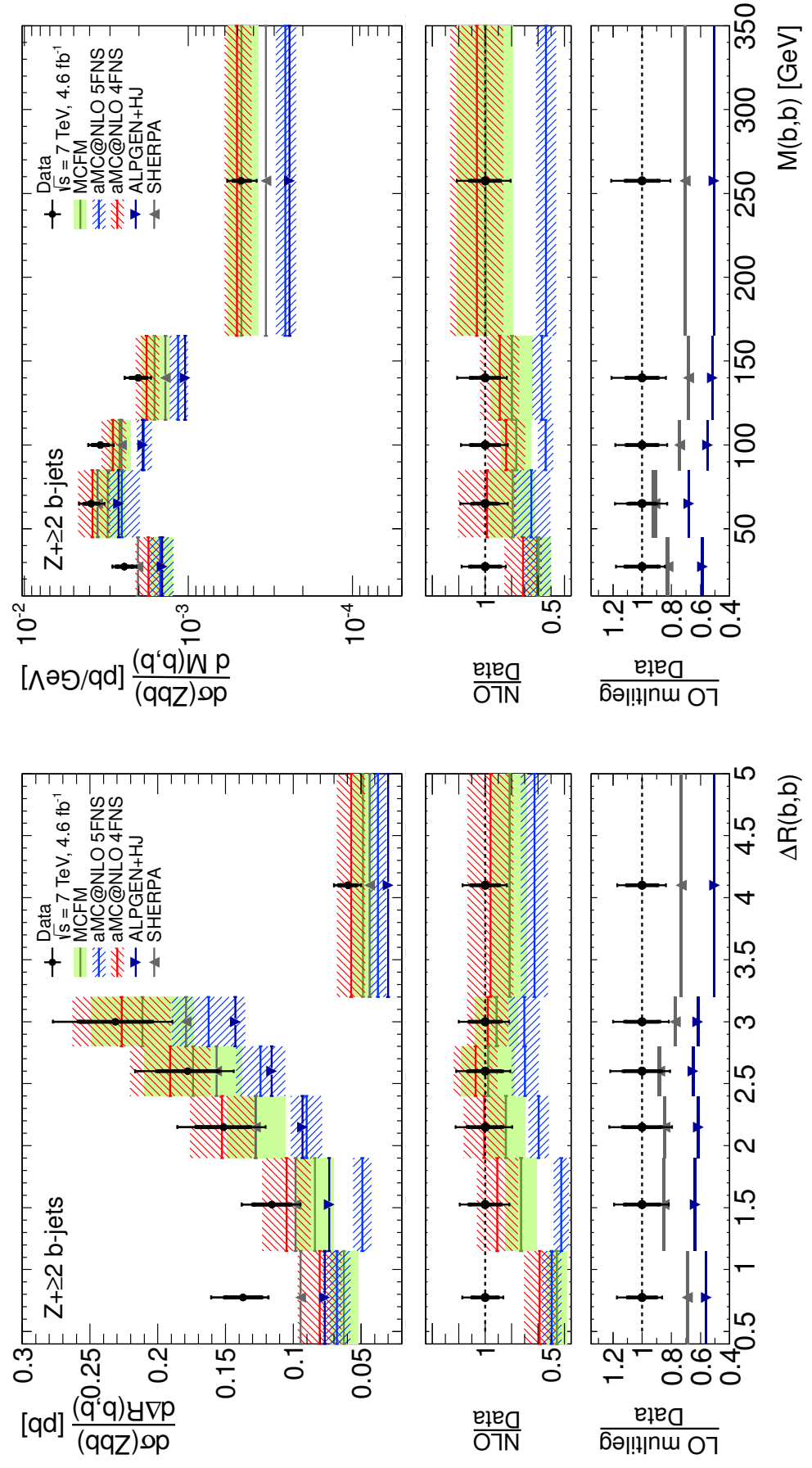

Figure 78: Differential cross section for the production of a Z boson in association with at least two b–jet as function of $\Delta R(b,b)$ (left) and $M(b,b)$ (right). The data points are presented along with their statistical (inner bars) and total uncertainty (outer bars); the MCFM calculation is shown with its total uncertainty (light green filled bands); the aMC@NLO calculations are presented with the uncertainty due to the μ_R–μ_F variations (red and blue shaded area) combined in quadrature with the statistical error; the LO multileg predictions are presented with their statistical uncertainty only.

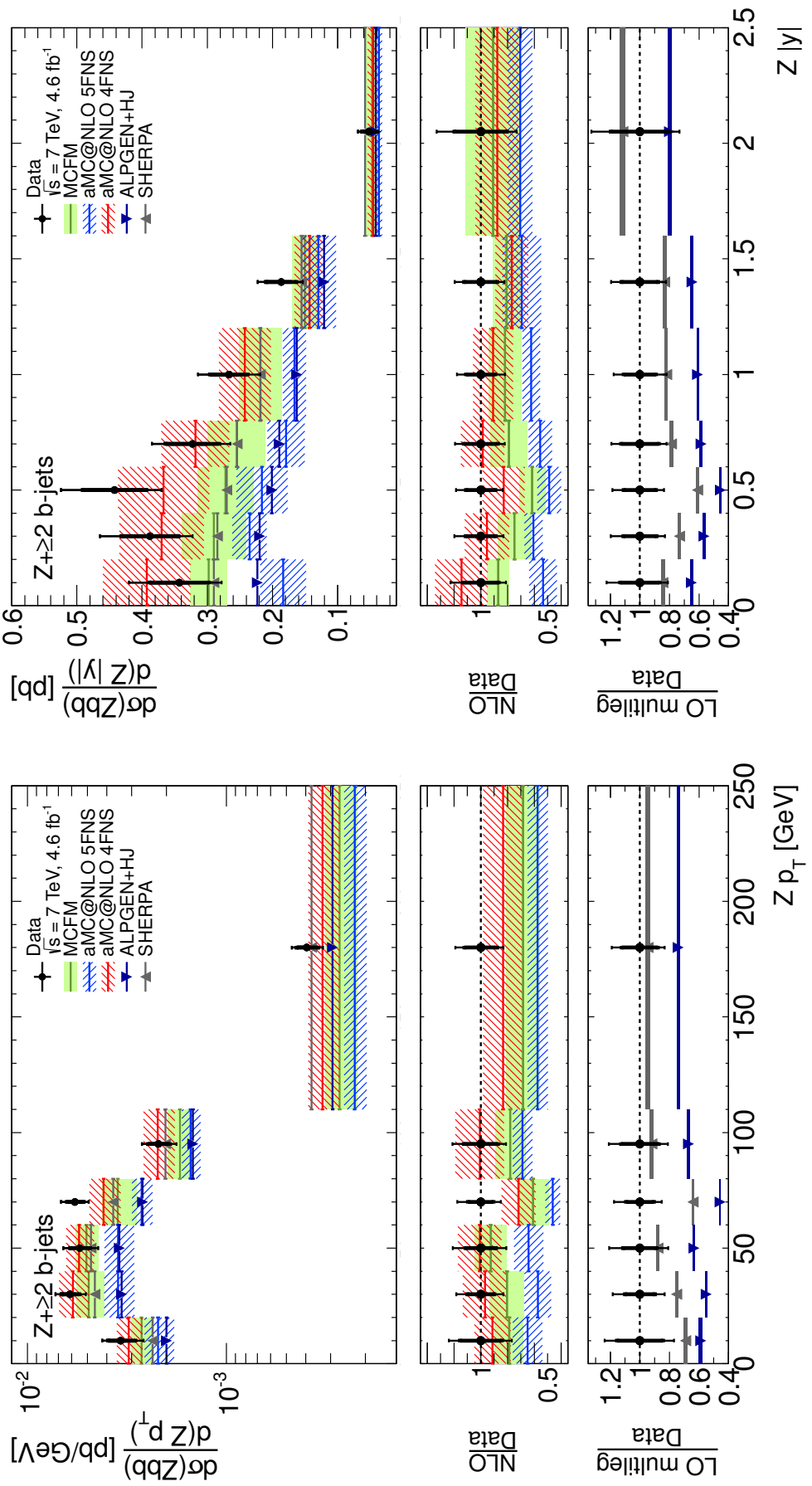

Figure 79: Differential cross section for the production of a Z boson in association with at least two b–jet as function of the Z p_T (left) and the Z |y| (right). The data points are presented along with their statistical (inner bars) and total uncertainty (outer bars); the MCFM calculation is shown with its total uncertainty (light green filled bands); the aMC@NLO calculations are presented with the uncertainty due to the μ_R–μ_F variations (red and blue shaded area) combined in quadrature with the statistical error; the LO multileg predictions are presented with their statistical uncertainty only.

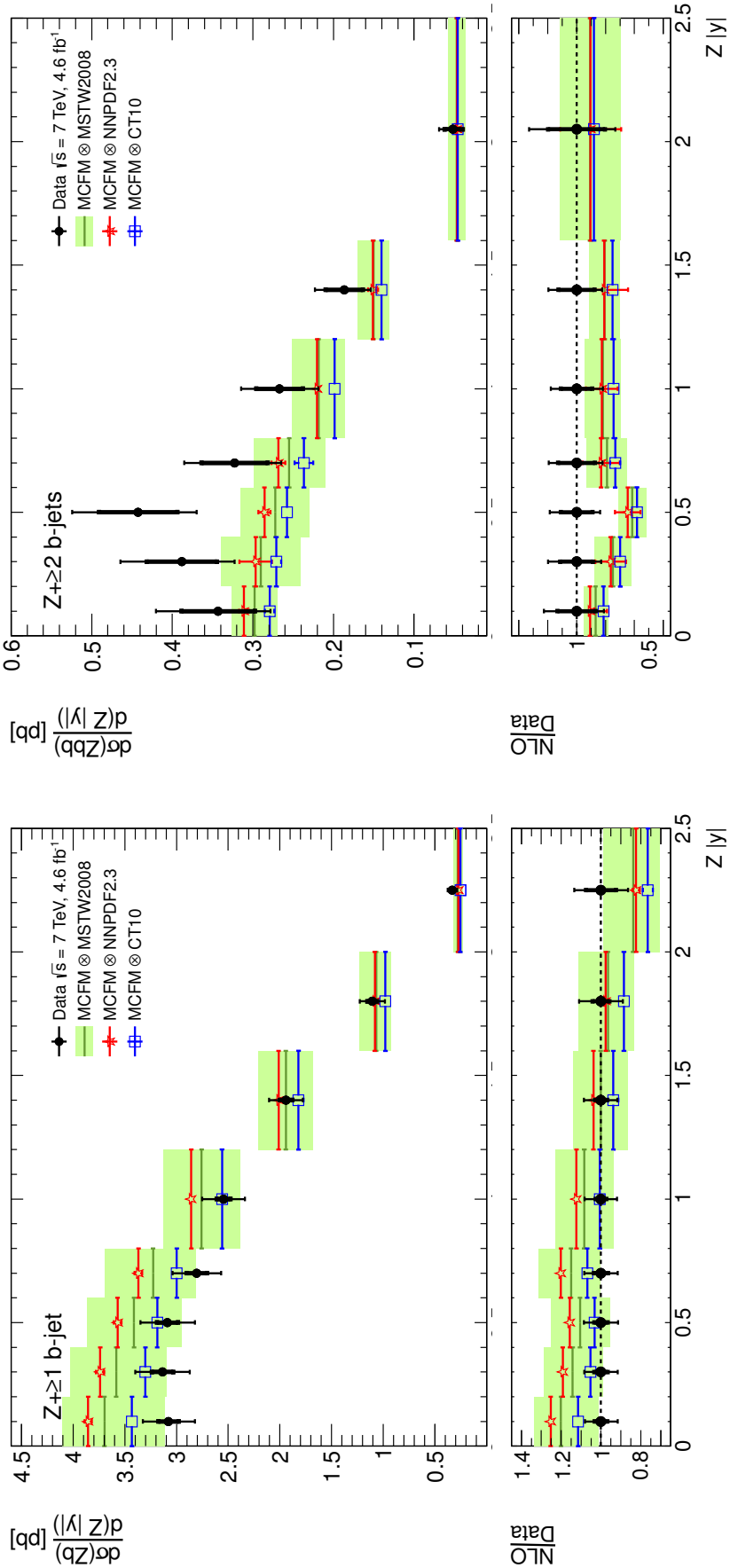

Figure 80: Differential cross section for the production of a Z boson in association with at least one b–jet (left) and at least two b–jets (right) as a function of the Z |y|. The data points are presented along with their statistical (inner bars) and total uncertainty (outer bars); the MCFM calculation performed with the MSTW2008 PDFs is shown with its total uncertainty (light green filled bands) while all the other predictions are presented with their statistical uncertainty only.

CONCLUSIONS AND PERSPECTIVES

In this thesis the first differential measurement of the cross section for b–jets produced in association with a Z boson in pp collisions at $\sqrt{s} = 7$ TeV at LHC has been presented; moreover, differential distributions characterizing the production of a Z boson and at least two b–jets have been reported.

The Z+b production has been studied by measuring the transverse momentum and rapidity spectra of the Z boson and b–jets and their angular correlations which has been characterized by means of four observables: $|y_{boost}(Z, b)|$, $|\Delta y(Z, b)|$, $\Delta\phi(Z, b)$ and $\Delta R(Z, b)$.

The Z+bb production has been studied as a function of the Z boson kinematics, by measuring the boson transverse momentum and rapidity; furthermore, the b–jet pair system is analyzed by measuring the invariant mass, $M(b, b)$, and the $\Delta R(b, b)$ distributions.

Several observables have been presented in this thesis for the first time to date. This is the case for $|y_{boost}(Z, b)|$, $|\Delta y(Z, b)|$, $\Delta R(Z, b)$, $M(b, b)$ and Z $|y|$ in events with at least one b–jet or two b–jets.

Other distributions have been presented in this thesis and, at the same time, by the CMS Collaboration [87, 88]; this is the case of the Z p_T in events with at least two b–hadrons and of the angular separation $\Delta R(b, b)$; the CMS measurement is based on b–hadron reconstruction while the results presented in this thesis use observables defined using b–jets.

The b–jet and the Z boson transverse momentum in events with at least one b–jet have been already measured at Tevatron a few years ago; our measurement extends over a significantly wider kinematic range and has a greater experimental precision. In addition it has a more robust phenomenological interpretation thanks to a large variety of theory predictions which have become available more recently.

Four integrated cross sections have been measured to characterize the total rate of the production of a Z boson in association with one b–jet and two b–jets. These results are consistent with the ATLAS analysis of the early LHC data and with results from CDF, D$\emptyset$ and CMS experiments.

The precision on the integrated cross section is considerably improved compared to previous published results; in particular, the statistical uncertainty for the integrated cross section measurements is of about 1% for the Z+b final state. The data is now able to discriminate between the available theory calculation at NLO in QCD, favoring the 5FNS over the 4FNS for the Z+b production. However, as discussed in Chap. 6, the prediction obtained with the latter calculation scheme agrees with the data within the factorization and renormalization scale variations; thus the disagreement between the data and the theory in 4FNS is an indication of non trivial dependence on the scale setting of the calculation. Lower values for the renormalization scale in the 4FNS predictions are necessary to reproduce the observed Z+b cross section in data; this is consistent with what advocated in Ref. [128].

The Z+bb production is sensitive to a different dynamic compared to Z+b, as also pointed out in Chap. 6. For this final state, both 4FNS and 5FNS are expected to provide consistent results; all the NLO calculations are observed to reproduce well the measurement of the fiducial Z+bb cross section.

Our results and their interpretation is consistent with a publication of the CMS experiment [87, 88], regarding the measurements of the total production cross section for the Z+b and Z+bb final states, which has been released during the finalization of this thesis. In addition, as detailed in Chap. 6, the results on the differential measurements shown in this thesis are in agreement with previous pubblications from CDF and D$\emptyset$, which were suffering form limited statistics, and from CMS for the $Z + b\bar{b}$ final state.

The b–jet transverse momentum is well described by the current theoretical calculations. On the other hand, some tensions between data and calculations are observed for the Z p_T distribution in events with at least one b–jet. In all cases, the parton shower brings the NLO calculations closer to the data compared to the fixed order prediction.

The rapidity distributions of the b–jets and Z bosons in events with at least one b–jet exhibit an interesting shape difference among the 4FNS and 5FNS calculations with the data favoring the latter.

The observables $\Delta\phi(Z, b)$ and $\Delta R(Z, b)$, describing the angular correlation between the Z boson and the b–jets, highlight clearly the limitation of fixed order NLO QCD predictions which are not able to cover the full measured phase space for kinematic restrictions as described in Sec. 6.

The other measured angular correlations, $|y_{boost}(Z, b)|$ and $|\Delta y(Z, b)|$, are reasonably well modeled. The observable $|y_{boost}(Z, b)|$, points to a shape difference between the predictions derived in 4FNS and 5FNS; the data favor the description given by the 5FNS calculations.

The analysis results show that the multileg event generators, widely used by the LHC experimental collaborations, are able, broadly speaking, to reproduce well the data distributions. However, small tensions can be observed for a few distributions, such as the Z boson transverse momentum in Z+b events.

Among the observables measured in the production of the Z boson plus two b–jets, $\Delta R(b, b)$ shows the most interesting structures; all the calculations underpredict the data for b–quarks with low opening angle confirming other independent measurements from ATLAS and CMS. These results are hint of a possible limitation in the current description of the gluon slitting in $b\bar{b}$ pairs by the current predictions.

The Z+b production offers a clean experimental probe of many aspects of the strong interactions phenomenology at LHC. The current ATLAS data has a precision typically comparable, or better, to the available calculations. An improvement of the accuracy of theory predictions would be at this point worthwhile for further clearing up the scenario. In particular, it is worth noticing that the long standing theoretical debate on the equivalence and differences between the 4FNS and 5FNS implementation of perturbative QCD predictions for processes with b–quark in the initial and final state can find in the rather accurate Z+b and Z+bb measurements a very useful and experimentally unambiguous ground for testing.

In perspective, it is important to notice that some experimental systematic uncertainties will decrease for example by exploiting larger control samples or new methods to improve the precision on the reconstruction efficiency; the most obvious source of systematic to be improved in the near future will the b–tagging calibration precision. Moreover, the full data sample collected by the ATLAS experiment during the Run 1 data taking is expected to bring to an improvement on the experimental statistical uncertainties by more than a factor of two compared to the current precision.

Part III

APPENDIX

A

ATLAS REFERENCE FRAME AND REMINDER OF KINEMATIC DEFINITIONS

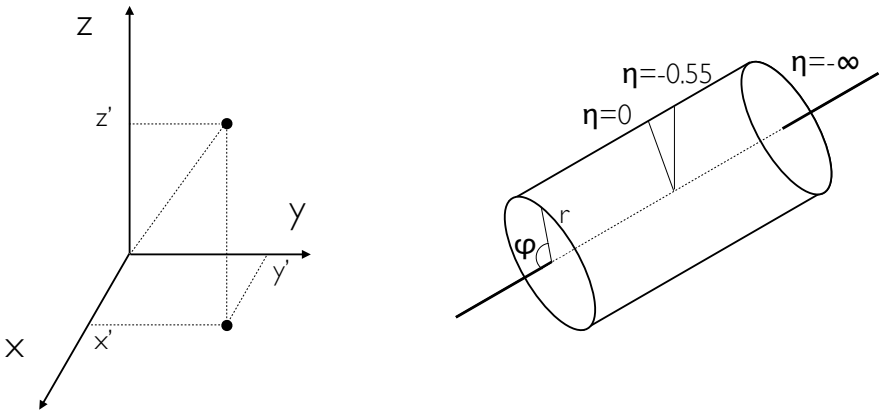

Figure 81: Right handed cartesian reference frame (left) and the cylindrical reference frame (right) described in the text.

The geometry typically used in collider physics is based on a cylindrical coordinate system with symmetry axis coincident with the beam line. This description is convenient given the approximate azimuthal symmetry of the detectors operating at colliders such as LHC.

ATLAS uses a right–handed coordinate system with its origin at the nominal interaction point (IP) at the center of the detector and the z–axis coincident with the beam pipe. The x–axis points from the IP to the center of the LHC ring and the y–axis points upward. Cylindrical coordinates (r,φ) are used in the transverse plane, φ being the azimuthal angle around the beam pipe.

The third coordinate, the polar angle θ, is often replaced with the pseudorapidity $\eta = -\ln[\tan(\theta/2)]$, which for massless particles corresponds to the rapidity y

$$y = \frac{1}{2} \ln \frac{E - p_z}{E + p_z} , \tag{54}$$

where p_z in the momentum projection along the z–axis. The y coordinate is appropriate for the description of the kinematic of relativistic particles because of its invariance under boost transformations along the z–axis.

To quantify the angular separation between two particles or physics objects (a, b), the variable

$$\Delta R(a, b) = \sqrt{(\varphi_a - \varphi_b)^2 + (\lambda_a - \lambda_b)^2} \qquad (\lambda = y \text{ or } \eta) \tag{55}$$

is commonly introduced; the coordinate φ is the azimuthal angle, also indicated by ϕ, and $\lambda = y$ ($\lambda = \eta$) is used for massive (massless) objects.

Furthermore, it is often useful to measure the closest approach distance of physics objects (e.g., tracks) with respect to the primary vertex in the event; this information is retained by the track impact parameter. The impact parameter is decomposed into the longitudinal component, indicated as z_0, and its transverse component, d_0.

The ATLAS reference frame is illustrated in Fig. 81.

B

MONTE CARLO SAMPLES

Here the Monte Carlo samples used in the data analysis described in Chap. 4 are presented for the signal, Tab. 40, as well as for the background processes, Tab. 41.

The Monte Carlo samples are reported along with the *dataset ID* (DSID), a number used to classify each sample in the MC production framework, the total cross section, σ, multiplied by the efficiency for the filter of the event generation, ϵ_F, the k–factors applied (as described in Chap. 4) and the number of simulated events in the sample.

DSID	description	MC generator(s)	$\epsilon_F \cdot \sigma$ [pb]	k-factor	N_{evts}
109300	$Zb\bar{b}$+0 part., $Z \to ee$	Alpgen+Jimmy	6.57	1.25	409999
109301	$Zb\bar{b}$+1 part., $Z \to ee$	Alpgen+Jimmy	2.48	1.25	160000
109302	$Zb\bar{b}$+2 part., $Z \to ee$	Alpgen+Jimmy	0.89	1.25	60000
109303	$Zb\bar{b}$+3 part., $Z \to ee$	Alpgen+Jimmy	0.39	1.25	30000
107650	Z+0 part., $Z \to ee$	Alpgen+Jimmy	668.32	1.25	6618284
107651	Z+1 part., $Z \to ee$	Alpgen+Jimmy	134.36	1.25	1334897
107652	Z+2 part., $Z \to ee$	Alpgen+Jimmy	40.54	1.25	2004195
107653	Z+3 part., $Z \to ee$	Alpgen+Jimmy	11.16	1.25	549949
107654	Z+4 part., $Z \to ee$	Alpgen+Jimmy	2.88	1.25	149948
107655	Z+5 part., $Z \to ee$	Alpgen+Jimmy	0.83	1.25	50000
109305	$Zb\bar{b}$+0 part., $Z \to \mu\mu$	Alpgen+Jimmy	6.56	1.25	409949
109306	$Zb\bar{b}$+1 part., $Z \to \mu\mu$	Alpgen+Jimmy	2.47	1.25	160000
109307	$Zb\bar{b}$+2 part., $Z \to \mu\mu$	Alpgen+Jimmy	0.89	1.25	60000
109308	$Zb\bar{b}$+3 part., $Z \to \mu\mu$	Alpgen+Jimmy	0.39	1.25	29999
107660	Z+0 part., $Z \to \mu\mu$	Alpgen+Jimmy	668.68	1.25	6615230
107661	Z+1 part., $Z \to \mu\mu$	Alpgen+Jimmy	134.14	1.25	1334296
107662	Z+2 part., $Z \to \mu\mu$	Alpgen+Jimmy	40.3	1.25	1999941
107663	Z+3 part., $Z \to \mu\mu$	Alpgen+Jimmy	11.19	1.25	309899
107664	Z+4 part., $Z \to \mu\mu$	Alpgen+Jimmy	2.75	1.25	35000
107665	Z+5 part., $Z \to \mu\mu$	Alpgen+Jimmy	0.77	1.25	50000

Table 40: Signal MC samples, filter efficiency times cross section, k-factor and number of generated events.

DSID	description	MC generator(s)	$\epsilon_F \cdot \sigma$ [pb]	k-factor	N_{evts}
105200	$t\bar{t}$	MC@NLO+JIMMY	79.01	1.146	14983835
108346	Wt inclusive	MC@NLO+JIMMY	14.59	1.079	899694
108344	Wt s-channel	MC@NLO+JIMMY	0.47	1.064	299998
108341	Wt t-channel	MC@NLO+JIMMY	7.12	0.979	299999
105930	ZZ, $\ell\ell qq$	MC@NLO+JIMMY	0.559	1	25000
105942	W^+Z, $qq\ell\ell$	MC@NLO+JIMMY	0.5415	1	24950
105972	W^-Z, $qq\ell\ell$	MC@NLO+JIMMY	0.2944	1	100000
107680	W+0 part., $W \to e\nu$	ALPGEN+JIMMY	6930.50	1.196	10495000
107681	W+1 part., $W \to e\nu$	ALPGEN+JIMMY	1305.30	1.196	7570000
107682	W+2 part., $W \to e\nu$	ALPGEN+JIMMY	378.13	1.196	3770000
107683	W+3 part., $W \to e\nu$	ALPGEN+JIMMY	101.86	1.196	1010000
107684	W+4 part., $W \to e\nu$	ALPGEN+JIMMY	25.68	1.196	1075000
107685	W+5 part., $W \to e\nu$	ALPGEN+JIMMY	6.99	1.196	1000000
107690	W+0 part., $W \to \mu\nu$	ALPGEN+JIMMY	6932.40	1.195	10495000
107691	W+1 part., $W \to \mu\nu$	ALPGEN+JIMMY	1305.90	1.195	7500000
107692	W+2 part., $W \to \mu\nu$	ALPGEN+JIMMY	378.07	1.195	3770000
107693	W+3 part., $W \to \mu\nu$	ALPGEN+JIMMY	101.85	1.195	1010000
107694	W+4 part., $W \to \mu\nu$	ALPGEN+JIMMY	25.72	1.195	1000000
107695	W+5 part., $W \to \mu\nu$	ALPGEN+JIMMY	7.00	1.195	1000000
107280	$Wb\bar{b}$+0 part., $W \to \ell\nu$	ALPGEN+JIMMY	47.35	1.2	1000000
107281	$Wb\bar{b}$+1 part., $W \to \ell\nu$	ALPGEN+JIMMY	35.76	1.2	1240000
107282	$Wb\bar{b}$+2 part., $W \to \ell\nu$	ALPGEN+JIMMY	17.33	1.2	175000
107283	$Wb\bar{b}$+3 part., $W \to \ell\nu$	ALPGEN+JIMMY	7.61	1.2	700000

Table 41: Background MC samples, filter efficiency times cross section, k-factor and number of generated events.

C

DETAILS ON B–YIELD EXTRACTION RESULTS

The fit method for the signal yield measurement has been described in Sec. 4.5. Here the fit results are reported in full detail for all the distributions and collected in tables (from Tab. 42 to Tab. 49); the results are shown for the electron channel, the muon channel and their combination.

The non Z+jets backgrounds are shown in each analysis bin; the multijet background is determined as described in Sec. 4.3, while all the other backgrounds also reported are estimated with Monte Carlo simulations as discussed in Sec. 4.2.2.

The quality of the fit results is quantified by calculating the reduced χ^2 between the data and the fit model with the Z+jets flavor fractions adjusted to the fit results. For the combined $e + \mu$ results, corresponding to the obtained χ^2 values, the p–value is also tabulated.

jet p_T[GeV]	[20-30]	[30-50]	[50-75]	[75-110]	[110-200]	[200-500]
Combined channel						
Total data	$1.874e+04$	$1.613e+04$	8088	4148	2261	333
Pre fit N_b	4082	4395	2240	1120	566	66
Pre fit N_{charm}	3781	4073	2125	1106	555	83
Pre fit N_{light}	8648	4634	2022	1118	697	163
$t\bar{t}$	113.8	328.2	390.1	319.7	165.6	8.588
Single top	10.49	24.14	25.75	15.85	4.23	0.201
Dibosons	84.24	190	112.6	58.25	34.19	4.956
Multijets	9.499	8.274	4.181	2.068	1.187	0.165
Fitted N_b	5719 ± 129	6440 ± 119	3330 ± 83	1635 ± 58	764 ± 41	85 ± 14
Fitted N_{c+l}	$1.28e+04 \pm 154$	9141 ± 128	4226 ± 86	2116 ± 60	1291 ± 45	233 ± 19
Reduced χ^2	0.99	0.93	1	1.5	1.3	0.78
p–value	0.4586	0.5331	0.4254	0.0873	0.1681	0.6941
Electron channel						
Total data	7888	6904	3499	1706	1000	135
Pre fit N_b	1724	1859	956	476	239	31
Pre fit N_{charm}	1580	1769	880	472	243	39
Pre fit N_{light}	3665	1909	876	463	311	73
$t\bar{t}$	52.53	142.1	162.8	140	75.36	4.091
Single top	5.571	11.71	10.5	6.539	1.5	0.02
Dibosons	35.4	77.75	47.08	26.23	13.52	2.779
Multijets	7.889	6.903	3.499	1.707	1	0.135
Fitted N_b	2389 ± 84	2805 ± 78	1509 ± 55	676 ± 37	324 ± 27	42 ± 10
Fitted N_{c+l}	5397 ± 100	3861 ± 83	1766 ± 56	855 ± 38	585 ± 30	86 ± 12
Reduced χ^2	0.84	1.3	1.2	1.1	0.61	0.45
Muon channel						
Total data	$1.085e+04$	9228	4589	2442	1261	198
Pre fit N_b	2358	2536	1284	644	327	36
Pre fit N_{charm}	2201	2303	1245	634	312	44
Pre fit N_{light}	4983	2724	1145	655	386	90
$t\bar{t}$	61.24	186.2	227.3	179.7	90.28	4.497
Single top	4.915	12.43	15.25	9.313	2.73	0.181
Dibosons	48.85	112.2	65.46	32.02	20.66	2.177
Multijets	1.611	1.371	0.682	0.363	0.187	0.03
Fitted N_b	3333 ± 98	3638 ± 90	1821 ± 62	959 ± 45	439 ± 30	45 ± 10
Fitted N_{c+l}	7402 ± 117	5277 ± 97	2459 ± 65	1262 ± 46	707 ± 33	146 ± 14
Reduced χ^2	0.94	0.6	0.81	0.88	1.3	1.2

Table 42: Summary of the fit results in the electron and muon channel as well as their combination in bins of jet p_T; for each analysis bin the estimation of the backgrounds and of the signal is presented. For the combined channel the χ^2 probability (p–value) is reported.

jet $\lvert y\rvert$	[0-0.2]	[0.2-0.4]	[0.4-0.6]	[0.6-0.8]	[0.8-1.2]	[1.2-1.6]	[1.6-2.0]	[2.0-2.4]
Combined channel								
Total data	5862	5821	5926	5139	9356	7896	5606	4095
Pre fit N_b	1421	1408	1408	1330	2370	1993	1468	1072
Pre fit N_{charm}	1495	1493	1487	1361	2276	1783	1149	679
Pre fit N_{light}	1961	2011	2051	1562	2979	2677	2147	1894
$t\bar{t}$	177.7	188.6	172.3	154	263.5	185.6	118	66.2
Single top	10.87	11.27	11.9	9.386	15.07	9.217	9.076	3.874
Dibosons	53.33	57.61	50.93	47.77	91.28	77.79	55.28	50.17
Multijets	3.001	2.986	3.096	2.671	4.807	3.945	2.831	2.038
Fitted N_b	2108 ± 68	2118 ± 68	2183 ± 69	1936 ± 65	3534 ± 88	2861 ± 83	1916 ± 72	1315 ± 67
Fitted N_{c+l}	3508 ± 76	3442 ± 76	3506 ± 77	2989 ± 72	5449 ± 97	4758 ± 93	3504 ± 82	2656 ± 76
Reduced χ^2	0.8	2	1.8	1.1	1.6	1.4	1.1	2
p–value	0.6873	0.0112	0.0299	0.3129	0.0647	0.1336	0.3623	0.0115
Electron channel								
Total data	2502	2491	2602	2241	4013	3257	2347	1679
Pre fit N_b	610	584	607	567	999	853	623	441
Pre fit N_{charm}	630	648	647	566	972	756	479	286
Pre fit N_{light}	844	887	873	633	1246	1115	909	790
$t\bar{t}$	74.57	83.06	76.94	67.26	115.3	80.87	50.83	28.01
Single top	4.456	5.468	5.069	3.805	7.469	3.97	3.85	1.751
Dibosons	24.72	24.6	17.3	20.9	40.18	32.9	24.28	17.91
Multijets	2.502	2.491	2.602	2.242	4.012	3.257	2.347	1.678
Fitted N_b	898 ± 44	914 ± 45	980 ± 46	849 ± 43	1569 ± 58	1193 ± 54	845 ± 47	529 ± 43
Fitted N_{c+l}	1497 ± 50	1461 ± 49	1522 ± 51	1298 ± 48	2278 ± 63	1943 ± 60	1421 ± 53	1101 ± 49
Reduced χ^2	1.1	2.2	1.1	1.5	0.94	2.8	1	1.2
Muon channel								
Total data	3360	3330	3324	2898	5343	4639	3259	2416
Pre fit N_b	811	824	801	763	1371	1139	845	630
Pre fit N_{charm}	864	845	840	795	1304	1028	670	393
Pre fit N_{light}	1117	1124	1178	929	1733	1561	1238	1104
$t\bar{t}$	103.1	105.5	95.39	86.73	148.2	104.8	67.18	38.2
Single top	6.415	5.798	6.832	5.58	7.596	5.247	5.226	2.123
Dibosons	28.6	33.01	33.63	26.88	51.11	44.9	31	32.27
Multijets	0.499	0.494	0.494	0.43	0.793	0.688	0.483	0.359
Fitted N_b	1210 ± 52	1204 ± 52	1206 ± 52	1092 ± 49	1967 ± 66	1674 ± 63	1071 ± 54	789 ± 51
Fitted N_{c+l}	2011 ± 58	1980 ± 58	1983 ± 58	1687 ± 54	3170 ± 73	2809 ± 70	2084 ± 62	1553 ± 58
Reduced χ^2	0.75	0.7	2.2	0.76	2.1	0.86	0.5	1.4

Table 43: Summary of the fit results in the electron and muon channel as well as their combination in bins of jet $\lvert y\rvert$; for each analysis bin the estimation of the backgrounds and of the signal is presented. For the combined channel the χ^2 probability (p–value) is reported.

$\lvert y_{boost}(Z,jet)\rvert$	[0-0.2]	[0.2-0.4]	[0.4-0.6]	[0.6-0.8]	[0.8-1.2]	[1.2-1.6]	[1.6-2]	[2-2.5]
Combined channel								
Total data	8287	7933	7435	6738	1.046e + 04	6109	2414	326
Pre fit N_b	2001	1961	1848	1630	2693	1620	637	79
Pre fit N_{charm}	2036	1961	1767	1588	2508	1348	456	58
Pre fit N_{light}	2655	2638	2446	2223	3590	2381	1158	192
$t\bar{t}$	226.6	218.2	206.2	182.2	280.9	158.5	49.13	4.32
Single top	15.48	12.99	13.63	9.67	18.4	7.624	2.348	0.517
Dibosons	78.97	73.17	65.53	62.27	100.1	63.73	36.34	4.061
Multijets	4.4	4.146	3.834	3.462	5.311	2.91	1.143	0.166
Fitted N_b	3051 ± 82	2871 ± 81	2810 ± 80	2543 ± 78	3753 ± 94	2182 ± 74	748 ± 46	97 ± 17
Fitted N_{c+l}	4911 ± 92	4754 ± 91	4336 ± 88	3937 ± 85	6302 ± 105	3695 ± 83	1577 ± 54	220 ± 20
Reduced χ^2	1.3	1.9	0.89	1.1	1.4	1.2	0.91	0.62
p–value	0.1863	0.0165	0.5714	0.3433	0.1191	0.2574	0.5483	0.8613
Electron channel								
Total data	3724	3486	3206	2891	4413	2352	921	139
Pre fit N_b	872	848	817	699	1134	638	243	34
Pre fit N_{charm}	895	867	761	688	1034	532	181	26
Pre fit N_{light}	1175	1152	1038	951	1497	939	465	82
$t\bar{t}$	104.1	98.14	89.39	82.65	118.9	62.66	19.23	1.762
Single top	7.777	5.854	6.383	3.9	8.128	2.894	0.68	0.225
Dibosons	38.84	32.19	26.04	27.81	39.71	27.46	9.033	1.689
Multijets	3.723	3.486	3.206	2.89	4.412	2.351	0.921	0.139
Fitted N_b	1386 ± 55	1308 ± 54	1258 ± 53	1113 ± 52	1564 ± 61	851 ± 47	269 ± 28	41 ± 11
Fitted N_{c+l}	2183 ± 61	2039 ± 59	1822 ± 57	1661 ± 56	2679 ± 69	1405 ± 52	623 ± 33	94 ± 13
Reduced χ^2	1	2	0.86	1.1	1.2	0.96	0.85	0.73
Muon channel								
Total data	4563	4447	4229	3847	6046	3757	1493	187
Pre fit N_b	1128	1113	1031	931	1560	982	394	44
Pre fit N_{charm}	1141	1094	1007	900	1473	816	275	33
Pre fit N_{light}	1480	1486	1408	1272	2092	1442	693	111
$t\bar{t}$	122.5	120.1	116.8	99.5	162	95.84	29.9	2.558
Single top	7.704	7.133	7.244	5.771	10.28	4.73	1.668	0.292
Dibosons	40.13	40.98	39.49	34.47	60.38	36.27	27.3	2.372
Multijets	0.678	0.661	0.628	0.571	0.897	0.558	0.222	0.027
Fitted N_b	1662 ± 61	1562 ± 60	1550 ± 60	1433 ± 58	2191 ± 72	1335 ± 57	487 ± 36	57 ± 12
Fitted N_{c+l}	2730 ± 68	2718 ± 68	2516 ± 67	2273 ± 64	3622 ± 80	2285 ± 64	949 ± 42	125 ± 15
Reduced χ^2	1.3	1.1	1.2	0.94	0.86	0.84	0.73	0.8

Table 44: Summary of the fit results in the electron and muon channel as well as their combination in bins of $\lvert y_{boost}(Z,jet)\rvert$; for each analysis bin the estimation of the backgrounds and of the signal is presented. For the combined channel the χ^2 probability (p–value) is reported.

$\lvert\Delta y(Z,jet)\rvert$	[0-0.2]	[0.2-0.4]	[0.4-0.6]	[0.6-0.8]	[0.8-1.2]	[1.2-1.6]	[1.6-2]	[2-3]	[3-5]
Combined channel									
Total data	4783	4802	4526	4286	7492	5597	3926	4749	1082
Pre fit N_b	1321	1282	1221	1145	1953	1405	924	1013	198
Pre fit N_{charm}	1249	1272	1183	1092	1809	1322	869	884	166
Pre fit N_{light}	1493	1447	1466	1344	2280	1746	1259	1512	465
$t\bar{t}$	197.2	196.2	178.4	158.2	241.9	152.4	65.63	37.48	1.74
Single top	9.601	10.46	12.27	9.538	13.42	10.29	5.318	4.922	0.408
Dibosons	55.1	52.17	48.02	54.62	76.53	57.11	38.33	46.85	10.63
Multijets	2.431	2.447	2.38	2.205	3.844	2.94	1.98	2.349	0.498
Fitted N_b	1835 ± 65	1812 ± 63	1832 ± 62	1631 ± 61	3016 ± 82	2032 ± 67	1491 ± 57	1658 ± 62	304 ± 29
Fitted N_{c+l}	2684 ± 69	2731 ± 69	2453 ± 66	2431 ± 66	4141 ± 87	3342 ± 76	2325 ± 63	2999 ± 72	765 ± 36
Reduced χ^2	0.79	1.8	0.67	0.56	2.1	0.97	1.4	0.52	1.5
p–value	0.6945	0.0287	0.8216	0.9067	0.0090	0.4812	0.1399	0.9315	0.1026
Electron channel									
Total data	2021	2038	2006	1843	3209	2477	1640	1931	398
Pre fit N_b	572	549	521	491	830	604	397	419	76
Pre fit N_{charm}	535	549	512	472	761	563	369	369	55
Pre fit N_{light}	653	627	640	555	981	740	517	628	179
$t\bar{t}$	86.78	84.93	77.28	68.95	104.9	68.12	27.84	15.81	0.704
Single top	4.668	4.868	4.938	3.586	6.471	4.185	1.794	3.124	0.352
Dibosons	22.33	21.54	20.52	22.09	32.51	23.83	18.75	18.81	4.178
Multijets	2.021	2.038	2.005	1.843	3.209	2.477	1.641	1.93	0.397
Fitted N_b	790 ± 42	768 ± 41	794 ± 41	738 ± 41	1309 ± 54	897 ± 45	680 ± 38	688 ± 40	105 ± 17
Fitted N_{c+l}	1117 ± 45	1157 ± 45	1107 ± 44	1009 ± 43	1754 ± 57	1482 ± 51	909 ± 41	1203 ± 46	287 ± 22
Reduced χ^2	0.74	0.63	1.1	0.82	1.8	0.87	1.2	0.63	1
Muon channel									
Total data	2762	2764	2520	2443	4283	3120	2286	2818	684
Pre fit N_b	749	733	701	654	1123	801	526	595	122
Pre fit N_{charm}	714	723	671	619	1048	758	500	516	111
Pre fit N_{light}	840	819	826	789	1299	1005	742	884	286
$t\bar{t}$	110.4	111.2	101.1	89.21	137	84.3	37.78	21.67	1.036
Single top	4.933	5.587	7.33	5.951	6.951	6.105	3.524	1.798	0.056
Dibosons	32.77	30.63	27.5	32.53	44.01	33.28	19.59	28.05	6.45
Multijets	0.41	0.411	0.374	0.363	0.635	0.464	0.339	0.418	0.101
Fitted N_b	1046 ± 49	1043 ± 48	1041 ± 47	899 ± 46	1707 ± 62	1134 ± 50	809 ± 42	968 ± 48	198 ± 23
Fitted N_{c+l}	1567 ± 53	1574 ± 52	1343 ± 49	1418 ± 50	2387 ± 66	1861 ± 56	1416 ± 48	1797 ± 56	478 ± 29
Reduced χ^2	1.9	2.3	0.82	1.6	1.2	0.59	1.5	0.65	1

Table 45: Summary of the fit results in the electron and muon channel as well as their combination in bins of $\lvert\Delta y(Z,jet)\rvert$; for each analysis bin the estimation of the backgrounds and of the signal is presented. For the combined channel the χ^2 probability (p–value) is reported.

$\Delta\phi$(Z,jet)[rad.]	[0-0.5]	[0.5-1]	[1-1.5]	[1.5-2]	[2-2.4]	[2.4-2.8]	[2.8-3]	[3-π]
Combined channel								
Total data	1313	1474	1941	3098	4481	9356	9543	$1.004e+04$
Pre fit N_b	365	410	542	846	1187	2396	2331	2385
Pre fit N_{charm}	263	288	383	600	876	2101	2448	2887
Pre fit N_{light}	483	522	677	930	1307	2679	2924	3490
$t\bar{t}$	80.6	94	131.9	192.7	209.5	263.2	147.6	109.6
Single top	4.155	2.589	4.326	8.769	13.23	19.31	12.61	11.23
Dibosons	20.97	20.25	30.53	53.86	70.12	114.9	76.02	52.67
Multijets	0.639	0.747	0.995	1.552	2.324	4.769	4.915	5.137
Fitted N_b	423 ± 35	510 ± 37	694 ± 43	1121 ± 53	1773 ± 64	3709 ± 92	3763 ± 88	3604 ± 87
Fitted N_{c+l}	784 ± 39	846 ± 40	1078 ± 46	1721 ± 57	2414 ± 68	5247 ± 98	5540 ± 97	6255 ± 101
Reduced χ^2	0.87	1.2	1.1	0.98	1	1.7	1.3	1.6
p–value	0.5945	0.2522	0.3559	0.4732	0.4052	0.0382	0.1797	0.0486
Electron channel								
Total data	522	620	830	1282	1949	3969	4108	4283
Pre fit N_b	155	175	226	358	496	1031	1002	1015
Pre fit N_{charm}	114	118	164	253	373	890	1048	1225
Pre fit N_{light}	203	203	280	400	548	1155	1280	1453
$t\bar{t}$	34.83	40.66	59.02	86.51	90.07	113.8	64.49	45.99
Single top	2.132	0.996	1.657	4.309	6.232	7.639	6.237	4.785
Dibosons	10.19	10.31	13.17	24.5	26.15	46.9	32.51	20.84
Multijets	0.522	0.62	0.829	1.282	1.949	3.968	4.109	4.283
Fitted N_b	152 ± 22	233 ± 25	337 ± 29	491 ± 35	724 ± 41	1575 ± 59	1692 ± 59	1565 ± 57
Fitted N_{c+l}	325 ± 25	335 ± 26	419 ± 29	674 ± 37	1101 ± 45	2223 ± 64	2309 ± 63	2643 ± 66
Reduced χ^2	0.75	0.72	0.86	0.62	1.1	1.4	1.2	1.3
Muon channel								
Total data	791	854	1111	1816	2532	5387	5435	5754
Pre fit N_b	210	235	316	488	691	1365	1329	1370
Pre fit N_{charm}	148	170	219	347	503	1211	1400	1662
Pre fit N_{light}	280	319	398	530	760	1524	1644	2037
$t\bar{t}$	45.77	53.35	72.89	106.2	119.4	149.5	83.08	63.62
Single top	2.022	1.593	2.67	4.46	7.002	11.67	6.374	6.446
Dibosons	10.79	9.94	17.36	29.36	43.98	68.04	43.51	31.83
Multijets	0.118	0.127	0.164	0.27	0.376	0.8	0.807	0.854
Fitted N_b	274 ± 27	278 ± 27	358 ± 32	630 ± 39	1051 ± 50	2139 ± 70	2069 ± 66	2044 ± 66
Fitted N_{c+l}	457 ± 29	510 ± 30	659 ± 35	1046 ± 43	1312 ± 51	3020 ± 75	3233 ± 74	3608 ± 76
Reduced χ^2	0.61	1.5	1.5	0.89	1.5	1.2	1.5	1.3

Table 46: Summary of the fit results in the electron and muon channel as well as their combination in bins of $\Delta\phi$(Z,jet); for each analysis bin the estimation of the backgrounds and of the signal is presented. For the combined channel the χ^2 probability (p–value) is reported.

ΔR(Z,jet)	[0-1]	[1-1.5]	[1.5-2]	[2-2.5]	[2.5-3]	[3-3.5]	[3.5-4]	[4-4.5]	[4.5-6]
Combined channel									
Total data	947	1380	2431	4555	$1.201e+04$	$1.564e+04$	3220	846	217
Pre fit N_b	287	403	680	1284	3185	3769	669	148	36
Pre fit N_{charm}	202	287	490	916	2879	4207	688	142	35
Pre fit N_{light}	323	464	735	1351	3518	5151	1058	319	94
$t\bar{t}$	80.55	129	192.2	266.3	349.7	195.6	14.27	1.379	0.076
Single top	2.685	3.603	7.65	14.12	26.66	19.22	1.809	0.47	0
Dibosons	15.93	28.19	41.96	74.09	136.1	106.8	26.11	8.5	1.751
Multijets	0.475	0.705	1.232	2.355	6.131	8.071	1.618	0.385	0.105
Fitted N_b	392 ± 32	480 ± 36	807 ± 46	1758 ± 65	4855 ± 104	5867 ± 111	1119 ± 49	273 ± 26	57 ± 12
Fitted N_{c+l}	455 ± 31	738 ± 38	1380 ± 50	2441 ± 68	6636 ± 110	9443 ± 125	2058 ± 58	562 ± 31	158 ± 16
Reduced χ^2	0.97	0.57	0.74	1.4	2.1	1.7	0.72	0.6	1.1
p–value	0.4879	0.8974	0.7164	0.1497	0.0061	0.0334	0.7666	0.8775	0.3496
Electron channel									
Total data	393	588	1023	1972	5107	6751	1339	305	85
Pre fit N_b	125	168	293	544	1367	1610	277	60	12
Pre fit N_{charm}	86	123	210	390	1238	1789	287	51	10
Pre fit N_{light}	134	198	310	566	1541	2169	436	136	33
$t\bar{t}$	35.61	55.37	86.67	115.3	153.4	82.16	6.049	0.671	0.106
Single top	0.933	1.627	3.595	6.588	11.34	8.458	1.238	0.214	0
Dibosons	7.565	13.65	18.47	31.24	55.5	42.32	11.62	2.685	1.509
Multijets	0.393	0.588	1.023	1.972	5.106	6.751	1.339	0.305	0.085
Fitted N_b	175 ± 21	223 ± 24	353 ± 31	724 ± 42	2091 ± 68	2604 ± 74	481 ± 32	95 ± 16	25 ± 7
Fitted N_{c+l}	175 ± 20	295 ± 24	559 ± 33	1093 ± 45	2792 ± 72	4008 ± 82	838 ± 37	205 ± 19	59 ± 9
Reduced χ^2	0.68	0.79	0.8	1.9	1.2	1.4	1.3	0.71	0.81
Muon channel									
Total data	554	792	1408	2583	6900	8889	1881	541	132
Pre fit N_b	162	235	386	741	1817	2159	392	88	24
Pre fit N_{charm}	116	164	280	526	1641	2418	401	90	24
Pre fit N_{light}	189	266	425	785	1977	2982	622	184	61
$t\bar{t}$	44.94	73.6	105.6	151	196.3	113.4	8.226	0.708	−0.03
Single top	1.752	1.977	4.056	7.535	15.32	10.77	0.571	0.255	0
Dibosons	8.369	14.54	23.49	42.85	80.57	64.44	14.49	5.815	0.242
Multijets	0.081	0.118	0.208	0.384	1.025	1.321	0.279	0.08	0.02
Fitted N_b	218 ± 24	260 ± 27	452 ± 34	1031 ± 49	2762 ± 79	3267 ± 83	639 ± 37	176 ± 21	30 ± 9
Fitted N_{c+l}	280 ± 24	440 ± 29	821 ± 38	1350 ± 51	3846 ± 84	5432 ± 95	1218 ± 44	358 ± 25	102 ± 12
Reduced χ^2	1	0.96	1.2	1.3	2.4	1.4	0.82	0.63	0.83

Table 47: Summary of the fit results in the electron and muon channel as well as their combination in bins of ΔR(Z,jet); for each analysis bin the estimation of the backgrounds and of the signal is presented. For the combined channel the χ^2 probability (p–value) is reported.

Z p_T[GeV]	[0-20]	[20-30]	[30-40]	[40-60]	[60-80]	[80-110]	[110-200]	[200-500]
Combined channel								
Total data	8170	7464	7472	$1.063e+04$	6002	4076	2870	452
Pre fit N_b	1894	1464	1635	2698	1579	1146	862	138
Pre fit N_{charm}	1845	1875	1859	2649	1447	998	685	108
Pre fit N_{light}	4191	2839	2464	3123	1745	1307	1025	218
$t\bar{t}$	68.75	77.4	94.28	210.1	195.5	187.1	89.53	2.436
Single top	4.283	6.378	7.631	16.94	14.89	14.82	5.968	0.657
Dibosons	39.5	46.76	48.81	99.46	63.29	56.64	57.2	11.69
Multijets	4.148	3.799	3.822	5.417	3.033	2.136	1.511	0.229
Fitted N_b	2282 ± 83	2365 ± 77	2803 ± 80	4033 ± 93	2420 ± 71	1593 ± 58	1008 ± 46	176 ± 19
Fitted N_{c+l}	5769 ± 102	4965 ± 92	4516 ± 90	6266 ± 103	3305 ± 76	2224 ± 62	1707 ± 53	261 ± 21
Reduced χ^2	1.5	1.4	2	1.6	1.1	2.1	1	1.3
p–value	0.0862	0.1187	0.0134	0.0630	0.3954	0.0067	0.4119	0.1643
Electron channel								
Total data	3447	3159	3185	4507	2515	1798	1275	190
Pre fit N_b	782	613	702	1149	660	493	366	65
Pre fit N_{charm}	781	806	778	1135	588	427	307	51
Pre fit N_{light}	1750	1190	1039	1314	725	567	459	100
$t\bar{t}$	29.61	33.42	39.24	88.96	86.06	81.63	42.87	0.75
Single top	1.665	2.536	3.611	7.387	7.696	6.628	1.855	0.287
Dibosons	16.48	21.81	21.21	36.12	25.7	24.42	24.76	5.328
Multijets	3.447	3.159	3.184	4.507	2.515	1.798	1.275	0.19
Fitted N_b	959 ± 54	1056 ± 52	1192 ± 52	1729 ± 61	1070 ± 47	720 ± 38	439 ± 30	68 ± 12
Fitted N_{c+l}	2436 ± 66	2042 ± 61	1926 ± 58	2640 ± 67	1323 ± 49	965 ± 41	765 ± 35	116 ± 14
Reduced χ^2	0.75	1.1	1.1	1	1.4	1.6	1.1	2
Muon channel								
Total data	4723	4305	4287	6125	3487	2278	1595	262
Pre fit N_b	1112	851	934	1549	919	653	496	73
Pre fit N_{charm}	1064	1069	1081	1514	859	571	379	58
Pre fit N_{light}	2441	1649	1424	1809	1020	740	566	119
$t\bar{t}$	39.14	43.98	55.04	121.1	109.5	105.5	46.65	1.686
Single top	2.618	3.843	4.021	9.553	7.198	8.19	4.113	0.369
Dibosons	23.02	24.95	27.61	63.34	37.58	32.22	32.44	6.363
Multijets	0.701	0.639	0.636	0.911	0.518	0.337	0.237	0.039
Fitted N_b	1321 ± 64	1310 ± 57	1610 ± 61	2302 ± 71	1353 ± 53	875 ± 44	568 ± 35	106 ± 15
Fitted N_{c+l}	3335 ± 77	2922 ± 69	2589 ± 68	3627 ± 78	1980 ± 58	1258 ± 47	944 ± 39	147 ± 16
Reduced χ^2	1.2	1.1	1.8	1.3	0.85	1.3	0.81	0.97

Table 48: Summary of the fit results in the electron and muon channel as well as their combination in bins of Z p_T; for each analysis bin the estimation of the backgrounds and of the signal is presented. For the combined channel the χ^2 probability (p–value) is reported.

Z $\lvert y \rvert$	[0.0-0.2]	[0.2-0.4]	[0.4-0.6]	[0.6-0.8]	[0.8-1.2]	[1.2-1.6]	[1.6-2.0]	[2.0-2.5]
Combined channel								
Total data	5954	5952	5812	5551	9890	7651	4772	1556
Pre fit N_b	1548	1505	1477	1381	2418	1743	1033	308
Pre fit N_{charm}	1535	1543	1463	1406	2435	1781	986	318
Pre fit N_{light}	1859	1825	1840	1862	3490	3070	2170	795
$t\bar{t}$	151	153.1	138.3	122.5	195.1	113.7	43.94	7.399
Single top	13.4	11.29	12	7.788	13.84	9.052	3.26	0.933
Dibosons	53.83	55.35	51.88	50.15	80.19	65.17	50.27	16.52
Multijets	3.298	3.302	3.1	2.953	4.915	3.548	2.157	0.825
Fitted N_b	2245 ± 71	2265 ± 73	2246 ± 72	2013 ± 68	3546 ± 91	2538 ± 77	1393 ± 59	415 ± 31
Fitted N_{c+l}	3489 ± 78	3462 ± 79	3363 ± 78	3355 ± 76	6051 ± 103	4922 ± 90	3280 ± 73	1116 ± 41
Reduced χ^2	1.1	2.2	2.1	1.9	1.3	0.59	0.54	1.4
p–value	0.3129	0.0055	0.0054	0.0191	0.1944	0.8914	0.9289	0.1433
Electron channel								
Total data	2835	2840	2626	2500	4046	2833	1700	696
Pre fit N_b	739	690	663	603	989	641	380	123
Pre fit N_{charm}	702	726	674	605	1011	667	347	142
Pre fit N_{light}	903	844	838	830	1422	1153	806	348
$t\bar{t}$	75.67	70.2	61.21	54.41	79.44	42.43	15.97	3.204
Single top	6.053	5.403	5.621	3.858	5.416	4.054	0.916	0.344
Dibosons	26.91	25.34	25.33	20.7	32.99	25.45	14.47	4.641
Multijets	2.836	2.839	2.627	2.5	4.047	2.832	1.699	0.697
Fitted N_b	1076 ± 49	1157 ± 51	1023 ± 48	951 ± 47	1417 ± 58	947 ± 48	490 ± 34	170 ± 20
Fitted N_{c+l}	1648 ± 54	1577 ± 54	1509 ± 53	1468 ± 51	2508 ± 66	1810 ± 56	1176 ± 43	517 ± 28
Reduced χ^2	1.7	2.7	1.2	2.6	0.68	0.83	0.44	0.52
Muon channel								
Total data	3119	3112	3186	3051	5844	4818	3072	860
Pre fit N_b	810	814	814	778	1429	1103	653	185
Pre fit N_{charm}	833	818	789	801	1424	1114	639	176
Pre fit N_{light}	955	980	1002	1032	2068	1918	1364	448
$t\bar{t}$	75.38	82.87	77.13	68.1	115.6	71.28	27.97	4.195
Single top	7.346	5.888	6.381	3.93	8.427	4.998	2.345	0.589
Dibosons	26.91	30.02	26.55	29.45	47.2	39.71	35.79	11.88
Multijets	0.463	0.462	0.473	0.453	0.868	0.715	0.456	0.127
Fitted N_b	1172 ± 52	1102 ± 52	1224 ± 53	1068 ± 49	2130 ± 70	1589 ± 60	905 ± 48	247 ± 24
Fitted N_{c+l}	1838 ± 57	1891 ± 58	1853 ± 58	1881 ± 56	3542 ± 79	3112 ± 71	2100 ± 59	597 ± 30
Reduced χ^2	1.2	1.6	1.5	1	1	0.74	0.52	1.3

Table 49: Summary of the fit results in the electron and muon channel as well as their combination in bins of Z $\lvert y \rvert$; for each analysis bin the estimation of the backgrounds and of the signal is presented. For the combined channel the χ^2 probability (p–value) is reported.

D

SYSTEMATIC UNCERTAINTIES DETAILS

The treatment of the systematic uncertainties in the Z+b analysis has been discussed in Chap. 5. It has been pointed out that some systematics are correlated between the fit and the unfolding. Among them, the most important are the JES and the b–tagging efficiency uncertainties.

In this appendix, the systematic errors on the fitted b–yield due to the JES and b–tagging uncertainties are presented. The ratio of the fit results obtained with shifted JES to the nominal fitted b–yields is shown in Fig. 82. On the same foot the systematic variations of the fit results due to the uncertainties on b-tagging efficiency, charm and light jets mis–tag rate are presented normalized to the nominal fit results in Fig. 83.

The full breakdown of the systematic uncertainties is summarized in Tab. 50 to Tab. 57 for all the Z+b analysis bins.

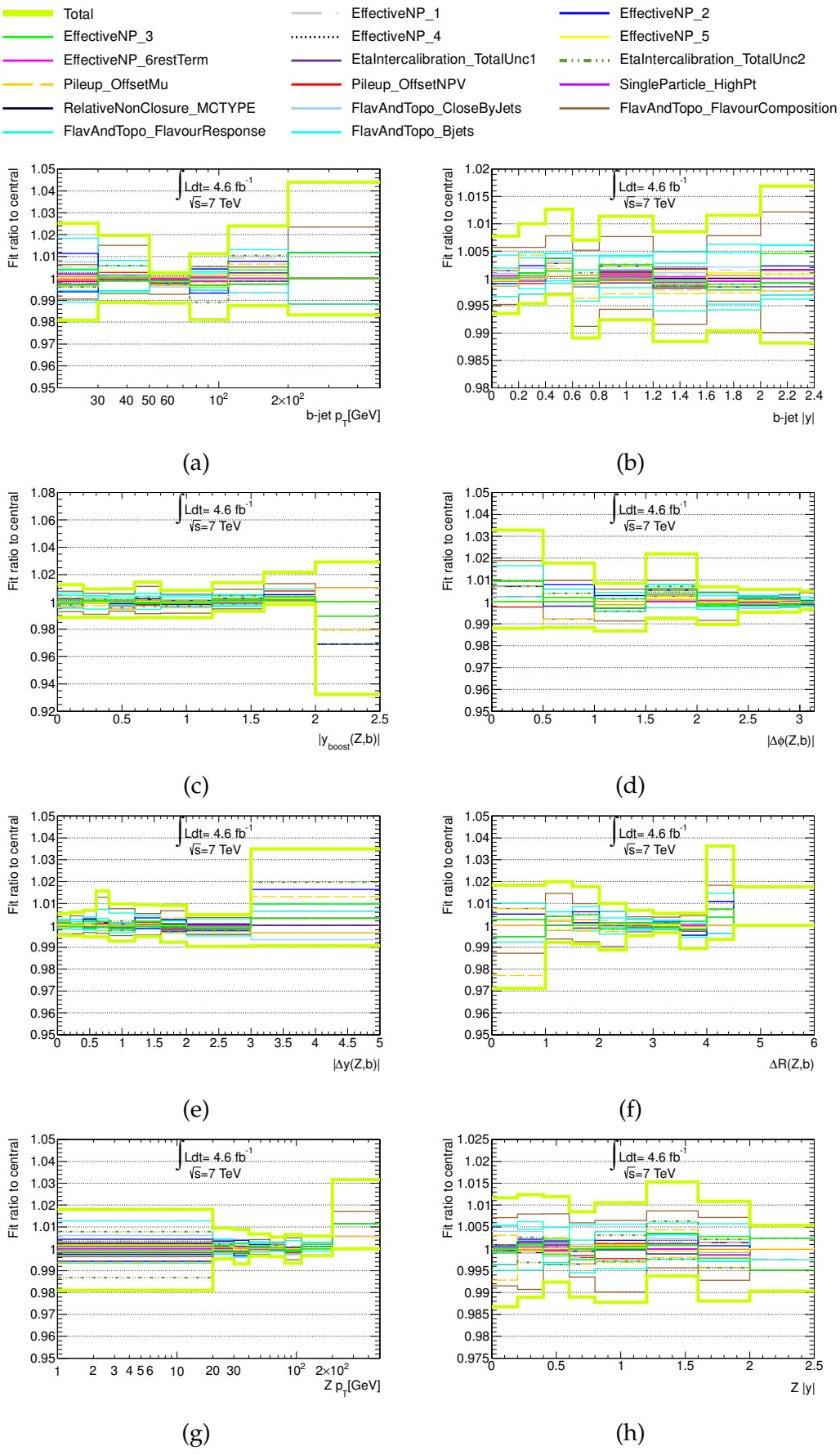

Figure 82: Flavor fit systematic uncertainty from the error on the jet energy scale, in all distributions: b–jet p_T (a), b–jet $|y|$ (b), $y_{boost}(Z,b)$ (c), $|\Delta y(Z,b)|$ (d), $\Delta\phi(Z,b)$ (e), $\Delta R(Z,b)$ (f), Z p_T (g) and Z $|y|$ (h). The contributions from all sources of the JES error are shown, along with the total error.

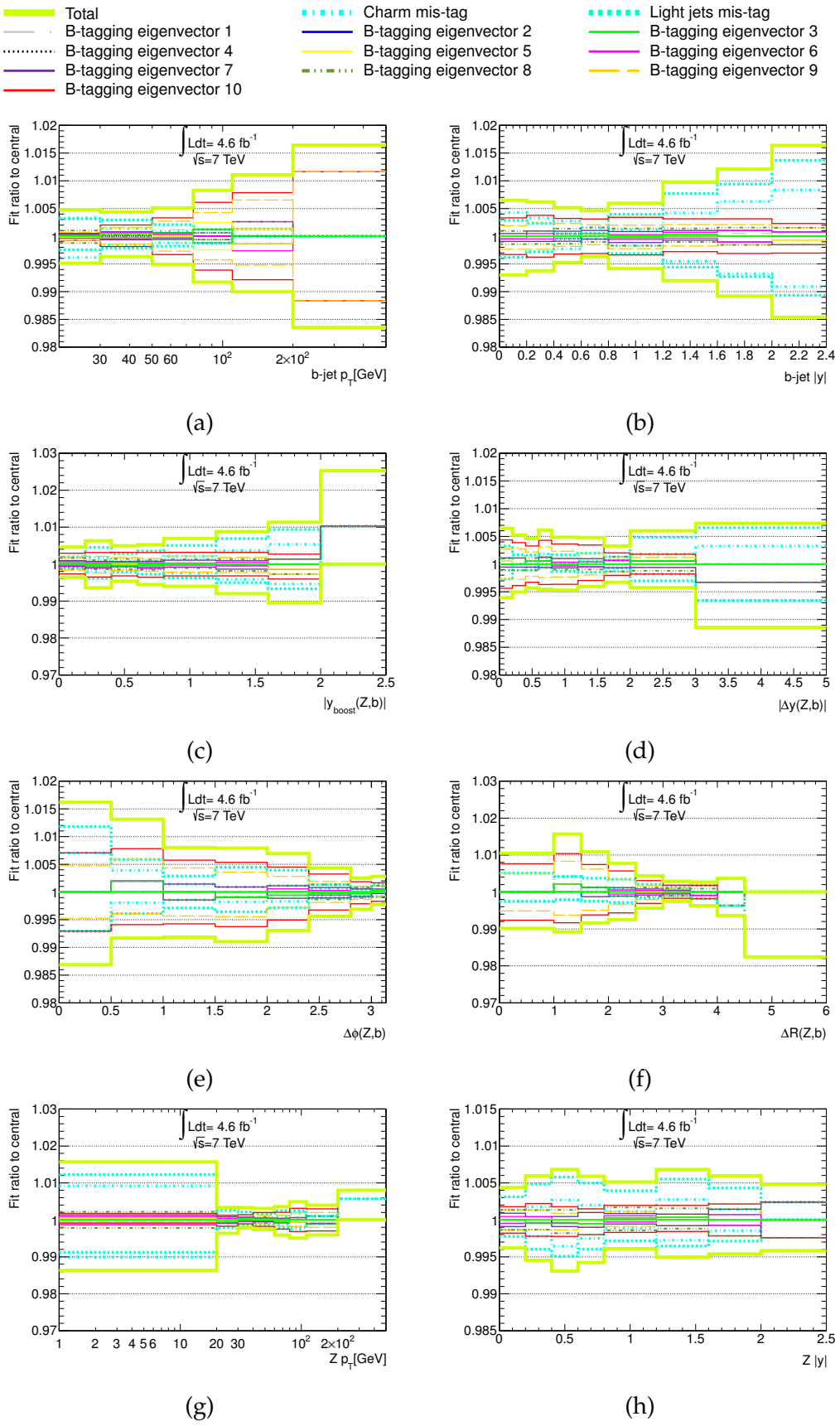

Figure 83: Flavor fit systematic uncertainty from the error on the b-tagging efficiency and light–charm mistag-rate, in all distributions: b–jet p_T (a), b–jet $|y|$ (b), $y_{boost}(Z,b)$ (c), $|\Delta y(Z,b)|$ (d), $\Delta\phi(Z,b)$ (e), $\Delta R(Z,b)$ (f), Z p_T (g) and Z $|y|$ (h). The contributions from all sources of the total error are shown, along with the total error.

b–jet p_T [GeV]	(20-30)	(30-50)	(50-75)	(75-110)	(110-200)	(200-500)
σ[pb/GeV]	0.196336	0.093764	0.035126	0.011840	0.002142	0.000101
Statistical	±2.73	±2.21	±2.96	±4.22	±6.04	±18.27
Total systematic ↑	11.10	8.42	8.27	10.88	12.13	21.69
Total systematic ↓	11.27	7.63	8.94	11.33	11.44	18.18
MPI ↑	−1.97	−1.38	−0.95	−0.55	−0.29	−0.38
MPI ↓	±2.36	±1.44	±1.01	±0.57	±0.26	±0.27
Gluon splitting ↑	0.36	0.43	0.46	0.16	−0.38	0.70
Gluon splitting ↓	−0.40	−0.50	−0.58	−0.15	0.59	−0.63
Luminosity	1.80	1.80	1.80	1.80	1.80	1.80
Electron identification efficiency ↑	1.03	1.08	1.13	1.09	0.99	1.04
Electron identification efficiency ↓	−1.05	−1.10	−1.16	−1.11	−1.00	−1.08
Electron energy scale ↑	0.08	0.16	0.02	0.07	0.25	−0.32
Electron energy scale ↓	−0.10	−0.06	−0.06	−0.09	0.11	0.11
Electron energy resolution ↑	0.02	0.05	−0.03	−0.21	0.17	−0.50
Electron energy resolution ↓	−0.05	0.09	−0.00	0.05	0.30	0.04
Muon reconstruction efficiency ↑	0.31	0.33	0.35	0.40	0.47	0.57
Muon reconstruction efficiency ↓	−0.31	−0.33	−0.35	−0.40	−0.47	−0.57
Muon energy scale ↑	0.01	0.03	0.03	−0.02	0.08	0.00
Muon energy scale ↓	0.02	−0.02	−0.02	−0.03	−0.05	0.00
Muon ID resolution ↑	−0.01	0.01	0.00	−0.03	0.03	0.04
Muon ID resolution ↓	0.00	−0.00	0.00	0.01	−0.03	0.25
Muon MS resolution ↑	0.04	−0.03	−0.01	−0.07	−0.02	−0.04
Muon MS resolution ↓	0.00	0.01	0.00	0.02	0.07	0.65
Electron trigger efficiency ↑	±0.14	±0.16	±0.18	±0.21	±0.24	±0.32
Electron trigger efficiency ↓	−0.14	−0.16	−0.18	−0.22	−0.24	−0.32
Muon trigger efficiency ↑	0.28	0.28	0.28	0.28	0.29	0.25
Muon trigger efficiency ↓	−0.28	−0.28	−0.28	−0.28	−0.28	−0.25
Pile-up ↑	−0.20	−0.12	−0.00	0.08	0.08	−1.44
Pile-up ↓	−0.26	−0.07	−0.08	−0.25	−0.11	−0.11
MET resolution soft terms ↑	−0.03	−0.04	−0.02	0.05	0.05	0.07
MET resolution soft terms ↓	−0.01	−0.01	−0.01	−0.01	0.05	−0.25
MET scale soft terms ↑	−0.08	−0.05	−0.07	−0.05	−0.16	−0.25
MET scale soft terms ↓	0.02	0.03	0.04	0.10	0.19	0.14
Reweighting vertex z–coordinate	±0.42	±0.26	±0.49	±0.05	±0.25	±1.76
Background ↑	0.44	0.81	1.62	2.57	2.75	1.18
Background ↓	−0.37	−0.78	−1.56	−2.45	−2.75	−2.35
Template shape l-jets	±1.89	±0.54	±0.30	±0.18	±0.26	±0.00
Template shape c-jets	±0.12	±0.23	±0.48	±0.37	±0.39	±0.00
Template shape b-jets	±4.60	±4.67	±4.35	±5.44	±6.54	±4.71
Jet energy resolution	±6.09	±0.16	±3.06	±0.79	±2.26	±1.36
Charm mis-tag ↑	−0.33	−0.14	−0.09	−0.12	0.00	0.00
Charm mis-tag ↓	0.38	0.16	0.12	0.12	0.00	0.00
Light jets mis-tag ↑	0.24	0.22	0.18	0.12	0.00	0.00
Light jets mis-tag ↓	−0.31	−0.29	−0.21	−0.12	−0.13	0.00
B tagging efficiency eigenvector 1 ↑	−0.027	0.31	−0.88	0.28	0.16	−0.035
B tagging efficiency eigenvector 1 ↓	0.03	−0.33	0.87	−0.29	−0.15	0.035
B tagging efficiency eigenvector 2 ↑	−0.17	0.68	−0.87	0.066	0.085	−0.035
B tagging efficiency eigenvector 2 ↓	0.2	−0.7	0.87	−0.087	−0.074	0.035
B tagging efficiency eigenvector 3 ↑	0.11	0.13	−0.85	0.8	0.15	−0.035
B tagging efficiency eigenvector 3 ↓	−0.11	−0.15	0.84	−0.83	−0.14	0.035
B tagging efficiency eigenvector 4 ↑	0.1	−0.46	0.25	0.5	−0.14	−0.071
B tagging efficiency eigenvector 4 ↓	−0.1	0.44	−0.25	−0.53	0.15	0.071
B tagging efficiency eigenvector 5 ↑	−0.51	0.94	0.098	−1.7	0.91	0.035
B tagging efficiency eigenvector 5 ↓	0.54	−0.97	−0.094	1.7	−0.89	−0.035
B tagging efficiency eigenvector 6 ↑	1.1	−1.2	−0.43	−0.032	1.5	−0.071
B tagging efficiency eigenvector 6 ↓	−1.1	1.1	0.43	0.016	−1.6	0.071
B tagging efficiency eigenvector 7 ↑	1.6	−0.59	−0.74	−0.85	0.75	0
B tagging efficiency eigenvector 7 ↓	−1.6	0.57	0.74	0.82	−0.74	0
B tagging efficiency eigenvector 8 ↑	−4.8	−0.41	0.26	0.22	1	−0.35
B tagging efficiency eigenvector 8 ↓	4.5	0.43	−0.26	−0.23	−1.2	0.35
B tagging efficiency eigenvector 9 ↑	1.7	2.4	2.3	2.4	3.4	−11
B tagging efficiency eigenvector 9 ↓	−1.8	−2.5	−2.4	−2.5	−3.7	9.7
B tagging efficiency eigenvector 10 ↑	−0.92	−3.2	−3.1	−3.4	−3.9	−15
B tagging efficiency eigenvector 10 ↓	0.95	3	3	3.2	3.7	12
Jet energy scale EffectiveNP 1 ↑	−0.21	−0.029	1.1	1.8	2.6	2.3
Jet energy scale EffectiveNP 1 ↓	0.54	−0.48	−0.44	−1.5	−2.7	−2.7
Jet energy scale EffectiveNP 2 ↑	−1	−1.9	−0.84	−1.6	−2.2	−0.72
Jet energy scale EffectiveNP 2 ↓	1.2	1.3	1.8	1.9	1.7	−1
Jet energy scale EffectiveNP 3 ↑	2	1.4	0.5	−0.21	−1.2	−0.83
Jet energy scale EffectiveNP 3 ↓	−1.6	−1.4	−0.64	0.57	1.2	−0.93
Jet energy scale EffectiveNP 4 ↑	−0.46	−0.46	−0.017	0.8	0.49	−0.11
Jet energy scale EffectiveNP 4 ↓	0.6	0.27	0.085	−0.44	−0.82	−0.43
Jet energy scale EffectiveNP 5 ↑	0.82	0.069	−0.055	−0.61	−0.32	0.036
Jet energy scale EffectiveNP 5 ↓	−0.72	−0.31	0.24	0.95	0.028	−0.57
Jet energy scale EffectiveNP 6restTerm ↑	−0.3	0.084	0.27	0.23	0.16	−0.036
Jet energy scale EffectiveNP 6restTerm ↓	0.21	−0.18	−0.024	−0.19	−0.42	−0.036
Jet energy scale EtaIntercalibration TotalUnc1 ↑	0.2	0.36	0.22	0.71	0.41	−0.072
Jet energy scale EtaIntercalibration TotalUnc1 ↓	0.11	−0.55	−0.1	−0.43	−0.63	−0.36
Jet energy scale EtaIntercalibration TotalUnc2 ↑	0.19	1	1.8	2.5	2	1.5
Jet energy scale EtaIntercalibration TotalUnc2 ↓	0.87	−2	−0.95	−1.9	−3	−2.8
Jet energy scale Pileup OffsetMu ↑	0.64	0.015	1.1	0.12	0.011	0.5
Jet energy scale Pileup OffsetMu ↓	0.37	−0.92	0.11	0.32	−0.89	−0.22
Jet energy scale Pileup OffsetNPV ↑	0.13	−0.034	0.23	−0.082	0.37	−1.6
Jet energy scale Pileup OffsetNPV ↓	0.45	−0.62	0.32	0.68	−0.25	−1.7
Jet energy scale SingleParticle HighPt ↑	0.031	0.0035	−0.0012	0.0053	−0.017	0
Jet energy scale SingleParticle HighPt ↓	0.0045	0.0018	−0.0099	0.0079	−0.011	0
Jet energy scale RelativeNonClosure MCTYPE ↑	−0.24	0.26	0.35	0.21	0.42	−0.036
Jet energy scale RelativeNonClosure MCTYPE ↓	0.53	−0.54	−0.1	−0.25	−0.46	−0.32
Jet energy scale FlavAndTopo CloseByJets ↑	−0.87	0.019	1.6	2.6	2.3	0.61
Jet energy scale FlavAndTopo CloseByJets ↓	1	−0.79	−0.94	−2.2	−2.2	−2.2
Jet energy scale FlavAndTopo FlavourComposition ↑	0.94	0.7	0.72	0.55	0.13	−2.4
Jet energy scale FlavAndTopo FlavourComposition ↓	−0.63	−1.5	0.24	−0.55	−0.52	1.2
Jet energy scale FlavAndTopo FlavourResponse ↑	0.56	0.61	0.12	0.43	0	−1.2
Jet energy scale FlavAndTopo FlavourResponse ↓	−0.37	−0.82	0.27	−0.31	−0.26	1.2
Jet energy scale FlavAndTopo Bjets ↑	−1.6	0.58	2.6	2.7	3.7	2.2
Jet energy scale FlavAndTopo Bjets ↓	1.7	−1.3	−2.1	−2.5	−4.5	−4.2
MC stat. (fit)	±1.40	±0.90	±1.00	±1.30	±1.90	±6.20
MC stat. (unfolding)	±1.10	±0.80	±1.10	±1.50	±2.00	±5.70
Unfolding Bias	±3.14	±0.79	±0.54	±0.27	±0.45	±1.29

Table 50: Systematic uncertainties for the differential Zb measurement (in b-jet p_T).

b–jet |y|	(0-0.2)	(0.2-0.4)	(0.4-0.6)	(0.6-0.8)	(0.8-1.2)	(1.2-1.6)	(1.6-2.0)	(2.0-2.4)
σ[pb/a.u.]	2.995969	2.935592	3.036675	2.706656	2.540045	2.136394	1.637068	1.212090
Statistical	±3.44	±3.68	±3.58	±3.89	±2.67	±3.15	±4.05	±5.43
Total systematic ↑	7.75	7.51	7.48	7.35	7.60	8.47	9.88	11.07
Total systematic ↓	7.61	7.39	6.99	7.55	7.41	8.67	9.76	11.37
MPI ↑	−1.27	−1.55	−1.73	−1.68	−1.59	−1.91	−3.85	−3.96
MPI ↓	±1.30	±1.62	±1.80	±1.77	±1.69	±2.11	±4.41	±4.84
Gluon splitting ↑	1.62	0.88	0.82	1.12	1.06	1.19	1.37	0.27
Gluon splitting ↓	−1.85	−0.98	−0.90	−1.26	−1.20	−1.33	−1.47	−0.28
Luminosity	1.80	1.80	1.80	1.80	1.80	1.80	1.80	1.80
Electron identification efficiency ↑	1.09	1.05	1.08	1.08	1.08	1.07	1.09	1.04
Electron identification efficiency ↓	−1.11	−1.07	−1.11	−1.10	−1.10	−1.09	−1.12	−1.06
Electron energy scale ↑	0.08	0.19	0.09	0.09	0.02	0.09	0.20	0.14
Electron energy scale ↓	−0.07	−0.07	−0.10	−0.03	−0.11	−0.07	0.02	0.01
Electron energy resolution ↑	−0.06	−0.00	−0.02	0.06	0.02	−0.08	0.08	0.07
Electron energy resolution ↓	0.04	0.05	0.07	0.02	−0.01	0.03	0.08	0.07
Muon reconstruction efficiency ↑	0.33	0.34	0.33	0.34	0.34	0.35	0.35	0.35
Muon reconstruction efficiency ↓	−0.33	−0.35	−0.34	−0.34	−0.35	−0.35	−0.35	−0.35
Muon energy scale ↑	0.04	0.02	0.04	0.02	−0.01	0.02	0.05	0.03
Muon energy scale ↓	−0.03	−0.01	−0.06	−0.01	−0.03	0.00	−0.02	0.12
Muon ID resolution ↑	0.03	−0.01	0.02	−0.01	0.00	0.01	−0.01	−0.01
Muon ID resolution ↓	0.00	0.01	0.00	0.00	−0.01	0.02	−0.01	0.00
Muon MS resolution ↑	−0.01	−0.01	−0.00	−0.04	−0.02	−0.02	−0.07	0.13
Muon MS resolution ↓	0.01	0.01	0.05	−0.02	0.01	0.05	0.00	0.00
Electron trigger efficiency ↑	±0.17	±0.17	±0.17	±0.17	±0.17	±0.16	±0.17	±0.16
Electron trigger efficiency ↓	−0.17	−0.17	−0.17	−0.17	−0.18	−0.16	−0.17	−0.16
Muon trigger efficiency ↑	0.29	0.28	0.29	0.28	0.28	0.28	0.28	0.27
Muon trigger efficiency ↓	−0.29	−0.29	−0.29	−0.28	−0.28	−0.28	−0.28	−0.28
Pile-up ↑	0.44	0.56	0.37	0.25	−0.04	−0.41	−0.64	−0.88
Pile-up ↓	−0.11	−0.29	−0.24	−0.18	−0.13	−0.08	−0.07	−0.02
MET resolution soft terms ↑	−0.02	−0.05	−0.01	−0.02	−0.03	0.00	−0.01	−0.01
MET resolution soft terms ↓	−0.00	0.01	0.04	−0.04	−0.02	−0.02	0.00	−0.01
MET scale soft terms ↑	−0.05	−0.08	−0.09	−0.06	−0.04	−0.06	−0.07	−0.13
MET scale soft terms ↓	0.10	0.05	0.06	0.03	0.03	0.03	0.05	0.02
Reweighting vertex z–coordinate	±0.40	±0.29	±0.10	±0.62	±0.40	±0.63	±0.40	±1.01
Background ↑	1.28	1.37	1.15	1.14	1.13	1.01	0.94	0.91
Background ↓	−1.23	−1.32	−1.15	−1.08	−1.10	−1.01	−0.94	−0.91
Template shape l-jets	±0.38	±0.42	±0.41	±0.46	±0.62	±0.94	±1.46	±1.90
Template shape c-jets	±0.33	±0.33	±0.37	±0.26	±0.20	±0.03	±0.16	±0.15
Template shape b-jets	±4.93	±4.67	±4.35	±4.24	±4.75	±5.17	±5.32	±6.54
Jet energy resolution	±0.37	±0.67	±0.16	±0.92	±1.10	±1.95	±0.31	±0.30
Charm mis-tag ↑	0.38	0.28	0.23	0.05	−0.11	−0.42	−0.63	−0.84
Charm mis-tag ↓	−0.43	−0.33	−0.27	−0.15	0.17	0.45	0.68	0.91
Light jets mis-tag ↑	−0.28	−0.24	−0.05	0.00	0.31	0.56	0.73	1.06
Light jets mis-tag ↓	0.38	0.28	0.05	−0.05	−0.40	−0.77	−0.94	−1.37
B tagging efficiency eigenvector 1 ↑	−0.024	−0.032	−0.088	−0.02	−0.019	−0.056	−0.058	0.0022
B tagging efficiency eigenvector 1 ↓	0.087	0.02	0.081	0.02	0.057	−0.0026	0.0083	0
B tagging efficiency eigenvector 2 ↑	0.036	0.02	0.022	0.046	0.067	0.018	0.028	0.027
B tagging efficiency eigenvector 2 ↓	−0.024	−0.028	−0.029	−0.048	−0.029	−0.041	−0.025	−0.029
B tagging efficiency eigenvector 3 ↑	0.024	0.0019	0.0072	−0.066	0.015	−0.043	0.032	0.047
B tagging efficiency eigenvector 3 ↓	−0.011	−0.0093	−0.011	0.006	0.025	−0.018	−0.025	−0.049
B tagging efficiency eigenvector 4 ↑	−0.0018	−0.059	−0.0036	−0.062	−0.027	−0.083	−0.068	−0.09
B tagging efficiency eigenvector 4 ↓	0.064	0.048	0	0.002	0.067	0.022	0.075	0.09
B tagging efficiency eigenvector 5 ↑	0.13	0.097	0.1	0.075	0.12	0.11	0.13	0.25
B tagging efficiency eigenvector 5 ↓	−0.12	−0.1	−0.11	−0.14	−0.078	−0.13	−0.12	−0.17
B tagging efficiency eigenvector 6 ↑	−0.17	−0.23	−0.17	−0.24	−0.18	−0.24	−0.24	−0.24
B tagging efficiency eigenvector 6 ↓	0.24	0.22	0.16	0.18	0.22	0.18	0.25	0.24
B tagging efficiency eigenvector 7 ↑	−0.06	−0.12	−0.11	−0.13	−0.094	−0.094	−0.005	0.029
B tagging efficiency eigenvector 7 ↓	0.12	0.11	0.11	0.068	0.13	0.033	0.0083	0.052
B tagging efficiency eigenvector 8 ↑	−0.92	−0.94	−0.95	−1	−0.97	−1.2	−1.3	−1.4
B tagging efficiency eigenvector 8 ↓	0.96	0.97	0.92	0.94	0.99	1.1	1.3	1.3
B tagging efficiency eigenvector 9 ↑	2.2	2.2	2.1	2.2	2.2	2.2	2.2	2.2
B tagging efficiency eigenvector 9 ↓	−2.2	−2.3	−2.3	−2.3	−2.3	−2.3	−2.3	−2.2
B tagging efficiency eigenvector 10 ↑	−2.9	−2.9	−2.8	−2.9	−2.8	−2.8	−2.7	−2.5
B tagging efficiency eigenvector 10 ↓	2.7	2.8	2.7	2.7	2.7	2.6	2.6	2.5
Jet energy scale EffectiveNP 1 ↑	0.58	0.43	0.35	0.54	0.33	0.71	0.63	1
Jet energy scale EffectiveNP 1 ↓	−0.36	−0.45	−0.62	−0.56	−0.61	−0.38	−0.78	−0.68
Jet energy scale EffectiveNP 2 ↑	−1.5	−1.3	−1.8	−1.2	−1.4	−1.7	−2.4	−2.5
Jet energy scale EffectiveNP 2 ↓	1.4	1.4	1.1	1.8	1.3	2.1	2.2	2.4
Jet energy scale EffectiveNP 3 ↑	0.96	0.89	0.51	1.4	0.69	1.5	1.7	1.6
Jet energy scale EffectiveNP 3 ↓	−1.1	−0.96	−1.1	−0.89	−0.98	−0.96	−1.5	−1.7
Jet energy scale EffectiveNP 4 ↑	−0.15	−0.067	−0.39	−0.34	−0.2	−0.1	−0.37	−0.26
Jet energy scale EffectiveNP 4 ↓	0.19	0.16	0.16	0.29	0.2	0.17	0.2	0.19
Jet energy scale EffectiveNP 5 ↑	0.14	0.12	0.05	0.26	0.18	0.12	0.077	0.13
Jet energy scale EffectiveNP 5 ↓	−0.055	−0.071	−0.29	−0.26	−0.11	−0.078	−0.28	−0.29
Jet energy scale EffectiveNP 6restTerm ↑	0.013	0.12	−0.011	0.058	0.027	0.059	0.025	0.052
Jet energy scale EffectiveNP 6restTerm ↓	−0.033	−0.022	−0.14	−0.02	−0.058	−0.037	−0.052	−0.28
Jet energy scale EtaIntercalibration TotalUnc1 ↑	0.29	0.21	0.19	0.43	0.25	0.28	0.5	0.75
Jet energy scale EtaIntercalibration TotalUnc1 ↓	−0.17	−0.17	−0.46	−0.48	−0.31	−0.21	−0.47	−0.39
Jet energy scale EtaIntercalibration TotalUnc2 ↑	0.0073	0.015	−0.07	0.42	0.5	1.9	2.5	3.3
Jet energy scale EtaIntercalibration TotalUnc2 ↓	0.0036	0.0056	−0.065	−0.43	−0.78	−1.3	−2.9	−3.2
Jet energy scale Pileup OffsetMu ↑	0.23	0.13	0.0072	0.76	0.45	0.58	0.16	0.92
Jet energy scale Pileup OffsetMu ↓	−0.38	−0.25	−0.36	0.13	−0.3	−0.18	0.067	−0.67
Jet energy scale Pileup OffsetNPV ↑	0.12	0.091	0.0018	0.18	−0.2	0.061	0.13	0.088
Jet energy scale Pileup OffsetNPV ↓	−0.077	0.17	−0.15	0.13	−0.034	−0.069	0.12	−0.24
Jet energy scale SingleParticle HighPt ↑	0.0073	0.015	−0.049	0.002	−0.017	0.022	0.013	−0.009
Jet energy scale SingleParticle HighPt ↓	0.0055	0.0056	−0.061	0.004	−0.026	0.0013	0.0017	−0.0045
Jet energy scale RelativeNonClosure MCTYPE ↑	−0.075	−0.06	−0.16	0.29	0.33	−0.017	−0.12	0.71
Jet energy scale RelativeNonClosure MCTYPE ↓	0.14	0.12	−0.0054	−0.19	−0.45	0.072	0.06	−0.88
Jet energy scale FlavAndTopo CloseByJets ↑	0.68	0.52	0.47	0.79	0.59	0.65	0.58	0.9
Jet energy scale FlavAndTopo CloseByJets ↓	−0.54	−0.81	−0.76	−0.64	−0.66	−0.92	−0.84	−0.49
Jet energy scale FlavAndTopo FlavourComposition ↑	0.47	0.28	0.27	0.88	0.57	0.84	0.42	0.99
Jet energy scale FlavAndTopo FlavourComposition ↓	−0.57	−0.57	−0.78	−0.52	−0.76	−0.49	−0.78	−1.2
Jet energy scale FlavAndTopo FlavourResponse ↑	0.33	0.28	0.092	0.41	0.17	0.59	0.57	0.3
Jet energy scale FlavAndTopo FlavourResponse ↓	−0.19	−0.38	−0.46	−0.15	−0.4	−0.28	−0.63	−0.61
Jet energy scale FlavAndTopo Bjets ↑	0.79	0.8	0.86	1.1	0.86	1.4	1.4	1.6
Jet energy scale FlavAndTopo Bjets ↓	−1.3	−1	−1.3	−1.2	−1	−1.6	−1.8	−1.4
MC stat. (fit)	±1.40	±1.30	±1.40	±1.50	±1.20	±1.50	±2.10	±2.90
MC stat. (unfolding)	±1.20	±1.40	±1.30	±1.40	±1.00	±1.10	±1.30	±1.60
Unfolding Bias	±0.31	±0.11	±0.37	±0.21	±0.27	±0.37	±0.40	±0.69

Table 51: Systematic uncertainties for the differential Zb measurement (in b-jet |y|).

$\lvert y_{boost}(Z,b)\rvert$	(0-0.2)	(0.2-0.4)	(0.4-0.6)	(0.6-0.8)	(0.8-1.2)	(1.2-1.6)	(1.6-2)	(2-2.5)
σ[pb/a.u.]	4.328249	4.075786	4.008528	3.789802	2.781049	1.769883	0.689683	0.087968
Statistical	±2.78	±3.04	±3.06	±3.28	±2.61	±3.52	±6.45	±18.64
Total systematic ↑	7.80	7.50	7.32	8.09	7.72	8.57	11.78	13.84
Total systematic ↓	8.02	7.78	7.56	8.03	7.87	8.47	11.58	15.76
MPI ↑	−2.06	−2.16	−2.18	−2.48	−2.14	−2.84	−4.01	−3.65
MPI ↓	±2.23	±2.37	±2.37	±2.70	±2.37	±3.10	±4.39	±4.18
Gluon splitting ↑	1.33	1.07	1.20	0.82	1.08	1.09	2.12	−1.50
Gluon splitting ↓	−1.50	−1.23	−1.36	−0.90	−1.16	−1.21	−2.38	1.74
Luminosity	1.80	1.80	1.80	1.80	1.80	1.80	1.80	1.80
Electron identification efficiency ↑	1.08	1.06	1.09	1.07	1.07	1.05	1.07	1.34
Electron identification efficiency ↓	−1.11	−1.09	−1.12	−1.10	−1.09	−1.07	−1.10	−1.34
Electron energy scale ↑	0.06	0.08	0.19	0.15	−0.00	0.17	0.25	0.05
Electron energy scale ↓	−0.15	−0.06	0.08	−0.17	−0.07	−0.05	0.14	−0.22
EER ↑	−0.15	0.04	0.09	0.02	−0.06	0.05	0.35	−0.30
EER ↓	−0.07	0.03	0.16	0.06	−0.00	0.09	0.35	−0.30
Muon reconstruction efficiency ↑	0.28	0.28	0.28	0.31	0.35	0.46	0.60	0.74
Muon reconstruction efficiency ↓	−0.28	−0.28	−0.29	−0.31	−0.36	−0.47	−0.61	−0.74
Muon energy scale ↑	0.01	0.03	0.04	0.02	0.02	0.03	0.05	0.00
Muon energy scale ↓	−0.02	−0.02	−0.05	0.02	−0.01	0.02	0.02	0.00
Muon ID resolution ↑	0.06	−0.05	−0.00	0.01	0.00	−0.01	−0.02	0.00
Muon ID resolution ↓	0.04	−0.04	−0.02	0.02	−0.01	0.03	−0.03	0.00
Muon MS resolution ↑	−0.01	0.05	−0.12	0.06	−0.02	−0.02	−0.02	0.02
Muon MS resolution ↓	0.08	−0.06	−0.00	0.01	0.03	0.00	0.07	−0.12
Electron trigger efficiency ↑	±0.15	±0.16	±0.16	±0.16	±0.16	±0.18	±0.24	±0.55
Electron trigger efficiency ↓	−0.15	−0.16	−0.17	−0.16	−0.16	−0.18	−0.24	−0.52
Muon trigger efficiency ↑	0.30	0.30	0.29	0.29	0.28	0.26	0.20	0.15
Muon trigger efficiency ↓	−0.30	−0.31	−0.29	−0.29	−0.28	−0.26	−0.20	−0.12
Pile-up ↑	0.11	−0.09	0.12	0.03	−0.20	−0.31	−0.39	0.20
Pile-up ↓	−0.16	−0.13	−0.22	−0.18	−0.01	−0.08	−0.37	−0.15
MET resolution soft terms ↑	−0.05	0.01	−0.03	−0.02	−0.01	−0.03	0.01	−0.12
MET resolution soft terms ↓	−0.02	0.00	0.01	−0.01	−0.02	−0.01	0.01	0.00
MET scale soft terms ↑	−0.06	−0.06	−0.04	−0.05	−0.08	−0.11	−0.06	−0.12
MET scale soft terms ↓	0.07	0.06	0.06	0.04	0.02	0.03	0.07	0.00
Reweighting vertex z–coordinate	±0.15	±0.16	±0.40	±0.20	±0.63	±0.48	±1.16	±1.14
Background ↑	1.11	1.15	1.10	1.14	1.17	1.10	1.20	0.00
Background ↓	−1.05	−1.11	−1.03	−1.10	−1.12	−1.10	−1.20	−1.03
Template shape l-jets	±0.59	±0.70	±0.71	±0.75	±0.85	±1.05	±1.47	±1.03
Template shape c-jets	±0.26	±0.31	±0.28	±0.28	±0.19	±0.09	±0.00	±1.03
Template shape b-jets	±4.95	±4.63	±4.41	±4.92	±4.96	±5.00	±7.35	±5.15
Jet energy resolution	±0.80	±0.26	±0.01	±0.38	±0.57	±0.33	±3.37	±2.85
Charm mis-tag ↑	−0.03	−0.17	−0.07	−0.08	−0.21	−0.37	−0.53	0.00
Charm mis-tag ↓	0.00	0.21	0.07	0.12	0.24	0.41	0.53	−1.03
Light jets mis-tag ↑	0.10	0.38	0.21	0.27	0.37	0.50	0.67	0.00
Light jets mis-tag ↓	−0.20	−0.45	−0.28	−0.35	−0.51	−0.69	−0.93	0.00
B tagging efficiency eigenvector 1 ↑	−0.01	−0.034	−0.019	−0.027	−0.023	−0.023	−0.0079	0.025
B tagging efficiency eigenvector 1 ↓	0.027	0.03	0.026	0.017	0.012	0.0062	0.016	0
B tagging efficiency eigenvector 2 ↑	0.043	0.023	0.034	0.017	0.03	0.028	0.02	0.074
B tagging efficiency eigenvector 2 ↓	−0.027	−0.027	−0.026	−0.029	−0.041	−0.045	−0.012	−0.05
B tagging efficiency eigenvector 3 ↑	0.032	0.0067	0.022	0.012	−0.002	−0.04	0	0.025
B tagging efficiency eigenvector 3 ↓	0.019	−0.015	0.023	−0.025	0.019	−0.025	0.012	0
B tagging efficiency eigenvector 4 ↑	−0.049	−0.058	−0.03	−0.077	−0.038	−0.076	−0.048	−0.099
B tagging efficiency eigenvector 4 ↓	0.066	0.052	0.075	0.064	0.056	0.0093	0.06	0.12
B tagging efficiency eigenvector 5 ↑	0.13	0.11	0.13	0.13	0.11	0.12	0.13	0.25
B tagging efficiency eigenvector 5 ↓	−0.11	−0.12	−0.12	−0.14	−0.12	−0.14	−0.12	−0.22
B tagging efficiency eigenvector 6 ↑	−0.19	−0.19	−0.17	−0.22	−0.19	−0.21	−0.16	−0.27
B tagging efficiency eigenvector 6 ↓	0.21	0.18	0.22	0.2	0.18	0.19	0.31	0.27
B tagging efficiency eigenvector 7 ↑	−0.042	−0.06	−0.029	−0.042	−0.045	−0.082	0.04	−0.05
B tagging efficiency eigenvector 7 ↓	0.059	0.054	0.072	0.072	0.062	0.015	0.11	0.074
B tagging efficiency eigenvector 8 ↑	−1	−1	−1	−1	−1.1	−1.1	−1	−1.1
B tagging efficiency eigenvector 8 ↓	1	1	1	1	1	1	1.1	1.1
B tagging efficiency eigenvector 9 ↑	2	2	2	2	2	2	2	2.1
B tagging efficiency eigenvector 9 ↓	−2.1	−2.1	−2.1	−2.1	−2.1	−2.1	−1.9	−2.2
B tagging efficiency eigenvector 10 ↑	−2.5	−2.5	−2.6	−2.6	−2.5	−2.5	−2.4	−2.5
B tagging efficiency eigenvector 10 ↓	2.5	2.4	2.5	2.5	2.4	2.4	2.3	2.4
Jet energy scale EffectiveNP 1 ↑	0.86	0.55	0.43	0.63	0.51	0.66	0.8	0.27
Jet energy scale EffectiveNP 1 ↓	−0.64	−0.39	−0.45	−0.57	−0.53	−0.84	−0.44	−0.65
Jet energy scale EffectiveNP 2 ↑	−1.8	−1.7	−1.4	−2.1	−1.6	−1.9	−1.8	−1.1
Jet energy scale EffectiveNP 2 ↓	1.9	2	1.7	1.8	1.6	1.8	1.3	4.4
Jet energy scale EffectiveNP 3 ↑	1.5	1.3	1.1	1.1	1.1	1.1	0.98	1.8
Jet energy scale EffectiveNP 3 ↓	−1.2	−1.2	−1	−1	−1	−1.3	−1.2	−0.6
Jet energy scale EffectiveNP 4 ↑	−0.25	−0.12	−0.19	−0.28	−0.25	−0.28	−0.36	−0.2
Jet energy scale EffectiveNP 4 ↓	0.27	0.28	0.13	0.24	0.23	0.4	−0.056	0.35
Jet energy scale EffectiveNP 5 ↑	0.22	0.23	0.17	0.088	0.15	0.27	−0.044	0.17
Jet energy scale EffectiveNP 5 ↓	−0.21	−0.023	−0.18	−0.21	−0.13	−0.3	−0.056	−0.05
Jet energy scale EffectiveNP 6restTerm ↑	0.11	0.098	0.093	0.014	0.012	0.07	0.052	0.15
Jet energy scale EffectiveNP 6restTerm ↓	−0.1	0.004	−0.11	−0.068	−0.043	−0.15	−0.032	−0.05
Jet energy scale EtaIntercalibration TotalUnc1 ↑	0.5	0.35	0.22	0.4	0.34	0.5	0.7	0.27
Jet energy scale EtaIntercalibration TotalUnc1 ↓	−0.4	−0.15	−0.25	−0.39	−0.36	−0.44	−0.36	−0.57
Jet energy scale EtaIntercalibration TotalUnc2 ↑	0.93	0.78	0.98	1.2	1.4	2.1	1.8	4.4
Jet energy scale EtaIntercalibration TotalUnc2 ↓	−0.96	−0.58	−0.87	−1.4	−1.1	−2.2	−2.4	−2.1
Jet energy scale Pileup OffsetMu ↑	0.78	0.48	0.77	−0.18	0.56	0.3	0.36	2.3
Jet energy scale Pileup OffsetMu ↓	−0.25	−0.063	−0.48	−0.079	−0.38	−0.48	−0.27	1.1
Jet energy scale Pileup OffsetNPV ↑	0.4	0.052	0.23	−0.0072	0.086	−0.21	−0.39	2.5
Jet energy scale Pileup OffsetNPV ↓	−0.068	0.24	−0.0014	0.12	0.012	−0.22	−0.091	−0.69
Jet energy scale SingleParticle HighPt ↑	0.018	0.012	0.027	−0.014	−0.003	0.02	0	0
Jet energy scale SingleParticle HighPt ↓	−0.0051	0.0067	0.0082	−0.0072	−0.002	0.0015	−0.004	0.025
Jet energy scale RelativeNonClosure MCTYPE ↑	0.035	0.15	0.11	0.2	0.14	0.28	0.75	0.25
Jet energy scale RelativeNonClosure MCTYPE ↓	−0.067	0.0013	−0.09	−0.3	−0.14	−0.42	0.016	−0.67
Jet energy scale FlavAndTopo CloseByJets ↑	0.67	0.66	0.37	0.8	0.67	0.78	0.32	4.8
Jet energy scale FlavAndTopo CloseByJets ↓	−0.58	−0.95	−0.79	−0.72	−0.64	−0.8	−0.8	−0.4
Jet energy scale FlavAndTopo FlavourComposition ↑	2.9	3.3	2.8	3.2	3	2.9	2.3	4.4
Jet energy scale FlavAndTopo FlavourComposition ↓	−3.2	−3.3	−3.3	−3.9	−3.2	−3.5	−3.9	−2.3
Jet energy scale FlavAndTopo FlavourResponse ↑	1.8	1.9	1.8	1.7	1.6	1.7	1.5	2
Jet energy scale FlavAndTopo FlavourResponse ↓	−1.8	−1.7	−1.5	−2.1	−1.6	−2	−2.1	−1.1
Jet energy scale FlavAndTopo Bjets ↑	1.7	1.7	1.6	1.5	1.4	1.6	1.3	4.4
Jet energy scale FlavAndTopo Bjets ↓	−1.6	−1.6	−1.4	−2	−1.4	−1.8	−1.8	−1.1
MC stat. (fit)	±1.30	±1.40	±1.40	±1.50	±1.30	±1.70	±3.00	±8.20
MC stat. (unfolding)	±1.00	±1.10	±1.10	±1.20	±0.90	±1.20	±1.90	±5.60
Unfolding Bias	±0.27	±0.04	±0.26	±0.06	±0.20	±0.45	±0.57	±2.05

Table 52: Systematic uncertainties for the differential Zb measurement (in y_{boost}).

$\lvert\Delta y(Z,b)\rvert$	(0-0.2)	(0.2-0.4)	(0.4-0.6)	(0.6-0.8)	(0.8-1.2)	(1.2-1.6)	(1.6-2)	(2-3)	(3-5)
σ[pb/a.u.]	2.589466	2.561052	2.611447	2.276628	2.151346	1.465778	1.132133	0.516235	0.057008
Statistical	±3.79	±4.02	±3.86	±4.36	±2.90	±3.58	±4.11	±3.88	±9.93
Total systematic ↑	7.46	7.67	7.30	8.32	7.80	7.29	7.47	7.97	11.61
Total systematic ↓	7.44	7.53	7.26	7.74	7.71	6.92	7.39	7.77	10.95
MPI ↑	−1.01	−0.86	−0.75	−0.63	−0.74	−0.98	−1.51	−2.20	−3.00
MPI ↓	±1.03	±0.86	±0.77	±0.65	±0.76	±1.01	±1.55	±2.34	±3.63
Gluon splitting ↑	0.23	1.72	0.64	0.41	1.40	0.76	1.74	1.66	3.87
Gluon splitting ↓	−0.21	−1.93	−0.67	−0.38	−1.61	−0.85	−2.04	−1.95	−4.91
Luminosity	1.80	1.80	1.80	1.80	1.80	1.80	1.80	1.80	1.80
Electron identification efficiency ↑	1.12	1.12	1.10	1.12	1.09	1.11	1.12	1.10	1.12
Electron identification efficiency ↓	−1.15	−1.14	−1.13	−1.14	−1.12	−1.13	−1.15	−1.12	−1.14
Electron energy scale ↑	0.12	0.06	0.06	0.29	−0.03	0.14	0.06	0.15	0.01
Electron energy scale ↓	−0.08	−0.16	−0.21	0.10	−0.23	−0.02	−0.22	−0.07	−0.09
Electron energy resolution ↑	0.17	−0.21	−0.06	0.27	−0.10	0.02	−0.26	−0.02	−0.15
Electron energy resolution ↓	0.07	−0.02	−0.14	0.29	−0.09	0.16	−0.26	−0.02	−0.15
Muon reconstruction efficiency ↑	0.34	0.33	0.34	0.33	0.33	0.35	0.35	0.44	0.66
Muon reconstruction efficiency ↓	−0.34	−0.34	−0.34	−0.34	−0.34	−0.35	−0.36	−0.44	−0.66
Muon energy scale ↑	0.04	0.06	−0.01	0.06	0.02	0.08	0.02	0.04	0.03
Muon energy scale ↓	−0.02	−0.04	−0.06	−0.02	−0.04	0.06	−0.04	−0.02	0.00
Muon ID resolution ↑	−0.01	0.05	−0.09	0.00	0.01	0.03	−0.04	0.01	0.33
Muon ID resolution ↓	0.01	0.01	−0.02	0.05	0.01	0.03	0.04	−0.03	−0.09
Muon MS resolution ↑	0.02	0.04	−0.10	0.04	−0.06	0.15	−0.07	−0.06	0.01
Muon MS resolution ↓	0.02	0.05	−0.05	−0.07	0.10	0.03	−0.02	−0.01	0.19
Electron trigger efficiency ↑	±0.18	±0.17	±0.17	±0.17	±0.17	±0.18	±0.18	±0.21	±0.31
Electron trigger efficiency ↓	−0.17	−0.17	−0.17	−0.18	−0.17	−0.18	−0.18	−0.21	−0.31
Muon trigger efficiency ↑	0.28	0.28	0.29	0.28	0.29	0.28	0.27	0.26	0.20
Muon trigger efficiency ↓	−0.28	−0.28	−0.29	−0.29	−0.29	−0.28	−0.28	−0.26	−0.19
Pile-up ↑	0.03	0.11	0.34	0.18	0.02	0.02	0.27	0.08	−0.60
Pile-up ↓	−0.14	−0.08	−0.45	−0.13	−0.07	−0.02	−0.16	−0.30	−0.11
MET resolution soft terms ↑	−0.00	−0.03	−0.08	−0.01	−0.01	−0.04	0.03	−0.00	−0.07
MET resolution soft terms ↓	−0.01	−0.00	−0.01	−0.06	0.02	−0.01	0.02	−0.01	−0.09
MET scale soft terms ↑	−0.07	−0.04	−0.13	−0.10	−0.05	−0.09	−0.02	−0.04	−0.08
MET scale soft terms ↓	0.03	0.04	0.04	0.06	0.08	0.06	0.06	0.04	0.08
Reweighting vertex z–coordinate	±0.84	±0.31	±0.07	±0.84	±0.32	±0.14	±0.44	±0.76	±1.10
Background ↑	1.63	1.55	1.36	1.47	1.23	1.13	0.67	0.48	0.33
Background ↓	−1.53	−1.49	−1.31	−1.47	−1.16	−1.03	−0.60	−0.36	0.00
Template shape l-jets	±0.60	±0.55	±0.38	±0.61	±0.63	±0.64	±0.67	±0.84	±1.64
Template shape c-jets	±0.33	±0.33	±0.33	±0.31	±0.33	±0.34	±0.27	±0.12	±0.00
Template shape b-jets	±4.74	±4.86	±5.02	±5.40	±5.31	±4.53	±4.43	±4.58	±3.62
Jet energy resolution	±0.63	±0.49	±0.35	±0.90	±0.51	±0.13	±0.81	±0.50	±3.18
Charm mis-tag ↑	−0.11	0.00	−0.05	0.06	0.00	0.00	0.13	−0.18	−0.33
Charm mis-tag ↓	0.11	0.00	0.05	−0.18	0.00	−0.05	−0.13	0.18	0.66
Light jets mis-tag ↑	0.27	0.11	0.11	0.00	0.13	0.15	0.07	0.30	0.66
Light jets mis-tag ↓	−0.33	−0.17	−0.16	−0.12	−0.17	−0.20	−0.07	−0.48	−0.66
B tagging efficiency eigenvector 1 ↑	−0.086	−0.0085	−0.096	−0.091	−0.058	−0.093	−0.043	−0.017	0.0096
B tagging efficiency eigenvector 1 ↓	0.032	0.053	0.033	0.022	0.067	0.011	0.027	0.017	−0.0096
B tagging efficiency eigenvector 2 ↑	0.038	0.045	0.025	0.041	0.035	0.024	0.039	0.032	0.029
B tagging efficiency eigenvector 2 ↓	−0.034	−0.0043	−0.088	−0.11	−0.027	−0.11	−0.053	−0.095	−0.019
B tagging efficiency eigenvector 3 ↑	−0.019	0.0043	−0.061	−0.079	−0.011	−0.082	0.0024	−0.04	0.038
B tagging efficiency eigenvector 3 ↓	0.021	0.036	−0.0021	0.012	0.02	0	−0.019	−0.025	−0.029
B tagging efficiency eigenvector 4 ↑	−0.044	−0.017	−0.05	−0.055	−0.01	−0.071	−0.063	−0.076	−0.067
B tagging efficiency eigenvector 4 ↓	−0.011	0.062	−0.013	−0.012	0.019	−0.011	0.046	0.074	0.067
B tagging efficiency eigenvector 5 ↑	0.074	0.13	0.046	0.12	0.12	0.13	0.11	0.12	0.13
B tagging efficiency eigenvector 5 ↓	−0.13	−0.081	−0.11	−0.12	−0.11	−0.15	−0.13	−0.12	−0.13
B tagging efficiency eigenvector 6 ↑	−0.2	−0.17	−0.18	−0.28	−0.22	−0.27	−0.26	−0.23	−0.13
B tagging efficiency eigenvector 6 ↓	0.21	0.2	0.18	0.2	0.22	0.24	0.24	0.17	0.14
B tagging efficiency eigenvector 7 ↑	−0.2	−0.18	−0.13	−0.19	−0.15	−0.17	−0.11	−0.051	0.086
B tagging efficiency eigenvector 7 ↓	0.15	0.15	0.13	0.11	0.13	0.086	0.092	0.049	0.26
B tagging efficiency eigenvector 8 ↑	−0.79	−0.82	−0.87	−0.94	−0.9	−0.95	−1	−1.1	−1.1
B tagging efficiency eigenvector 8 ↓	0.78	0.84	0.86	0.85	0.89	0.91	0.96	1	1.4
B tagging efficiency eigenvector 9 ↑	2.3	2.3	2.2	2.2	2.2	2.2	2.1	2.1	2.4
B tagging efficiency eigenvector 9 ↓	−2.4	−2.4	−2.3	−2.4	−2.3	−2.3	−2.2	−2.2	−2.2
B tagging efficiency eigenvector 10 ↑	−3	−3	−2.9	−3	−2.9	−2.9	−2.7	−2.7	−2.4
B tagging efficiency eigenvector 10 ↓	2.9	2.9	2.7	2.8	2.8	2.7	2.6	2.6	2.7
Jet energy scale EffectiveNP 1 ↑	0.38	0.25	0.41	0.34	0.54	0.32	0.51	0.42	0.41
Jet energy scale EffectiveNP 1 ↓	−0.52	−0.26	−0.27	−0.51	−0.5	−0.3	−0.35	−0.37	−0.52
Jet energy scale EffectiveNP 2 ↑	−1.1	−1.1	−0.87	−1.7	−1.3	−1.3	−1.2	−1.6	−1.9
Jet energy scale EffectiveNP 2 ↓	1.2	1.1	0.96	1.1	1.3	0.96	1.2	1.2	0.65
Jet energy scale EffectiveNP 3 ↑	0.8	0.63	0.58	0.69	0.98	0.61	0.88	1	0.22
Jet energy scale EffectiveNP 3 ↓	−0.66	−0.68	−0.51	−1.1	−0.8	−0.86	−0.74	−0.95	−0.99
Jet energy scale EffectiveNP 4 ↑	−0.33	−0.16	−0.061	−0.24	−0.11	−0.14	−0.094	−0.17	−0.36
Jet energy scale EffectiveNP 4 ↓	0.24	0.098	0.31	0.094	0.26	0.12	0.34	0.15	0.42
Jet energy scale EffectiveNP 5 ↑	0.19	0.09	0.24	0.062	0.14	0.095	0.19	0.18	0.61
Jet energy scale EffectiveNP 5 ↓	−0.19	−0.11	−0.094	−0.17	−0.095	−0.14	−0.11	−0.14	−0.58
Jet energy scale EffectiveNP 6restTerm ↑	0.11	0.045	0.061	−0.05	0.1	0.032	0.077	0.04	0.42
Jet energy scale EffectiveNP 6restTerm ↓	−0.046	−0.034	−0.027	−0.096	−0.051	0.011	−0.068	−0.049	−0.46
Jet energy scale EtaIntercalibration TotalUnc1 ↑	0.24	0.21	0.33	0.19	0.33	0.19	0.43	0.29	0.59
Jet energy scale EtaIntercalibration TotalUnc1 ↓	−0.43	−0.15	−0.096	−0.25	−0.18	−0.26	−0.17	−0.25	−0.41
Jet energy scale EtaIntercalibration TotalUnc2 ↑	0.49	0.36	0.47	0.46	0.85	0.63	0.87	1.2	0.5
Jet energy scale EtaIntercalibration TotalUnc2 ↓	−0.52	−0.46	−0.39	−0.8	−0.79	−0.89	−0.55	−1.4	−2.7
Jet energy scale Pileup OffsetMu ↑	0.39	0.29	0.12	0.54	0.072	−0.02	0.34	0.53	−0.59
Jet energy scale Pileup OffsetMu ↓	−0.15	−0.32	0.24	−0.68	−0.27	−0.52	−0.53	−0.18	−0.79
Jet energy scale Pileup OffsetNPV ↑	−0.021	0.036	0.065	−0.13	0.18	−0.21	0.096	−0.087	0.24
Jet energy scale Pileup OffsetNPV ↓	−0.021	0.017	0.19	−0.39	0.19	−0.089	0.23	−0.049	0.43
Jet energy scale SingleParticle HighPt ↑	0.015	0.0021	0.013	−0.07	0.0051	0	0	0	0.0096
Jet energy scale SingleParticle HighPt ↓	0.0063	0	0.0021	−0.082	0.0025	0.0019	−0.0048	0	0.0096
Jet energy scale RelativeNonClosure MCTYPE ↑	0.036	0.026	0.065	0.065	0.095	0.073	0.2	0.24	−0.18
Jet energy scale RelativeNonClosure MCTYPE ↓	−0.084	−0.034	0.065	−0.17	−0.034	−0.16	−0.14	−0.082	−0.077
Jet energy scale FlavAndTopo CloseByJets ↑	0.77	0.43	0.43	0.51	0.56	0.4	0.42	0.53	0.23
Jet energy scale FlavAndTopo CloseByJets ↓	−0.5	−0.4	−0.37	−1.1	−0.53	−0.89	−0.33	−0.54	−0.31
Jet energy scale FlavAndTopo FlavourComposition ↑	0.38	0.39	0.33	0.37	0.46	0.44	0.34	0.42	−0.66
Jet energy scale FlavAndTopo FlavourComposition ↓	−0.22	−0.44	−0.33	−1.3	−0.76	−0.54	−0.67	−0.36	−0.99
Jet energy scale FlavAndTopo FlavourResponse ↑	0.16	0.17	0.22	0.25	0.33	0.098	0.13	0.06	−0.33
Jet energy scale FlavAndTopo FlavourResponse ↓	−0.22	−0.28	−0.22	−0.74	−0.56	−0.15	−0.2	−0.3	−0.99
Jet energy scale FlavAndTopo Bjets ↑	0.9	0.71	0.67	0.6	0.83	0.59	1	1.1	0.84
Jet energy scale FlavAndTopo Bjets ↓	−1.1	−0.98	−0.76	−1.2	−0.91	−1.2	−0.88	−1.2	−1.1
MC stat. (fit)	±1.50	±1.60	±1.30	±1.60	±1.30	±1.50	±1.80	±2.00	±5.40
MC stat. (unfolding)	±1.20	±1.30	±1.30	±1.30	±0.90	±1.10	±1.40	±1.40	±3.20
Unfolding Bias	±0.24	±0.18	±0.11	±0.39	±0.09	±0.19	±0.38	±0.06	±0.37

Table 53: Systematic uncertainties for the differential Zb measurement (in $|\Delta y(Z, b-jet)|$).

$\Delta\phi(Z, b)$	(0-0.5)	(0.5-1)	(1-1.5)	(1.5-2)	(2-2.4)	(2.4-2.8)	(2.8-3)	(3-π)
σ[pb/rad.]	0.258716	0.321299	0.428997	0.680451	1.318914	2.662429	5.325996	7.152546
Statistical	±8.84	±8.08	±6.86	±5.25	±4.07	±2.83	±2.87	±2.71
Total systematic ↑	11.04	10.81	10.48	9.80	8.62	7.93	6.74	7.03
Total systematic ↓	9.97	9.80	10.37	8.72	8.14	7.36	6.38	6.71
MPI ↑	−1.43	−2.94	−2.01	−1.24	−0.92	−0.91	−0.73	−0.91
MPI ↓	±1.78	±3.17	±2.19	±1.37	±0.95	±0.93	±0.73	±0.91
Gluon splitting ↑	0.45	1.81	1.05	0.56	1.45	1.06	0.58	1.13
Gluon splitting ↓	−0.43	−2.03	−1.15	−0.54	−1.63	−1.18	−0.66	−1.33
Luminosity	1.80	1.80	1.80	1.80	1.80	1.80	1.80	1.80
Electron identification efficiency ↑	1.05	1.08	1.09	1.11	1.10	1.12	1.12	1.12
Electron identification efficiency ↓	−1.07	−1.11	−1.12	−1.13	−1.12	−1.14	−1.15	−1.14
Electron energy scale ↑	−0.08	0.14	0.00	0.28	0.13	0.22	0.01	0.01
Electron energy scale ↓	−0.37	−0.01	−0.14	−0.05	−0.02	−0.10	−0.20	−0.09
Electron energy resolution ↑	0.13	−0.16	−0.58	0.20	0.29	−0.10	0.07	−0.16
Electron energy resolution ↓	−0.05	0.07	−0.23	0.12	0.11	0.10	0.07	−0.16
Muon reconstruction efficiency ↑	0.35	0.35	0.37	0.37	0.36	0.35	0.34	0.35
Muon reconstruction efficiency ↓	−0.35	−0.36	−0.37	−0.37	−0.36	−0.36	−0.35	−0.35
Muon energy scale ↑	−2.27	−3.11	−2.97	−2.77	−2.86	−2.48	−1.81	−1.26
Muon energy scale ↓	−2.25	−3.49	−2.89	−2.80	−2.90	−2.49	−1.86	−1.35
Muon ID resolution ↑	0.02	−0.01	−0.17	−0.01	−0.06	0.13	−0.08	0.03
Muon ID resolution ↓	0.02	0.07	0.02	−0.04	−0.07	0.07	0.02	−0.01
Muon MS resolution ↑	0.14	0.01	−0.33	0.05	−0.11	0.13	0.00	−0.06
Muon MS resolution ↓	−0.14	0.03	0.06	−0.01	0.08	−0.06	0.06	0.06
Electron trigger efficiency ↑	±0.17	±0.18	±0.18	±0.18	±0.18	±0.18	±0.18	±0.18
Electron trigger efficiency ↓	−0.18	−0.19	−0.17	−0.18	−0.18	−0.18	−0.18	−0.18
Muon trigger efficiency ↑	0.28	0.27	0.27	0.27	0.29	0.28	0.28	0.28
Muon trigger efficiency ↓	−0.29	−0.28	−0.27	−0.27	−0.29	−0.28	−0.28	−0.28
Pile-up ↑	−0.41	−0.32	−0.08	0.07	−0.02	0.16	0.14	0.20
Pile-up ↓	−0.31	−0.13	−0.16	−0.20	−0.15	−0.11	−0.08	−0.22
MET resolution soft terms ↑	−0.13	−0.02	0.00	−0.04	−0.00	−0.03	−0.01	−0.01
MET resolution soft terms ↓	−0.12	0.05	0.01	−0.01	0.01	−0.01	−0.01	−0.00
MET scale soft terms ↑	−0.09	−0.10	−0.10	−0.07	−0.03	−0.07	−0.07	−0.07
MET scale soft terms ↓	0.02	0.08	0.09	0.07	0.06	0.01	0.06	0.06
Reweighting vertex z–coordinate	±0.22	±0.66	±0.70	±0.55	±0.62	±0.55	±0.13	±0.36
Background ↑	2.84	2.55	2.74	2.32	1.69	1.11	0.64	0.55
Background ↓	−2.84	−2.55	−2.74	−2.32	−1.69	−1.05	−0.58	−0.50
Template shape l-jets	±0.95	±0.78	±0.86	±0.71	±0.51	±0.59	±0.50	±0.72
Template shape c-jets	±0.24	±0.00	±0.14	±0.18	±0.17	±0.16	±0.35	±0.44
Template shape b-jets	±5.20	±5.88	±6.34	±5.80	±5.19	±5.15	±4.09	±4.61
Jet energy resolution	±1.81	±0.97	±1.09	±0.29	±0.15	±0.58	±0.71	±0.68
Charm mis-tag ↑	−0.71	−0.39	−0.14	−0.09	−0.11	0.05	0.08	0.00
Charm mis-tag ↓	0.71	0.20	0.14	0.18	0.17	−0.05	−0.08	−0.03
Light jets mis-tag ↑	0.71	0.39	0.29	0.36	0.28	0.11	0.08	0.08
Light jets mis-tag ↓	−1.18	−0.59	−0.29	−0.45	−0.39	−0.13	−0.05	−0.14
B tagging efficiency eigenvector 1 ↑	0	−0.2	−0.025	−0.0096	−0.0021	−0.04	−0.022	−0.083
B tagging efficiency eigenvector 1 ↓	−0.017	−0.014	0	0.12	0.079	0.046	0.074	0.044
B tagging efficiency eigenvector 2 ↑	0.042	0.047	0.015	0.15	0.027	0.03	0.076	0.023
B tagging efficiency eigenvector 2 ↓	−0.059	−0.26	−0.041	−0.035	−0.01	−0.052	−0.02	−0.06
B tagging efficiency eigenvector 3 ↑	0.025	−0.24	0.015	0.022	0.029	−0.014	−0.015	−0.056
B tagging efficiency eigenvector 3 ↓	−0.042	0.02	−0.041	0.086	0.048	0.019	0.069	0.018
B tagging efficiency eigenvector 4 ↑	−0.076	−0.3	−0.066	0.051	−0.054	−0.05	−0.0041	−0.0032
B tagging efficiency eigenvector 4 ↓	0.059	0.081	0.046	0.061	0.066	0.057	0.053	−0.0032
B tagging efficiency eigenvector 5 ↑	0.12	0.12	0.12	0.13	0.13	0.13	0.13	0.065
B tagging efficiency eigenvector 5 ↓	−0.14	−0.12	−0.14	−0.12	−0.11	−0.15	−0.072	−0.1
B tagging efficiency eigenvector 6 ↑	−0.1	−0.35	−0.14	−0.16	−0.24	−0.25	−0.2	−0.23
B tagging efficiency eigenvector 6 ↓	0.084	0.14	0.11	0.27	0.25	0.25	0.25	0.19
B tagging efficiency eigenvector 7 ↑	0.13	−0.14	−0.086	−0.048	−0.12	−0.14	−0.15	−0.19
B tagging efficiency eigenvector 7 ↓	−0.15	−0.081	0.066	0.061	0.13	0.15	0.21	0.15
B tagging efficiency eigenvector 8 ↑	−1.4	−1.4	−1.2	−1.2	−1.1	−0.95	−0.78	−0.65
B tagging efficiency eigenvector 8 ↓	1.4	1.2	1.3	1.2	1.1	0.91	0.82	0.6
B tagging efficiency eigenvector 9 ↑	2.5	2.5	2.4	2.5	2.3	2.2	2.1	2
B tagging efficiency eigenvector 9 ↓	−2.6	−2.8	−2.6	−2.5	−2.4	−2.3	−2.2	−2.1
B tagging efficiency eigenvector 10 ↑	−3.1	−3.2	−3.1	−3	−3	−2.9	−2.7	−2.8
B tagging efficiency eigenvector 10 ↓	3	2.9	2.9	3	2.9	2.7	2.7	2.7
Jet energy scale EffectiveNP 1 ↑	0.89	0.37	1.1	0.24	0.83	0.34	0.25	0.24
Jet energy scale EffectiveNP 1 ↓	−1.1	−0.14	−0.44	−1	−0.58	−0.38	−0.27	−0.25
Jet energy scale EffectiveNP 2 ↑	−3.1	−1.7	−2	−2.4	−1.6	−1.1	−0.97	−0.71
Jet energy scale EffectiveNP 2 ↓	2.3	1.1	2.3	1.6	1.7	1.1	0.87	0.62
Jet energy scale EffectiveNP 3 ↑	1.6	1	1.5	0.9	1.3	0.6	0.57	0.38
Jet energy scale EffectiveNP 3 ↓	−1.9	−1	−1.3	−1.8	−0.93	−0.73	−0.54	−0.46
Jet energy scale EffectiveNP 4 ↑	−0.16	−0.17	−0.15	−0.45	−0.25	−0.21	−0.12	−0.12
Jet energy scale EffectiveNP 4 ↓	0.19	0.22	0.71	−0.019	0.36	0.14	0.12	0.15
Jet energy scale EffectiveNP 5 ↑	0.13	−0.014	0.63	0.16	0.28	0.071	0.11	0.067
Jet energy scale EffectiveNP 5 ↓	−0.14	−0.034	−0.17	−0.36	−0.17	−0.16	−0.088	−0.1
Jet energy scale EffectiveNP 6restTerm ↑	0.051	0.068	0.27	0.099	0.085	0.058	0.013	0.059
Jet energy scale EffectiveNP 6restTerm ↓	−0.093	0	−0.066	−0.071	−0.13	−0.033	−0.054	−0.074
Jet energy scale EtaIntercalibration TotalUnc1 ↑	0.24	0.33	0.92	0.13	0.42	0.26	0.19	0.17
Jet energy scale EtaIntercalibration TotalUnc1 ↓	−0.23	−0.088	−0.24	−0.42	−0.45	−0.3	−0.15	−0.15
Jet energy scale EtaIntercalibration TotalUnc2 ↑	1.3	0.49	1.7	1.1	0.83	0.56	0.62	0.36
Jet energy scale EtaIntercalibration TotalUnc2 ↓	−2	−0.92	−1.2	−1.8	−0.94	−0.87	−0.5	−0.43
Jet energy scale Pileup OffsetMu ↑	1.2	1.3	0.23	−0.36	0.51	0.23	0.13	0.067
Jet energy scale Pileup OffsetMu ↓	−0.8	−0.22	0.051	−0.32	−0.26	−0.27	−0.45	−0.096
Jet energy scale Pileup OffsetNPV ↑	0.19	0.27	−0.18	−0.6	0.18	−0.021	0.0082	−0.011
Jet energy scale Pileup OffsetNPV ↓	0.32	−0.16	0.33	−0.31	0.23	0.081	−0.13	0.0097
Jet energy scale SingleParticle HighPt ↑	−0.025	0.0068	0.025	0.0032	0.025	0.0051	0.0062	−0.0097
Jet energy scale SingleParticle HighPt ↓	−0.025	0.014	−0.01	−0.0032	0.014	−0.0021	0.001	−0.0054
Jet energy scale RelativeNonClosure MCTYPE ↑	0.14	0.075	0.42	0.11	0.17	0.053	0.011	0.1
Jet energy scale RelativeNonClosure MCTYPE ↓	−0.86	0.061	−0.051	0.045	−0.11	−0.11	−0.032	−0.11
Jet energy scale FlavAndTopo CloseByJets ↑	0.52	0.49	1.4	0.75	0.55	0.57	0.38	0.21
Jet energy scale FlavAndTopo CloseByJets ↓	−1.2	−1.3	−1.2	−1	−0.53	−0.48	−0.54	−0.25
Jet energy scale FlavAndTopo FlavourComposition ↑	−0.24	0.78	0.86	0.71	0.85	0.16	0.24	0.17
Jet energy scale FlavAndTopo FlavourComposition ↓	−1.9	−0.98	−0.58	−0.98	−0.45	−0.27	−0.35	−0.42
Jet energy scale FlavAndTopo FlavourResponse ↑	0	0	0.43	0.27	0.34	0.11	0.19	0.028
Jet energy scale FlavAndTopo FlavourResponse ↓	−1.7	−0.59	−0.43	−0.8	−0.39	−0.3	−0.19	−0.22
Jet energy scale FlavAndTopo Bjets ↑	1.5	0.67	1.8	0.97	1.1	0.8	0.56	0.46
Jet energy scale FlavAndTopo Bjets ↓	−1.7	−1.6	−1.7	−1.7	−1.4	−0.96	−0.77	−0.57
MC stat. (fit)	±3.50	±2.60	±2.30	±1.80	±1.40	±1.10	±1.10	±1.30
MC stat. (unfolding)	±2.30	±2.30	±2.00	±1.50	±1.30	±0.90	±1.00	±0.90
Unfolding Bias	±1.16	±0.47	±0.89	±0.12	±0.26	±0.23	±0.12	±0.10

Table 54: Systematic uncertainties for the differential Zb measurement (in $|\Delta\phi(Z, b - jet)|$).

ΔR(b-jet,Z)	[0-1]	[1-1.5]	[1.5-2]	[2-2.5]	[2.5-3]	[3-3.5]	[3.5-4]	[4-4.5]	[4.5-6]
σ[pb/a.u.]	0.118174	0.291116	0.479091	1.030053	2.775920	3.315635	0.689159	0.194539	0.014181
Statistical	±8.53	±8.20	±6.28	±4.09	±2.37	±2.02	±4.73	±10.08	±23.76
Total systematic ↑	8.46	10.30	9.43	8.20	7.19	6.73	6.70	12.72	18.84
Total systematic ↓	9.18	10.26	9.29	8.44	7.21	6.57	6.71	11.54	18.12
MPI ↑	−1.90	−1.38	−1.01	−1.21	−0.82	−1.03	−1.77	−2.79	−1.03
MPI ↓	±2.06	±1.50	±1.14	±1.21	±0.83	±1.04	±1.85	±3.07	±1.55
Gluon splitting ↑	0.76	0.85	0.59	0.97	0.81	1.15	1.43	3.16	6.55
Gluon splitting ↓	−0.73	−0.88	−0.64	−1.10	−0.89	−1.34	−1.73	−3.72	−9.19
Luminosity	1.80	1.80	1.80	1.80	1.80	1.80	1.80	1.80	1.80
Electron identification efficiency ↑	1.11	1.08	1.10	1.10	1.11	1.12	1.11	1.17	1.08
Electron identification efficiency ↓	−1.13	−1.10	−1.13	−1.12	−1.14	−1.14	−1.13	−1.19	−1.08
Electron energy scale ↑	−0.05	0.36	0.10	−0.08	0.19	0.06	0.14	0.21	−1.33
Electron energy scale ↓	−0.55	0.26	−0.06	−0.24	−0.03	−0.18	0.05	−0.12	−1.28
Electron energy resolution ↑	−0.43	0.26	0.10	−0.08	−0.07	0.02	0.01	−0.12	−1.59
Electron energy resolution ↓	−0.37	0.34	−0.05	−0.09	0.06	0.06	0.01	−0.12	−1.59
Muon reconstruction efficiency ↑	0.31	0.35	0.34	0.34	0.34	0.35	0.43	0.58	0.82
Muon reconstruction efficiency ↓	−0.31	−0.34	−0.34	−0.35	−0.34	−0.35	−0.43	−0.58	−0.82
Muon energy scale ↑	0.16	0.05	0.04	0.03	0.04	0.04	0.04	0.00	0.00
Muon energy scale ↓	−0.04	−0.06	−0.02	−0.03	−0.03	−0.00	−0.06	0.01	0.00
Muon ID resolution ↑	−0.04	−0.17	0.08	−0.03	−0.02	0.04	−0.05	0.00	1.75
Muon ID resolution ↓	0.01	0.06	−0.08	0.14	0.01	−0.01	−0.07	0.09	0.00
Muon MS resolution ↑	−0.09	−0.14	0.06	−0.02	0.01	0.02	−0.11	0.07	−0.31
Muon MS resolution ↓	−0.18	−0.08	0.08	0.11	−0.02	0.05	−0.11	0.34	−0.15
Electron trigger efficiency ↑	±0.16	±0.17	±0.17	±0.17	±0.17	±0.18	±0.20	±0.27	±0.41
Electron trigger efficiency ↓	−0.16	−0.17	−0.17	−0.18	−0.17	−0.18	−0.20	−0.26	−0.36
Muon trigger efficiency ↑	0.29	0.29	0.27	0.29	0.28	0.28	0.27	0.21	0.21
Muon trigger efficiency ↓	−0.29	−0.29	−0.28	−0.29	−0.28	−0.28	−0.26	−0.21	−0.15
Pile-up ↑	0.40	−0.05	0.25	−0.15	0.11	0.10	0.24	0.46	−0.36
Pile-up ↓	−0.40	−0.24	−0.29	−0.00	−0.14	−0.15	−0.23	−0.49	0.36
MET resolution soft terms ↑	−0.10	0.02	−0.07	−0.01	−0.02	−0.02	0.04	−0.03	0.00
MET resolution soft terms ↓	−0.06	0.03	0.02	−0.00	−0.01	−0.01	0.04	0.00	−0.26
MET scale soft terms ↑	−0.18	−0.02	−0.11	−0.06	−0.06	−0.08	−0.01	−0.06	0.00
MET scale soft terms ↓	0.00	0.07	0.15	0.05	0.04	0.05	0.08	0.10	0.00
Reweighting vertex z–coordinate	±0.53	±0.16	±0.38	±0.36	±0.53	±0.37	±0.60	±0.50	±1.23
Background ↑	3.06	3.75	3.35	2.10	1.09	0.56	0.36	0.37	0.00
Background ↓	−2.81	−3.75	−3.22	−2.10	−1.07	−0.55	−0.27	0.00	0.00
Template shape l-jets	±0.77	±0.63	±0.74	±0.46	±0.58	±0.63	±0.63	±1.47	±1.75
Template shape c-jets	±0.26	±0.21	±0.25	±0.17	±0.27	±0.36	±0.27	±0.00	±0.00
Template shape b-jets	±3.57	±6.88	±6.07	±5.57	±5.11	±4.53	±3.13	±5.49	±5.26
Jet energy resolution	±1.14	±1.12	±0.79	±0.18	±0.89	±0.47	±0.36	±3.77	±3.29
Charm mis-tag ↑	0.00	−0.42	−0.12	−0.11	0.00	−0.02	0.09	0.00	0.00
Charm mis-tag ↓	0.25	0.21	0.00	0.11	0.00	0.00	0.00	0.37	1.75
Light jets mis-tag ↑	0.25	0.21	0.25	0.28	0.16	0.10	0.18	0.37	0.00
Light jets mis-tag ↓	−0.51	−0.42	−0.37	−0.34	−0.21	−0.15	−0.18	−0.37	0.00
B tagging efficiency eigenvector 1 ↑	0.26	0.19	0.1	0.17	0.057	−0.011	−0.041	−0.011	0
B tagging efficiency eigenvector 1 ↓	0.27	0.19	0.13	0.21	0.13	0.09	0.13	0.034	0
B tagging efficiency eigenvector 2 ↑	0.33	0.23	0.15	0.21	0.14	0.082	0.12	0.034	0
B tagging efficiency eigenvector 2 ↓	0.19	0.15	0.086	0.097	0.07	−0.0039	−0.035	−0.011	0
B tagging efficiency eigenvector 3 ↑	0.26	0.19	0.13	0.13	0.078	0.011	−0.0032	0.022	0.1
B tagging efficiency eigenvector 3 ↓	0.27	0.18	0.25	0.18	0.11	0.069	0.089	0	−0.1
B tagging efficiency eigenvector 4 ↑	0.19	0.097	0.064	0.14	0.047	0.0092	0.038	−0.045	−0.15
B tagging efficiency eigenvector 4 ↓	0.32	0.28	0.18	0.18	0.14	0.07	0.048	0.067	0.15
B tagging efficiency eigenvector 5 ↑	0.4	0.34	0.23	0.31	0.21	0.14	0.1	0.12	0.21
B tagging efficiency eigenvector 5 ↓	0.13	0.037	0.0091	0.068	−0.025	−0.064	−0.016	−0.1	−0.21
B tagging efficiency eigenvector 6 ↑	0.11	0.052	−0.032	−0.042	−0.14	−0.17	−0.18	−0.16	−0.31
B tagging efficiency eigenvector 6 ↓	0.41	0.32	0.41	0.35	0.33	0.25	0.27	0.18	0.31
B tagging efficiency eigenvector 7 ↑	0.32	0.24	0.17	0.14	−0.019	−0.12	−0.051	0.011	−0.1
B tagging efficiency eigenvector 7 ↓	0.2	0.13	0.2	0.24	0.21	0.19	0.14	0.011	0.1
B tagging efficiency eigenvector 8 ↑	−1	−0.91	−1.1	−0.92	−0.78	−0.68	−0.91	−0.83	−1.1
B tagging efficiency eigenvector 8 ↓	1.5	1.5	1.3	1.2	0.95	0.75	0.96	1.2	1
B tagging efficiency eigenvector 9 ↑	2.3	2.2	2.2	2.1	2.1	2	2.1	2.1	2
B tagging efficiency eigenvector 9 ↓	−1.8	−1.9	−2	−1.9	−2	−2	−2.1	−2.2	−2.1
B tagging efficiency eigenvector 10 ↑	−2.2	−2.3	−2.3	−2.4	−2.5	−2.6	−2.6	−2.6	−2.3
B tagging efficiency eigenvector 10 ↓	2.6	2.6	2.4	2.6	2.6	2.6	2.6	2.5	2.2
Jet energy scale EffectiveNP 1 ↑	0.8	0.43	0.48	0.83	0.34	0.24	0.32	0.39	1.3
Jet energy scale EffectiveNP 1 ↓	−0.83	−0.58	−0.59	−0.77	−0.4	−0.28	−0.18	−1.1	0.15
Jet energy scale EffectiveNP 2 ↑	−2.3	−2	−2.3	−1.8	−1.1	−0.96	−0.85	−2.6	−0.87
Jet energy scale EffectiveNP 2 ↓	2.3	1.8	1.9	1.9	1.2	0.73	0.9	0.45	2.2
Jet energy scale EffectiveNP 3 ↑	1.9	0.98	1.1	1.4	0.66	0.45	0.59	0.35	1.7
Jet energy scale EffectiveNP 3 ↓	−1.1	−1.2	−1.6	−1.3	−0.72	−0.57	−0.53	−1.6	0.21
Jet energy scale EffectiveNP 4 ↑	−0.2	−0.045	−0.25	−0.24	−0.25	−0.13	−0.035	−0.99	0.1
Jet energy scale EffectiveNP 4 ↓	0.2	0.22	0.46	0.28	0.17	0.12	0.18	0.11	0.36
Jet energy scale EffectiveNP 5 ↑	0.14	0.0075	0.51	0.17	0.098	0.061	0.17	0.11	0.31
Jet energy scale EffectiveNP 5 ↓	−0.35	0.045	−0.14	−0.23	−0.19	−0.097	−0.051	−0.99	0.15
Jet energy scale EffectiveNP 6restTerm ↑	−0.018	0.18	0.25	0.019	0.017	0.041	0.0063	0.09	0
Jet energy scale EffectiveNP 6restTerm ↓	−0.037	−0.068	−0.082	−0.11	−0.055	−0.052	−0.067	−0.91	0.1
Jet energy scale EtaIntercalibration TotalUnc1 ↑	0.27	0.27	0.51	0.41	0.26	0.16	0.24	0.4	0.41
Jet energy scale EtaIntercalibration TotalUnc1 ↓	−0.19	−0.23	−0.16	−0.42	−0.29	−0.18	−0.12	−1.1	0.15
Jet energy scale EtaIntercalibration TotalUnc2 ↑	1.1	0.98	1.1	1.1	0.51	0.47	1	0.94	0.82
Jet energy scale EtaIntercalibration TotalUnc2 ↓	−1.1	−1.1	−1.1	−0.84	−0.74	−0.61	−1	−2.8	−1.4
Jet energy scale Pileup OffsetMu ↑	2.3	0.14	−0.059	0.56	0.26	0.024	0.49	−0.55	0.82
Jet energy scale Pileup OffsetMu ↓	−0.18	−0.67	0.096	−0.3	−0.3	−0.23	−0.38	−0.76	−0.21
Jet energy scale Pileup OffsetNPV ↑	0.45	−0.52	−0.31	0.21	−0.05	−0.04	−0.076	−0.056	0.82
Jet energy scale Pileup OffsetNPV ↓	0.23	−0.0075	0.046	0.036	0.086	−0.051	−0.1	0.27	0
Jet energy scale SingleParticle HighPt ↑	−0.028	0.038	−0.0091	0.025	−0.01	−0.02	−0.0095	−0.011	0
Jet energy scale SingleParticle HighPt ↓	−0.018	0.0075	−0.014	0.015	−0.017	−0.02	−0.0063	−0.011	0
Jet energy scale RelativeNonClosure MCTYPE ↑	0.26	0.11	0.14	0.18	0.01	0.043	0.24	0.21	0.51
Jet energy scale RelativeNonClosure MCTYPE ↓	−0.31	−0.015	−0.11	−0.098	−0.065	−0.07	−0.1	−0.49	0.41
Jet energy scale FlavAndTopo CloseByJets↑	0.71	1.3	0.94	0.74	0.44	0.31	0.4	0.21	0.87
Jet energy scale FlavAndTopo CloseByJets↓	−1.6	−1.1	−1.6	−0.51	−0.5	−0.47	−0.32	−0.12	−0.41
Jet energy scale FlavAndTopo FlavourComposition ↑	1.3	0.63	0.74	0.97	0.29	0.19	0.27	0	0
Jet energy scale FlavAndTopo FlavourComposition ↓	−0.77	−1.5	−0.99	−0.63	−0.39	−0.37	−0.45	−1.8	0
Jet energy scale FlavAndTopo FlavourResponse ↑	0.77	0	0.25	0.4	0.21	0.1	−0.089	−0.37	0
Jet energy scale FlavAndTopo FlavourResponse ↓	−1	−0.63	−0.87	−0.63	−0.31	−0.22	−0.18	−1.5	0
Jet energy scale FlavAndTopo Bjets ↑	1.1	1.1	1.3	1.2	0.77	0.46	0.92	0.97	2.1
Jet energy scale FlavAndTopo Bjets ↓	−1.5	−1.9	−1.6	−1.5	−0.98	−0.77	−0.62	−0.95	−1.1
MC stat. (fit)	±2.80	±2.40	±2.00	±1.30	±1.00	±1.00	±2.20	±5.70	±11.50
MC stat. (unfolding)	±2.50	±2.20	±1.70	±1.20	±0.80	±0.70	±1.70	±3.60	±8.00
Unfolding Bias	±0.25	±0.47	±0.14	±0.43	±0.09	±0.11	±0.21	±0.91	±2.24

Table 55: Systematic uncertainties for the differential Zb measurement (in $|\Delta R(Z, b-jet)|$).

Z p_T [GeV]	[0-20]	[20-30]	[30-40]	[40-60]	[60-80]	[80-110]	[110-200]	[200-500]
σ[pb/GeV]	0.038103	0.077657	0.088236	0.056102	0.031694	0.013054	0.002612	0.000143
Statistical	±3.87	±3.68	±3.21	±2.50	±3.18	±3.92	±4.77	±11.21
Total systematic ↑	10.81	8.51	7.59	7.00	6.31	7.71	6.77	8.98
Total systematic ↓	12.37	8.05	7.32	6.84	6.23	7.69	6.54	8.24
MPI ↑	−4.05	−1.51	−1.83	−1.14	−0.99	−1.17	−1.11	−0.43
MPI ↓	±6.02	±1.75	±1.90	±1.16	±1.00	±1.18	±1.11	±0.43
Gluon splitting ↑	0.43	−0.62	0.01	0.03	0.42	0.18	1.36	1.36
Gluon splitting ↓	−0.45	0.66	0.04	−0.01	−0.46	−0.09	−1.70	−1.77
Luminosity	1.80	1.80	1.80	1.80	1.80	1.80	1.80	1.80
Electron identification efficiency ↑	0.89	0.99	1.09	1.19	1.20	1.10	0.96	0.94
Electron identification efficiency ↓	−0.90	−1.01	−1.11	−1.22	−1.23	−1.12	−0.98	−0.94
Electron energy scale ↑	0.14	−0.02	0.00	0.09	0.03	0.55	0.13	0.97
Electron energy scale ↓	0.24	0.01	0.24	−0.25	−0.22	−0.06	−0.54	−0.79
Electron energy resolution ↑	0.22	−0.06	0.13	0.04	−0.19	0.07	−0.13	−0.08
Electron energy resolution ↓	0.06	0.19	0.10	−0.04	−0.14	0.19	−0.13	−0.08
Muon reconstruction efficiency ↑	0.28	0.28	0.29	0.32	0.36	0.41	0.53	0.76
Muon reconstruction efficiency ↓	−0.29	−0.29	−0.29	−0.32	−0.36	−0.42	−0.54	−0.79
Muon energy scale ↑	−0.07	−0.06	0.08	−0.02	0.17	0.03	0.09	0.18
Muon energy scale ↓	0.07	0.06	0.01	−0.03	−0.06	−0.08	−0.11	−0.10
Muon ID resolution ↑	0.01	−0.05	0.08	−0.05	0.03	0.00	−0.00	0.15
Muon ID resolution ↓	−0.07	−0.05	0.03	0.03	−0.01	0.07	−0.05	−0.03
Muon MS resolution ↑	−0.04	0.06	0.03	−0.03	−0.03	0.03	−0.01	−0.33
Muon MS resolution ↓	−0.02	−0.01	−0.09	0.15	−0.02	0.09	−0.14	0.25
Electron trigger efficiency ↑	±0.11	±0.12	±0.14	±0.15	±0.19	±0.23	±0.30	±0.36
Electron trigger efficiency ↓	−0.11	−0.12	−0.14	−0.15	−0.19	−0.23	−0.31	−0.36
Muon trigger efficiency ↑	0.28	0.28	0.28	0.28	0.28	0.28	0.28	0.28
Muon trigger efficiency ↓	−0.28	−0.28	−0.28	−0.28	−0.29	−0.28	−0.28	−0.28
Pile-up ↑	−1.02	−0.06	0.20	0.12	0.15	−0.20	−0.00	−0.33
Pile-up ↓	−0.01	−0.06	−0.20	−0.15	−0.27	−0.02	−0.13	−0.41
MET resolution soft terms ↑	−0.02	−0.01	0.00	−0.02	−0.05	0.02	0.04	0.03
MET resolution soft terms ↓	−0.01	−0.03	−0.01	−0.01	−0.01	0.04	−0.02	−0.05
MET scale soft terms ↑	−0.06	−0.03	−0.04	−0.04	−0.10	−0.08	−0.12	−0.23
MET scale soft terms ↓	0.02	0.03	0.03	0.03	0.03	0.13	0.13	0.05
Reweighting vertex z–coordinate	±0.35	±0.03	±0.66	±0.25	±0.07	±0.09	±0.63	±2.09
Background ↑	0.66	0.59	0.61	0.87	1.20	1.63	1.29	0.00
Background ↓	−0.66	−0.59	−0.54	−0.82	−1.12	−1.57	−1.19	−0.57
Template shape l-jets	±1.93	±1.18	±0.86	±0.57	±0.37	±0.38	±0.40	±0.57
Template shape c-jets	±0.18	±0.08	±0.18	±0.35	±0.41	±0.38	±0.30	±0.00
Template shape b-jets	±4.34	±4.99	±4.82	±4.91	±3.93	±5.78	±3.97	±3.41
Jet energy resolution	±3.28	±0.18	±1.26	±0.30	±0.87	±0.20	±0.42	±0.13
Charm mis-tag ↑	−0.92	−0.04	0.00	0.00	−0.08	−0.19	−0.10	−0.57
Charm mis-tag ↓	1.01	0.08	−0.04	−0.02	0.12	0.25	0.10	0.00
Light jets mis-tag ↑	0.88	0.21	0.14	0.12	0.21	0.19	0.10	0.00
Light jets mis-tag ↓	−1.23	−0.25	−0.21	−0.17	−0.25	−0.25	−0.10	−0.57
B tagging efficiency eigenvector 1 ↑	0.021	0.027	−0.0087	−0.00099	−0.1	−0.12	−0.042	0.025
B tagging efficiency eigenvector 1 ↓	−0.03	−0.025	−0.024	−0.0058	0.16	0.11	0.014	0
B tagging efficiency eigenvector 2 ↑	0.0029	0.029	0.054	0.058	−0.0069	0.0084	0.0093	−0.025
B tagging efficiency eigenvector 2 ↓	−0.011	−0.028	−0.085	−0.09	0.022	−0.017	−0.037	0.051
B tagging efficiency eigenvector 3 ↑	0.12	0.074	0.03	−0.09	−0.088	0.0056	0.023	0.051
B tagging efficiency eigenvector 3 ↓	−0.13	−0.027	−0.062	0.057	0.15	−0.014	−0.051	−0.025
B tagging efficiency eigenvector 4 ↑	−0.13	−0.12	−0.13	−0.073	0.11	0.05	−0.074	−0.051
B tagging efficiency eigenvector 4 ↓	0.12	0.12	0.097	0.04	−0.048	−0.058	0.046	0.076
B tagging efficiency eigenvector 5 ↑	0.11	0.15	0.23	0.21	0.074	−0.11	−0.07	0.051
B tagging efficiency eigenvector 5 ↓	−0.17	−0.15	−0.26	−0.22	−0.017	0.17	0.037	−0.051
B tagging efficiency eigenvector 6 ↑	−0.11	−0.13	−0.3	−0.35	−0.24	−0.095	0.13	0.025
B tagging efficiency eigenvector 6 ↓	0.095	0.18	0.26	0.34	0.3	0.084	−0.16	0
B tagging efficiency eigenvector 7 ↑	0.24	0.16	0.026	−0.17	−0.27	−0.31	−0.084	0.28
B tagging efficiency eigenvector 7 ↓	−0.3	−0.16	−0.058	0.16	0.33	0.3	0.16	−0.28
B tagging efficiency eigenvector 8 ↑	−1.9	−1.6	−1.4	−0.91	−0.48	−0.29	−0.023	−0.2
B tagging efficiency eigenvector 8 ↓	1.8	1.6	1.3	0.88	0.53	0.28	−0.0046	0.23
B tagging efficiency eigenvector 9 ↑	1.9	2	2	2	2	1.9	1.9	0.28
B tagging efficiency eigenvector 9 ↓	−2.1	−2	−2.1	−2.1	−2	−2	−2	−0.25
B tagging efficiency eigenvector 10 ↑	−2.1	−2.2	−2.4	−2.6	−2.6	−2.7	−2.9	−3.5
B tagging efficiency eigenvector 10 ↓	2	2.1	2.2	2.4	2.5	2.6	2.7	3.3
Jet energy scale EffectiveNP 1 ↑	1.3	0.74	0.36	0.32	0.21	0.2	0.17	0.33
Jet energy scale EffectiveNP 1 ↓	−0.96	−1.1	−0.45	−0.3	−0.17	−0.11	−0.13	−0.1
Jet energy scale EffectiveNP 2 ↑	−3.1	−2.6	−1.5	−1.1	−0.61	−0.54	−0.56	−1.5
Jet energy scale EffectiveNP 2 ↓	4.1	2.2	1.2	0.9	0.47	0.59	0.41	0.79
Jet energy scale EffectiveNP 3 ↑	2.9	1.3	0.75	0.56	0.34	0.43	0.27	0.51
Jet energy scale EffectiveNP 3 ↓	−2.3	−1.6	−1	−0.65	−0.38	−0.26	−0.38	−1.3
Jet energy scale EffectiveNP 4 ↑	−0.31	−0.49	−0.19	−0.18	−0.064	−0.067	−0.1	−0.025
Jet energy scale EffectiveNP 4 ↓	0.21	0.45	0.088	0.15	0.074	0.15	0.093	0.1
Jet energy scale EffectiveNP 5 ↑	0.1	0.36	0.089	0.08	0.048	0.13	0.056	0
Jet energy scale EffectiveNP 5 ↓	−0.2	−0.42	−0.14	−0.15	−0.043	−0.061	0.0046	0
Jet energy scale EffectiveNP 6restTerm ↑	−0.013	0.089	0.0087	0.03	−0.0017	0.086	0.046	0
Jet energy scale EffectiveNP 6restTerm ↓	−0.097	−0.22	−0.074	−0.049	−0.019	−0.033	0.0046	0
Jet energy scale EtaIntercalibration TotalUnc1 ↑	0.75	0.63	0.16	0.21	0.12	0.18	0.084	0.36
Jet energy scale EtaIntercalibration TotalUnc1 ↓	−0.56	−0.73	−0.22	−0.22	−0.076	−0.086	−0.0046	0
Jet energy scale EtaIntercalibration TotalUnc2 ↑	4.4	1.3	0.77	0.46	0.29	0.29	0.2	0.59
Jet energy scale EtaIntercalibration TotalUnc2 ↓	−3.3	−1.8	−0.93	−0.57	−0.47	−0.35	−0.18	−1.2
Jet energy scale Pileup OffsetMu ↑	1.1	0.53	0.32	0.24	0.045	0.05	0.06	−0.46
Jet energy scale Pileup OffsetMu ↓	0.34	−0.4	−0.76	−0.18	−0.2	−0.039	0.1	−0.74
Jet energy scale Pileup OffsetNPV ↑	0.45	−0.1	−0.017	0.013	−0.043	0.017	−0.11	0.1
Jet energy scale Pileup OffsetNPV ↓	−0.024	0.13	−0.15	−0.012	−0.014	0.078	0.019	−0.28
Jet energy scale SingleParticle HighPt ↑	0.021	−0.0056	0.0037	0.0068	−0.0034	−0.011	0.019	−0.025
Jet energy scale SingleParticle HighPt ↓	0.0029	−0.0098	−0.011	0.0019	0.0017	−0.014	0.023	0
Jet energy scale RelativeNonClosure MCTYPE ↑	0.61	0.23	0.071	0.023	0.077	0.075	−0.056	0.076
Jet energy scale RelativeNonClosure MCTYPE ↓	−0.6	−0.31	−0.12	−0.11	−0.012	0.031	0.042	0.025
Jet energy scale FlavAndTopo CloseByJets ↑	1	0.48	0.4	0.44	0.34	0.41	0.31	0.43
Jet energy scale FlavAndTopo CloseByJets ↓	−1.3	−0.83	−0.49	−0.44	−0.52	−0.31	−0.45	−0.94
Jet energy scale FlavAndTopo FlavourComposition ↑	0.57	0.085	0.21	0.25	0.33	0.5	0.3	0
Jet energy scale FlavAndTopo FlavourComposition ↓	0.18	−0.38	−0.39	−0.42	−0.29	−0.5	−0.3	−1.7
Jet energy scale FlavAndTopo FlavourResponse ↑	0.66	0.13	0.071	0.074	0.12	0.25	0.099	0
Jet energy scale FlavAndTopo FlavourResponse ↓	0.088	−0.25	−0.29	−0.32	−0.21	−0.38	−0.3	−1.1
Jet energy scale FlavAndTopo Bjets ↑	2.8	1.7	1.1	0.62	0.23	0.22	0.17	0.76
Jet energy scale FlavAndTopo Bjets ↓	−3.1	−2.3	−1.3	−0.75	−0.55	−0.36	−0.4	−0.28
MC stat. (fit)	±2.30	±1.90	±1.50	±1.10	±1.20	±1.40	±1.60	±4.00
MC stat. (unfolding)	±1.30	±1.40	±1.30	±0.90	±1.20	±1.40	±1.50	±3.70
Unfolding Bias	±0.38	±0.10	±0.26	±0.08	±0.28	±0.46	±0.45	±0.86

Table 56: Systematic uncertainties for the differential Zb measurement (in Z p_T).

Z |y|	[0.0-0.2]	[0.2-0.4]	[0.4-0.6]	[0.6-0.8]	[0.8-1.2]	[1.2-1.6]	[1.6-2.0]	[2.0-2.5]
σ[pb/a.u.]	3.077631	3.135388	3.087059	2.803850	2.543685	1.940420	1.107935	0.332534
Statistical	±3.23	±3.35	±3.33	±3.51	±2.62	±3.09	±4.30	±7.60
Total systematic ↑	7.37	7.72	7.80	7.57	7.80	7.92	10.04	11.14
Total systematic ↓	7.71	7.66	7.94	7.57	7.59	7.70	10.21	11.35
MPI ↑	−1.88	−2.13	−2.59	−2.40	−2.63	−2.83	−4.42	−5.94
MPI ↓	±2.05	±2.29	±2.80	±2.64	±2.89	±3.11	±4.89	±6.60
Gluon splitting ↑	−0.07	0.35	0.26	0.86	1.30	0.68	2.23	3.52
Gluon splitting ↓	0.10	−0.36	−0.26	−0.92	−1.46	−0.80	−2.73	−4.51
Luminosity	1.80	1.80	1.80	1.80	1.80	1.80	1.80	1.80
Electron identification efficiency ↑	1.15	1.10	1.07	1.08	1.05	0.98	1.05	1.24
Electron identification efficiency ↓	−1.18	−1.13	−1.09	−1.10	−1.08	−1.00	−1.07	−1.27
Electron energy scale ↑	0.09	0.27	0.06	−0.13	0.16	0.15	0.14	0.12
Electron energy scale ↓	−0.09	0.19	−0.12	−0.33	−0.05	−0.02	−0.07	0.08
Electron energy resolution ↑	0.08	−0.09	0.10	−0.08	−0.03	0.24	−0.13	−0.05
Electron energy resolution ↓	0.01	0.11	0.08	−0.13	0.07	0.06	−0.13	−0.05
Muon reconstruction efficiency ↑	0.18	0.19	0.22	0.25	0.32	0.49	0.70	0.91
Muon reconstruction efficiency ↓	−0.18	−0.20	−0.22	−0.25	−0.33	−0.50	−0.71	−0.93
Muon energy scale ↑	0.05	0.01	0.03	0.02	0.03	0.03	−0.01	0.05
Muon energy scale ↓	−0.05	−0.02	−0.03	−0.05	0.01	0.01	0.07	−0.05
Muon ID resolution ↑	0.01	−0.01	0.01	−0.04	0.03	0.01	−0.01	0.00
Muon ID resolution ↓	−0.01	−0.04	0.04	0.01	0.00	−0.03	0.04	0.02
Muon MS resolution ↑	0.00	−0.01	0.01	−0.09	−0.02	0.02	0.03	−0.09
Muon MS resolution ↓	0.07	−0.07	0.02	0.01	0.04	0.07	−0.05	0.07
Electron trigger efficiency ↑	±0.18	±0.15	±0.13	±0.13	±0.13	±0.15	±0.23	±0.60
Electron trigger efficiency ↓	−0.18	−0.15	−0.13	−0.13	−0.13	−0.15	−0.23	−0.60
Muon trigger efficiency ↑	0.31	0.31	0.31	0.32	0.30	0.24	0.17	0.14
Muon trigger efficiency ↓	−0.31	−0.31	−0.31	−0.32	−0.31	−0.24	−0.16	−0.14
Pile-up ↑	0.03	−0.15	−0.18	−0.02	−0.14	−0.11	0.01	0.22
Pile-up ↓	−0.15	−0.07	−0.11	−0.24	−0.01	−0.20	−0.15	−0.26
MET resolution soft terms ↑	−0.00	−0.04	0.01	−0.01	0.00	−0.02	0.01	−0.06
MET resolution soft terms ↓	−0.03	0.01	−0.01	−0.01	−0.01	−0.01	0.02	−0.03
MET scale soft terms ↑	−0.04	−0.07	−0.04	−0.16	−0.03	−0.07	−0.03	−0.06
MET scale soft terms ↓	0.06	0.04	0.06	0.04	0.04	0.05	0.05	0.00
Reweighting vertex z–coordinate	±0.55	±0.30	±0.37	±0.07	±0.17	±0.27	±0.72	±0.21
Background ↑	1.07	1.06	0.98	0.94	0.90	0.75	0.72	0.48
Background ↓	−1.02	−1.02	−0.93	−0.89	−0.85	−0.71	−0.65	−0.48
Template shape l-jets	±0.67	±0.75	±0.76	±0.79	±0.87	±0.99	±1.15	±0.72
Template shape c-jets	±0.22	±0.31	±0.36	±0.25	±0.23	±0.12	±0.14	±0.00
Template shape b-jets	±4.72	±4.86	±4.99	±4.67	±4.60	±4.37	±6.03	±5.06
Jet energy resolution	±0.74	±0.90	±0.31	±0.08	±0.18	±0.67	±0.61	±0.17
Charm mis-tag ↑	−0.13	−0.18	−0.27	−0.20	−0.11	−0.28	−0.14	0.00
Charm mis-tag ↓	0.13	0.22	0.36	0.25	0.11	0.28	0.14	0.00
Light jets mis-tag ↑	0.22	0.40	0.49	0.40	0.28	0.35	0.29	0.00
Light jets mis-tag ↓	−0.31	−0.49	−0.58	−0.50	−0.39	−0.55	−0.43	−0.24
B tagging efficiency eigenvector 1 ↑	−0.018	−0.0052	−0.019	−0.025	−0.053	−0.053	−0.094	−0.033
B tagging efficiency eigenvector 1 ↓	0.028	0.066	0.053	0.072	0.011	0.017	0.0049	−0.0066
B tagging efficiency eigenvector 2 ↑	0.034	0.031	0.06	0.076	0.026	0.037	0.0099	0
B tagging efficiency eigenvector 2 ↓	−0.021	−0.016	−0.025	−0.029	−0.068	−0.073	−0.027	−0.046
B tagging efficiency eigenvector 3 ↑	0.023	0.017	0.0018	0.023	−0.024	−0.014	0.0074	−0.026
B tagging efficiency eigenvector 3 ↓	−0.012	0.043	0.032	0.023	−0.018	−0.022	−0.025	−0.013
B tagging efficiency eigenvector 4 ↑	−0.064	−0.0052	−0.062	−0.0058	−0.069	−0.059	−0.079	−0.072
B tagging efficiency eigenvector 4 ↓	0.074	0.068	0.051	0.052	0.027	0.022	−0.0098	0.033
B tagging efficiency eigenvector 5 ↑	0.15	0.13	0.09	0.13	0.073	0.07	0.1	0.079
B tagging efficiency eigenvector 5 ↓	−0.13	−0.12	−0.1	−0.08	−0.11	−0.11	−0.12	−0.12
B tagging efficiency eigenvector 6 ↑	−0.2	−0.21	−0.15	−0.18	−0.21	−0.17	−0.23	−0.15
B tagging efficiency eigenvector 6 ↓	0.21	0.22	0.19	0.22	0.17	0.13	0.22	0.11
B tagging efficiency eigenvector 7 ↑	−0.082	−0.021	−0.021	−0.1	−0.063	−0.035	−0.12	−0.25
B tagging efficiency eigenvector 7 ↓	0.094	0.037	0.058	0.1	0.021	0.039	0.032	0.2
B tagging efficiency eigenvector 8 ↑	−0.97	−0.97	−0.97	−0.9	−1	−1.1	−0.95	−0.94
B tagging efficiency eigenvector 8 ↓	0.96	0.97	0.98	0.93	0.97	1	0.91	0.87
B tagging efficiency eigenvector 9 ↑	2	2	2	1.9	1.9	1.9	1.9	1.8
B tagging efficiency eigenvector 9 ↓	−2.1	−2.1	−2	−2	−2	−2	−2.1	−1.9
B tagging efficiency eigenvector 10 ↑	−2.4	−2.5	−2.5	−2.4	−2.5	−2.4	−2.5	−2.5
B tagging efficiency eigenvector 10 ↓	2.3	2.4	2.4	2.4	2.3	2.3	2.4	2.4
Jet energy scale EffectiveNP 1 ↑	0.77	0.64	0.51	0.45	0.41	0.6	0.47	0.85
Jet energy scale EffectiveNP 1 ↓	−0.4	−0.59	−0.5	−0.29	−0.6	−0.64	−0.67	−0.33
Jet energy scale EffectiveNP 2 ↑	−1.6	−1.5	−1.6	−1.4	−1.8	−1.9	−1.8	−1
Jet energy scale EffectiveNP 2 ↓	1.9	1.5	1.7	1.5	1.5	1.8	1.9	1.6
Jet energy scale EffectiveNP 3 ↑	1.4	0.97	0.97	0.91	1	1	1.5	1.5
Jet energy scale EffectiveNP 3 ↓	−0.76	−1	−0.86	−0.83	−1.3	−1.3	−1.4	−0.93
Jet energy scale EffectiveNP 4 ↑	−0.16	−0.25	−0.12	−0.18	−0.28	−0.39	−0.15	−0.072
Jet energy scale EffectiveNP 4 ↓	0.27	0.19	0.2	0.25	0.15	0.3	0.17	0.11
Jet energy scale EffectiveNP 5 ↑	0.14	0.18	0.18	0.13	0.098	0.21	0.14	0.052
Jet energy scale EffectiveNP 5 ↓	−0.14	−0.22	−0.087	−0.17	−0.19	−0.19	−0.16	0.026
Jet energy scale EffectiveNP 6restTerm ↑	0.067	0.11	0.05	0.066	0.011	−0.031	0.054	0.052
Jet energy scale EffectiveNP 6restTerm ↓	−0.05	−0.2	−0.042	−0.033	−0.1	−0.058	−0.042	0.026
Jet energy scale EtaIntercalibration TotalUnc1 ↑	0.43	0.35	0.33	0.33	0.28	0.52	0.42	0.12
Jet energy scale EtaIntercalibration TotalUnc1 ↓	−0.3	−0.36	−0.24	−0.2	−0.36	−0.43	−0.22	−0.32
Jet energy scale EtaIntercalibration TotalUnc2 ↑	1.1	1.1	1.5	1.2	1.2	1.3	1.6	1.4
Jet energy scale EtaIntercalibration TotalUnc2 ↓	−0.97	−1.1	−1	−0.99	−1.4	−1.7	−1.3	−0.95
Jet energy scale Pileup OffsetMu ↑	0.95	0.34	0.28	0.24	0.37	0.58	0.86	0.63
Jet energy scale Pileup OffsetMu ↓	−0.085	0.047	−0.29	−0.32	−0.34	−0.56	−0.13	−0.62
Jet energy scale Pileup OffsetNPV ↑	0.31	0.012	0.2	−0.21	0.086	−0.062	0.17	1
Jet energy scale Pileup OffsetNPV ↓	0.096	−0.03	0.039	0.22	−0.061	−0.3	0.081	−0.32
Jet energy scale SingleParticle HighPt ↑	0.014	0.007	0.0035	0.016	−0.0043	0.0014	0	0.0066
Jet energy scale SingleParticle HighPt ↓	0.0089	−0.0018	0	0	−0.0075	−0.0084	0.0049	0.026
Jet energy scale RelativeNonClosure MCTYPE ↑	0.085	0.22	0.14	0.16	0.12	0.29	0.24	0.085
Jet energy scale RelativeNonClosure MCTYPE ↓	−0.15	−0.21	−0.2	0	−0.22	−0.25	−0.22	−0.11
Jet energy scale FlavAndTopo CloseByJets ↑	0.46	0.43	0.63	0.54	0.55	0.37	1.2	0.77
Jet energy scale FlavAndTopo CloseByJets ↓	−0.47	−0.87	−0.47	−0.66	−0.7	−0.88	−0.56	−0.72
Jet energy scale FlavAndTopo FlavourComposition ↑	0.85	0.93	0.36	0.65	0.99	0.43	0.72	0
Jet energy scale FlavAndTopo FlavourComposition ↓	−0.71	−0.79	−0.8	−0.6	−0.65	−0.87	−0.72	0.24
Jet energy scale FlavAndTopo FlavourResponse ↑	0.49	0.49	0.31	0.55	0.45	0.24	0.29	0.24
Jet energy scale FlavAndTopo FlavourResponse ↓	−0.53	−0.44	−0.49	−0.2	−0.39	−0.59	−0.57	0.24
Jet energy scale FlavAndTopo Bjets ↑	1.2	0.82	1.1	0.61	0.9	1.2	1.3	1.2
Jet energy scale FlavAndTopo Bjets ↓	−1	−1.2	−1.1	−1.4	−1.3	−1.3	−1.3	−1.2
MC stat. (fit)	±1.50	±1.60	±1.60	±1.70	±1.30	±1.50	±2.10	±3.40
MC stat. (unfolding)	±1.20	±1.20	±1.30	±1.30	±1.00	±1.20	±1.50	±2.70
Unfolding Bias	±0.32	±0.10	±0.26	±0.12	±0.20	±0.36	±0.81	±0.72

Table 57: Systematic uncertainties for the differential Zb measurement (in Z |y|).

Total cross section	$ff(Zb) \times N_{b-jet}$	$ff(Zb)$	$ff^{\star}(Zb) \times N_{b-jet}$
σ[pb]	5.390	4.820	4540
Statistical	± 1.14	± 1.19	± 1.20
Total systematic $\uparrow$	7.94	7.70	7.36
Total systematic $\downarrow$	-7.94	-8.05	-7.69
MPI $\uparrow$	2.64	3.07	-1.20
MPI $\downarrow$	-2.44	-2.82	-1.17
Gluon splitting $\uparrow$	-1.24	-0.85	-1.18
Gluon splitting $\downarrow$	1.10	0.76	1.05
Luminosity	± 1.80	± 1.80	± 1.80
Electron identification efficiency $\uparrow$	1.07	1.07	1.11
Electron identification efficiency $\downarrow$	-1.10	-1.09	-1.14
Electron energy scale $\uparrow$	0.10	0.11	0.09
Electron energy scale $\downarrow$	-0.06	-0.06	-0.12
Electron energy resolution $\uparrow$	0.00	0.02	-0.03
Electron energy resolution $\downarrow$	0.04	0.05	0.03
Muon reconstruction efficiency $\uparrow$	0.34	0.34	0.35
Muon reconstruction efficiency $\downarrow$	-0.34	-0.34	-0.36
Muon energy scale $\uparrow$	0.02	0.03	0.04
Muon energy scale $\downarrow$	-0.01	-0.01	-0.02
Muon ID resolution $\uparrow$	0.00	0.00	0.00
Muon ID resolution $\downarrow$	0.00	0.00	0.01
Muon MS resolution $\uparrow$	-0.01	-0.01	-0.00
Muon MS resolution $\downarrow$	0.02	0.02	0.02
Electron trigger efficiency $\uparrow$	± 0.17	± 0.17	± 0.18
Electron trigger efficiency $\downarrow$	-0.17	-0.17	-0.18
Muon trigger efficiency $\uparrow$	0.28	0.28	0.28
Muon trigger efficiency $\downarrow$	-0.28	-0.28	-0.28
Pile-up $\uparrow$	-0.10	-0.17	-0.02
Pile-up $\downarrow$	-0.14	2.25	2.96
MET resolution soft terms $\uparrow$	-0.02	-0.01	-0.02
MET resolution soft terms $\downarrow$	-0.01	-0.01	-0.01
MET scale soft terms $\uparrow$	-0.07	-0.06	-0.07
MET scale soft terms $\downarrow$	0.05	0.05	0.05
Reweighting vertex z–coordinate	± 0.34	± 0.38	± 0.46
Background $\uparrow$	1.14	0.92	1.18
Background $\downarrow$	-1.09	-0.87	-1.13
Template shape l-jets	± 0.83	± 0.86	± 0.63
Template shape c-jets	± 0.22	± 0.21	± 0.29
Template shape b-jets	± 4.92	± 4.82	± 4.90
Jet energy resolution	± 0.31	± 0.34	± 0.43
Charm mis-tag $\uparrow$	-0.29	-0.19	-0.21
Charm mis-tag $\downarrow$	0.15	0.22	0.24
Light jets mis-tag $\uparrow$	0.29	0.35	0.38
Light jets mis-tag $\downarrow$	-0.58	-0.46	-0.49
B tagging efficiency eigenvector 1 $\uparrow$	-0.038	-0.031	-0.046
B tagging efficiency eigenvector 1 $\downarrow$	0.041	0.028	0.051
B tagging efficiency eigenvector 2 $\uparrow$	0.041	0.032	0.045
B tagging efficiency eigenvector 2 $\downarrow$	-0.037	-0.035	-0.04
B tagging efficiency eigenvector 3 $\uparrow$	-0.0051	0.0016	-0.025
B tagging efficiency eigenvector 3 $\downarrow$	0.003	0.0016	0.024
B tagging efficiency eigenvector 4 $\uparrow$	-0.047	-0.045	-0.034
B tagging efficiency eigenvector 4 $\downarrow$	0.045	0.048	0.034
B tagging efficiency eigenvector 5 $\uparrow$	0.12	0.11	0.12
B tagging efficiency eigenvector 5 $\downarrow$	-0.12	-0.11	-0.11
B tagging efficiency eigenvector 6 $\uparrow$	-0.2	-0.19	-0.23
B tagging efficiency eigenvector 6 $\downarrow$	0.2	0.19	0.23
B tagging efficiency eigenvector 7 $\uparrow$	-0.078	-0.059	-0.14
B tagging efficiency eigenvector 7 $\downarrow$	0.082	0.062	0.15
B tagging efficiency eigenvector 8 $\uparrow$	-1.1	-0.99	-0.88
B tagging efficiency eigenvector 8 $\downarrow$	1	0.97	0.87
B tagging efficiency eigenvector 9 $\uparrow$	2.2	2	2.2
B tagging efficiency eigenvector 9 $\downarrow$	-2.3	-2	-2.3
B tagging efficiency eigenvector 10 $\uparrow$	-2.8	-2.5	-2.9
B tagging efficiency eigenvector 10 $\downarrow$	2.7	2.4	2.7
Jet energy scale EffectiveNP 1 $\uparrow$	0.59	0.55	0.41
Jet energy scale EffectiveNP 1 $\downarrow$	-0.54	-0.52	-0.42
Jet energy scale EffectiveNP 2 $\uparrow$	-1.7	-1.6	-1.3
Jet energy scale EffectiveNP 2 $\downarrow$	1.7	1.7	1.2
Jet energy scale EffectiveNP 3 $\uparrow$	1.2	1.1	0.76
Jet energy scale EffectiveNP 3 $\downarrow$	-1.1	-1.1	-0.8
Jet energy scale EffectiveNP 4 $\uparrow$	-0.23	-0.23	-0.19
Jet energy scale EffectiveNP 4 $\downarrow$	0.24	0.21	0.2
Jet energy scale EffectiveNP 5 $\uparrow$	0.17	0.15	0.14
Jet energy scale EffectiveNP 5 $\downarrow$	-0.17	-0.16	-0.14
Jet energy scale EffectiveNP 6restTerm $\uparrow$	0.053	0.043	0.052
Jet energy scale EffectiveNP 6restTerm $\downarrow$	-0.076	-0.077	-0.064
Jet energy scale EtaIntercalibration TotalUnc1 $\uparrow$	0.38	0.36	0.28
Jet energy scale EtaIntercalibration TotalUnc1 $\downarrow$	-0.33	-0.32	-0.25
Jet energy scale EtaIntercalibration TotalUnc2 $\uparrow$	1.3	1.3	0.69
Jet energy scale EtaIntercalibration TotalUnc2 $\downarrow$	-1.2	-1.2	-0.82
Jet energy scale Pileup OffsetMu $\uparrow$	0.49	0.48	0.23
Jet energy scale Pileup OffsetMu $\downarrow$	-0.27	-0.25	-0.29
Jet energy scale Pileup OffsetNPV $\uparrow$	0.084	0.077	-0.015
Jet energy scale Pileup OffsetNPV $\downarrow$	-0.0053	-0.019	0.02
Jet energy scale SingleParticle HighPt $\uparrow$	0.0093	0.005	0.0039
Jet energy scale SingleParticle HighPt $\downarrow$	0.00041	-0.00091	-0.00048
Jet energy scale RelativeNonClosure MCTYPE $\uparrow$	0.17	0.17	0.09
Jet energy scale RelativeNonClosure MCTYPE $\downarrow$	-0.17	-0.18	-0.085
Jet energy scale FlavAndTopo CloseByJets $\uparrow$	0.64	0.58	0.5
Jet energy scale FlavAndTopo CloseByJets $\downarrow$	-0.72	-0.68	-0.58
Jet energy scale FlavAndTopo FlavourComposition $\uparrow$	0.71	0.69	0.4
Jet energy scale FlavAndTopo FlavourComposition $\downarrow$	-0.72	-0.7	-0.54
Jet energy scale FlavAndTopo FlavourResponse $\uparrow$	0.42	0.4	0.19
Jet energy scale FlavAndTopo FlavourResponse $\downarrow$	-0.37	-0.37	-0.29
Jet energy scale FlavAndTopo Bjets $\uparrow$	1.2	1.1	0.87
Jet energy scale FlavAndTopo Bjets $\downarrow$	-1.2	-1.2	-0.93
MC stat. (fit)	± 0.60	± 0.60	± 0.60
MC stat. (unfolding)	± 0.80	± 0.85	± 0.73
Unfolding Bias	± 0.09	± 0.1	± 0.09

Table 58: Systematic uncertainties for the total cross sections for the three selections corresponding to the differential distributions measured.

E

PDFS VARIATIONS ON THE MCFM PREDICTIONS

The measured Z rapidity distribution in events with at least one or two b–jets have been presented in Chap. 6 in comparison with the MCFM calculation, corrected for non–perturbative effects, obtained with the three PDFs sets MSTW2008, CT10 and NNPDF2.3. For completeness all the Z+b and Z+bb distributions are reported here; the MCFM calculations are presented with their statistical error for CT10 and NNPDF2.3, while the full error is evaluated for the predictions obtained with the MSTW2008 set.

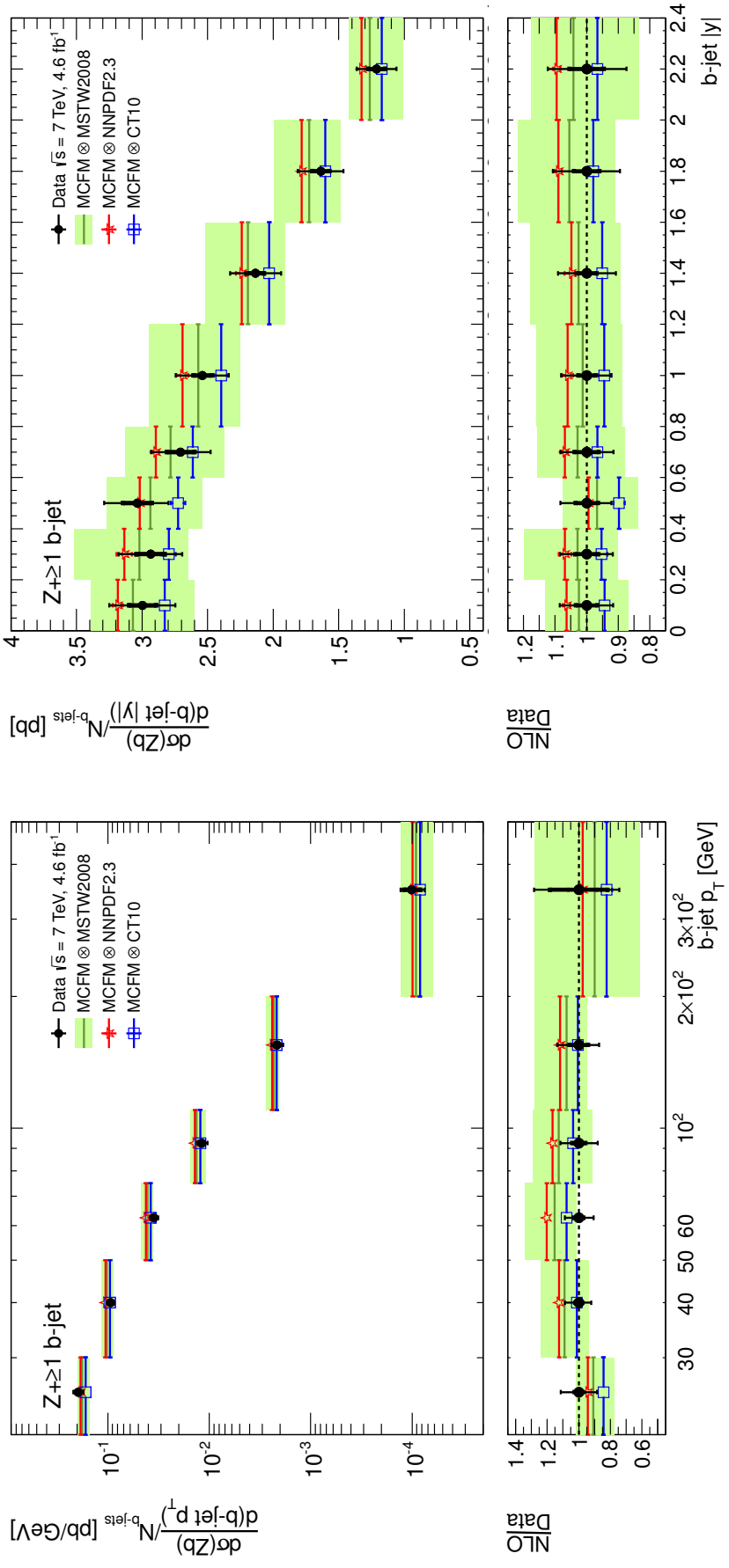

Table 59: Differential cross section for the production of a Z boson in association with at least one b–jet as function of the b–jet p_T (left) and the b–jet $|y|$ (right). The data point are presented along with their statistical (inner bars) and total uncertainty (outer bars); the MCFM calculation interfaced with MSTW2008 PDFs is shown with its total uncertainty (light green shaded bands) while all the other predictions are presented with their statistical uncertainty only.

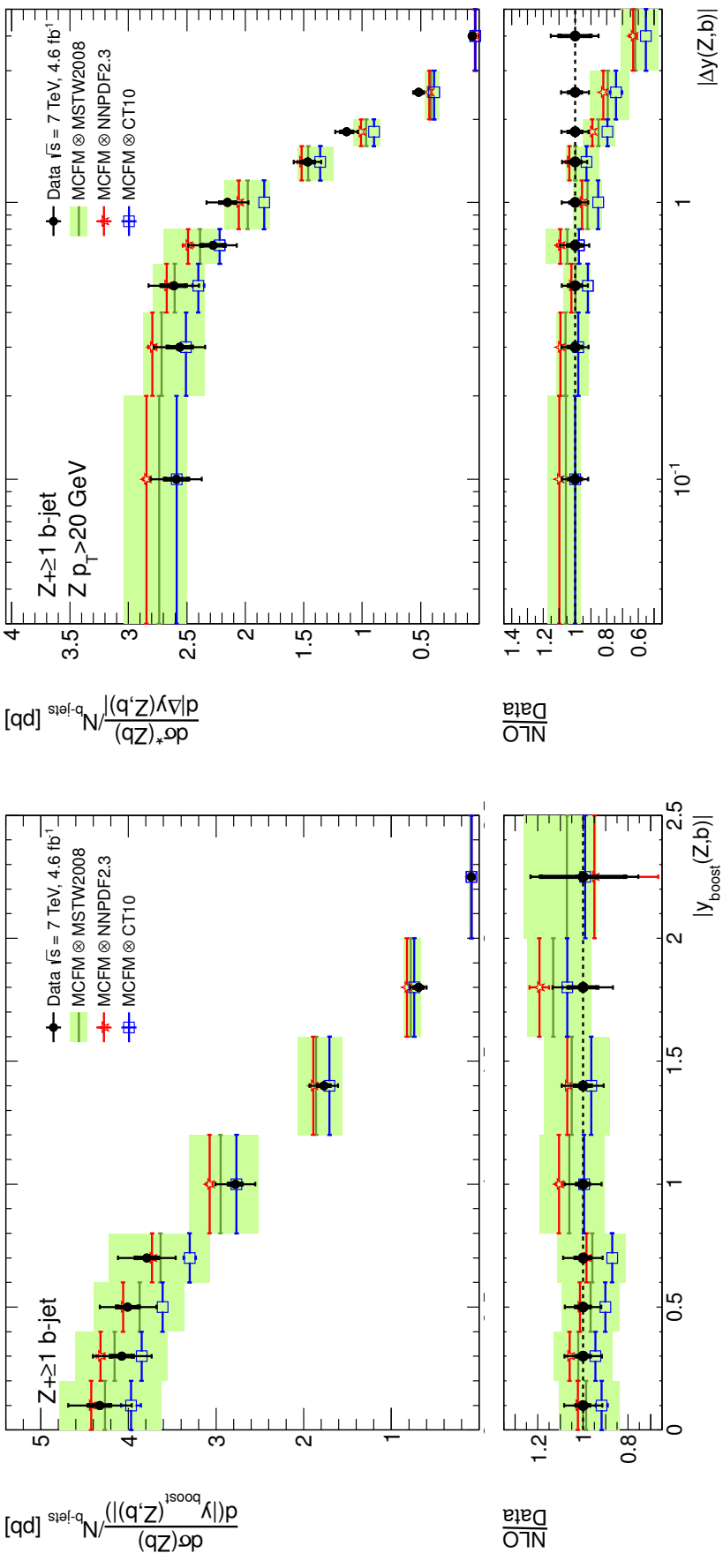

Table 60: Differential cross section for the production of a Z boson in association with at least one b–jet as function of $|y_{boost}(Z,b)|$ (left) and $|\Delta y(Z,b)|$ (right). The data point are presented along with their statistical (inner bars) and total uncertainty (outer bars); the MCFM calculation interfaced with MSTW2008 PDFs is shown with its total uncertainty (light green shaded bands) while all the other predictions are presented with their statistical uncertainty only.

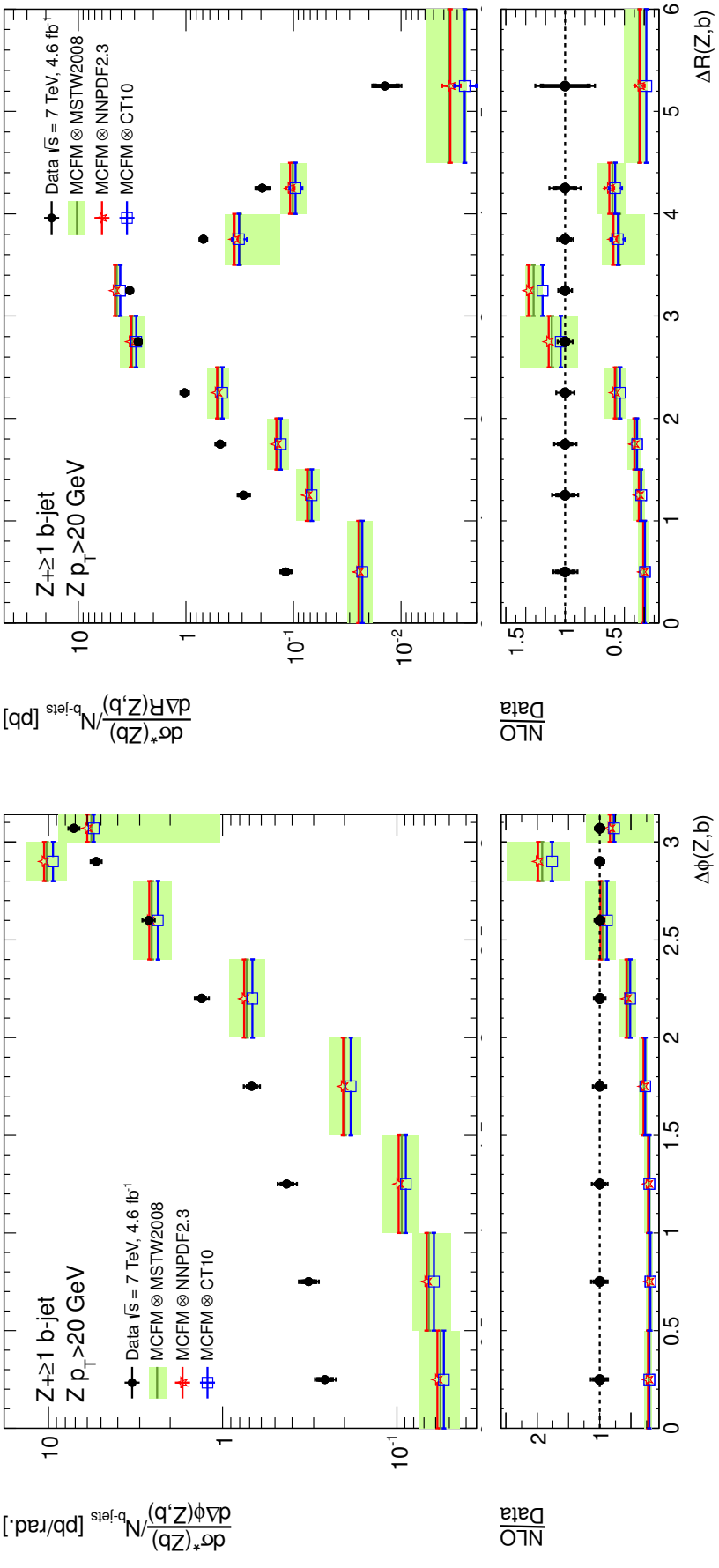

Table 61: Differential cross section for the production of a Z boson in association with at least one b–jet as function of $|\Delta\phi(Z,b)|$ (left) and $\Delta R(Z,b)$ (right). The data point are presented along with their statistical (inner bars) and total uncertainty (outer bars); the MCFM calculation interfaced with MSTW2008 PDFs is shown with its total uncertainty (light green shaded bands) while all the other predictions are presented with their statistical uncertainty only.

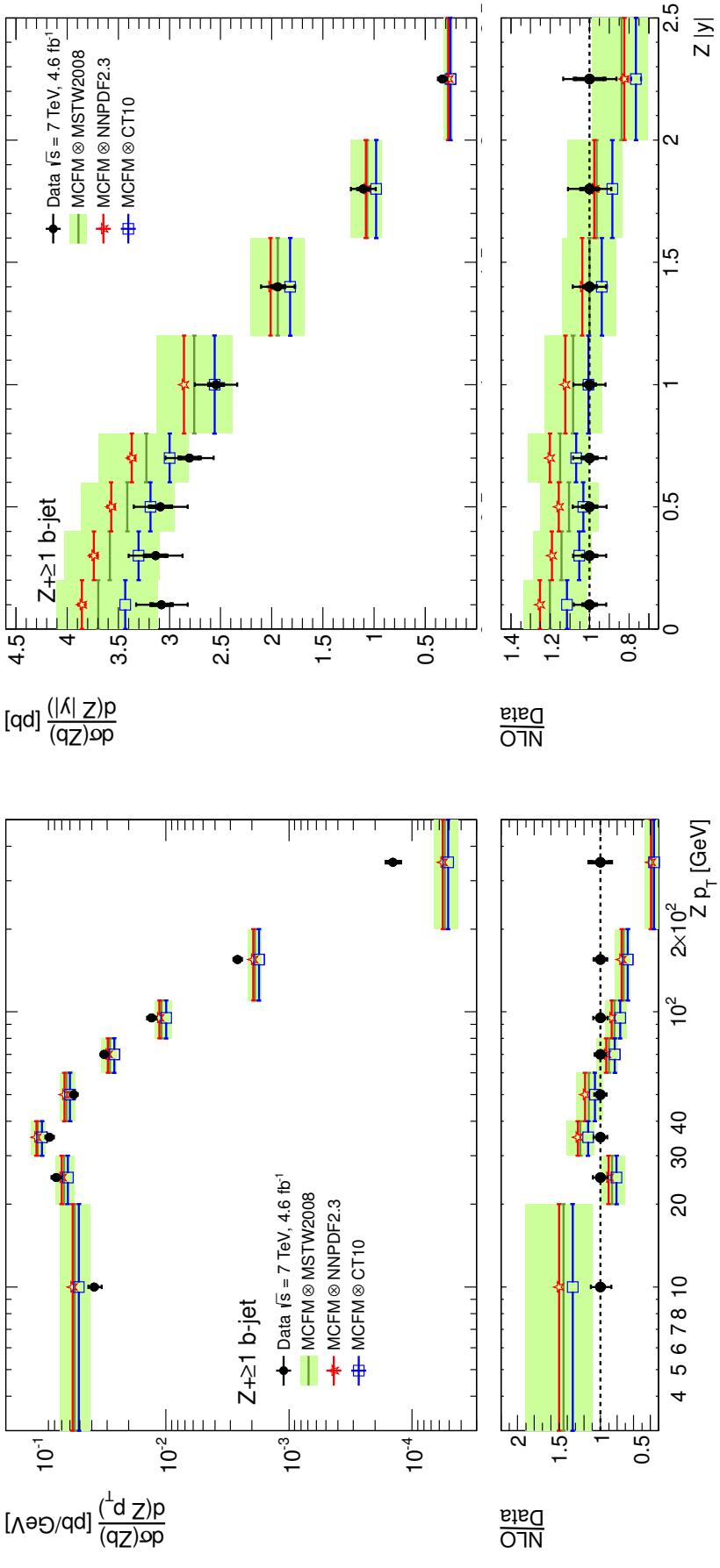

Table 62: Differential cross section for the production of a Z boson in association with at least one b–jet as function of the Z p_T (left) and the Z |y| (right). The data point are presented along with their statistical (inner bars) and total uncertainty (outer bars); the MCFM calculation interfaced with MSTW2008 PDFs is shown with its total uncertainty (light green shaded bands) while all the other predictions are presented with their statistical uncertainty only.

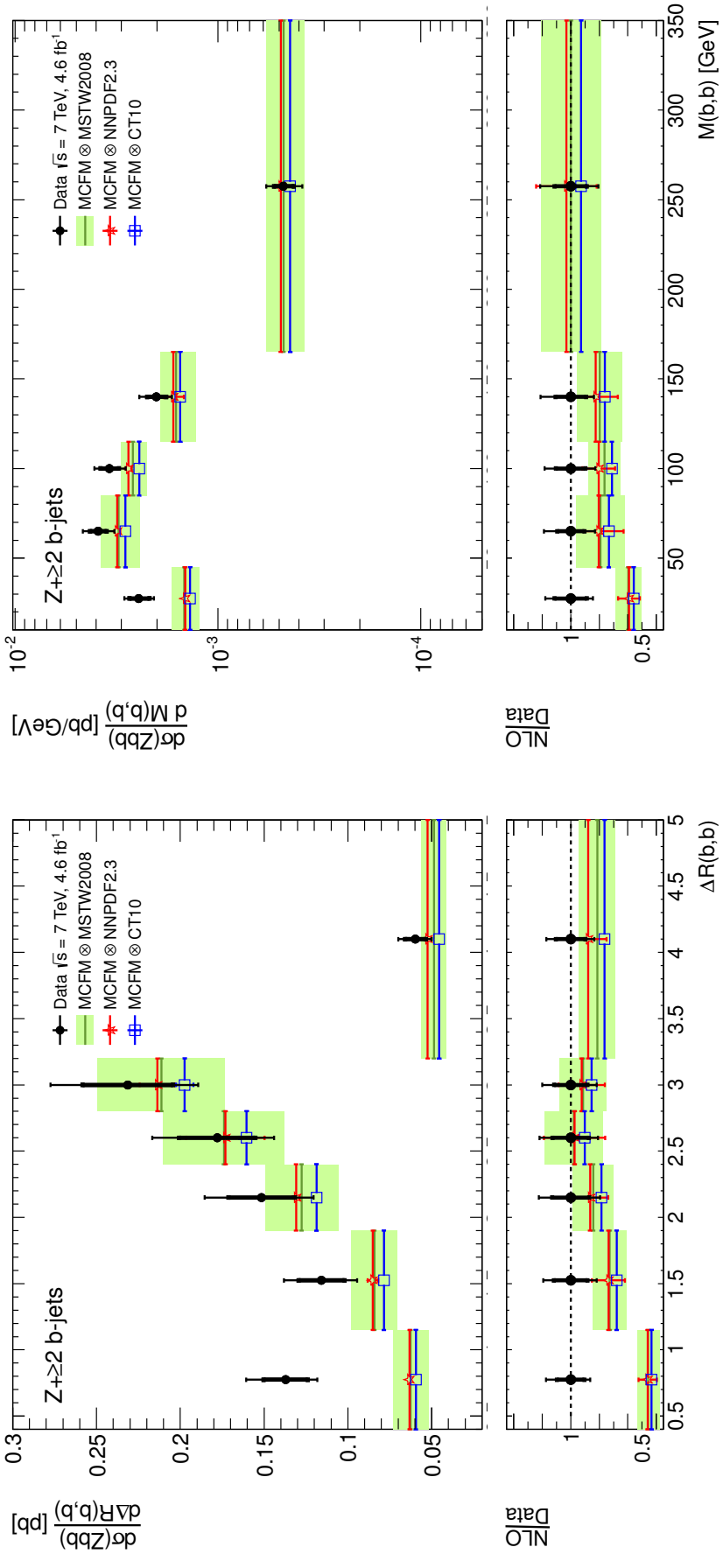

Table 63: Differential cross section for the production of a Z boson in association with at least two b–jet as function of $\Delta R(b, b)$ (left) and $M(b, b)$ (right). The data point are presented along with their statistical (inner bars) and total uncertainty (outer bars); the MCFM calculation interfaced with MSTW2008 PDFs is shown with its total uncertainty (light green shaded bands) while all the other predictions are presented with their statistical uncertainty only.

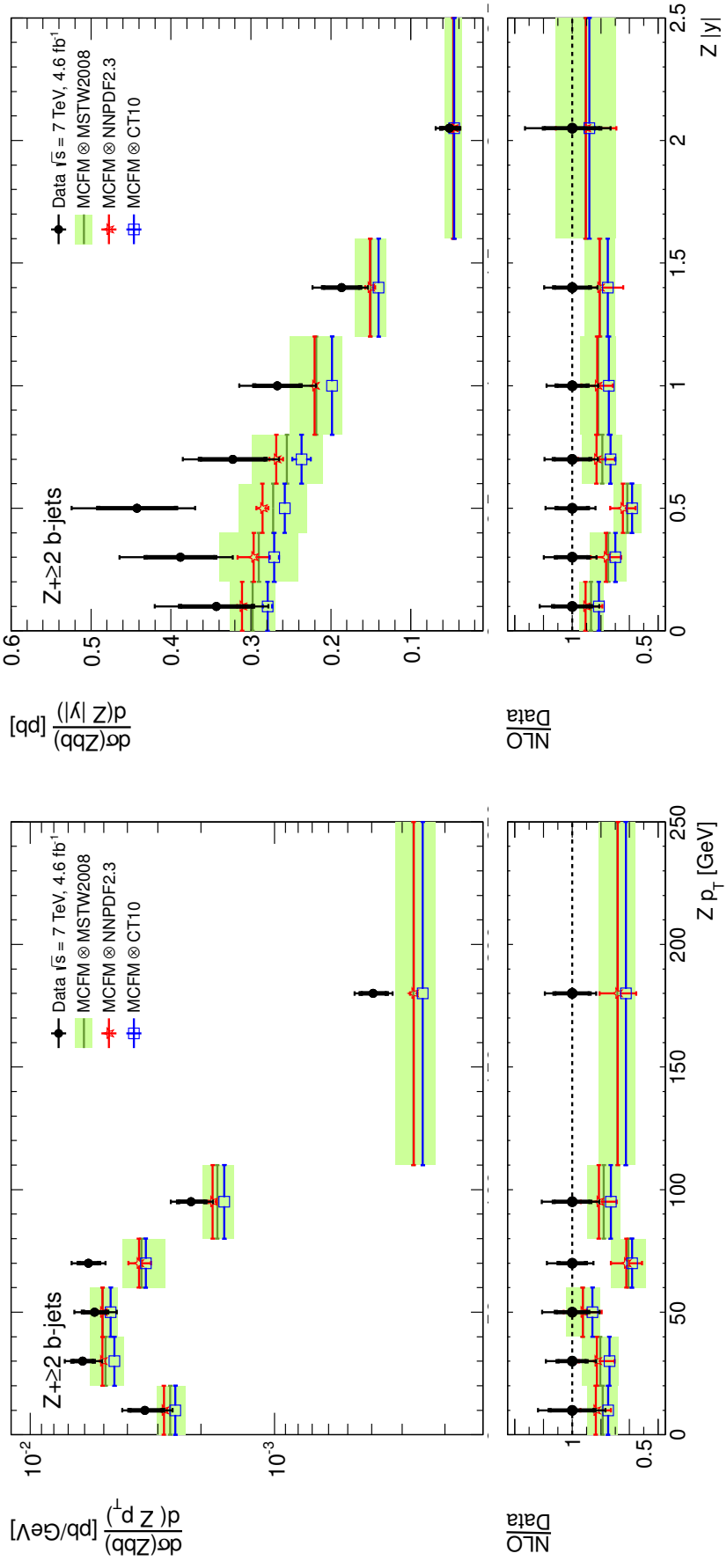

Table 64: Differential cross section for the production of a Z boson in association with at least two b–jet as function of the Z p_T (left) and the Z |y| (right). The data point are presented along with their statistical (inner bars) and total uncertainty (outer bars); the MCFM calculation interfaced with MSTW2008 PDFs is shown with its total uncertainty (light green shaded bands) while all the other predictions are presented with their statistical uncertainty only.

[1] ATLAS Collaboration, "Measurement of differential production cross-sections for a Z boson in association with b-jets in 7 TeV proton-proton collisions with the ATLAS detector", to be submitted to JHEP.

[2] S. L. Glashow, "Partial Symmetries of Weak Interactions," Nucl. Phys. **22** (1961) 579.

[3] S. Weinberg, "A Model of Leptons," Phys. Rev. Lett. **19** (1967) 1264.

[4] A. Salam, "Weak and electromagnetic interactions," Proc. of the 8th Nobel Symposium on 'Elementary Particle Theory, Relativistic Groups and Analyticity', Stockholm, Sweden, 1968, edited by N. Svartholm, p. 367-377.

[5] J. Beringer *et al.* [Particle Data Group Collaboration], "Review of Particle Physics (RPP)," Phys. Rev. D **86** (2012) 010001.

[6] H. P. Nilles, "Supersymmetry, Supergravity and Particle Physics," Phys. Rept. **110** (1984) 1.

[7] I. Antoniadis, N. Arkani-Hamed, S. Dimopoulos and G. R. Dvali, "New dimensions at a millimeter to a Fermi and superstrings at a TeV," Phys. Lett. B **436** (1998) 257 [hep-ph/9804398].

[8] L. Randall and R. Sundrum, "A Large mass hierarchy from a small extra dimension," Phys. Rev. Lett. **83** (1999) 3370 [hep-ph/9905221].

[9] L. Randall and R. Sundrum, "An Alternative to compactification," Phys. Rev. Lett. **83** (1999) 4690 [hep-th/9906064].

[10] The ATLAS and CMS Collaborations "Latest update in the search for the Higgs boson," https://indico.cern.ch/event/197461/

[11] ATLAS Collaboration, "Observation of a new particle in the search for the Standard Model Higgs boson with the ATLAS detector at the LHC," Phys. Lett. B **716** (2012) 1 [arXiv:1207.7214 [hep-ex]].

[12] CMS Collaboration, "Observation of a new boson at a mass of 125 GeV with the CMS experiment at the LHC," Phys. Lett. B **716** (2012) 30 [arXiv:1207.7235 [hep-ex]].

[13] T. Aaltonen *et al.* [CDF and Do Collaborations], "Evidence for a particle produced in association with weak bosons and decaying to a bottom-antibottom quark pair in Higgs boson searches at the Tevatron," Phys. Rev. Lett. **109** (2012) 071804 [arXiv:1207.6436 [hep-ex]].

[14] F. Englert and R. Brout, "Broken Symmetry and the Mass of Gauge Vector Mesons," Phys. Rev. Lett. **13** (1964) 321.

[15] P. W. Higgs, "Broken symmetries, massless particles and gauge fields," Phys. Lett. **12** (1964) 132.

[16] P. W. Higgs, "Broken Symmetries and the Masses of Gauge Bosons," Phys. Rev. Lett. **13** (1964) 508.

[17] P. W. Higgs, "Spontaneous Symmetry Breakdown without Massless Bosons," Phys. Rev. **145** (1966) 1156.

[18] M. Baak, M. Goebel, J. Haller, A. Hoecker, D. Kennedy, R. Kogler, K. Moenig and M. Schott *et al.*, "The Electroweak Fit of the Standard Model after the Discovery of a New Boson at the LHC," Eur. Phys. J. C **72** (2012) 2205 [arXiv:1209.2716 [hep-ph]].

[19] ATLAS Collaboration, "Measurements of Higgs boson production and couplings in diboson final states with the ATLAS detector at the LHC," Phys. Lett. B **726** (2013) 88 [arXiv:1307.1427 [hep-ex]].

[20] CMS Collaboration, "Combination of standard model Higgs boson searches and measurements of the properties of the new boson with a mass near 125 GeV," CMS-PAS-HIG-13-005.

[21] H. Flacher, M. Goebel, J. Haller, A. Hocker, K. Monig and J. Stelzer, "Revisiting the Global Electroweak Fit of the Standard Model and Beyond with Gfitter," Eur. Phys. J. C **60** (2009) 543 [Erratum-ibid. C **71** (2011) 1718] [arXiv:0811.0009 [hep-ph]].

[22] A. Hocker and Z. Ligeti, "CP violation and the CKM matrix," Ann. Rev. Nucl. Part. Sci. **56** (2006) 501 [hep-ph/0605217].

[23] G. F. Sterman, "Partons, factorization and resummation, TASI 95," In *Boulder 1995, QCD and beyond* 327-406 [hep-ph/9606312].

[24] R. K. Ellis, W. J. Stirling and B. R. Webber, "QCD and collider physics," Camb. Monogr. Part. Phys. Nucl. Phys. Cosmol. **8** (1996) 1.

[25] M. E. Peskin and D. V. Schroeder, "An Introduction to quantum field theory," Reading, USA: Addison-Wesley (1995) 842 p

[26] M. R. Whalley, D. Bourilkov and R. C. Group, "The Les Houches accord PDFs (LHAPDF) and LHAGLUE," hep-ph/0508110.

[27] R. D. Ball, V. Bertone, S. Carrazza, C. S. Deans, L. Del Debbio, S. Forte, A. Guffanti and N. P. Hartland *et al.*, "Parton distributions with LHC data," Nucl. Phys. B **867** (2013) 244 [arXiv:1207.1303 [hep-ph]].

[28] H. -L. Lai, M. Guzzi, J. Huston, Z. Li, P. M. Nadolsky, J. Pumplin and C. -P. Yuan, "New parton distributions for collider physics," Phys. Rev. D **82** (2010) 074024 [arXiv:1007.2241 [hep-ph]].

[29] A. D. Martin, W. J. Stirling, R. S. Thorne and G. Watt, "Parton distributions for the LHC," Eur. Phys. J. C **63** (2009) 189 [arXiv:0901.0002 [hep-ph]].

[30] S. Alekhin, J. Blumlein, S. Klein and S. Moch, "The 3, 4, and 5-flavor NNLO Parton from Deep-Inelastic-Scattering Data and at Hadron Colliders," Phys. Rev. D **81** (2010) 014032 [arXiv:0908.2766 [hep-ph]].

[31] S. Alekhin, S. Alioli, R. D. Ball, V. Bertone, J. Blumlein, M. Botje, J. Butterworth and F. Cerutti *et al.*, "The PDF4LHC Working Group Interim Report," arXiv:1101.0536 [hep-ph].

[32] S. Forte and G. Watt, "Progress in the Determination of the Partonic Structure of the Proton," Ann. Rev. Nucl. Part. Sci. **63** (2013) 291 [arXiv:1301.6754 [hep-ph]].

[33] P. Jimenez–Delgado, V. Radescu, "PDF Session Summary," QCD at LHC 2013, https://indico.desy.de/conferenceTimeTable.py?confId=6889#all.detailed

[34] See the indico catalogue "PDF4LHC meeting," https://indico.cern.ch/categoryDisplay.py?categId=2689

[35] Z. Bern *et al.* [NLO Multileg Working Group Collaboration], "The NLO multileg working group: Summary report," arXiv:0803.0494 [hep-ph].

[36] See Les Houches 2013 wiki https://phystev.in2p3.fr/wiki/.

[37] ATLAS Collaboration, "Measurement of the inclusive $W^{\pm}$ and Z/gamma cross sections in the electron and muon decay channels in pp collisions at $\sqrt{s} = 7$ TeV with the ATLAS detector," Phys. Rev. D **85** (2012) 072004 [arXiv:1109.5141 [hep-ex]].

[38] P. Skands, "Introduction to QCD," arXiv:1207.2389 [hep-ph].

[39] L. J. Dixon, "A brief introduction to modern amplitude methods," arXiv:1310.5353 [hep-ph].

[40] L. Barze, G. Montagna, P. Nason, O. Nicrosini, F. Piccinini and A. Vicini, Eur. Phys. J. C **73** (2013) 2474 [arXiv:1302.4606 [hep-ph]].

[41] A. Buckley, J. Butterworth, S. Gieseke, D. Grellscheid, S. Hoche, H. Hoeth, F. Krauss and L. Lonnblad *et al.*, "General-purpose event generators for LHC physics," Phys. Rept. **504** (2011) 145 [arXiv:1101.2599 [hep-ph]].

[42] S. Hoeche, F. Krauss, N. Lavesson, L. Lonnblad, M. Mangano, A. Schalicke and S. Schumann, "Matching parton showers and matrix elements," hep-ph/0602031.

[43] M. L. Mangano, M. Moretti and R. Pittau, "Multijet matrix elements and shower evolution in hadronic collisions: $Wb\bar{b}$ + n jets as a case study," Nucl. Phys. B **632** (2002) 343 [hep-ph/0108069].

[44] J. Alwall, S. Hoche, F. Krauss, N. Lavesson, L. Lonnblad, F. Maltoni, M. L. Mangano and M. Moretti *et al.*, "Comparative study of various algorithms for the merging of parton showers and matrix elements in hadronic collisions," Eur. Phys. J. C **53** (2008) 473 [arXiv:0706.2569 [hep-ph]].

[45] B. R. Webber, "Fragmentation and hadronization," Int. J. Mod. Phys. A **15S1** (2000) 577 [eConf C **990809** (2000) 577] [hep-ph/9912292].

[46] T. Sjostrand, S. Mrenna and P. Z. Skands, "PYTHIA 6.4 Physics and Manual," JHEP **0605** (2006) 026 [hep-ph/0603175].

[47] G. Corcella, I. G. Knowles, G. Marchesini, S. Moretti, K. Odagiri, P. Richardson, M. H. Seymour and B. R. Webber, "HERWIG 6: An Event generator for hadron emission reactions with interfering gluons (including supersymmetric processes)," JHEP **0101** (2001) 010 [hep-ph/0011363].

[48] M. Bahr, S. Gieseke, M. A. Gigg, D. Grellscheid, K. Hamilton, O. Latunde-Dada, S. Platzer and P. Richardson *et al.*, "Herwig++ Physics and Manual," Eur. Phys. J. C **58** (2008) 639 [arXiv:0803.0883 [hep-ph]].

[49] T. Gleisberg, S. .Hoeche, F. Krauss, M. Schonherr, S. Schumann, F. Siegert and J. Winter, "Event generation with SHERPA 1.1," JHEP **0902** (2009) 007 [arXiv:0811.4622 [hep-ph]].

[50] D. J. Lange, "The EvtGen particle decay simulation package," Nucl. Instrum. Meth. A **462** (2001) 152.

[51] S. Catani, Y. L. Dokshitzer, M. H. Seymour and B. R. Webber, "Longitudinally invariant K_t clustering algorithms for hadron hadron collisions," Nucl. Phys. B **406** (1993) 187.

[52] M. Cacciari, G. P. Salam and G. Soyez, "The Anti-k(t) jet clustering algorithm," JHEP **0804** (2008) 063 [arXiv:0802.1189 [hep-ph]].

[53] Y. L. Dokshitzer, G. D. Leder, S. Moretti and B. R. Webber, "Better jet clustering algorithms," JHEP **9708** (1997) 001 [hep-ph/9707323].

[54] M. Wobisch and T. Wengler, "Hadronization corrections to jet cross-sections in deep inelastic scattering," In *Hamburg 1998/1999, Monte Carlo generators for HERA physics* 270-279 [hep-ph/9907280].

[55] ATLAS Collaboration, "Performance of jet substructure techniques for large-R jets in proton-proton collisions at $\sqrt{s}$ = 7 TeV using the ATLAS detector," JHEP **1309** (2013) 076 [arXiv:1306.4945 [hep-ex]].

[56] CMS Collaboration, "Pseudorapidity and leading transverse momentum distributions of charged particles in pp collisions at 8 TeV," CMS-PAS-FSQ-12-026.

[57] ATLAS Collaboration, "The underlying event in jet events at 7 TeV with the ATLAS experiment," ATLAS-CONF-2012-164.

[58] R. D. Ball, M. Bonvini, S. Forte, S. Marzani and G. Ridolfi, "Higgs production in gluon fusion beyond NNLO," Nucl. Phys. B **874** (2013) 746 [arXiv:1303.3590 [hep-ph]].

[59] C. Anastasiou, C. Duhr, F. Dulat and B. Mistlberger, "Soft triple-real radiation for Higgs production at N3LO," JHEP **1307** (2013) 003 [arXiv:1302.4379 [hep-ph]].

[60] C. Anastasiou, C. Duhr, F. Dulat, F. Herzog and B. Mistlberger, "Real-Virtual contributions to the inclusive Higgs cross-section at N3LO," arXiv:1311.1425 [hep-ph].

[61] ATLAS Collaboration, "Measurement of the inclusive jet cross section in pp collisions at $\sqrt{(}s) = 2.76$ TeV and comparison to the inclusive jet cross section at $\sqrt{s} = 7$ TeV using the ATLAS detector," Eur. Phys. J. C **73** (2013) 2509 [arXiv:1304.4739 [hep-ex]].

[62] CMS Collaboration, "PDF constraints and extraction of the strong coupling constant from the inclusive jet cross section at 7 TeV," CMS-PAS-SMP-12-028.

[63] H. Ita, Z. Bern, L. J. Dixon, F. Febres Cordero, D. A. Kosower and D. Maitre, "Precise Predictions for Z + 4 Jets at Hadron Colliders," Phys. Rev. D **85** (2012) 031501 [arXiv:1108.2229 [hep-ph]].

[64] ATLAS Collaboration, "Measurement of the production cross section of jets in association with a Z boson in pp collisions at $\sqrt{s}$ = 7 TeV with the ATLAS detector," JHEP **1307** (2013) 032 [arXiv:1304.7098 [hep-ex]].

[65] ATLAS Collaboration, "Measurement of isolated-photon pair production in pp collisions at $\sqrt{s} = 7$ TeV with the ATLAS detector," JHEP **1301** (2013) 086 [arXiv:1211.1913 [hep-ex]].

[66] ATLAS Collaboration, "The ATLAS Experiment at the CERN Large Hadron Collider," JINST **3** (2008) S08003.

[67] ATLAS Collaboration, https://twiki.cern.ch/twiki/bin/view/AtlasPublic/LuminosityPublicResults.

[68] N. Orlando [ATLAS Collaboration], "Muon reconstruction efficiency measurement in the ATLAS experiment," EPJ Web Conf. **28** (2012) 12040.

[69] ATLAS Collaboration, "A measurement of the muon reconstruction efficiency in 2010 ATLAS data using jpsi decays," ATLAS-CONF-2012-125.

[70] ATLAS Collaboration, "Muon reconstruction efficiency and momentum resolution of the ATLAS experiment in proton-proton collisions at $\sqrt{s}$=7 TeV in 2010," arXiv:1404.4562 [hep-ex].

[71] ATLAS Collaboration, "Preliminary results on the muon reconstruction efficiency, momentum resolution, and momentum scale in ATLAS 2012 pp collision data," ATLAS-CONF-2013-088.

[72] ATLAS Collaboration, https://atlas.web.cern.ch/Atlas/GROUPS/PHYSICS/EGAMMA/PublicPlots/20121403/EfficiencyPileup/ATL-COM-PHYS-2012-260/index.html.

[73] ATLAS Collaboration, "Electron performance measurements with the ATLAS detector using the 2010 LHC proton-proton collision data," Eur. Phys. J. C **72** (2012) 1909 [arXiv:1110.3174 [hep-ex]].

[74] ATLAS Collaboration, "Measurements of the photon identification efficiency with the ATLAS detector using 4.9 fb-1 of pp collision data collected in 2011," ATLAS-CONF-2012-123.

[75] ATLAS Collaboration, "Jet energy scale and its systematic uncertainty in proton-proton collisions at $\sqrt{s} = 7$ TeV with ATLAS 2011 data," ATLAS-CONF-2013-004.

[76] ATLAS Collaboration, "Single hadron response measurement and calorimeter jet energy scale uncertainty with the ATLAS detector at the LHC," Eur. Phys. J. C **73** (2013) 2305 [arXiv:1203.1302 [hep-ex]].

[77] ATLAS Collaboration, "Determination of the tau energy scale and the associated systematic uncertainty in proton-proton collisions at $\sqrt{s} = 8$ TeV with the ATLAS detector at the LHC in 2012," ATLAS-CONF-2013-044.

[78] ATLAS Collaboration, "Identification of the Hadronic Decays of Tau Leptons in 2012 Data with the ATLAS Detector," ATLAS-CONF-2013-064.

[79] ATLAS Collaboration, "Performance of Missing Transverse Momentum Reconstruction in ATLAS with 2011 Proton-Proton Collisions at sqrts = 7 TeV," ATLAS-CONF-2012-101.

[80] ATLAS Collaboration, "Commissioning of the ATLAS high-performance b-tagging algorithms in the 7 TeV collision data," ATLAS-CONF-2011-102.

[81] ATLAS Collaboration, "Calibrating the b-Tag and Mistag Efficiencies of the SV0 b-Tagging Algorithm in 3 pb^{-1} of Data with the ATLAS Detector," ATLAS-CONF-2010-099.

[82] ATLAS Collaboration, "Measurement of the b-tag Efficiency in a Sample of Jets Containing Muons with 5 fb-1 of Data from the ATLAS Detector," ATLAS-CONF-2012-043.

[83] ATLAS Collaboration, "b-Jet Tagging Efficiency Calibration using the System8 Method," ATLAS-CONF-2011-143.

[84] ATLAS Collaboration, "Measuring the b-tag efficiency in a top-pair sample with 4.7 fb-1 of data from the ATLAS detector," ATLAS-CONF-2012-097.

[85] ATLAS Collaboration, https://twiki.cern.ch/twiki/bin/view/AtlasPublic/FlavourTaggingPublicResultsCollisionData.

[86] ATLAS Collaboration, "Measurement of the Mistag Rate with 5 fb-1 of Data Collected by the ATLAS Detector," ATLAS-CONF-2012-040.

[87] CMS Collaboration, "Measurement of the cross section and angular correlations for associated production of a Z boson with b hadrons in pp collisions at $\sqrt{s} = 7$ TeV," JHEP **1312** (2013) 039 [arXiv:1310.1349 [hep-ex]].

[88] CMS Collaboration, "Measurement of the production cross sections for a Z boson and one or more b jets in pp collisions at $\sqrt{s} = 7$ TeV," arXiv:1402.1521 [hep-ex].

[89] V. M. Abazov *et al.* [Do Collaboration], "A measurement of the ratio of inclusive cross sections $\sigma(p\bar{p} \to Z + b - jet)/\sigma(p\bar{p} \to Z + jet)$ at $\sqrt{s} = 1.96$ TeV," Phys. Rev. Lett. **94** (2005) 161801 [hep-ex/0410078].

[90] T. Aaltonen *et al.* [CDF Collaboration], "Measurement of Cross Sections for b Jet Production in Events with a Z Boson in p^- anti-p Collisions at $\sqrt{s}$ = 1.96-TeV," Phys. Rev. D **79** (2009) 052008 [arXiv:0812.4458 [hep-ex]].

[91] V. M. Abazov *et al.* [Do Collaboration], "Measurement of the ratio of differential cross sections $\sigma(p\bar{p} \to Z + bjet)/\sigma(p\bar{p} \to Z + jet)$ in $p\bar{p}$ collisions at $\sqrt{(s)} = 1.96$ TeV," Phys. Rev. D **87** (2013) 9, 092010 [arXiv:1301.2233 [hep-ex]].

[92] ATLAS Collaboration, "Measurement of the cross-section for b^- jets produced in association with a Z boson at $\sqrt{s} = 7$ TeV with the ATLAS detector," Phys. Lett. B **706** (2012) 295 [arXiv:1109.1403 [hep-ex]].

[93] CMS Collaboration, "Measurement of the Z/gamma*+b-jet cross section in pp collisions at 7 TeV," JHEP **1206** (2012) 126 [arXiv:1204.1643 [hep-ex]].

[94] S. Agostinelli *et al.* [GEANT4 Collaboration], "GEANT4: A Simulation toolkit," Nucl. Instrum. Meth. A **506** (2003) 250.

[95] M. L. Mangano, M. Moretti, F. Piccinini, R. Pittau and A. D. Polosa, "ALPGEN, a generator for hard multiparton processes in hadronic collisions," JHEP **0307** (2003) 001 [hep-ph/0206293].

[96] P. M. Nadolsky, H. -L. Lai, Q. -H. Cao, J. Huston, J. Pumplin, D. Stump, W. -K. Tung and C. -P. Yuan, "Implications of CTEQ global analysis for collider observables," Phys. Rev. D **78** (2008) 013004 [arXiv:0802.0007 [hep-ph]].

[97] J. M. Butterworth, J. R. Forshaw and M. H. Seymour, "Multiparton interactions in photoproduction at HERA," Z. Phys. C **72** (1996) 637 [hep-ph/9601371].

[98] C. Anastasiou, L. J. Dixon, K. Melnikov and F. Petriello, "High precision QCD at hadron colliders: Electroweak gauge boson rapidity distributions at NNLO," Phys. Rev. D **69** (2004) 094008 [hep-ph/0312266].

[99] S. Frixione and B. R. Webber, "Matching NLO QCD computations and parton shower simulations," JHEP **0206** (2002) 029 [hep-ph/0204244].

[100] S. Frixione, P. Nason and B. R. Webber, "Matching NLO QCD and parton showers in heavy flavor production," JHEP **0308** (2003) 007 [hep-ph/0305252].

[101] B. P. Kersevan and E. Richter-Was, "The Monte Carlo event generator AcerMC version 2.0 with interfaces to PYTHIA 6.2 and HERWIG 6.5," hep-ph/0405247.

[102] A. Sherstnev and R. S. Thorne, "Different PDF approximations useful for LO Monte Carlo generators," arXiv:0807.2132 [hep-ph].

[103] M. Aliev, H. Lacker, U. Langenfeld, S. Moch, P. Uwer and M. Wiedermann, "HATHOR: HAdronic Top and Heavy quarks crOss section calculatoR," Comput. Phys. Commun. **182** (2011) 1034 [arXiv:1007.1327 [hep-ph]].

[104] ATLAS Collaboration, "Performance of the ATLAS Electron and Photon Trigger in p-p Collisions at sqrts = 7 TeV in 2011," ATLAS-CONF-2012-048.

[105] ATLAS Collaboration, "Performance of the ATLAS muon trigger in 2011," ATLAS-CONF-2012-099.

[106] M. Cacciari, G. P. Salam and G. Soyez, "The Anti-k(t) jet clustering algorithm," JHEP **0804** (2008) 063 [arXiv:0802.1189 [hep-ph]].

[107] M. Cacciari, G. P. Salam and G. Soyez, "FastJet User Manual," Eur. Phys. J. C **72** (2012) 1896 [arXiv:1111.6097 [hep-ph]].

[108] ATLAS Collaboration, "Pile-up jet energy scale corrections using the jet-vertex fraction method," ATL-COM-PHYS-2009-180.

[109] ATLAS Collaboration, "Measuring the b-tag efficiency in a top-pair sample with 4.7 fb^{-1} of data from the ATLAS detector," ATLAS-CONF-2012-097.

[110] ATLAS Collaboration, "Measurement of the Mistag Rate with 5 fb^{-1} of Data Collected by the ATLAS Detector," ATLAS-CONF-2012-040.

[111] ATLAS Collaboration, "b-jet tagging calibration on c-jets containing D^{*+} mesons," ATLAS-CONF-2012-039.

[112] W. Verkerke and D. P. Kirkby, "The RooFit toolkit for data modeling," eConf C **0303241** (2003) MOLT007 [physics/0306116].

[113] ATLAS Collaboration, "Performance of the ATLAS Secondary Vertex b-tagging Algorithm in 7 TeV Collision Data," ATLAS-CONF-2010-042.

[114] ATLAS Collaboration, "Measurement of the cross-section for W boson production in association with b-jets in pp collisions at $\sqrt{s}$ = 7 TeV with the ATLAS detector," JHEP **1306** (2013) 084 [arXiv:1302.2929 [hep-ex]].

[115] A. Bundock, G. Chiodini, P. Davison, D. Hellmich, G. Hesketh, S. Hillert, E. Jansen, P. Laycock, N. Orlando, M. Sanders, S. Spagnolo, M. Tibbetts, D. Vladoiu, "Measurement of Zb and Zbb cross sections with 4.6 fb-1 of 7 TeV ATLAS data," ATL-COM-PHYS-2012-1504.

[116] G. Cowan, "Statistical data analysis," Oxford, UK: Clarendon (1998) 197 p

[117] N. D. Gagunashvili, "chi**2 test for the comparison of weighted and unweighted histograms,"

[118] J. M. Butterworth, A. Arbey, L. Basso, S. Belov, A. Bharucha, F. Braam, A. Buckley and M. Campanelli *et al.*, arXiv:1003.1643 [hep-ph], arXiv:1003.1643 [hep-ph].

[119] G. D'Agostini, "A Multidimensional unfolding method based on Bayes' theorem," Nucl. Instrum. Meth. A **362** (1995) 487.

[120] T. Adye, "Unfolding algorithms and tests using RooUnfold," arXiv:1105.1160 [physics.data-an].

[121] ATLAS Collaboration, "Improved luminosity determination in pp collisions at $\sqrt{s}$ = 7 TeV using the ATLAS detector at the LHC," Eur. Phys. J. C **73** (2013) 2518 [arXiv:1302.4393 [hep-ex]].

[122] ATLAS Collaboration, "Measurement of hard double-parton interactions in $W(\rightarrow l\nu)$+ 2 jet events at $\sqrt{s}$=7 TeV with the ATLAS detector," New J. Phys. **15** (2013) 033038 [arXiv:1301.6872 [hep-ex]].

[123] ATLAS Collaboration, "Measurement of the inclusive and dijet cross-sections of b^- jets in pp collisions at $\sqrt{s} = 7$ TeV with the ATLAS detector," Eur. Phys. J. C **71** (2011) 1846 [arXiv:1109.6833 [hep-ex]].

[124] R. Frederix, S. Frixione, V. Hirschi, F. Maltoni, R. Pittau and P. Torrielli, "W and $Z/\gamma*$ boson production in association with a bottom-antibottom pair," JHEP **1109** (2011) 061 [arXiv:1106.6019 [hep-ph]].

[125] J. M. Campbell and R. K. Ellis, "MCFM for the Tevatron and the LHC," Nucl. Phys. Proc. Suppl. **205-206** (2010) 10 [arXiv:1007.3492 [hep-ph]].

[126] J. M. Campbell, R. K. Ellis, F. Maltoni and S. Willenbrock, "Production of a Z boson and two jets with one heavy-quark tag," Phys. Rev. D **73** (2006) 054007 [Erratum-ibid. D **77** (2008) 019903] [hep-ph/0510362].

[127] J. M. Campbell, R. K. Ellis, F. Maltoni and S. Willenbrock, "Associated production of a Z Boson and a single heavy quark jet," Phys. Rev. D **69** (2004) 074021 [hep-ph/0312024].

[128] F. Maltoni, G. Ridolfi and M. Ubiali, "b-initiated processes at the LHC: a reappraisal," JHEP **1207** (2012) 022 [Erratum-ibid. **1304** (2013) 095] [arXiv:1203.6393 [hep-ph]].

[129] P. Golonka and Z. Was, "PHOTOS Monte Carlo: A Precision tool for QED corrections in Z and *W* decays," Eur. Phys. J. C **45** (2006) 97 [hep-ph/0506026].

[130] J. -C. Winter, F. Krauss and G. Soff, "A Modified cluster hadronization model," Eur. Phys. J. C **36** (2004) 381 [hep-ph/0311085].

[131] J. Campbell, K. Ellis, C. Williams, "A Monte Carlo for FeMtobarn processes at Hadron Colliders," http://mcfm.fnal.gov

[132] P. Z. Skands, "Tuning Monte Carlo Generators: The Perugia Tunes," Phys. Rev. D **82** (2010) 074018 [arXiv:1005.3457 [hep-ph]].

[133] A. D. Martin, W. J. Stirling, R. S. Thorne and G. Watt, "Heavy-quark mass dependence in global PDF analyses and 3- and 4-flavour parton distributions," Eur. Phys. J. C **70** (2010) 51 [arXiv:1007.2624 [hep-ph]].

[134] ATLAS Collaboration, "Dynamics of isolated-photon plus jet production in pp collisions at $\sqrt{(s)} = 7$ TeV with the ATLAS detector," Nucl. Phys. B **875** (2013) 483 [arXiv:1307.6795 [hep-ex]].